Spring 2013

Spin Dependence in Polarized Proton-Proton Elastic Scattering at RHIC

Donika Plyku
Old Dominion University

SPIN DEPENDENCE IN POLARIZED PROTON-PROTON ELASTIC SCATTERING AT RHIC

by

Donika Plyku
Integrated B.S. and M.S. in Physics Education, January 2005, Middle East Technical University, Turkey
M.S. in Physics, May 2007, Old Dominion University

A Dissertation Submitted to the Faculty of
Old Dominion University in Partial Fulfillment of the
Requirements for the Degree of

DOCTOR OF PHILOSOPHY

PHYSICS

OLD DOMINION UNIVERSITY
May 2013

Approved by:

Stephen Bültmann (Director)

Gail Dodge (Member)

Leposava Vuskovic (Member)

G. Wallace Van Orden (Member)

Richard Zimmerman (Member)

ABSTRACT

SPIN DEPENDENCE IN POLARIZED PROTON-PROTON ELASTIC SCATTERING AT RHIC

Donika Plyku
Old Dominion University, 2013
Director: Dr. Stephen Bültmann

The STAR (Solenoidal Tracker At RHIC - Relativistic Heavy Ion Collider) experiment is equipped with Roman Pots, insertion devices that allow detectors to be moved close to the beam for the measurement of high energy protons scattered at very small angles. This setup, together with the unique capability of RHIC to collide spin-polarized proton beams, allows STAR to study both the dynamics and the spin-dependence of the proton-proton (pp) elastic scattering process. Silicon strip detectors, installed inside the Roman Pots, measure tracks of protons scattered diffractively at very small angles. In a dedicated run with special beam optics during the 2009 RHIC run, the collaboration collected about 20 million elastic events with transversely polarized proton beams at the center of mass energy $\sqrt{s} = 200$ GeV and four momentum transfer squared (t) range of $0.003 \leq |t| \leq 0.035$ $(\mathrm{GeV}/c)^2$, where, due to the Coulomb Nuclear Interference (CNI), a measurable single spin asymmetry arises. While the electromagnetic interaction can be determined in QED, the description of the hadronic interaction at small-t scattering requires the use of non-perturbative techniques in QCD, and, phenomenological models, rather than pQCD, are used to describe the exchange mechanism. High energy diffractive scattering at small-t is dominated by the Pomeron exchange, treated in pQCD as a color singlet combination of two gluons carrying quantum numbers of the vacuum ($J^{PC} = 0^{++}$). In this dissertation, I report on a high precision measurement of the transverse single spin asymmetry A_N at $\sqrt{s} = 200$ GeV in pp elastic scattering at RHIC. The measured A_N and its t-dependence are consistent with the absence of a hadronic spin-flip amplitude. The major contribution to the uncertainty in A_N comes from the uncertainty in the beam polarization measurement. The presented results provide a precise measurement in the non-perturbative QCD regime, where experimental data are indispensable, and, a significant constraint on the spin-flip component of the Pomeron.

To my parents.

ACKNOWLEDGEMENTS

The completion of the research work presented in this dissertation, would not have been possible without the continuous support, guidance, help and encouragement of my dissertation advisor and my mentor through the years of graduate school, Dr. Stephen L. Bültmann and my fellow graduate student and friend Ivan Koralt. They have both showed me how to approach challenges with calmness and confidence.

I am deeply grateful to Dr. Bültmann for his continuous and patient support and guidance through these years, for always sharing his knowledge and experience so naturally with everyone, for always being there to listen and give a good advice not only on problems encountered during research, but also on different matters, for the care that he has shown while at ODU and during several trips to Brookhaven National Laboratory (BNL), for always encouraging me and helping me see the way to the solutions, and for always being very understanding and willing to help. I thank Dr. Bültmann for his detailed and constructive editing comments on this manuscript. I would like to thank Dr. Bültmann also, for encouraging and supporting me to participate in several major conferences and for always helping during the preparation phase. I have always felt much more motivated and enthusiastic about Nuclear, High-Energy, Particle Physics and especially Spin Physics after attending major international conferences in these fields, RHIC/AGS users meetings and STAR collaboration meetings. I was always amazed by the work that has been done on resolving the famous proton spin puzzle. Recently, Dr. Bültmann has provided his great help during my search for and application to post-doctoral positions, by supporting my enthusiastic interest in Medical Physics and in Teaching, and, by giving valuable advice on job interview matters.

The road to this thesis has not been an easy one. Fortunately, I was surrounded by encouraging folks who offered a helping hand when I faced difficulties. The research work and traveling to BNL, became more enjoyable when Ivan joined the experiment. I owe special thanks to Ivan, for always helping me with the computational difficulties I faced, for reminding me that asking questions is not a sign of weakness, but it is valued, for always helping me believe in myself and for many helpful discussions in trying to solve various analysis problems. He has contributed to the completion of this work immensely. I will always be grateful to him.

I am deeply grateful to my dissertation committee members: Dr. Gail Dodge,

Dr. Leposava Vuskovic, Dr. J. Wallace Van-Orden and Dr. Richard Zimmerman, for their valuable comments during my annual review presentations, their understanding and patience during the preparation of this dissertation and their contributions to my thesis.

I would like to thank Dr. Bültmann and the Experimental Nuclear Physics Group at ODU, for managing and providing the funding support for this work, which required traveling often to BNL. Without this financial support, the work would not have been possible. I would also like to thank all the exceptional professors in the Experimental Nuclear Physics Group at ODU: Dr. Sebastian Kuhn, Dr. Moskov Amaryan, Dr. Charles Hyde, Dr. Larry Weinstein, Dr. Gail Dodge and Dr. Stephen Bültmann, for their efforts in training the next generation of nuclear and particle physicists. It has been a privilege to work beside outstanding faculty members like you all. I had the opportunity to teach Physics 101/102 courses with an exceptional teacher, Dr. Larry Weinstein, who has showed me how to explain complicated physics concepts in a simple way. I would also like to recognize the help of Dr. Charles Sukenik, Dr. Desmond Cook and Dr. Svetozar Popovic during my graduate studies.

I would like to express my gratitude to Dr. Gail Dodge and Dr. Leposava Vuskovic, for their efforts in motivating and helping all the women students at the Physics Dept. at ODU in pursuing a physics career. I thank them for their hospitality and warm conversations, during our several "women in physics" gatherings and dinners.

I would also like to acknowledge the help of many faculty and staff members at the Physics Dept. at ODU: Mr. Walt Hooks, Mrs. Delicia Malin, Mrs. Annette Guzman-Smith and Mrs. Lisa Okun for their help in facilitating our work at the department. I would like to recognize the late Mr. Bob Evans, for his help in facilitating the physics laboratory classes during my time as a TA.

This work would not have started without the completion of the experiment at RHIC in 2009. I owe a big debt of gratitude to our experiment's spokes-person, Dr. Wlodek Guryn, for his great efforts and constant communication with RHIC and STAR management to make the experiment run, for sharing his expertise and knowledge on different matters related to the experiment and the analysis, for very valuable suggestions and discussions during our weekly meetings and for his guidance and help during this work. I owe special thanks to all the members of our experiment

at STAR: Dr. Igor Alekseev and Dr. Dimitri Svirida for their efforts and outstanding work in the commissioning of the experimental setup and their very valuable inputs and expertise in the analysis work; Dr. Jeong-Hun Lee, for sharing his expertise in both computational and theoretical knowledge and for always giving valuable comments and suggestions on how to solve analysis problems; Dr. Kin Yip, for always being ready to help with analysis questions and computational problems, for his work on preparing the online monitoring software for Run09, his work on the "cooking" of the raw data, and for sharing his expertise in this work; Dr. Steve Tepikian, Dr. Philip Pile and Dr. Angelika Drees, who, with their expertise in accelerator physics, had important roles on beam and optics commissioning for Run09 and during analysis work; Dr. Ron Gill, for his help during the run and Tomek Obrebski for his contribution in the analysis. They all provided inner wisdom and indispensable suggestions in their fields of expertise, which contributed immensely to this dissertation. Congratulations to all of you in the recently published paper and I wish you all success in the future.

I sincerely believe that I have been very privileged to have been part of the STAR collaboration and to have been working with internationally well-known scientists in the Nuclear and High-Energy Physics field. It was an exciting and highly educational experience to be working at STAR IR and STAR control room, and at our experiment setup located inside the RHIC tunnel, to participate in the shifts with other STAR group members, and to join several STAR collaboration/analysis meetings. This has been a unique experience for me. I always enjoyed attending the RHIC/AGS annual group meetings, where I had the opportunity to listen to and learn from outstanding scientists in the High-Energy and Accelerator Physics fields. I would like to acknowledge the help of many scientists and STAR collaboration members and experts, especially Dr. Bill Christie, Dr. Yury Gorbunov, Dr. Andrzej Sandacz, Dr. Jeff Landgraf, Dr. Dana Beavis, Dr. Tonko Ljubicic and Dr. William Llope, who with their inputs, helped us have a smooth experimental run.

Traveling often to BNL as a graduate student was at times an isolating experience, but the feelings of loneliness were often broken by the company of my friend Dr. Astrid Morreale, with whom I had many interesting discussions over coffee, especially on spin physics, and the help of Mrs. Melanie Echmalian, who I could always have a nice conversation with and who was ready to help with different issues at the department. I had a nice opportunity to get to know and speak to Dr. Christine

Aidala, who motivated me with her successful physics career.

My heartfelt thanks to my friends and colleagues at ODU: Maha Omar, Dr. Heghine Seraydaryan, Dr. Senthilraja Singaravelu, Michael Mayer, Dr. Sharon Careccia, Dr. Jan Drake, Dr. Giovanni Chirilli, Dr. Jixie Zhang, Krishna Adhikari and Suman Koirala, who were always ready to help with different questions I had and who shared their knowledge, and from whom I learned a lot about different cultures and languages and whom I shared good moments with. Special thanks to Michael Mayer who was always ready to help on C++ and ROOT when I needed help. My heartfelt thanks to Maha Omar and Dr. Heghine Seraydaryan, who always motivated me to succeed and who always were there when I needed someone to talk to. Their company always made me happier. My dear friend Maha Omar, you have done a lot for me and listened to me as patiently as a sister would do. I will always be indebted to you. I wish I can provide the same support to you during the writing of your dissertation. I will always remember the great help of Dr. Heghine Seraydaryan and Dr. Senthilraja Singaravelu, during the preparation for the qualifying exam. I wish success to all my friends at the physics department at ODU.

I would like to extend my profound gratitude to my good friend Mark J. Shaw and his parents, Florence and Arthur Shaw. They helped me greatly during my first few years of graduate school. I thank Mark for helping me immensely from the first time I came to US, while taking graduate physics courses, while preparing for the qualifying exam, while working as a TA and beginning as a RA on this experiment. I owe my TA award to him. But, most importantly I would like to thank Mark for sharing his wisdom on different life matters. I thank Mrs. Florence Shaw and Mr. Arthur Shaw for their hospitality and generosity, for wonderful thanksgiving dinners, for their help and support and most importantly their care. I have learned a lot from you all and I will always remember you.

I would like to express my deep gratitude to my close friends: Drilona Haxhiu, Dr. Valbona Hoxha, Eglantina Stergu, Aynur Er, Meral Balik, Yeter Canan and Kubra Gölge for their support during all these years in the US. With their wisdom and prayers, they have helped me become a better person. I would like to thank my colleagues, Dr. Indrit Hoxha, Dr. Oguz Er, Dr. Salim Balik, Dr. Mustafa Canan, Dr. Serkan Gölge and Bayram Torayev, for their help and advice on various matters. I extend my sincere gratitude to all the ladies in the Turkish community of Hampton Roads and several other friends, especially Dr. Nihal Colakoglu-Göküs,

Hanife Cetin, Monika Cami, Özgül Yasar, Mualla Kahraman, Rukiye Kahraman, Liz Garcia Rios, Anna Udalova, Sara Ozar, Fatma Üstün and Fatmana Kocaogul, for their unmatchable company and care, and their hospitality. The Er family became my family here in the US, and supported me during a hard time in my life. Their amazing children, Alper and Bahar have always made me smile and be happier.

I save my biggest gratitude to those closest to me, my family. I dedicate this dissertation to my father Kadri Plyku and my mother Natasha Plyku. They are my role models in life and their love is irreplaceable. As physics and bio-chemistry teachers themselves, they inspired in me the interest for science, education and teaching, which pushed me towards this path. Succeeding in any of the trips of this journey would not have been possible without my parents. I thank from the bottom of my heart my sister Marsela Plyku Demaj, my brother Shefqet Plyku for their unconditional love and support they have given me, my brother-in-law Armando Demaj, who has been like a big brother to me all the years I have known him and my cousin Ivianela Prifti. My two little nephews, Saim and Imran Demaj, have filled my heart and our family with joy ever since they were born.

Whatever words of thankfulness I try to use, it would not be enough to express my deepest and sincerest gratitude to all the people that greatly contributed and helped me in many various ways to complete this work. The guidance and help of many professors, scientists, staff members and fellow graduate students here at ODU and BNL, the moral support and love of my family back at home and the company and care of good friends around, made the work easier and life more beautiful during my graduate studies at ODU.

I thank the one and only GOD for bringing all of you into my life. I have been greatly blessed.

TABLE OF CONTENTS

LIST OF TABLES

LIST OF FIGURES

CHAPTER 1

INTRODUCTION

A proton is a spin-1/2 particle, composed of three valence quarks, gluons and sea quarks. Quarks are held together by the strong nuclear force mediated by gluons. Protons and neutrons, also referred to as nucleons, compose all atomic nuclei except hydrogen (^{1}H), which has no neutrons. Compared to the electron, which is a point-like particle, the proton has a composite structure and a larger mass. Understanding the structure of this fundamental particle is an important, but complicated task that requires the use of Quantum Chromodynamics (QCD). [1]

QCD describes the strong interaction of quarks and gluons in hadrons, such as protons. The protons and their interactions can be studied in particle colliders or in fixed target experiments, at facilities such as the Large Hadron Collider (LHC) at CERN (Conseil Européenne pour la Recherche Nucléaire - European Organization for Nuclear Research), Tevatron at Fermilab, and the Relativistic Heavy Ion Collider (RHIC) at Brookhaven National Laboratory (BNL). Experiments that focus on high-energy proton collisions at these facilities can study the dynamics of the scattering processes in both polarized and unpolarized proton beam collisions, depending on whether the opportunity of providing polarized proton beams exists at the facility.

Previous proton-proton (pp) and proton-antiproton ($p\bar{p}$) scattering experiments carried out at CERN and at the Tevatron, have provided pp total and differential cross sections at different center of mass energies $\sqrt{s}$ and four-momentum transfer squared t. The total cross section, in both pp and $p\bar{p}$ data reaches a minimum at $\sqrt{s} = 10$ GeV, and shows a characteristic rise at higher energies. Phenomenological models have been developed in order to describe this behavior. Regge theory, for example, describes the total cross section at very high energy by introducing a Reggeon with vacuum quantum numbers, called the Pomeron. The Pomeron is a color singlet combination of gluons, has mass, no spin and no electric or color charge. The Pomeron was postulated in order to explain the slowly rising cross section of the hadronic collisions at high energies.

[1] This Dissertation follows the style of *The Physical Review, C*

The highest $\sqrt{s}$ energy achieved in experiments in pp collisions is by the TOTEM experiment at LHC, reaching 7 TeV with unpolarized beams and by CERN ISR experiments at 20 GeV with polarized beams. RHIC has the capability of accelerating and colliding identical particles, i.e. protons at a wide and previously unexplored center of mass energy range of 50 GeV $\leq \sqrt{s} \leq$ 500 GeV, and a unique capability of accelerating spin-polarized protons. Thus, RHIC provides a unique opportunity to study both the dynamics and the spin-dependence of pp scattering at a previously unexplored energy range and four-momentum transfer squared range of $2 \times 10^{-4} \leq |t| \leq 1.5$ $(\mathrm{GeV}/c)^2$. In comparison, the TOTEM experiment at LHC will measure elastic and diffractive pp scattering with unpolarized beams up to $\sqrt{s} = 14$ TeV.

The first part of Chapter 2, describes the kinematics of the diffractive processes, concentrating on elastic scattering. A discussion of the measurements of the spin-independent variables in pp and $p\bar{p}$ scattering experiments, including a summary of the pp and $p\bar{p}$ experiments in the world (Appendix B) and the motivation for the measurement of the spin-independent observables, is given in the Section 2.3 of Chapter 2. The measurement of the spin-averaged observables at different cms energies (the total cross section σ_{tot}, the exponential slope parameter-B of the elastic cross section and the ρ parameter), is important for understanding the exchange mechanisms dominating the diffractive processes at low and high energies, as well as understanding the features that the total and elastic cross sections exhibit at different energy regimes.

Elastic scattering is in some sense the most fundamental type of reaction, but it is also the most difficult to understand theoretically [1]. In this discussion, it is also important to take into account the kinematic region of interest. In our experiment we are interested (the reason will be explained later), in measuring pp elastic scattering in the small momentum transfer t region. This is the domain of non-perturbative QCD, where the large coupling constant (α) does not allow perturbation theory to be applicable in the description of the process. To study the dynamics of the small-t scattering process in pp elastic collisions, we need to examine our understanding of the underlying interactions and the associated exchange mechanisms. While the electromagnetic interaction can be described by Quantum Electrodynamics (QED), the hadronic interaction is not well understood, and the calculation of cross sections for the small-t scattering requires the use of non-perturbative techniques in QCD, a theoretical approach which is still in development.

Phenomenological models, rather than pQCD, are used to describe the exchange mechanism and much work has been done in connecting Regge phenomenology to QCD concepts [2], by associating Pomeron (P) exchange with the exchange of $n \geq 2$ (non-perturbative) gluons [3–5]. As stated in [6], for the case $n \geq 2$ (charge conjugation $C = +1$), this mechanism generates a bare hard Pomeron, while for $n = 3$, containing both $C = \pm 1$, the $C = -1$ amplitude leads to another Reggeon, a bare Odderon (O), which corresponds to a odd-signature partner of P [7–12]. Sections 2.5 and 2.6, give a review of several phenomenological models: Regge theory, the Geometrical Models by Chou and Yang [13], the Impact Picture Model by Bourrely *et al.* [14] and the Multiple Exchange Model by Donnachie and Landshoff [15].

RHIC capabilities enable us to measure the spin dependent observables of elastic pp scattering: the transverse single spin asymmetry A_N and the transverse and longitudinal double spin asymmetries (A_{NN}, A_{SS}, A_{LL}), and cross section differences ($\Delta\sigma_T$, $\Delta\sigma_L$), corresponding to transverse and longitudinal polarization of the colliding beams. The measurement of the spin-dependent observables at the high energy range available at RHIC, will help deepen our understanding of the asymptotic spin dependence of the nucleon-nucleon scattering with energy. Consequently, a better understanding of the asymptotic spin dependence can be used to help identify the dynamical mechanisms dominant at high energies [16]. RHIC presents a wonderful opportunity to do these measurements, and, with precise measurement of the double spin asymmetries, to possibly distinguish between a Pomeron vs. Odderon or other exchange mechanisms dominant at high energies. If the dynamics is well approximated by a pure Pomeron pole, the spin asymmetries will be quite small and require very sensitive experiments to measure [16]. In this context, one of the objectives of the STAR experiment at RHIC is the characterization of the dynamics of high energy scattering by means of measuring of the spin-dependent observables and the study of the spin-dependence in polarized pp elastic collisions.

Spin dependent elastic scattering of two spin 1/2 particles is described by five-independent helicity amplitudes (depending on the helicity of initial and final states: two of the amplitudes are helicity conserving amplitudes, two are double spin-flip amplitudes and the fifth is the single spin-flip amplitude), each of them having contributions from both the electromagnetic and hadronic interactions, [17]. Measuring

in the small-t kinematic region is important since this is the region where the electromagnetic and hadronic amplitudes have comparable magnitudes, and their interference results in a measurable asymmetry in the scattering. This kinematic region is the Coulomb-Nuclear Interference (CNI) region. The single-spin asymmetry A_N, also referred to as the analyzing power in polarimetry terminology, is defined as the left-right cross section asymmetry with respect to transversely polarized beams. In terms of the scattering process, A_N is manifested as a measurable asymmetry in the azimuthal plane or "anisotropy" of the scattered proton counts in the left and right detector areas. The measurement is based on a geometric mean method [18], which, in the case of two polarized proton beams, makes use of the alternating spin patterns of the proton beams.

Therefore, proton-proton elastic scattering in the CNI region (small-angle forward region and small momentum transfer t), results in a measurable asymmetry A_N, which, in the absence of the hadronic spin-flip amplitude, is calculable and predicted to have a maximum $\sim$4% at RHIC energies. A_N arises mainly from the interference between the Coulomb spin-flip amplitude, which is generated by the anomalous magnetic moment of the proton, and the hadronic non spin-flip amplitude. The pure Coulomb-Nuclear Interference term (CNI), is precisely determined in QED. However, a second interference term, between the Coulomb non spin-flip amplitude and the hadronic spin-flip amplitude, can also contribute to A_N. Therefore, a measurement of A_N in the CNI region, is a sensitive probe of the contribution from hadronic spin-flip amplitude, which is the scope of the experiment and analysis work presented in this dissertation.

Since the CNI region falls in the non-perturbative regime of QCD, the hadronic amplitudes can and have only been described by several phenomenological models, i.e. *Regge* poles exchange phenomenology. For this reason, experimental data are indispensable. The measurement of the hadronic spin-flip amplitude at high energies is directly related to the understanding of the nature and the spin-flip component of the dominating exchange mechanism at high energies, i.e. the Pomeron. Moreover, the study of the energy-dependence of the hadronic spin-flip amplitude using measurements from different experiments, gives information on the energy-(in)dependence of the spin-flip component. Some of the questions we are trying to answer are: What is the nature of the dominant exchange mechanism in diffractive processes at high-energies? Does the exchange mechanism of the hadronic interaction at high energies

(the Pomeron or gluonic exchange) have a contribution to the spin-flip amplitude in polarized hadron collisions? If yes, what is the magnitude of its contribution and does it depend on the energy regime?

Section 2.8 of Chapter 2 gives a detailed theoretical description of the spin-dependent *pp* elastic scattering, including the helicity formalism of the spin observables and a detailed discussion on the parametrization of A_N. There are several theoretical approaches that predict non-zero spin-dependent Pomeron amplitudes for elastic scattering: a model that treats the Pomeron helicity-flip coupling analogously to the isoscalar magnetic moment of the nucleon [11]; the Pion Exchange Model [19]; the Impact Picture Model based on a rotating matter picture [20]; and the quark-diquark model which predicts a non-zero Pomeron helicity flip if the spatial distribution of the quarks in the proton is asymmetric [21]. The models are also discussed in Section 2.8.

Measurements of spin-dependent observables have been performed at different center of mass (cms $\sqrt{s}$) energies, and the various experiments to date are summarized in Table 3 of Section 2.8. Among the experiments, we highlight high precision experiments from RHIC polarimeters, where it has been observed that the measured A_N and its t-dependence is compatible with the CNI prediction at $\sqrt{s} = 13.7$ GeV by Alekseev *et al.* [22] and at 21.7 GeV by Bazilevsky *et al.* [23], but the measurement of A_N at 6.8 and 7.7 GeV from the same experiments may indicate a non-zero hadronic spin-flip contribution at lower energies.

Since the beginnings of the RHIC operation in 2000, an experiment was proposed for measuring *pp* elastic scattering in the forward region (small momentum transfer-t region) using movable insertion devices called Roman Pots. This was the PP2PP experiment at RHIC, which ran in 2003 and was successful in measuring, for the first time, *pp* elastic scattering of polarized protons and the exponential slope B of the elastic cross section at the cms energy $\sqrt{s} = 200$ GeV [24], the first measurement of the transverse single spin asymmetry A_N [25], and the transverse double spin asymmetries A_{NN} and A_{SS} [26]. In 2008, the PP2PP experimental setup and the physics program was integrated with the STAR experiment at RHIC, and the STAR experiment was equipped with the very forward detectors, Roman Pots, which are now part of the experiment named "Physics with Tagged Forward Protons at STAR".

With this experimental setup, we had a successful data collection period in 2009 (Run09), with transversely polarized proton beam collisions at 200 GeV cms energy,

in which a sample of 33 million elastic triggers was collected. The experimental setup and the detector performance during Run09 are discussed in detail in Chapters 3 and 5, respectively. A simulation study of the detector acceptance is given in Chapter 4. Chapter 6 gives a detailed description of the data analysis procedure followed and the selection criteria for elastic events. The selected elastic events were then used in the calculation of spin asymmetries, and the measurement of the single spin asymmetry A_N, described in Chapter 7. The first high precision measurement of the transverse single-spin asymmetry A_N is presented in Chapter 7 and a discussion of the systematic errors of the measurement is given in Chapter 8.

CHAPTER 2

THEORETICAL FORMALISM AND PHYSICS MOTIVATION

2.1 HADRONIC PROCESSES

Hadronic processes are traditionally classified in two distinct groups: *soft processes* and *hard processes* [27].

- *Soft processes* are characterized by an energy scale of the order of the hadron size R (~ 1 fm). The momentum transfer squared is generally small: $|t| \sim 1/\ R^2$ and the t-dependence of the cross sections is exponential $\mathrm{d}\sigma/\mathrm{d}t \sim\ e^{\ -R^2|t|}$, and large-$|t|$ events are highly suppressed [27]. Elastic hadron-hadron scattering and diffractive dissociation are classical examples of soft hadronic processes. Soft hadronic processes are characterized by a large length scale (R), which makes them intrinsically non-perturbative. These processes cannot be described by perturbative quantum chromodynamics (QCD) since the coupling constant is not small enough to allow perturbative techniques to be applicable. According to Regge theory, an approach that has been adopted since the 60's [28], soft hadronic phenomena at high energies are dominated by the exchange of a hypothetical object, the *Pomeron*. The *Pomeron* is a Reggeon with vacuum quantum numbers $J^{PC} = 0^{++}$, where J is the total angular momentum quantum number, P is the parity or the eigenvalue under reflection (parity operator (P) reverses the sign of the spatial coordinates: x, y, z) and C is the charge parity or a multiplicative quantum number that describes particles' behavior under the symmetry operation of charge conjugation. Hence no quantum numbers are being exchanged in the reaction.

- *Hard processes* are characterized by two (or more) energy scales: one is still the hadron size, the other is a "hard" energy scale [27]. The momentum transfer squared is large $|t| \geq 1\ \ (\mathrm{GeV}/c)^2$ and the t-dependence of the cross sections is

power-like. Two examples of hard hadronic processes are deep inelastic scattering (DIS) and large-p_T jet production, where a jet is a narrow cone of hadrons and other particles produced by the hadronization of a quark or gluon in a particle physics/heavy ion experiment and p_T is the component of the momentum of the scattering particles in the transverse plane ($x - y$ plane). The physics phenomenon of confinement in QCD shows that color charged particles (such as quarks) cannot be isolated singularly, but, in turn they clump together to form hadrons, either mesons (one quark, one anti-quark) or baryons (three quarks). The high value of the momentum transfer allows the use of perturbative QCD to describe these processes. Part of the process is still of non-perturbative origin. This component is embodied in the quark and gluon distribution, or the fragmentation fractions of hadrons [27]. The study of hard hadronic processes gives us the possibility to study the scattering process in a perturbative QCD framework, allowing investigation of the nature of the *Pomeron*.

2.1.1 DIFFRACTIVE PHENOMENA

Diffraction is a phenomenon that takes place asymptotically (i.e., as the energy increases), whenever the particles diffused have the same quantum numbers as the incident particles [27]. In this viewpoint, a hadronic diffractive reaction at high energy is defined as a reaction in which no quantum numbers are exchanged between the colliding particles. The hadronic processes listed below can be described as diffractive reactions according to this definition of the diffractive phenomenon:

- Elastic Scattering ($p + p \rightarrow p + p$)

  In the elastic scattering process, the initial particles are detected after the collision, (see Fig. 1 (a)).

- Single Diffraction ($p + p \rightarrow p + X_2$)

  In the single diffractive process, one of the incident particles remains intact while the other gives rise to a state of final particles (or a resonance) with the same quantum numbers, (see Fig. 1 (b)).

- Central Production ($p + p \rightarrow p + p + X$)

  The central production process of two particles (i.e. protons) results in the

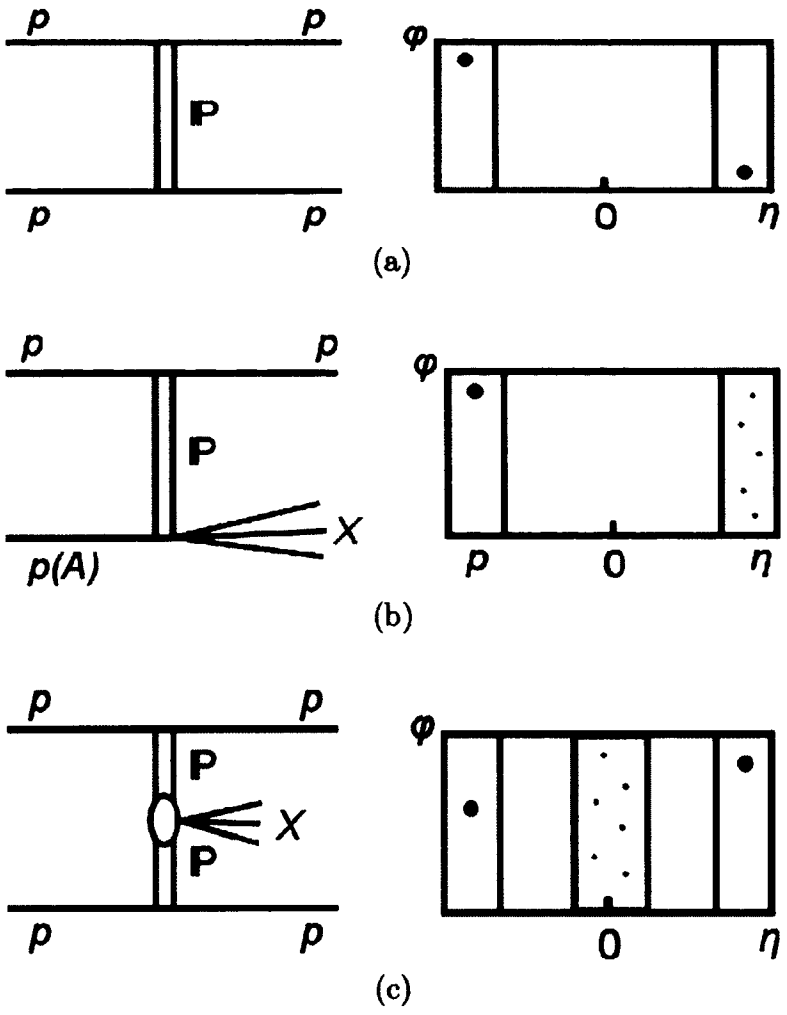

FIG. 1. (a) Elastic Scattering, (b) Single Diffractive Dissociation and (c) Central Production (Double Pomeron Exchange). The double line (IP) marks the Pomeron exchange. ϕ is the azimuthal angle and η is the pseudorapidity (see Appendix A).

production of a centrally produced system of final state particles (X), and two scattered protons in the forward direction (see Fig. 1 (c)).

- Double Diffraction ($p + p \rightarrow X_1 + X_2$)

  In the double diffractive process, each of the incident particles gives rise to a state of final particles (or a resonance) with the same quantum numbers as the two initial particles.

The cross sections (σ) for diffractive processes at small-$|t|$ behave as:

$$\frac{d\sigma}{dt} = \frac{d\sigma}{dt}\,|_{t=0}\, e^{-B|t|} \approx \frac{d\sigma}{dt}\,|_{t=0}\,(1 - B|t|), \tag{1}$$

where B is the slope parameter and is proportional to the squared radius of the target hadron [27]. At larger $|t|$ other secondary maxima appear.

The traditional framework for diffraction is Regge theory (discussed later in this chapter) which describes hadronic reactions at high energies in terms of the exchange of objects called *Reggeons*. The exchange of other scalars with vacuum quantum numbers, contributing to non-diffractive events, is suppressed at high energy [27]. The Reggeon with vacuum quantum numbers which dominates asymptotically is the *Pomeron*. Because of this reason in Regge theory the diffractive reactions are dominated by *Pomeron* exchange. The colliding particles in Fig. 1, protons in this case, interact by exchanging a *Pomeron*, and thus no quantum numbers are exchanged in this reaction. As the center of mass of the reaction $\sqrt{s}$ decreases, other Reggeons contribute and the non-diffractive contamination gets larger [27].

2.2 PROTON-PROTON (pp) ELASTIC SCATTERING

In a proton-proton collision, the elementary constituents of the colliding hadrons interact via the fundamental strong interaction. The parameter that determines the size of the smallest structure that can be resolved in elastic scattering is the energy transferred between the incoming and the outgoing particles, or the four momentum transfer squared:

$$t = (p_{in} - p_{out})^2, \tag{2}$$

where p_{in} and p_{out} are the four-momenta of the incoming and the outgoing protons, respectively.

In a proton-proton collision, the colliding hadrons are charged particles and thus, they also interact via the fundamental electromagnetic (Coulomb) interaction, which is well understood and calculable in quantum electro-dynamics (QED). The hadronic interaction, however, is very complex and the description of the scattering process depends on the value of momentum transfer squared t. When the momentum transfer is small ($|t| \leq 1$ GeV^2), this is the non-perturbative regime of quantum chromo-dynamics (QCD), in which the scattering process is described by phenomenological

models rather than perturbation theory, since the strong coupling constant $\alpha_s(t)$ is not small enough for these techniques to be applicable. The strong coupling constant $\alpha_s(t)$ increases with decreasing momentum transfer. This phenomenon, referred to as the running of $\alpha_s(t)$ has different implications for two different regimes of momentum transfer. For low momentum transfers, $\alpha_s(t)$ is very large, preventing the use of perturbative techniques in QCD calculations. However, for large momentum transfers, $\alpha_s(t) \to 0$ as $t \to \infty$, permitting the use of perturbative techniques to be applied to QCD calculations. QCD, the theory of strong interaction, can calculate reliably only at high momentum transfers ($|t| \geq 8$ GeV^2), because only at sufficiently high-$|t|$ the strong coupling constant is small enough for perturbative calculations to become valid. Typical hadron-hadron collisions involve many quarks and gluons and the individual momentum transfers are generally small [29]. In the case of large energy transfer, the underlying interaction involves only a pair of partons (quarks or gluons), while the others serve as spectators, and the interaction is no longer elastic, leading to a breakup of one or both participating hadrons [29].

The squared center of mass energy (cms) of the system in pp elastic scattering is:

$$s = (p_1 + p_2)^2, \tag{3}$$

where p_1 and p_2 are the energies of the two colliding proton beams, respectively.

Depending also on cms energy $\sqrt{s}$, different t values result in the system being probed at different dimensions, where either electromagnetic, hadronic, or the interference between these two interactions dominates. At small-t values, such as ($|t| \leq 10^{-4}$ GeV^2) or less, the dimension probed is larger than the range of strong hadronic interaction, therefore the electromagnetic interaction dominates. Medium-t values correspond to the Coulomb Nuclear Interference (CNI) region, where the Coulomb and hadronic interactions have comparable contributions to the elastic differential cross section. This is the smallest $|t|$-region accessible with the forward proton detectors at RHIC, which will be described in Chapter 3. Measurements in this region reveal valuable information on the strong nuclear amplitude and the pp total cross section, since the Coulomb amplitude is precisely calculable in QED. At values of $|t|$ beyond 1 GeV^2, the size probed is less than 1 fm, which is equal to the dimension of the proton. Therefore, this region is dominated by the strong interaction between constituent quarks. For values of $|t|$ well beyond 1 GeV^2 the interaction can be described by perturbative QCD.

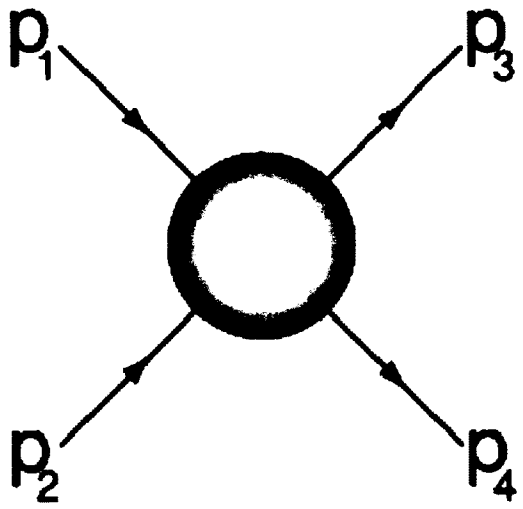

FIG. 2. Elastic pp Scattering (s-channel).

In Chapter 2, we will discuss the elastic scattering of two protons at high energy and small-to-medium momentum transfer. Sections 2.1 - 2.4, focus primarily on the dynamics of pp elastic scattering process and the measurement of the spin-averaged observables. Firstly, the kinematic variables of the elastic scattering process will be described. Appendices A and C provide additional information on variables and parameters that are very useful in high energy physics in general and in the description of elastic scattering process in particular. Section 2.3 gives an overview of the pp and $p\bar{p}$ world experiments. Several phenomenological models that are used in the interpretation of the experimental data, including the Donnachie-Landshoff model are discussed in Sections 2.6. The Pomeron is described in the framework of the Regge theory in Section 2.5 and the Multiple-Exchange model in Section 2.7. Sections 2.8 and 2.9 are devoted to the spin-dependence of the elastic scattering process and the measurement of the spin-dependent observables.

2.2.1 KINEMATICS

Consider two body exclusive scattering as shown in Fig. 2:

$$1 + 2 \rightarrow 3 + 4. \tag{4}$$

The reaction given in Eq. (4) is described by two independent variables. A special

case of Eq. (4) is elastic scattering:

$$1 + 2 \rightarrow 1' + 2', \tag{5}$$

where the two particles remain unaltered, but with a different kinematic configuration [27]. The variables are usually chosen among the *Mandelstam invariants*. *Mandelstam* variables are used to describe the interaction of the incoming particles in high-energy scattering processes and to characterize the kinematics of the scattering.

Consider the elastic scattering of two protons in the center of mass (cms) system shown in Fig. 2:

$$p_1 + p_2 \rightarrow p_3 + p_4, \tag{6}$$

where p_1 and p_2 are the four-momenta of the the two colliding protons, and p_3 and p_4 are the four-momenta of the the two scattered protons, respectively. The *Mandelstam* variables for the above reaction are:

$$s = (p_1 + p_2)^2 = (p_3 + p_4)^2, \tag{7}$$

$$t = (p_1 - p_3)^2 = (p_2 - p_4)^2, \tag{8}$$

$$u = (p_1 - p_4)^2 = (p_2 - p_3)^2. \tag{9}$$

The *Mandelstam* variables obey the identity:

$$s + t + u = \sum_{i=1}^{4} m_i^2, \tag{10}$$

where m_i is the mass of the i^{th} in the reaction.

In proton-proton elastic scattering two incoming protons collide and remain intact after the collision. In the center of mass system, assuming particles 1 and 2 are traveling along the z axis with equal and opposite three-momenta $\vec{p}_1$ and $\vec{p}_2$, (see Fig. 2), we have by definition:

$$\vec{p}_1 + \vec{p}_2 = 0. \tag{11}$$

The four-momenta of the particles can be written as:

$$p_1 = (E, \vec{p}) = (E, 0, 0, p_z), \tag{12}$$

$$p_2 = (E, -\vec{p}) = (E, 0, 0, -p_z), \tag{13}$$

$$p_3 = (E, \vec{p}') = (E, \vec{p}_\perp, p_z'), \tag{14}$$

$$p_4 = (E, -\vec{p}') = (E, -\vec{p}_\perp, -p_z'), \tag{15}$$

where $\vec{p}'$ is the three-momentum of the scattered particles, $\vec{p}_\perp = |p'| \sin\theta$, is the transverse two-vector momentum, $p'_z = |p'| \cos\theta$ and θ is the cms scattering angle. The 4-momentum of the system is conserved:

$$p_1 + p_2 = p_3 + p_4 . \tag{16}$$

Since in pp elastic scattering the particles have equal masses, m, the *Mandelstam* variables for the process can be expressed in terms of the cms variables as:

$$s = (p_1 + p_2)^2 = 4(p^2 + m^2), \tag{17}$$

$$t = (p_1 - p_3)^2 = p^2 + p'^2 - 2p \cdot p', \tag{18}$$

$$\text{For } |p| = |p'| \text{ then } t = -2p^2(1 - \cos\theta) = -4p^2 \sin^2(\theta/2). \tag{19}$$

For small-θ or very-forward scattering (which is the case in the experiment presented in this dissertation), the four-momentum transfer squared t can be approximated as:

$$t \approx -p^2\theta^2 . \tag{20}$$

Mandelstam variables are dot-products of four-vectors, therefore they are Lorentz scalars. The cms scattering angle θ can be expressed in terms of Lorentz scalars (for $s \to \infty$ or $s >> m^2$ in this experiment) :

$$\cos\theta = 1 + \frac{2t}{s} . \tag{21}$$

2.2.2 SCATTERING AMPLITUDE, DIFFERENTIAL ELASTIC CROSS SECTION AND FORWARD SCATTERING PARAMETERS σ_{tot}, ρ, B

The differential cross section is equal to the square of the scattering amplitude $f(\theta, s)$:

$$\frac{d\sigma}{d\Omega} = |f(\theta, s)|^2 , \tag{22}$$

where $d\Omega = d\phi d(\cos\theta)$ is the element of the solid angle. A Jacobian transformation gives $d\Omega = 2\pi d(\cos\theta)$. Thus we can express the differential cross section in terms of Mandelstam variables:

$$\frac{d\sigma}{dt} = \frac{d\Omega}{dt}\frac{d\sigma}{d\Omega} = 2\pi \frac{d(\cos\theta)}{dt}\frac{d\sigma}{d\Omega} . \tag{23}$$

Differentiating Equation (19) with respect to $\cos\theta$, we get:

$$\frac{dt}{d(\cos\theta)} = 2p^2. \tag{24}$$

Therefore, Equation (23) becomes:

$$\frac{d\sigma}{dt} = \frac{\pi}{p^2}\frac{d\sigma}{d\Omega} = \frac{\pi}{p^2}|f(\theta, s)|^2. \tag{25}$$

We now introduce an invariant scattering amplitude F:

$$F = \frac{\sqrt{\pi}}{p}|f(\theta, s)|. \tag{26}$$

The optical theorem (see Appendix A), relates the imaginary part of the elastic scattering amplitude f_{el} at $t = 0$ (scattering at very small scattering angle or very forward scattering) and the total cross section as [27]:

$$\sigma_{tot} = \frac{4\pi}{p}\mathrm{Im}f_{el}(t = 0), \tag{27}$$

where p is the center of mass three momentum of the incident particle. An important derivation of the optical theorem is to find the relation between the total cross section σ_{tot}, the forward differential cross section $d\sigma/dt$ $(t = 0)$, and the ratio between the real and the imaginary part of the scattering amplitude at $t = 0$:

The forward differential cross section is:

$$\left(\frac{d\sigma}{d\Omega}\right)_{\theta=0} = |f(t = 0)|^2 = [\mathrm{Re}f(t = 0)]^2 + [\mathrm{Im}f(t = 0)]^2. \tag{28}$$

The ρ-parameter is defined as the ratio of the real to the imaginary part of the scattering amplitude at $t = 0$:

$$\rho = \frac{\mathrm{Re}f(s, t = 0)}{\mathrm{Im}f(t = 0)}. \tag{29}$$

Using the optical theorem given in Eq. (27) and Eq. (28), the forward differential cross section can be expressed as:

$$\left(\frac{d\sigma}{d\Omega}\right)_{\theta=0} = \left(\frac{p\sigma_{tot}}{4\pi}\right)^2(1 + \rho^2). \tag{30}$$

Now, using the relation in Eq. (25), Equation (30) becomes:

$$\frac{d\sigma_{el}}{dt}_{t=0} = \left(\frac{\sigma_{tot}^2}{16\pi}\right)(1 + \rho^2), \tag{31}$$

where $\frac{d\sigma_{el}}{dt}$ is the differential elastic cross section.
The optical theorem can be expressed in terms of the previously defined invariant scattering amplitude F, such as:

$$\sigma_{tot} = \frac{4\pi}{p}\mathrm{Im}f_{el}(t=0) = 4\sqrt{\pi}\mathrm{Im}F(s,t=0). \tag{32}$$

Replacing σ_{tot} from Eq. (32) in Eq. (31) we get:

$$\frac{d\sigma}{dt} = |F|^2. \tag{33}$$

In order to express the differential elastic pp cross section in terms of the forward scattering parameters σ_{tot}, ρ and the nuclear slope parameter B, contributions from both the Coulomb and the strong hadronic/nuclear interactions need to be considered. The differential cross section is related to the invariant scattering amplitudes for the Coulomb and the hadronic interactions, the F_c and F_n, respectively, according to:

$$\frac{d\sigma_{el}}{dt} = |F_c + F_n|^2, \tag{34}$$

where F_c and F_n are functions of $\sqrt{s}$ and t.

The Coulomb interaction scattering amplitude can be derived precisely in Quantum Electro-Dynamics (QED); essentially the relativistic corrected Rutherford scattering cross section determines the scattering amplitude for the pure Coulomb interaction, for one-photon exchange approximation [27]:

$$\frac{d\sigma_c}{d\Omega_{cm}} = \left|\frac{-\alpha_{em}G_E^2(t)}{2p\sin^2\frac{\theta}{2}}\right|, \tag{35}$$

where $\alpha_{em} \sim 1/137$ is the fine-structure constant and $G_E(t)$ is the proton electric form factor given by:

$$G_E(t) = \left(\frac{1}{1+\frac{t}{\Lambda^2}}\right)^2, \tag{36}$$

where $\Lambda^2 = 0.71$ GeV^2.
Using Equation (25), the differential cross section for the Coulomb interaction can be rewritten as:

$$\frac{d\sigma_c}{dt} = \pi\left|-G_E^2(t)\frac{2\alpha_{em}}{|t|}\right|^2. \tag{37}$$

The invariant scattering amplitude for Coulomb interaction is:

$$F_c = -\sqrt{\pi} s G_E^2(t) \frac{2\alpha_{em}}{|t|}. \tag{38}$$

The hadronic interaction at small-$|t|$ is not well understood and, because of the non-perturbative nature of this kinematic regime, QCD perturbation theory cannot be used to describe the hadronic scattering amplitude. However, experiments performed at small-$|t|$ have shown that this amplitude can be very well approximated by a simple exponential function in $|t|$. The hadronic scattering amplitude can be empirically derived by using the definition of the ρ parameter (see Eq. (29)) and the optical theorem (see Appendix A):

$$F_n = \frac{s(\rho + i)\sigma_{tot} e^{-\frac{B|t|}{2}}}{4\sqrt{\pi}}. \tag{39}$$

Calculation of the differential elastic cross section requires that the two amplitudes, F_c (see Eq. (38)) and F_n (see Eq. (39)), are added together and squared (see Eq. (22)). Thus, an interference term arises. The two amplitudes have a relative phase with a phase factor which reflects the distortion of the pure amplitudes, F_c and F_n, due to simultaneous presence of both Coulomb and hadronic scattering. This phase is introduced in the Coulomb amplitude:

$$\frac{d\sigma_{el}}{dt} = \frac{1}{16\pi s^2} |F_c e^{\pm i\alpha_{em}\phi(t)} + F_n|^2, \tag{40}$$

where the factor $\alpha_{em}\phi(t)$ is the relative phase between the Coulomb and hadronic amplitudes, and $\pm$ is related to whether it is pp or $p\bar{p}$ collision, respectively. The differential elastic cross section at small-$|t|$ can be expressed in terms of the forward scattering parameters (σ_{tot}, ρ, b) as:

$$\frac{d\sigma}{dt} = 4\pi\alpha_{em}^2 \frac{G_E^4(t)}{|t|^2} + \frac{1+\rho^2}{16\pi}\sigma_{tot}^2 e^{-B|t|} - \alpha_{em}\frac{G_E^2(t)}{|t|}\sigma_{tot} e^{\frac{-Bt}{2}}(\rho + \alpha_{em}\phi). \tag{41}$$

The forward scattering parameters depend on the interaction energy $\sqrt{s}$.

The third term in Eq. (41) arises from the interference between the Coulomb and hadronic interactions. When $|t|$ is small enough to neglect F_n^2, then the interference term is proportional to $(\rho \pm \alpha_{em}\phi)$. The relative phase $\alpha_{em}\phi$, first calculated by Bethe (1958) [30] in a potential scattering model, was then investigated by several authors: West and Yennie (1968) [31]; Buttimore, Gotsman and Leader (1978) [32];

Cahn (1982) [33], [27]. The helicity independent Coulomb phase $\delta = \alpha_{em}\phi$, is approximately [32], [33]:

$$\delta = \alpha_{em}\phi = \alpha_{em}\left(\ln\frac{2}{|t|(b+8/\Lambda^2)} - \gamma\right), \tag{42}$$

where the so called slope-B is the logarithmic derivative of the differential cross section at $t = 0$, ~ 13 GeV^{-2} and rising with energy in the RHIC energy range [16], $\gamma = 0.5772$ is the Euler's constant. Replacing $\phi(t) = \ln(0.08/|t|) - 0.5772$ in Eq. (42), where $B = 15$ GeV^{-2}, we get for the Coulomb phase numerically $\delta \approx 0.027$ at $t = t_0$, the momentum transfer where the two amplitudes, Coulomb and hadronic, become comparable to each-other:

$$|t_0| \sim \frac{8\pi\alpha_{em}}{\sigma_{tot}}, \tag{43}$$

$|t_0| \sim 10^{-3}$ GeV^2 at present energies [27].

The dependence of the differential cross section on $|t|$ can be divided into three regions: the Coulomb region, the Coulomb Nuclear Interference (CNI) region and the hadronic region. In the low-$|t|$ region, the Coulomb term dominates (see Eq. (38)) and $d\sigma/dt$ has a $(1/t^2)$ dependence. As t increases, the relative contribution of the interference increases and at higher-$|t|$, the hadronic term (see Eq. (39)) dominates and the elastic differential cross section falls exponentially with $|t|$.

Coulomb Region

The low-$|t|$ region, the region where the Coulomb amplitude dominates, is the region where a partial total cross section in t can be measured by comparing to QED calculation. The total cross section of pp and $p\bar{p}$ scattering has been successfully measured at other colliders such as Tevatron at Fermilab and CERN Intersecting Storage Ring (ISR), at the respective available energies. Figure 3 shows the measurement of pp and $p\bar{p}$ total cross section at different cms energies $\sqrt{s}$ [34]. Data on both pp and $p\bar{p}$ total cross sections are shown up to the maximum energies available at the ISR ($\sqrt{s} = 62$ GeV). At these energies the pp and $p\bar{p}$ total cross sections tend to approach each other. The $p\bar{p}$ total cross section was measured at higher energies at the SPS/CERN and Tevatron/Fermilab. The pp total cross section can be measured at RHIC at a wide and previously unexplored energy range of 50 - 500 GeV. The pp total cross section was measured very recently by the TOTEM collaboration at

CERN at a much higher energy of $\sqrt{s} = 7$ TeV [35]. This result is not included in the plot in Fig. 3. The fit to the data comes from the predictions of the dispersion relations [36].

There are two approaches to the measurement of the total cross section: (a) *Luminosity-Dependent Method*, by measuring the scattering in the very-forward region and using the optical theorem (see Eq. (27)) to calculate the total cross section (however, this method requires knowledge of the absolute luminosity of the machine), and (b) *Luminosity-Independent Method*, this method can be used when the machine luminosity is not known or can not be measured precisely from other measurements. The total cross section and the integrated luminosity L of the machine are related as below:

$$N_{el} + N_{inel} = L\sigma_{tot}, \tag{44}$$

where N_{el} and N_{inel} are the observed numbers of elastic and inelastic interactions, respectively [34].

The first method requires measuring scattering in the very-forward region, which experimentally is very challenging. Thus, the Roman Pot technique has been very significant for this measurement in the very-forward direction. Measurements of the absolute luminosity can be done at RHIC via Van de Meer (Vernier) scans of the two proton beams. During a Vernier scan the two proton beams are scanned stepwise across each-other while the count rate in detectors near the interaction point (usually the zero-degree calorimeters, ZDCs), is recorded. The scan provides the transverse beam size and the luminosity of the collider. The relation between the differential elastic cross section and the measured distribution of the number of elastically scattered protons (the count rate dN_{el}/dt) is given by:

$$\left(\frac{dN_{el}}{dt}\right)_{t=0} = L\left(\frac{d\sigma_{el}}{dt}\right)_{t=0}, \tag{45}$$

where L is the machine luminosity and dN_{el}/dt is the number of elastically scattered protons or the measured count rate per fraction of the momentum transfer squared-t. This measurement method depends also on the acceptance and the efficiency of the detector system used. Thus another factor appears in Eq. (45):

$$\left(\frac{dN_{el}}{dt}\right)_{t=0} = L\mu\left(\frac{d\sigma_{el}}{dt}\right)_{t=0}, \tag{46}$$

where μ is the efficiency/acceptance coefficient related to the design of the experimental apparatus.

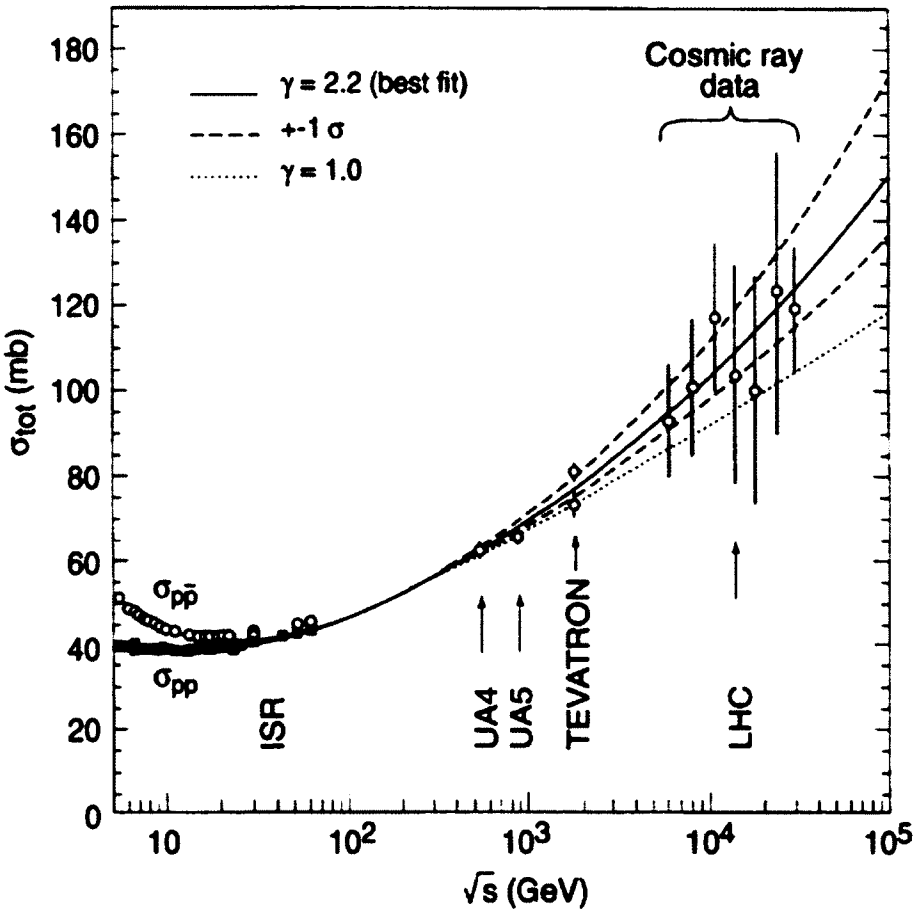

FIG. 3. The pp and $p\bar{p}$ total cross section σ_{tot} as a function of cms energy $\sqrt{s}$. The fit is from prediction of the dispersion relations [36]. The high energy behaviour is described by the term $(\log s)^{\gamma}$. The best fit solid line corresponds to $\gamma = 2.2$. The dotted line is the result obtained with $\gamma = 1$ [34]. Data on both pp and $p\bar{p}$ are shown up to the maximum energies of the ISR ($\sqrt{s} = 62$ GeV). The latest result on the pp total cross section measured by the TOTEM collaboration at CERN at $\sqrt{s} = 7$ TeV [35], is not included in this plot [37].

The second method, *Luminosity-Independent Method*, provides a practical way to measure the total cross section when luminosity of the machine is not known. The optical theorem (see Appendix A), also in relation to Eq. (45), leads to the following equation:

$$\left(\frac{dN_{el}}{dt}\right)_{t=0} = L\left(\frac{d\sigma_{el}}{dt}\right)_{t=0} = L\frac{\sigma_{tot}^2(1+\rho^2)}{16\pi}. \tag{47}$$

Combining Eq. (47) and Eq. (44), the luminosity can be eliminated and the total cross section can be written as a function of the measurable count rates as follows:

$$\sigma_{tot} = \frac{16\pi}{1+\rho^2}\frac{(dN_{el}/dt)_{t=0}}{N_{el}+N_{inel}} = \frac{16\pi}{1+\rho^2}\frac{(dN_{el}/dt)_{t=0}}{N_{tot}}, \tag{48}$$

where $N_{tot} = N_{el} + N_{inel}$. Since it is very difficult to measure scattering at $t = 0$ experimentally, $(dN_{el}/dt)_{t=0}$ in Eq. (48) is extrapolated from the measured t-region of nuclear scattering given by:

$$\frac{dN_{el}}{dt} = \left(\frac{dN_{el}}{dt}\right)_{t=0} \cdot e^{-bt}. \tag{49}$$

The *Luminosity-Independent Method* was followed by the TOTEM collaboration in the measurement of the pp total cross section at $\sqrt{s} = 7$ TeV [35]. The plot in Fig. 4 shows a compilation of the elastic (σ_{el}), inelastic (σ_{inel}) and total (σ_{tot}) cross section measurements as a function of cms energy $\sqrt{s}$.

Furthermore, if measurement of the scattering in the Coulomb region can be achieved experimentally, a normalization of the differential elastic count rate at very small-$|t|$, yields a direct determination of the collider luminosity L, since the Coulomb cross section is exactly calculable in QED.

Coulomb-Nuclear Interference Region

The Coulomb-Nuclear Interference (CNI) region, $t \sim 10^{-3}$ GeV^2 or the region where the Coulomb and hadronic amplitudes have comparable magnitude, is the region where the measurement of the ρ-parameter (see Eq. (29)) can be performed. The Coulomb and hadronic amplitudes are equal at:

$$-t_{max} \approx \sqrt{3}\frac{8\pi\alpha}{\sigma_{tot}}, \tag{50}$$

which for $\sqrt{s} = 200$ GeV with a pp total cross section of $\sigma_{tot} = 60$ mb, this occurs at $t_{max} \approx -2 \cdot 10^{-3}$ (GeV/c)^2 and corresponds to a scattering angle of 0.54 mrad. Measurement of the ρ-parameter is directly related to the measurement of the real

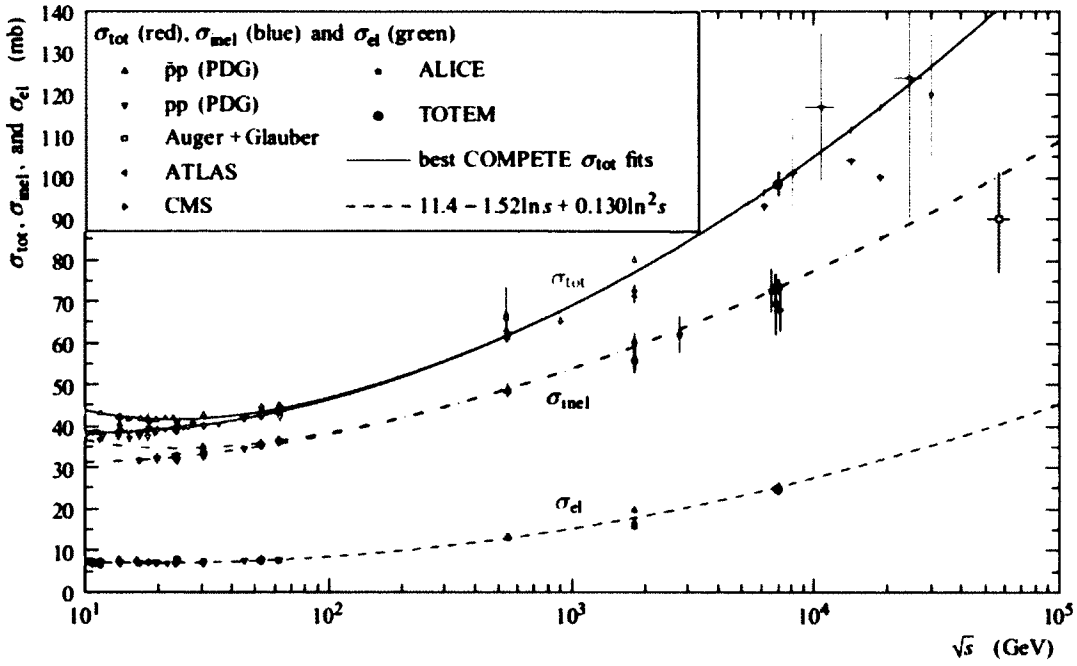

FIG. 4. Compilation of the elastic (σ_{el}), inelastic (σ_{inel}) and total (σ_{tot}) cross section measurements as a function of cms energy $\sqrt{s}$ [35].

part of the forward scattering amplitude, which in turn is complementary to the measurement of the total cross section. The real part of the forward scattering amplitude is related to the energy dependence of the total cross section [38]. The plot in Fig. 5 shows the measurement of the ρ-parameter as a function of cms energy $\sqrt{s}$.

The measurement of the spin-dependent variables, such as spin asymmetries, depends on the ability to measure polarized pp scattering in the CNI region. This is especially important for the measurement of the transverse single spin asymmetry, A_N, since the interference of the two amplitudes results in a measurable asymmetry in this kinematic region. A_N, also referred to as "the analyzing power", is maximum in the CNI region. The measurement of the single spin asymmetry A_N is the main subject of this dissertation and will be explained in detail in Section 2.8.

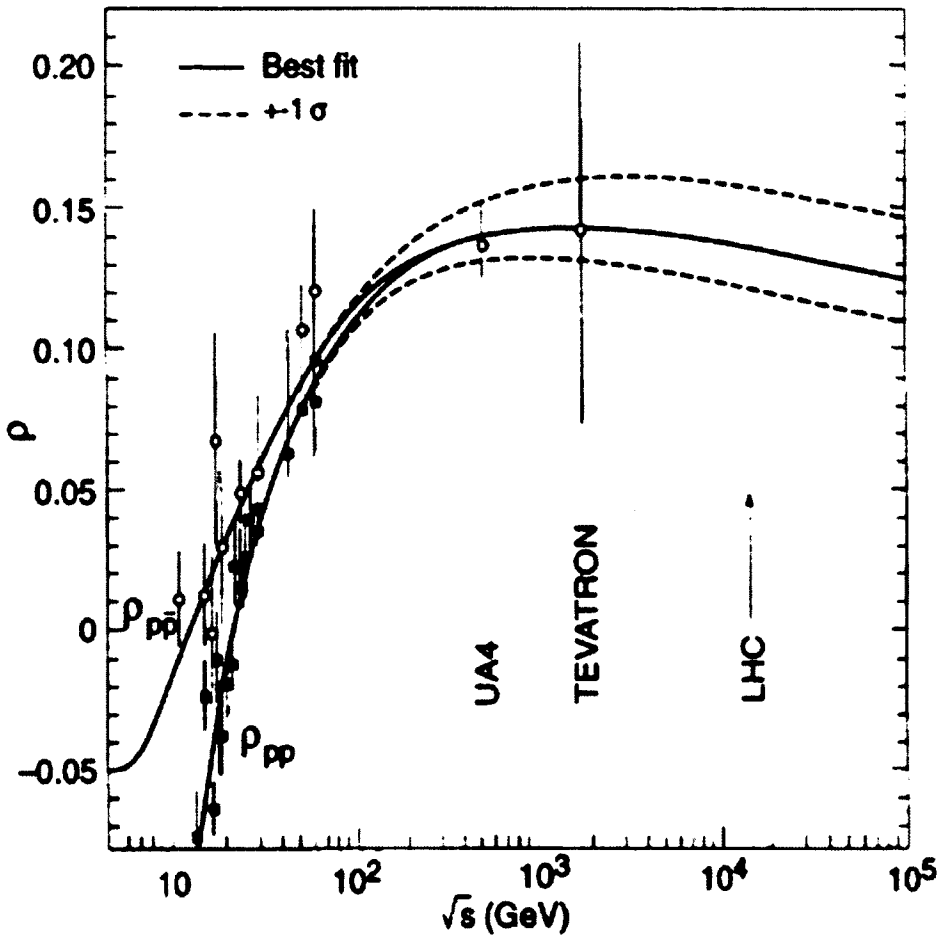

FIG. 5. Measurement of the ρ-parameter as a function of cms energy $\sqrt{s}$ [37]. The fit is from prediction of the dispersion relations [36].

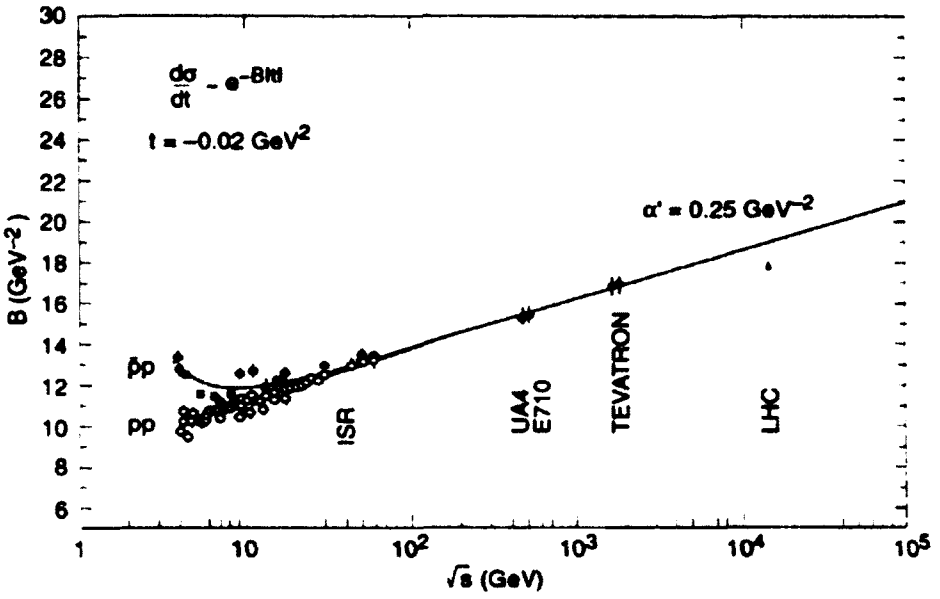

FIG. 6. Measurement of the slope-parameter (B) as a function of cms energy $\sqrt{s}$ [37].

Hadronic/Nuclear Region

The region where the hadronic amplitude is dominant is the region sensitive to the measurement of the 3^{rd} forward scattering parameter, the nuclear slope parameter B. The plot in Fig. 6 shows the measurement of the nuclear slope parameter as a function of of cms energy $\sqrt{s}$. The nuclear slope parameter B was successfully measured by PP2PP collaboration at RHIC at $\sqrt{s} = 200$ GeV, in 2003 [24] (not included in the plot).

2.3 OVERVIEW OF pp AND $p\bar{p}$ EXPERIMENTS

Elastic scattering, studied in pp and $p\bar{p}$ collisions at CERN Intersecting Storage Ring (ISR), Tevatron at Fermilab and RHIC at BNL, has been an important tool in the study of strong interaction and together with the measurement of the total cross section, have been the first measurements performed in a new accelerator. Table 29 in Appendix B gives a chronological overview (latest first) of the pp and $p\bar{p}$ elastic scattering experiments at high energy [29]. Table 29 in Appendix B includes detailed information on the location of the experiment, the type of experiment, the $\sqrt{s}$ and $|t|$ ranges covered during each experiment, the year when the experiment was performed and references.

Table 1 summarizes the highest energy for pp and $p\bar{p}$ elastic scattering experiments at the above-mentioned accelerator facilities. Additional information on whether the beams are polarized or not is indicated. At CERN ISR, the highest center of mass energy ($\sqrt{s}$) at which experimental studies have been performed in pp collisions is at $\sqrt{s} = 62.8$ GeV with unpolarized beams and at $\sqrt{s} = 20$ GeV with polarized beams. The $p\bar{p}$ collisions have been studied at the $\sqrt{s} = 53$ GeV at CERN ISR and at $\sqrt{s} = 1.8$ TeV at Tevatron (Fermilab). RHIC provides a unique opportunity to cover a previously unexplored center of mass energy in the study of polarized pp collisions, at a wide energy range of 50 GeV $\leq \sqrt{s} \leq$ 500 GeV. The PP2PP experiment at RHIC, designed to study pp elastic scattering collisions at the available wide $\sqrt{s}$ energy at RHIC and four momentum-transfer squared range of 2×10^{-4} (GeV/c)$^2 \leq |t| \leq 1.5$ (GeV/c)^2, had a successful period of data taking in 2002 and 2003, performing the first measurement of elastic scattering at $\sqrt{s} = 200$ GeV. Before the 2008 RHIC run, the Roman pots were installed on both sides of the STAR interaction point and the PP2PP experiment was integrated with the STAR experiment. This part of the STAR experiment physics program, called *Physics with Forward Tagged Protons at STAR*, makes use of the Roman pots as very-forward proton detectors and requires special running conditions (special beam optics), different from the other STAR experiments. With this experimental configuration, the STAR collaboration had a successful period of data taking during the 2009 RHIC run, collecting ~33M elastic triggers and ~1M Central Production (CP) (see Fig. 1 (c)) triggers at $\sqrt{s} = 200$ GeV. The physics program of Forward Tagged Protons at STAR entails measurement of both spin-averaged and spin-dependent observables in elastic and inelastic processes:

- **Spin-Averaged Observables in pp Elastic Scattering:** the differential elastic cross section $d\sigma/dt$, the total cross section σ_{tot}, the nuclear slope parameter B and the ratio of the real to the imaginary part of the forward scattering amplitude ρ

- **Spin-Dependent Observables in pp Elastic Scattering:**

  - **With Transverse Beam Polarization:** the analyzing power A_{N}, the double spin correlation parameters A_{NN} and A_{SS} and the difference in the total cross section as a function of initial transverse spin states $\Delta\sigma_{\mathrm{T}} = \sigma_{tot}^{\uparrow\downarrow} - \sigma_{tot}^{\uparrow\uparrow}$

  - **With Longitudinal Beam Polarization:** the double spin correlation parameter A_{LL}

- **Central Production** (see Fig. 1 (c)) and **Single Diffraction Dissociation** processes (see Fig. 1 (b)) and their spin dependence

A future goal of the physics program is to perform these experiments at RHIC at $\sqrt{s} = 500$ GeV.

2.3.1 THE TOTAL CROSS SECTION

The Pomeranchuk theorem [39], states that for any scattering process in which there is an exchange of charge, the total cross section vanishes asymptotically as $\sqrt{s}$ increases. Foldy and Peirels [40] proved that, for a particular scattering process, if the cross section does not fall as $\sqrt{s}$ increases, then the process must be dominated by the exchange of quantum numbers of the vacuum. Pomeranchuk [39] predicted that the total cross sections would approach a constant asymptotic limit, and the Regge trajectory whose exchange ensures this behaviour became known as the Pomeron. The Pomeron is a color singlet combination of gluons carrying quantum numbers of the vacuum $J^{PC} = 0^{++}$. The Pomeron is a Regge trajectory, which was postulated in order to explain and is believed to be responsible for the high-energy interaction at small-$|t|$.

Experimental data indicate that the total cross section σ_{tot} does not vanish, but rises slowly as $\sqrt{s}$ increases. The rate at which the pp total cross section rises is limited by the Froissart bound (see Eq. (51)).

TABLE 1. Overview of pp and $p\bar{p}$ elastic scattering experiments in the world

Collider Accelerator Facility	Type of Experiment	Center of Mass Energy $\sqrt{s}$
ISR at CERN	pp collisions (unpolarized beams)	62.8 GeV
ISR at CERN	pp collisions (polarized beams)	20 GeV
ISR at CERN	$p\bar{p}$ collisions	53 GeV
Tevatron at Fermilab	$p\bar{p}$ collisions	1.8 TeV
RHIC at BNL	pp collisions (polarized beams)	50 GeV $\leq \sqrt{s} \leq$ 500 GeV
LHC at CERN	pp collisions (unpolarized beams)	up to 14 TeV (TOTEM)
LHC at CERN	pp collisions (unpolarized beams)	up to 14 TeV (ALFA)

$$\sigma_{tot}(s \to \infty) < R^2 \ln^2 s, \tag{51}$$

where R is the finite range of the hadronic interaction. The Froissart bound implies that σ_{tot} cannot grow more quickly than $ln^2 s$, as s increases.

This behavior of the σ_{tot} at large-s, seems to be identical for pp and $p\bar{p}$ collisions. The plot shown in Fig. 7 summarizes existing world elastic scattering data for pp and $p\bar{p}$ collisions. The total cross section σ_{tot}, the ratio of the real to imaginary part of the forward scattering amplitude ρ and the slope parameter B (shown as b in the plot), are plotted as a function of the center of mass energy $\sqrt{s}$. The center of mass energy available at RHIC is indicated in Fig. 7 by "pp2pp" notation, which refers to the PP2PP experiment at RHIC.

There is a difference in the total cross sections of pp and $p\bar{p}$ collisions at small energy $\sqrt{s} \leq 10$ GeV. The total cross section of $p\bar{p}$ is higher and both cross sections are decreasing with increasing $\sqrt{s}$. This difference at low energy is due to the Coulomb interaction. As the energy increases this effect of the electromagnetic interaction becomes smaller and at large $\sqrt{s}$, the difference between the two cross section decreases and is expected to converge to zero:

$$\lim_{\sqrt{s}\to\infty} \frac{\sigma_{tot}(p\bar{p})}{\sigma_{tot}(pp)} \approx 1. \tag{52}$$

An observation of the total cross sections at $\sqrt{s} = 20$ GeV shows that both the pp and $p\bar{p}$ total cross sections rise. The total cross sections seem to converge slowly, although comparison is not possible after 60 GeV, because of the lack of data on pp σ_{tot}. Experiments at RHIC in pp collisions can provide data in the previously unexplored center of mass energy range of 50 GeV $\leq \sqrt{s} \leq$ 500 GeV.

2.3.2 DIFFERENTIAL CROSS SECTIONS

At small-$|t|$, including the CNI region, the differential cross section can be parametrized by the forward scattering parameters, σ_{tot}, ρ and B. The ρ-parameter, increases from -0.4 to 0.1, by changing sign around $\sqrt{s} = 10$ GeV, then it seems to remain constant for $p\bar{p}$ (see Fig. 7).

CERN ISR provided experimental data in the intermediate-$|t|$ region. At $|t| < 0.8$ $(\text{GeV}/c)^2$ the differential cross section decreases exponentially and after a diffraction dip at $|t| \sim 1.4$ $(\text{GeV}/c)^2$, it continues to decrease slowly. The Chou-Yang geometrical

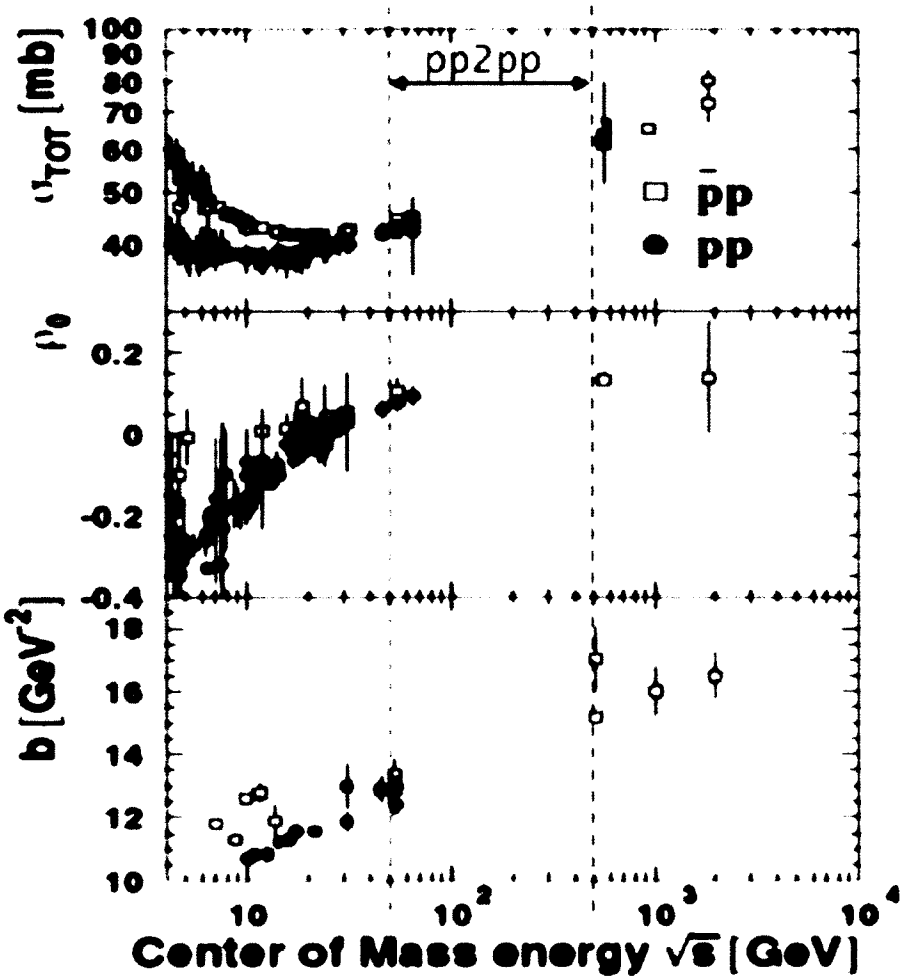

FIG. 7. Measurements of the forward scattering parameters (σ_{tot}, ρ and the slope parameter B, shown as b in the plot) in pp and $p\bar{p}$ collisions. The center of mass energy covered by the "pp2pp" experiment at RHIC is shown in the plot.

model [41] had previously predicted the existence of a diffraction dip in the differential cross section. The impact picture model by Bourrely *et al.* [20], [14] and [42], gives a good description of the experimental data in the dip region. The differential cross sections between $p\bar{p}$ and pp differ significantly, with $p\bar{p}$ showing a less pronounced dip structure than pp [29]. For large-$|t|$, $-t > 3.5$ (GeV/c)^2, the differential cross section can be described in the form:

$$\frac{d\sigma}{dt} = Ct^{-8}, \tag{53}$$

where C = 0.09 mb GeV^{14} [43].

2.4 MEASUREMENT OF SLOPE PARAMETER B IN pp ELASTIC SCATTERING AT RHIC

In this section we will talk briefly about the measurement of one of the spin-averaged observables, the exponential slope-parameter B of the pp differential elastic cross section, by the PP2PP experiment at $\sqrt{s} = 200$ GeV at RHIC. Bültmann *et al.* [24], performed the first measurement of the exponential slope parameter B of the diffractive peak of the elastic cross section at 200 GeV cms energy and in the t-range $0.010 \leq |t| \leq 0.019$ (GeV/c)^2. Fig. 8 shows the measured dN/dt distribution of the selected elastic events [24], as a function of t.

The distribution is fit by using equation for the differential elastic cross section Eq. (41), with B as a free parameter. The slope parameter B was measured to be 16.3 ± 1.6 (stat.) $\pm$ 0.9 (syst.) (GeV/c)$^{-2}$ at $\sqrt{s} = 200$ GeV at RHIC [24].

2.5 REGGE THEORY AND THE POMERON

Regge theory has been very successful as a phenomenological model, in describing a large class of reactions for which no alternative theoretical framework has been presently available [27]. The Regge pole idea was originally formulated based on the non-relativistic quantum mechanics. In quantum mechanics one denotes the partial wave amplitudes by $a_l(k)$. Regge's idea starts from the bound states for a spherically symmetric potential. These bound states appear as poles of the partial wave amplitudes $a_l(k)$. Regge (1959, 1960) continued $a_l(k)$ to complex values of l, thus obtaining an interpolating function $a(l,k)$, which reduces to $a_l(k)$ for angular momentum $l = 0, 1, 2....$ [27]. The singularities of $a(l,k)$ are the *Regge poles* located at values defined by the relation $l = \alpha(k)$, where $\alpha(k)$ is function of the energy

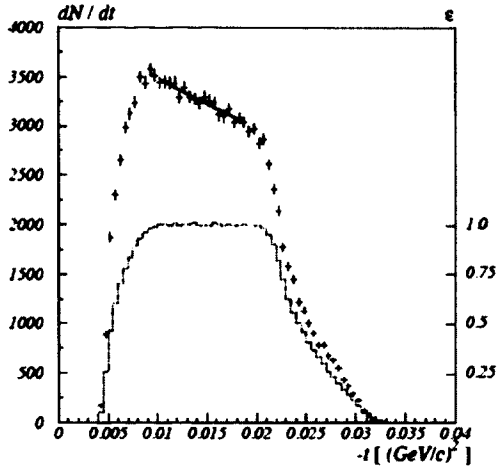

FIG. 8. The dN/dt distribution of selected elastic events as a function of t. The two distributions shown are the measured data and the simulated acceptance function (below). The fit is shown by the solid line [24].

called *Regge trajectory*. The extension of the Regge technique to high-energy particle physics is originally due to Chew and Frautschi (1961) and Gribov (1961), [27]. Regge theory belongs to the class of the so-called t-channel models. The Mandelstam variables for two related processes given as: (1) $a + b \rightarrow c + d$ and (2) $a + \bar{c} \rightarrow \bar{b} + d$ are defined as: (for reaction 1) $s_1 = (p_a + p_b)^2$ and $t_1 = (p_a - p_c)^2$; (for reaction 2) $s_2 = (p_a - p_{\bar{b}})^2 = t_1$ and $t_2 = (p_a + p_{\bar{c}})^2 = s_1$. In this example, reaction (1) is usually refereed to as s-channel and reaction (2) as t-channel.

Regge's approach for studying the scattering amplitude at large energy and finite momentum transfer, makes use of the s, t correspondence, where the amplitudes of the s-channel and t-channel are related by the crossing symmetry, such as: $T_{a+\bar{c}\rightarrow\bar{b}+d}$ $(s,t,u) = T_{a+b\rightarrow c+d}$ (t,s,u), where u is the third Mandelstam variable. The t-channel models describe the hadronic processes in terms of the t-channel exchange of a *virtual particle*. According to Regge theory, the strong interaction is not mediated by the exchange of particles with definite spin, but rather the exchange of a Regge trajectory, which is a family of resonances. The large s-limit of a hadronic process, known as the Froissart bound, is determined by the exchange of one or more Regge trajectories in the t-channel. Regge trajectories are often called *reggeons*. Exchanging *reggeons* instead of particles leads to scattering amplitudes which are in general less divergent

[27]. They do not violate the Frossart-Martin bound if $\alpha(0) < 1$.

2.5.1 REGGE TRAJECTORY

For the two-body t-channel scattering process given in reaction (2) $a + \bar{c} \rightarrow \bar{b} + d$, the scattering amplitude can be expanded in terms of Legendre Polynomials $P_l(\cos\theta)$, as a function of s and t:

$$T_{a+\bar{c}\rightarrow\bar{b}+d}(s,t) = \Sigma_{l=0}^{\infty}(2l+1)a_l(s)P_l(\cos\theta), \tag{54}$$

where the functions $a_l(s)$ are the partial wave amplitudes. By using the relation between the scattering angle θ and Mandelstam-t given in Eq. (21), and by interchanging s and t using the crossing symmetry, we obtain the scattering amplitude in the corresponding s-channel [29]:

$$T_{a+b\rightarrow c+d}(s,t) = \Sigma_{l=0}^{\infty}(2l+1)a_l(t)P_l\left(\frac{2s}{4m^2-t} - 1\right). \tag{55}$$

Using the Sommerfeld-Watson transformation [44], the wave expansion of Eq. (55) may be written in terms of a contour integral in the complex angular momentum plane [29]:

$$T(s,t) = \frac{1}{2i}\oint_C d\alpha(2\alpha+1)\frac{a(\alpha,t)}{\sin\pi\alpha}P\left(\alpha, 1+\frac{2s}{t}\right). \tag{56}$$

The denominator $\sin\pi\alpha$ in Eq. (56), vanishes for integer l when $\alpha = 1$, resulting in poles/singularities, called *Regge poles*. The analytic function $a(\alpha,t)$ is expressed in two forms according to the quantum number τ, the *signature* of the partial wave [27] which is expressed as $\tau = \pm 1$. Thus we have two analytic functions $a^{+1}(\alpha,t)$ and $a^{-1}(\alpha,t)$, called even- and odd-signature partial wave functions, respectively. The simple poles $\alpha_{n\tau}(t)$ are called even for $\tau = 1$ and odd for $\tau =$ -1 signature *Regge poles* [29].

Chew and Frautschi [45] plotted the spins of the low lying mesons against mass squared and noticed that they lie in a straight line, called *Regge trajectories*. This is shown in Fig. 9.

It can be shown that $a(\alpha,t)$ is unique when $a(\alpha,t) < e^{\pi|\alpha|}$ as $|\alpha| \rightarrow \infty$, [29,46]. The *Regge trajectories* are parametrized as: $\alpha(t) = \alpha(0) + \alpha' t$, where $\alpha(0)$ is the intercept and α' is the slope. Fig. 9 shows the leading mesonic trajectories with largest $\alpha(0)$. Each trajectory has quantum numbers: parity (P), charge conjugation (C), G-parity, isospin (I), strangeness (S) etc. [27], i.e. the trajectory f_2 has quantum

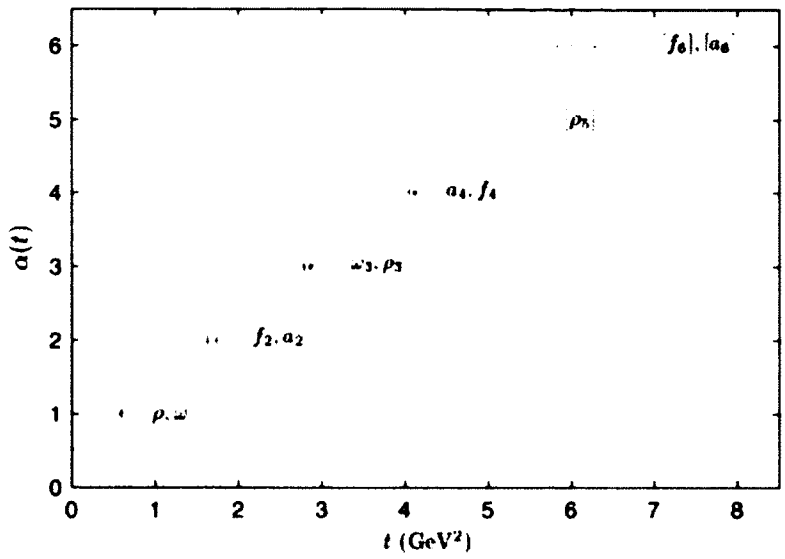

FIG. 9. The Chew-Frautschi plot for mesons, $\alpha(t)$ vs mass squared or t (GeV^2). *Regge trajectories* lie in a straight line.

numbers of the vacuum, like the Pomeron ($P = +1$, $C = +1$, $G = +1$, $I = 0$, $S = 0$, B (baryon number) $= 0$; τ (signature) $= 1$).

2.5.2 POMERON AS A REGGE TRAJECTORY

Using the *Regge trajectory* which dominates a particular scattering process, we obtain the asymptotic behavior of the total cross section:

$$\sigma_{tot} \sim \frac{1}{s}\mathrm{Im}T_{a+b\to c+d}(s, t = 0) \sim s^{\alpha(0)-1}, \tag{57}$$

where α is the leading trajectory exchanged in elastic scattering [29]. Since all total cross section are nearly constant at high energy, $\alpha(0) \approx 1$ in Eq. (57). The trajectory with $\alpha(0) = 1$ is the Pomeron, as this is not possible for meson trajectories. The *Regge trajectories* given in Fig. 9 have intercept which do not exceed 0.5, and their exchange leads to total cross sections decreasing with energy. However, it has been experimentally shown that the hadronic total cross sections as a function of s are flat around $\sqrt{s} \sim 10$ - 20 GeV^2 and increase at higher energies. In order to account for asymptotically constant total cross sections, Chew and Frautschi (1961) and Gribov (1961) introduced a *Regge trajectory* with intercept 1 [27], named "Pomeron" after I.Ya. Pomeranchuk (originally named as pomeranchukon after the Russian scientist, but then later abbreviated to Pomeron). The Pomeranchuk theorem [39] asserts that,

under certain quite strong assumptions, the total cross sections for collisions of a particle and the corresponding antiparticle on the same target become asymptotically equal at high energy [47]. Collins summarized in 1977 [48] that the inclusion of the Pomeron in the *Regge* theory, provides a very successful description of the experimental data in high-energy diffractive scattering. First attemts to explain Pomeron in terms of QCD were done by Low [3] and Nussinov [4]. However, the precise nature of the Pomeron is still not clear.

The slowly rising total cross section at high energy (at $\sqrt{s}$ beyond 200 GeV) is attributed to the exchange of a single Regge pole with intercept $\alpha(0) = 1$, carrying vacuum quantum numbers. Since the behavior of the total cross section seems to be independent of the flavor of the scattering hadrons (and thus independent of their quark structure) and since all the known trajectories involving quark structure have $\alpha(0) \geq 1$, the dominant mechanism at high energy (the Pomeron) in the elastic and diffractive processes, represents gluonic exchange. In the parton model, the Pomeron is defined as a colorless combination of two or more gluons. The Pomeron and the f meson have the same flavor properties, it may be expected that the longest-range part of the coupling at small $|t|$, comes from the formation of a virtual f meson.

Another *Regge trajectory* important in high energy scattering is the odd-signature partner of the Pomeron, the so-called "Odderon". The Odderon was introduced by Lukaszuk and Nicolescu (1973) and its existence would cause differences between the asymptotic scattering amplitudes and cross sections of pp and $p\bar{p}$ scattering.

2.6 PHENOMENOLOGICAL MODELS ON pp ELASTIC SCATTERING

The kinematic region of our interest in this experiment is the Coulomb-Nuclear Interference region, or the small-$|t|$. This kinematic region lies in the non-perturbative QCD regime, where the scattering process cannot be described by perturbative QCD, since the the coupling constant (α) is not small enough to allow the use of perturbation theory in QCD calculations. With the increasing of hadron-hadron scattering data at medium and high energy, several phenomenological models have been developed to understand the diffractive process at low-$|t|$ and to interpret the experimental data. *Regge* approach, which was described briefly in the previous section, tells us that the exchange of t-channel *reggeons* (with the Pomeron as the leading singularity), determines the asymptotic behavior of the cross sections in the direct s-channel [27].

The various phenomenological models that have been developed, have been successful in the explanation of various features (i.e. energy dependence of the cross sections, the diffractive slope, the ρ-parameter, the diffractive dip (minima) in the data), both qualitatively and quantitatively. These phenomenological models used to explain pp and $p\bar{p}$ elastic scattering include: the Geometrical/Optical Models proposed by Yang and collaborators [41, 49], (i.e. the Expanding Protons Model by Cheng and Wu (1987) [50]), the Impact Picture Model by Bourrely, Soffer and Wu [14, 20, 42] and a Multiple Exchange Model by Donnachie and Landshoff (the Donnachie Landshoff (DL) Model) [43, 47, 51].

2.6.1 GEOMETRICAL MODELS

The geometrical models used to describe hadronic processes are based on the similarities between optics and hadronic physics, although the two fields appear to be distant from each-other at first sight. The intersection point, or the similarity between the two fields in physics, is the diffractive phenomena that characterizes scattering processes. In this context, the interacting hadrons in high energy scattering are viewed as extended objects composed of hadronic matter (partons), flying through each-other [27]. At each point, the interaction is proportional to the local density of hadronic matter, assumed to have a distribution similar to the electric charge distribution [27]. The geometrical model is based on the spatial distribution of matter in the proton. The spatial distribution of the hadronic matter in the interacting hadrons can be related to the measured transfer of the three-momentum by the Fourier transformation.

This model is analogous to the phenomena of Fraunhofer diffraction from a black disk. When a macroscopic object is illuminated by an electromagnetic wave, and if the wavelength of the illuminating EM wave s small compared to the dimension of the obstacle/object, the diffractive phenomenon occurs and we observe diffractive maxima, separated by minima. Similarly in hadronic collisions, the incoming particle sees the target as a disk with a two-dimensional density. At very small wavelength compared to the disk's dimensions, which in the analogy corresponds to the high energy limit, the total cross section tends to be constant. With increasing energy, the target behaves more and more like a perfectly black disk [29]. The geometric/optical model treats elastic scattering as the shadow of absorption resulting from the passage of one hadron, with a certain hadronic matter distribution, through another [29]. In

this context, geometrical optics becomes relevant in the description of the high energy hadronic processes.

Chou and Yang [13], use the geometrical model to predict the existence of many diffraction dips in high energy hadron-hadron elastic scattering. In their model, the cross sections are written following the eikonal formalism. First as usual one starts from the scattering amplitude. The scattering amplitude based on the eikonal formalism is written as (for details on the derivation refer to p. 29 of [27]):

$$f(k,\theta,\phi) = \frac{ik}{2\pi}\int d^2\mathrm{b}e^{-iq\cdot\mathrm{b}}(1-e^{i\chi(\mathrm{b})}), \tag{58}$$

where k is the momentum, q is the momentum transfer such as $-q^2 = t$, b here is the impact parameter (not to be confused with the slope parameter-B), χ is the *eikonal function* defined as [27]:

$$\chi(\mathrm{b}) = -\frac{1}{2k}\int_{-\infty}^{+\infty} U(\mathrm{b},z)dz. \tag{59}$$

The quantity $\Gamma(\mathrm{b}) \equiv 1$ - $e^{i\chi(\mathrm{b})}$ is the *profile function* analogous to optics, [27].

In the geometrical model, the elastic differential cross section is written by adopting the eikonal approximation for very small wavelengths [13], such as:

$$\left(\frac{d\sigma}{dt}\right)_{el} = \frac{1}{4\pi}\left|\int e^{i\vec{k}\cdot\vec{\mathrm{b}}(1-e^{-\Omega(\mathrm{b})})d^2\mathrm{b}}\right|^2, \tag{60}$$

where $\vec{\mathrm{b}}$ is the two-dimensional impact parameter, $\vec{k}$ is the two-dimensional momentum transfer, $\Omega(\vec{\mathrm{b}})$ is the blackness at impact parameter $\vec{\mathrm{b}}$. The blackness function $\Omega(s,\mathrm{b})$, also called the *opacity*, is factorized as:

$$\Omega(s,\mathrm{b}) = K(s)D(\mathrm{b}), \tag{61}$$

where $K(s)$ is an energy-dependent free parameter of the model, to be determined from the energy dependence of the total cross section σ_{tot} data and $D(\mathrm{b})$ is related to the electric form factors (G_E) of the colliding hadrons. $D(\mathrm{b})$ is expressed as [27]:

$$D(\mathrm{b}) = \int d^2\mathrm{b}'\mathrm{T_A}(\mathrm{b}-\mathrm{b}')\mathrm{T_B}(\mathrm{b}'), \tag{62}$$

where A and B denote the two interacting hadrons, $T(\mathrm{b})$ is related to the charge density $\rho(\mathrm{b},z)$ of the hadron by $T(\mathrm{b}) = \int_{-\infty}^{+\infty} dz\ \rho(\mathrm{b},z)$. $D(\mathrm{b})$ is then expressed as:

$$D(\mathrm{b}) = \int \frac{d^2q}{(2\pi)^2}e^{iq\cdot\mathrm{b}}G_A(q^2)G_B(q^2), \tag{63}$$

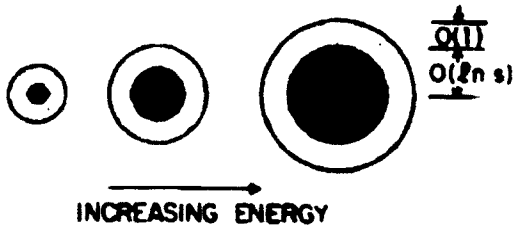

FIG. 10. The schematic representation of the appearance of a high-energy particle in the theory of expanding protons [50].

where $G_{A,B}$ are the form factors given as a function of momentum transfer $-q^2 = t$: $G_{A,B}(q^2) = \int d^2\mathrm{b}\, e^{-iq\cdot\mathrm{b}}\, T_{A,B}(\mathrm{b})$ [27].

$D(\mathrm{b})$ is related to the electric form factors (G_E) of the colliding hadrons. The *opacity* is taken to be real, so that the amplitude is purely imaginary. The total cross section is also expressed in terms of the *opacity* [13]:

$$\sigma_{tot} = 2\int (1 - e^{-\Omega(s,\mathrm{b})}) d^2\mathrm{b}. \tag{64}$$

In the "Expanding Protons" model by Cheng and Wu [50], the hadron radius is described increases logarithmically with the energy, and because of this expansion the total cross section must increase as $(\ln s)^2$ in the limit of high energies. The imaginary part of the elastic scattering amplitude also increases as $s(\ln s)^2$, which is the Froissart bound [50]. Cheng and Wu [50], give a schematic representation of the high-energy particle in the theory of expanding protons, shown in Fig. 10. At extremely high energies the particle acts like a Lorentz-contracted "pancake" [50], composed of two parts: a black core (completely absorptive), with a radius expanding logarithmically with energy; and a gray fringe (partially absorptive) with a width that is independent of s [27,50].

2.6.2 IMPACT PICTURE MODEL

The pp and $p\bar{p}$ elastic scattering are described by the following amplitudes:

$$a(s,t) = a^N(s,t) \pm a^C(t), \tag{65}$$

where the upper sign is for $p\bar{p}$ and the lower one is for pp, $a^N(s,t)$ is the hadronic amplitude and $a^C(t)$ is he Coulomb amplitude (see Eq. (38)) [42].

In the impact picture, the spin-independent hadronic amplitude for pp and $p\bar{p}$ elastic scattering is expressed in the form:

$$a^N(s,t) = \frac{i\,s}{2\pi}\int e^{-iq\cdot \mathrm{b}}(1 - e^{-\Omega_0(s,\mathrm{b})})d\mathrm{b}, \tag{66}$$

where q is the momentum transfer ($t = -q^2$) and $\Omega_0(s,\mathrm{b})$ is the *opaqueness* (blackness function) at impact parameter b and at a given energy s. The *opaqueness* $\Omega_0(s,\mathrm{b})$ is the sum of two terms [52]:

$$\Omega_0(s,\mathrm{b}) = S_0(s)F(\mathrm{b}^2) + R_0(s,\mathrm{b}). \tag{67}$$

The first term is associated with the Pomeron exchange, which generates the diffractive component of the scattering and the second is the Regge background, which is different for pp and $p\bar{p}$ and goes to zero rapidly as s increases. The Pomeron energy dependence is given by the crossing symmetric expression (modeled via the high-energy behavior of quantum field theory):

$$S_0(s) = \frac{s^c}{(\ln s)^{c'}} + \frac{u^c}{(\ln u)^{c'}}, \tag{68}$$

where u is the third Mandelstam variable. The Fourier transform $\tilde{F}(t)$ is chosen to be proportional to the square of the proton's electromagnetic form factor $G(t)$, with a slowly varying function:

$$\tilde{F}(t) = f[G(t)]^2\frac{a^2 + t}{a^2 - t}, \tag{69}$$

and the proton electromagnetic form factor is parametreized as:

$$G(t) = \frac{1}{(1 - t/m_1^2)(1 - t/m_2^2)}. \tag{70}$$

The slowly varying function given in Eq. (69) reflects the approximate proportionality between the charge density and the hadronic matter distribution inside the

proton [53]. The Pomeron part of the amplitude depends on only six parameters c, c', m_1, m_2, f and a [52]. The asymptotic energy regime of hadronic interactions is controlled by c and c', which are kept at the values obtained in 1984 [14] and are given as: $c = 0.167$ and $c' = 0.748$. The remaining four parameters are related to the reaction pp and $p\bar{p}$ and they have been fitted by the use of a large set of data [54]: $m_1 = 0.577$ GeV; $m_2 = 1.719$ GeV; $a = 1.858$ GeV; $f = 6.970$ GeV^{-2}, the Pomeron parameters for pp and $p\bar{p}$.

The spin-independent Regge background is gives as:

$$\tilde{R}_0(s,t) = [C_+ + C_- e^{-i\pi\alpha(t)}]s^{\alpha(t)}, \tag{71}$$

representing the standard even- and off-signature exchange contributions, with an exchange-degenerate trajectory $\alpha(t) = \alpha_0 + \alpha' t$ [20]. Summarizing all the above expressions Eq. (67), 69, 70 and 71, we get: $\tilde{\Omega}_0(s,\mathrm{b}) = S_0(s)\tilde{F}(t) + \tilde{R}_0(s,t)$, whose Fourier transform provides $\Omega_0(s,\mathrm{b})$. From this one can calculate the spin-independent elastic scattering amplitude:

$$a_0(s,t) = i\,s \int_0^\infty J_0(\mathrm{b}\sqrt{t})(1 - e^{-\Omega_0(s,\mathrm{b})})\mathrm{b}d\mathrm{b}, \tag{72}$$

where J_0 is the lowest order Bessel function.

Eq. (75) gives the expressions of the ratio of the real to the imaginary parts of the forward scattering amplitude, the total cross section and differential cross section, in terms of Eq. (72):

$$\rho(s) = \frac{\mathrm{Re}\, a(s,t=0)}{\mathrm{Im}\, a(s,t=0)}, \tag{73}$$

$$\sigma_{tot}(s) = \frac{4\pi}{s}\mathrm{Im}\, a(s,t=0), \tag{74}$$

$$\frac{d\sigma(s,t)}{dt} = \frac{\pi}{s^2}|a(s,t)|^2, \tag{75}$$

which completes the description of the scattering amplitudes.

2.7 MULTIPLE EXCHANGE MODEL

High-energy, small-t processes are believed to be controlled by single-Pomeron exchange [51]. Landshoff and Polkinghorne [55] observed that the Pomeron couples to the quarks rather like the photon, with a more-or-less constant γ^μ coupling, but with a *Regge* signature factor which gives it even C-parity. The model proposed by Donnachie and Landshoff in 1983 [43], is based essentially on three main contributions to the scattering amplitude at high energy scattering: the single Pomeron exchange for low-t region, the double-Pomeron exchange for medium-t region and the triple-gluon exchange which dominates at large-t. The dip observed in high-energy pp scattering (in the $-t$-range between 1-2 GeV^2) is provided by the interference of both the single-Pomeron exchange and the triple-Pomeron exchange with the double-Pomeron exchange. The model predicts that the dip will not be found in high-energy scattering [56] and the dip observed in low-energy $p\bar{p}$ scattering is a the result of the additional presence of reggeon-Pomeron exchange.

2.7.1 DONNACHIE AND LANDSHOFF (DL) MODEL

Starting in 1982, Donnachie and Landshoff analyzed the pp elastic scattering data at the CERN ISR range of energies, in terms of multi-gluon exchange. At small-t, the dominant mechanism is a version of the Chou-Yang model, improved to incorporate multi-gluon exchange, whereas at large-t values the three-gluon exchange dominates [43]. The dip-bump structure observed in pp at CERN ISR is produced by a cancellation in the imaginary part of the Pomeron between single and double exchanges, while the real part of the Pomeron is balanced by the triple-gluon term.

The differential pp elastic cross section at high energies (Fermilab and CERN ISR), and for $-t \geq 3.5$ GeV^2 obeys the power-law given in Eq. (53); this behavior is in agreement with the triple-gluon exchange. At very small-t, the amplitude is almost imaginary, while the triple gluon exchange is real (at least to lowest order in perturbative QCD). Triple gluon exchange describes the data well at large-t, but at smaller-t values additional gluons are needed. The simultaneous exchange of a large number of gluons between a pair of quarks is represented by the exchanged of a single object, the Pomeron [43]. In order to describe the energy dependence of the pp total cross section, the Pomeron trajectory is given an intercept $\alpha(0) = 1 + \epsilon$, where $\epsilon = 0.1$, without violating the Froissart bound.

Donnachie and Landshoff use six kind of exchanges in their (DL) model [56]: Pomeron (P) exchange, Reggeon (R) exchange, (RP) exchange, triple-gluon (ggg) exchange, triple-Pomeron (PPP) exchange, exchange of a Pomeron plus two gluons (Pgg) exchange, and double-Pomeron (PP) exchange.

Single-Pomeron (P) exchange gives the following contribution to the pp elastic scattering:

$$i[3\beta F_1(t)]^2 e^{[(\alpha_P(t)-1)(\log(s/m^2)-\frac{1}{2}i\pi)]}(\bar{u_3}\gamma^\mu u_1)(\bar{u_4}\gamma_\mu u_2), \tag{76}$$

where β is the (constant) coupling of the Pomeron to the quarks, 3 accounts for the three valence quarks in the proton, and u_1,....,u_4 are the spinor wave functions of the protons [56]. $F_1(t)$ is the Dirac form factor. Single Pomeron exchange between quarks is given by an amplitude similar to Eq. (76), but without the form factor $F_1(t)$. The contribution of Eq. (76) to the differential cross section for unpolarized pp and $\bar{p}$ scattering is:

$$\frac{d\sigma}{dt} = \frac{(3\beta_P F_1(t))^4}{4\pi}\left(\frac{s}{m^2}\right)^{(2\alpha_P(t)-2)}, \tag{77}$$

[56] and p.53 in [47]. A fit to the data for $F_1(t)$ in the region $|t| < 1$ GeV^2 is provided as:

$$F_1(t) = \frac{4m_p^2 - 2.79t}{4m_p^2 - t}\frac{1}{(1-t/0.71)^2}, \tag{78}$$

where m_p is proton mass [47]. The Pomeron trajectory is assumed to be linear in t, like the ρ, ω, f_2, a_2 trajectory but with a different slope: $\alpha_P(t) = 1 + \epsilon_P + \alpha'_P(t)$. The value of $\alpha'_P(t)$ is determined by comparing the shape of the formula given in Eq. (77) with the data from CERN ISR R211 experiment at $\sqrt{s} = 52.8$ GeV [57] and $\alpha'_P(t)$ is determined to be 0.25 GeV [47].

The *Reggeon (R)* exchange for (ρ, ω, f, a_2) is of concern only for very small-t and is omitted in the calculation [56]. At energies below the ISR range, the *Reggeon*-Pomeron (RP) exchange becomes important and it helps to provide the dip observed at 50 GeV/c in $p\bar{p}$ scattering [56].

Triple-exchange terms, particularly (ggg) are necessary to provide the dip. To calculate the triple gluon (ggg) exchange, (PPP) and (Pgg) exchanges, a form for the fractional longitudinal momentum distribution of the three constituent quarks needs to be assumed [43]. However, at any given energy pp and $p\bar{p}$ elastic scattering are predicted to be different in the dip region, because the ggg term contributes

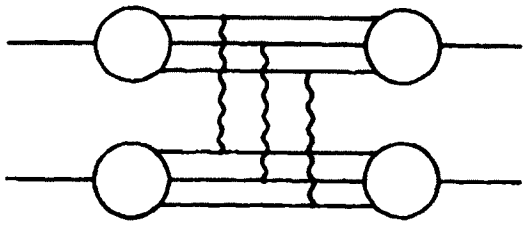

FIG. 11. The triple-gluon exchange in pp and $p\bar{p}$ elastic scattering [56].

to them with different signs [43]. Fig. 11 illustrates a diagram of the triple-gluon exchange. Refer to [56] for the contributions of the triple-exchange terms (ggg, PPP and Pgg) to the pp scattering amplitude.

Double-Pomeron (PP) exchange cannot be well calculated [55]. The s dependence of the double-Pomeron exchange is well-known, but its t-dependence remains uncertain. This becomes prominent in the dip-region of the high-energy pp data ($-t \cong 1.4$ GeV^2). For smaller values of t, the double-Pomeron exchange is hidden by the single-Pomeron exchange, and for larger t, by the ggg exchange [43]. The double-Pomeron amplitude (for small-t values) is chosen to be:

$$\frac{-iD\beta^4 F_1(t)}{\log(s/m^2)} e^{[(2\epsilon+\frac{1}{2}\alpha'_P t)(\log(s/m^2)-\frac{1}{2}i\pi)]}(\bar{u}_3\gamma^\mu u_1)(\bar{u}_4\gamma_\mu u_2), \tag{79}$$

with positive constant D the imaginary part of single Pomeron exchange cancels at the dip, but the real part does not [56].

2.8 SPIN DEPENDENCE IN pp ELASTIC SCATTERING

In the following description of the spin-dependence of proton-proton elastic scattering, we are going to use helicity instead of spin. Helicity is the projection of the spin vector in the direction of momentum vector of the incoming and outgoing protons. The spin dependent proton-proton elastic scattering process is described in terms of helicity amplitudes ϕ_i:

$$\phi_n(s,t) = \langle h_1 h_2 | M | h_3 h_4 \rangle, \tag{80}$$

where h_1 and h_2 are the helicity states of the colliding/incoming protons, h_3 and h_4 are the helicity states of the scattered/outgoing protons, M is the scattering matrix

containing all the dynamics of the scattering process. The helicity amplitudes ϕ_i have contributions from both the electromagnetic/Coulomb and hadronic interactions:

$$\phi_n(s,t) = \phi_n^{EM}(s,t)e^{i\delta} + \phi_n^{Had}(s,t). \tag{81}$$

Five independent helicity amplitudes are required to describe scattering of like-fermions such as proton-proton elastic scattering [16]:

$$\begin{aligned}
\phi_1(s,t) &= \langle ++|M|++\rangle, && (82)\\
\phi_2(s,t) &= \langle ++|M|--\rangle, && (83)\\
\phi_3(s,t) &= \langle +-|M|+-\rangle, && (84)\\
\phi_4(s,t) &= \langle +-|M|-+\rangle, && (85)\\
\phi_5(s,t) &= \langle ++|M|+-\rangle, && (86)
\end{aligned}$$

where Eq. (82) and Eq. (84) are the non helicity-flip amplitudes or the helicity conserving amplitudes; Eq. (83) and Eq. (85) are the double helicity-flip amplitudes and Eq. (86) is one of the 4 possible combinations of the single helicity-flip amplitude. All the above helicity amplitudes have contributions from the two interactions present in this reaction: Coulomb and Hadronic interactions.

To put this description in perspective, scattering of unlike-fermions require a sixth amplitude ϕ_6, a single helicity amplitude which degenerates to $-\phi_5$ for identical particles [16]. Both pp and $p\bar{p}$ scattering require 5 amplitudes, whereas the scattering of a proton on a spin-zero particle, like a pion or a spin-less nucleus (i.e. carbon), requires only two amplitudes, non-flip and flip amplitudes.

At very high $\sqrt{s}$ and very small momentum transfer squared-t, such as the center of mass energy and the momentum transfer of the reaction we are studying, the mass of the proton m can be neglected when compared to $\sqrt{s}$. Likewise momentum transfer t can be neglected with respect to m, simplifying the presentation of the following formulas. The total cross section and the differential elastic cross section are therefore expressed in terms of the helicity amplitudes:

$$\sigma_{tot} = \frac{4\pi}{s}\mathrm{Im}(\phi_1(s,t) + \phi_3(s,t))|_{t=0}. \tag{87}$$

$$\frac{d\sigma}{dt} = \frac{2\pi}{s^2}\{|\phi_1|^2 + |\phi_2|^2 + |\phi_3|^2 + |\phi_4|^2 + 4|\phi_5|^2\}. \tag{88}$$

Following this description and considering only initial state polarization, with one or both beams polarized, one can measure five spin-dependent asymmetries [16]:

$$A_{\rm N}\frac{d\sigma}{dt} = -\frac{4\pi}{s^2}{\rm Im}\{\phi_5^*(\phi_1+\phi_2+\phi_3-\phi_4)\}, \quad (89)$$

$$A_{\rm NN}\frac{d\sigma}{dt} = \frac{4\pi}{s^2}\{2|\phi_5|^2+{\rm Re}(\phi_1^*\phi_2-\phi_3^*\phi_4)\}, \quad (90)$$

$$A_{\rm SS}\frac{d\sigma}{dt} = \frac{4\pi}{s^2}{\rm Re}\{\phi_1\phi_2^*+\phi_3\phi_4^*\}, \quad (91)$$

$$A_{\rm SL}\frac{d\sigma}{dt} = \frac{4\pi}{s^2}{\rm Re}\{\phi_5^*(\phi_1+\phi_2-\phi_3+\phi_4)\}, \quad (92)$$

$$A_{\rm LL}\frac{d\sigma}{dt} = \frac{2\pi}{s^2}\{|\phi_1|^2+|\phi_2|^2-|\phi_3|^2-|\phi_4|^2\}, \quad (93)$$

where $A_{\rm N}$ is the analyzing power or the single spin asymmetry; $A_{\rm NN}$, $A_{\rm SS}$, $A_{\rm SL}$, $A_{\rm LL}$ are the double spin asymmetries corresponding to beams fully polarized along the different unit vectors: the normal vector to the scattering plane (unit vector $\vec{n}$); the vector in the scattering plane and normal to the initial momentum $\vec{p}$ (unit vector $\vec{s}$) and L is the longitudinal direction. The unit vector $\vec{s}$ is represented as $\vec{s}=\frac{\vec{n}\times\vec{p}}{|\vec{n}\times\vec{p}|}$.

Eq. (90) shows that the single spin asymmetry $A_{\rm N}$ results from the interference of the single helicity-flip amplitude ϕ with the other amplitudes. If we take a closer look at Eq. (90) and take into account that each of the helicity amplitudes consists of the Coulomb and hadronic contributions: $\phi_i=\phi_i^{em}+\phi_i^{had}$, we can express $A_{\rm N}$ in terms of the interference between the helicity amplitudes from Coulomb and hadronic interactions. The Coulomb/electromagnetic amplitudes ϕ_i^{em} can be described by QED [32].

The total cross section is expressed in terms of the hadronic amplitudes according to the optical theorem:

$$\sigma_{tot}=\frac{4\pi}{s}{\rm Im}(\phi_1^{had}+\phi_3^{had})|_{t=0}, \quad (94)$$

providing a constraint on the parametrization of the helicity conserving hadronic amplitudes ϕ_1^{had} and ϕ_3^{had}. We will introduce the following shorthands for easiness: $\phi_+=(\phi_1+\phi_3)/2$ and $\phi_-=(\phi_1-\phi_3)/2$. There are two cross section differences corresponding to longitudinal and transverse polarization:

$$\frac{{\rm Im}\phi_-(s,0)}{{\rm Im}\phi_+(s,0)} = \frac{1}{2}\frac{\Delta_{\rm L}(s)}{\sigma_{tot}(s)}, \Delta\sigma_{\rm L}=\sigma_{\rightleftarrows}-\sigma_{\rightrightarrows}, \quad (95)$$

$$\frac{{\rm Im}\phi_2(s,0)}{{\rm Im}\phi_+(s,0)} = -\frac{\Delta_{\rm T}(s)}{\sigma_{tot}(s)}, \Delta\sigma_{\rm T}=\sigma_{\uparrow\downarrow}-\sigma_{\uparrow\uparrow}. \quad (96)$$

At small values of t, the interference of the strong amplitudes with the single photon exchange amplitudes is important. This interference results in a measurable asymmetry in elastic scattering in the Coulomb-Nuclear Interference (CNI) region, the region where electromagnetic and strong amplitudes have comparable magnitude. The helicity amplitudes have two components, electromagnetic and hadronic:

$$\phi_i \rightarrow \phi_i^{had} + \phi_i^{em} e^{i\delta}, \tag{97}$$

where δ is the Coulomb phase and is approximately helicity independent [32,33]:

$$\delta = \alpha \ln \frac{2}{|t|(b + 8/\Lambda^2)} - \alpha\gamma, \tag{98}$$

where B is the logarithmic derivative of the differential cross section at $t = 0$, also called "the slope" of the forward peak in elastic scattering (a number about 13 GeV^{-2} and increasing through the RHIC region); α is the fine structure constant; $\gamma = 0.5772$ is the Euler's constant and $\Lambda^2 = 0.71\ \mathrm{GeV/c^2}$.

The proton form factors at small momentum transfer squared $-t$ are given as in Eq. (99):

$$G_E(-t) = G_M(-t)/\mu_p = (1 + |-t|/\Lambda^2)^{-2}, \tag{99}$$

where $\mu_p = \kappa + 1$ and is the proton's magnetic moment, and m is proton's mass. The electromagnetic amplitudes are expressed approximately:

$$\begin{aligned}
\phi_1^{em} &= \phi_3^{em} = \frac{\alpha s}{t} F_1^2, \\
\phi_3^{em} &= -\phi_4^{em} = \frac{\alpha s \kappa^2}{4m^2} F_2^2, \\
\phi_5^{em} &= -\frac{\alpha s \kappa}{2m\sqrt{-t}} F_1 F_2,
\end{aligned} \tag{100}$$

where F_1 and F_2 are the proton electromagnetic form factors related to G_E and G_M such as:

$$F_1 = \frac{G_E - G_M t/4m^2}{1 - t/4m^2}, \tag{101}$$

$$\kappa F_2 = \frac{G_M - G_E}{1 - t/4m^2}. \tag{102}$$

The relations between ϕ_1 and ϕ_3 and between ϕ_2 and ϕ_4, are special consequences of the quantum numbers of the exchanged photon, they are not generally true for the full amplitudes [16].

Each hadronic amplitude ϕ_i can be broken into two parts: $\phi_i \equiv \phi_i^R + \phi_i^{As}$, where the first one ϕ_i^R is controlled by Regge pole type dynamics and in the normalization according to [16], decreases with energy like $\approx s^{-1/2}$ with respect to the asymptotic part ϕ_i^{As}. The first term is essential in understanding the data in the low-to-moderate energy region which overlaps the RHIC range [16], while the second term is important in understanding of the rise of $\sigma_{tot}(pp)$ and $\sigma_{tot}(p\bar{p})$ asymptotically. The second term ϕ_i^{As} is related to the exchange mechanism which dominates at high energies. High energy diffractive scattering at small values of four-momentum transfer t, is dominated by an exchange mechanism of the Pomeron trajectory [27,47]. Pomeron is described in perturbative QCD as a color singlet combination of two gluons, carrying quantum numbers of the vacuum [27,47]. There are two forms for ϕ_+ to describe the high energy behavior of $\sigma_{tot}(pp)$: in the first the data are fit with $s \ln^p s$, where $p \leq 2$ [58,59], as suggested by Regge theory and the Froissart-Martin bound [60]:

$$|\phi_+| \leq cs \ln^2 s, \tag{103}$$

as $s \to \infty$. In this approach $\mathrm{Im}\phi_+^{As}$ receives contributions from the simple pomeron pole P, with intercept $\alpha_P = 1$, with a contribution growing at the maximum allowed rate sln^2s (sometimes referred to as a froissaron [58]): $\mathrm{Im}\phi_+^{As}(s) = a_P s + a_F sln^2 s$, [16]. In the second, the Landshoff-Donnachie pomeron [51], with $\alpha_P = 1 + \Delta_P$, where $\Delta_P \sim 0.08$, ensuing a behavior $\mathrm{Im}\phi_+^{As} \propto s^{1+\Delta_P}$, [16].

As $t \to 0$, the strong amplitudes ϕ_1, ϕ_2 and ϕ_3 go to a possibly non-zero constant while $\phi_4 \propto t$ and $\phi_5 \propto \sqrt{-t}$, as a consequence of angular momentum conservation [16]. The determination of the asymptotic spin dependence can be used to help identify the dynamical mechanisms dominant at high energies [16]. There are three classes of exchanges relevant to nucleon-nucleon scattering [61, 62], and their contribution to the pp amplitudes is shown in Table 2.

The various exchange mechanisms given in Table 2: Pomeron-P, Odderon-O etc. are classified according to the quantum numbers: parity-P, charge conjugation-C and signature-τ. An amplitude A_τ is called even or odd under crossing according as $\tau =$ +1 or -1, since $A_\tau(e^{i\pi}s, t) = \tau A_\tau^*(s, t)$. If the asymptotically dominant contribution has definite quantum numbers, then unitarity requires it has the quantum numbers of the vacuum [63]; this is the defining property of the Pomeron [16]. The quantum number C or C-parity determines the relative sign of the contribution of a given exchange, such as $A_{\tau,P,C}^{\bar{p}p}(s, t) = CA_{\tau,P,C}^{pp}(s, t)$. This implies that the Pomeron dominance and the absence of an Odderon requires that the total cross sections for pp and

TABLE 2. Classification of pp amplitudes by exchange symmetries and the associated Regge poles [16]

Class 1 $\tau = P = C$	Class 2 $\tau = -P = -C$	Class 3 $\tau = -P = C$
ϕ_+, ϕ_5, ϕ_2-ϕ_4	ϕ_-	ϕ_2+ϕ_4
P, O, ρ, ω, f, a_2	a_1	π, η, b

$\bar{p}p$ be equal [16]. The experimental data in pp and $p\bar{p}$ collisions performed at CERN and Tevatron at high energies show that the pp and $\bar{p}p$ total cross sections behave the same (rising equally) asymptotically. This may imply that the Pomeron is the exchange mechanism dominating asymptotically. However, if and how the Pomeron couples to ϕ_5 and ϕ_2 - ϕ_4 is open to experimental study. Does the dominant behavior become pure Pomeron/Froissaron as $s \rightarrow \infty$ or can there be a substantial Odderon contribution to these amplitudes [16]. An Odderon with nearly the same asymptotic behavior as the Pomeron/Froissaron will be approximately $\pi/2$ out of phase with it [16].

The helicity amplitudes ϕ_2 and ϕ_4 are important because they are directly related to the double spin asymmetries. An important observation here is that the angular momentum conservation forces ϕ_4 to vanish as $t \rightarrow 0$, [16]. If the dominant exchange has pure $CP = 1$ or CP = -1, then ϕ_2 must also vanish in the forward region [63]. Table 2 shows that $\phi_2 + \phi_4$ and ϕ_2 - ϕ_4 couple to opposite values of CP. Therefore, if only one value of CP is dominant asymptotically, $\phi_2 \sim \mp \phi_4$ as $s \rightarrow \infty$ and it, too, must vanish at $t = 0$ [16]. This makes the measurement of ϕ_2 near $t = 0$, or the measurement of the double spin asymmetries in the forward region a very interesting probe for the study of the dynamics, although the same fact implies that some asymmetries may be unmeasurably small.

Leader and Trueman [64], showed that the asymmetry A_{NN} is sensitive to the contribution from Odderon exchange, in high energy pp scattering. An enhancement

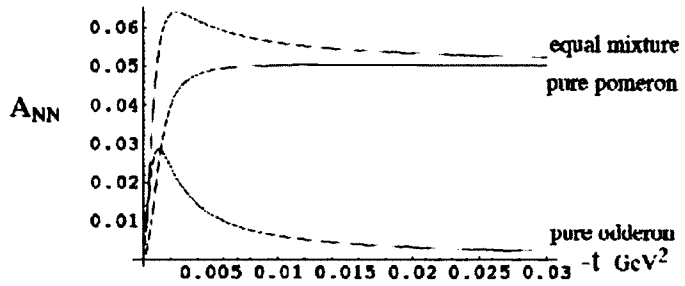

FIG. 12. The enhancement of Odderon contribution to A_{NN} due to interference with the one-photon exchange. The three curves correspond to ratios of helicity amplitudes: $\phi_2/\phi_+ = 0.05i$ (pure Odderon), $\phi_2/\phi_+ = 0.05$ (pure Pomeron) and $\phi_2/\phi_+ = 0.05(1+i)$ (equal mixture) [64].

illustration of the Odderon contribution to A_{NN} due to interference with the one-photon exchange is presented in [64], see Fig 12. So, the measurement of A_{NN} at high energies is a sensitive probe to the search of the negative charge conjugation partner of Pomeron. In addition, the Odderon can be observed in the dip region of pp and $p\bar{p}$ elastic scattering.

2.8.1 MODELS FOR THE POMERON HELICITY-FLIP

Several models have been introduced to understand the helicity-flip amplitudes of the Pomeron, the dominant exchange mechanism at high energies, and its spin coupling to the nucleon. Several theoretical approaches predict a non-zero spin-dependent amplitudes for elastic scattering. An early model that preceded the QCD formulation, introduced by Landshoff and Polkinghorne [55], is called the quark-parton model. The model shows that the t-dependence of the Pomeron coupling is determined by the electromagnetic form factors of the proton and neutron. This led to a conclusion that the helicity-flip coupling is given by the isoscalar anomalous magnetic moment of the nucleons, giving $r_5 = (\mu_p - 1 + \mu_n)/2 = -0.06$ [16]. This relation was obtained subsequently in a variety of models based on QCD [16].

Perturbative QCD

The perturbative Pomeron couples to a hadron through two gluons and the quark-gluon vertex conserves helicity [16]. However, the case for the proton needs to be considered carefully. Ryskin [11], introduced a model which evaluates the Pomeron helicity-flip coupling analogously to the isoscalar anomalous magnetic moment of the nucleon. This analogy was applied to the quark-gluon vertex and the anomalous color magnetic moment of the quark was found [11]. Ryskin calculated the helicity-flip part of the Pomeron-proton vertex, using the two-gluon model for the Pomeron and the non-relativistic constituent quark model for the nucleon. He showed that $\mathrm{Im}[r_5] = 0.13$, a result independent of energy. The spin-flip part of the three-gluon Odderon was also estimated in [11] and the helicity component was found to be nearly the same as for the Pomeron [16]. However, the helicity is defined relative to the direction of the proton momentum, and the quark momenta are oriented differently, making the proton helicity different from the sum of the quark helicities [21]. Perturbative QCD shows that the helicity-flip amplitude in pp elastic scattering correlates with the quark wave function of the proton and the spin effects cancel out if the spatial distribution of the constituent quarks in the proton is symmetric [16, 21]. However, if the proton wave function is dominated by a quark configuration containing a compact diquark (ud), the Pomeron helicity-flip is non-zero. The more the proton wave function is symmetric (the smaller the diquark is) the larger is $\mathrm{Im}[r_5]$ [16, 21]. As the diquark size is accepted to be 0.3 -0.4 fm, therefore $\mathrm{Im}[r_5]$ does not exceed 10%. In general, theoretical calculations emphasize values of $\mathrm{Im}[r_5]$, since the maximum of A_N in the CNI region can be evaluated as κ - $2\mathrm{Im}[r_5]$, as it will be shown in the sections to come.

Pion Exchange Model

A nucleon contains a pion cloud of large radius. Pumplin and Kane [19] introduced a model for the Pomeron-nucleon coupling, by focusing on the inelastic interactions of the colliding hadron with the virtual peripheral pions of the nucleon, since the helicity-flip amplitude is proportional to the impact parameter. This model predicts a value for $\mathrm{Im}[r_5] \approx 0.016(\ln s)^{3/2}$. The energy dependence is based on the radius of the pion cloud, assumed to be proportional to $(\ln s)^{1/2}$. A more detailed analysis which focused on the correlation of the value of r_5 with isospin, was undertaken

by [65]. This analysis led to $\mathrm{Im}[r_5] = 0.06$ for the Pomeron (and 0.15 for the f-reggeon) [16,65].

Impact Picture Model

The impact picture model, derived by Soffer, Bourrely and Wu [14,20,42], gives a successful description of pp and $p\bar{p}$ scattering up to ISR (Intersecting Storage Ring at CERN) energies. The spin-independent amplitude at high energies is shown as:

$$\phi_+^{impact}(s,t) = i\,s\int_0^\infty J_0(\mathrm{b}\sqrt{-t})(1-e^{-\Omega_0(s,\mathrm{b})})\mathrm{b}d\mathrm{b}, \tag{104}$$

where b is the impact parameter of the interaction, J_0 is the lowest order Bessel function and $\Omega_0(s,\mathrm{b})$ is defined to be the opaqueness and is associated with the Pomeron exchange. Ω_0 is assumed to factorize as $\Omega_0 = S_0(s)F(\mathrm{b}^2)$, where $S_0(s)$ is the crossing symmetric function which comes from the high energy behavior of quantum field theory. The t-dependence of $\phi_+^{impact}(s,t)$ is driven by $F(\mathrm{b}^2)$, which is related to the Fourier transform of the electromagnetic proton form factor [16]. The spin structure of the model [66], provides a good description of the polarization data up to highest available energy, $p_{\mathrm{L}} = 300$ GeV/c [16,66]. The spin dependent amplitude at RHIC energies is given by:

$$\phi_5^{impact}(s,t) = i\,s\int_0^\infty J_1(\mathrm{b}\sqrt{-t})\Omega_1(s,\mathrm{b})e^{-\Omega_0(s,\mathrm{b})}\mathrm{b}d\mathrm{b}, \tag{105}$$

where $\Omega_1(s,\mathrm{b})$ is the spin dependent opaqueness corresponding to the helicity-flip component of the Pomeron. $\Omega_1(s,\mathrm{b})$ factorizes as

$$\Omega_1(s,\mathrm{b}) = S_1(s)F_s(\mathrm{b}^2) + R_1(s,\mathrm{b}), \tag{106}$$

where $F_s(\mathrm{b}^2)$ is related to $F_0(\mathrm{b}^2)$ such as $F_s(\mathrm{b}^2) = b\omega(\mathrm{b}^2)F(\mathrm{b}^2)$ and $\omega(\mathrm{b}^2)$ is not very precisely known. The impact picture model is based on a rotating matter picture and w is the angular velocity that specifies a *rigid rotation* [20]. ω is replaced by a function of impact parameter $\omega(\mathrm{b})$, as given above, and is chosen such that $\omega(\mathrm{b}) \to 0$ as $\mathrm{b}^2 \to \infty$ [20]. In this case the motion is referred to as *soft rotation*, in contrast to *rigid rotation* [20]. Present theoretical knowledge does not allow a precise determination of the function $\omega(\mathrm{b}^2)$, therefore an arbitrary Gaussian form is chosen, [66]:

$$\omega(\mathrm{b}^2) = \omega_0 e^{-b^2/b_0^2}, \tag{107}$$

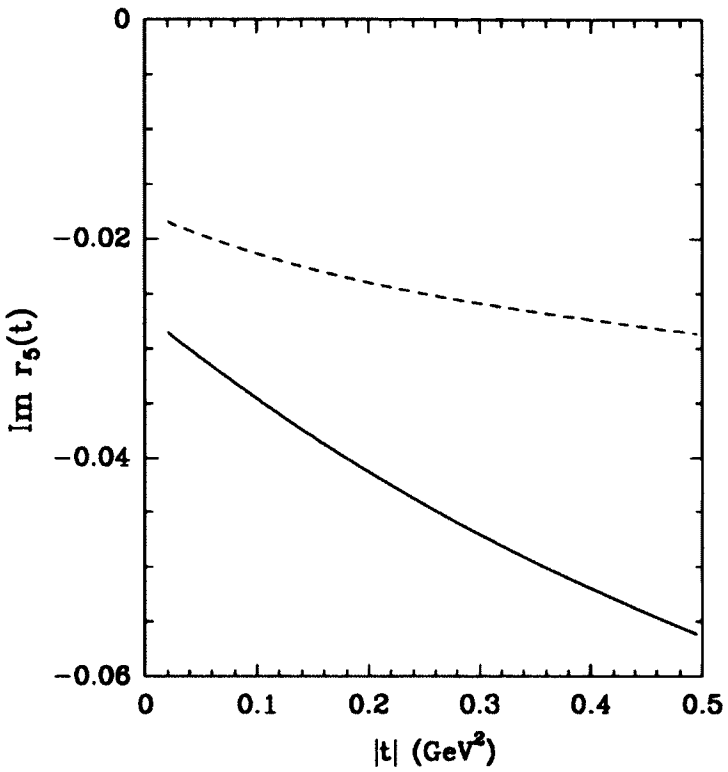

FIG. 13. Im[r_5] calculated in the impact picture model for two energy values: $\sqrt{s}$ = 50 GeV (dashed curve) and $\sqrt{s}$ = 500 GeV (solid curve) [16].

values of parameters ω_0 = -0.06 GeV and b_0 = 3.75 GeV^{-1}, obtained from the fit of 17 and 100 GeV/c data [66].

The second term in Eq. (106) is a necessary *Regge* spin-dependent contribution in order to study polarization and rotation parameters at low energies [20]. More explicitly, $R_1(s, b)$ is the Fourier transform of the standard *Regge* background, given in Eq. (71).

$$\tilde{R}_1(s,t) = \sqrt{t}[C'_+ + C'_- e^{-i\pi\alpha(t)}]e^{bt}s^{\alpha(t)}, \tag{108}$$

[20].

This model leads to a negative value for Im[r_5] $\approx$ -0.06, if one assumes that the flip component of the Pomeron is normalized at $t = 0$ by the nucleon isoscalar magnetic moment [16,67]. Fig. 13 shows the Im[r_5] value calculated in this model as a function of t. The graph shows that Imr_5 increases with energy.

The single spin asymmetry is given in terms of the Coulomb and hadronic amplitudes in the impact picture formalism:

$$A_{\rm N}(s,t) = \frac{4{\rm Im}((\phi_1^h(s,t))^* \phi_5^C(s,t))}{\Sigma_{i=1,\ldots,5}|\phi_i^h(s,t)+\phi_i^C(s,t)|^2}. \tag{109}$$

2.8.2 HELICITY FORMALISM AND SPIN OBSERVABLES $A_{\rm N}$, $A_{\rm NN}$, $A_{\rm SS}$

The spin dependent differential cross section for the polarized protons can be expressed in the form:

$$\sigma = \sigma_0[1 + A_{\rm N}(\vec{P}_b + \vec{P}_y)\cdot\vec{n} + \Sigma A_{ij}(\vec{P}_b\cdot\vec{i})(\vec{P}_y\cdot\vec{j})], \tag{110}$$

where $A_{\rm N}$ and A_{ij} are the asymmetry parameters, $\vec{P}_b$ and $\vec{P}_y$ are the beam polarization vectors, $\vec{n} = (\vec{k}_{in}\times\vec{k}_{out})/|\vec{k}_{in}\times\vec{k}_{out}|$; $\vec{k} = \vec{k}_{in}/|\vec{k}_{in}|$ where $\vec{k}_{in}$ and $\vec{k}_{out}$ are the momentum vectors of the incident and scattered particles; $\hat{s}$ is the unit vector pointing along the spin quantization axis, such as $\cos\beta = k\cdot s$, its the direction is given in terms of the angles β and ϕ (see Fig. 14), as given in [18].

For transversely polarized beams, Equation (110) can be rewritten in the following form:

$$\sigma = \sigma_0[1 + A_{\rm N}(\vec{P}_b + \vec{P}_y)\cdot\vec{n} + A_{\rm NN}(\vec{P}_b\cdot\vec{n})(\vec{P}_y\cdot\vec{n}) + A_{\rm SS}(\vec{P}_b\cdot\vec{s})(\vec{P}_y\cdot\vec{s})]. \tag{111}$$

where the term containing $A_{\rm SN}$ is not included since it has zero value due to parity conservation.

Equation (111) is written in terms of event count rates N instead of cross section σ, for the conditions of our experiment, as follows:

$$N^{++}(\phi) = N_0[1 + A_{\rm N}(P_b+P_y)\cos\phi + P_bP_y(A_{\rm NN}\cos^2\phi + A_{\rm SS}\sin^2\phi)], \tag{112}$$

$$N^{--}(\phi) = N_0[1 - A_{\rm N}(P_b+P_y)\cos\phi + P_bP_y(A_{\rm NN}\cos^2\phi + A_{\rm SS}\sin^2\phi)], \tag{113}$$

$$N^{+-}(\phi) = N_0[1 + A_{\rm N}(P_b-P_y)\cos\phi - P_bP_y(A_{\rm NN}\cos^2\phi + A_{\rm SS}\sin^2\phi)], \tag{114}$$

$$N^{-+}(\phi) = N_0[1 - A_{\rm N}(P_b-P_y)\cos\phi - P_bP_y(A_{\rm NN}\cos^2\phi + A_{\rm SS}\sin^2\phi)]. \tag{115}$$

where $P_b = |\vec{P}_b|$, $P_y = |\vec{P}_y|$ are the polarizations of the two beams and N^{++}, N^{--}, N^{+-} and N^{-+} are the azimuthal distributions of the scattered particles. N^{ij} are the normalized counting rates with respect to the luminosity for each spin combination.

G.G. Ohlsen and P.W. Keaton [18], have derived the expressions for measuring the spin-dependent asymmetries and ratios and the corresponding statistical uncertainties, i.e. the measurement of spin-1/2 analyzing power and its statistical uncertainty.

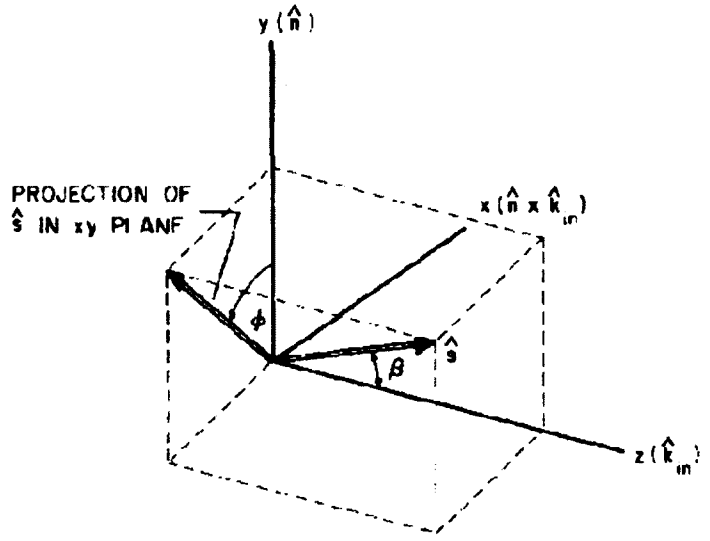

FIG. 14. Coordinate system for the spin angles definition (scattering is in the x-z plane): z is along the incident beam momentum, k_{in}; y is along $k_{in} \times k_{out}$ and k_{out} is scattered beam momentum; x completes a right-handed coordinate system; unit vectors along (x,y,z) are represented by $(\hat{l},\hat{n},\hat{k})$; the unit vector pointing along the spin quantization axis is denoted by s, its direction is defined by the angles β (the angle between the quantization axis and the beam direction such as $\cos\beta = k \cdot s$) and ϕ (the angle between the projection of s in the x-y plane and the y axis) [18].

We can make use of the square-root formula based on the calculation of geometric means [18], in order to exclude the external beam normalization (luminosity dependence), as follows:

$$\epsilon_1 = \frac{\sqrt{N^{++}(\phi)N^{--}(\pi-\phi)} - \sqrt{N^{++}(\pi-\phi)N^{--}(\phi)}}{\sqrt{N^{++}(\phi)N^{--}(\pi-\phi)} + \sqrt{N^{++}(\pi-\phi)N^{--}(\phi)}}$$

$$= \frac{A_N(P_b + P_y)\cos\phi}{1 + P_b P_y(A_{NN}\cos^2\phi + A_{SS}\sin^2\phi)}, \quad (116)$$

$$\epsilon_2 = \frac{\sqrt{N^{+-}(\phi)N^{-+}(\pi-\phi)} - \sqrt{N^{+-}(\pi-\phi)N^{-+}(\phi)}}{\sqrt{N^{+-}(\phi)N^{--}(\pi-\phi)} + \sqrt{N^{++}(\pi-\phi)N^{--}(\phi)}}$$

$$= \frac{A_N(P_b - P_y)\cos\phi}{1 - P_b P_y(A_{NN}\cos^2\phi + A_{SS}\sin^2\phi)}. \quad (117)$$

where ϵ_1, ϵ_2 are the "raw asymmetries" for $(\uparrow\uparrow, \downarrow\downarrow)$ and $(\uparrow\downarrow, \downarrow\uparrow)$ spin combinations. See Appendix C for a complete derivation of the spin-dependent parameters and the square-root formula, by the ITEP group at the STAR collaboration. (ϕ) and (π - ϕ) can also be and are often denoted as R and L, referring to *right* and *left* in the azimuthal plane.

The term $\delta(\phi) \equiv P_b P_y(A_{NN}\cos^2\phi + A_{SS}\sin^2\phi)$ is determined to be ≤ 0.002, according to the measurement of the double spin asymmetries A_{NN} and A_{SS} by the PP2PP experiment at RHIC in 2004, [26]. Thus, the term $\delta(\phi)$ can be safely neglected relative to 1, introducing a relative error less than 2%. Recent preliminary results on the double spin asymmetries A_{NN} and A_{SS} of our experiment (from the work performed by the ITEP group at the STAR collaboration, [68], has showed that both A_{NN} and A_{SS} are very small ≈ 0.005 (and compatible with zero), constraining $\delta(\phi)$ to ≈ 0.002, which can be safely neglected, refer to [69]. Ref. [69] is the recent result on the measurement of the single spin asymmetry A_N in polarized proton-proton elastic scattering at $\sqrt{s} = 200$ GeV at RHIC, by the STAR collaboration from our experiment.

The counting rates N^{++}, N^{--}, N^{+-} and N^{-+} can also be written as $N_{\uparrow\uparrow}$, $N_{\downarrow\downarrow}$, $N_{\uparrow\downarrow}$ and $N_{\downarrow\uparrow}$ for each combination of the two beams. The single spin asymmetry A_N (analyzing power) and double spin asymmetry A_{NN} can be expressed in the following form:

$$A_N = \frac{1}{P_1 \cos\phi} \frac{N_{\uparrow\uparrow} - N_{\downarrow\downarrow} + N_{\uparrow\downarrow} - N_{\downarrow\uparrow}}{N_{\uparrow\uparrow} + N_{\downarrow\downarrow} + N_{\uparrow\downarrow} + N_{\downarrow\uparrow}}, \tag{118}$$

$$A_N = \frac{1}{P_2 \cos\phi} \frac{N_{\uparrow\uparrow} - N_{\downarrow\downarrow} - N_{\uparrow\downarrow} + N_{\downarrow\uparrow}}{N_{\uparrow\uparrow} + N_{\downarrow\downarrow} + N_{\uparrow\downarrow} + N_{\downarrow\uparrow}}, \tag{119}$$

$$A_{NN} = \frac{1}{P_1 P_2 \cos^2\phi} \frac{N_{\uparrow\uparrow} + N_{\downarrow\downarrow} - N_{\uparrow\downarrow} - N_{\downarrow\uparrow}}{N_{\uparrow\uparrow} + N_{\downarrow\downarrow} + N_{\uparrow\downarrow} + N_{\downarrow\uparrow}}. \tag{120}$$

As suggested also by I.G. Alekseev *et al.*, see Appendix C, only N^{++} and N^{--} combinations carry information on A_N parameter in case of equal polarization of the two colliding beams, P_1 and P_2. The counting rates N^{+-} and N^{-+}, carry information about the difference in polarizations of the two colliding beams. The measurement of A_N using information from N^{+-} and N^{-+} combinations, can be used as a systematic error of the result, depending on the our knowledge and precision of the polarization values of the two beams and if their difference is expected to be zero. If the spin pattern consisted of only N^{++} and N^{--} combinations, it would be possible to measure A_N with an additional precision gain of $\sqrt{2}$, see Appendix C. A_N can also be measured in the case that only one of the beams is polarized. The "raw asymmetry" in this case is expected to be half of the "raw asymmetry" measured in the case where both beams are polarized. In addition, we would have twice as more statistics in the case where only one beam is polarized, giving a statistical precision of $\sqrt{2}$ times larger in the measurement of A_N.

2.8.3 THE TRANSVERSE SINGLE SPIN ASYMMETRY A_N

The contribution of the two double helicity-flip hadronic amplitudes (ϕ_2^{had} and ϕ_4^{had}) to the single spin asymmetry A_N is indicated to be small by both theoretical predictions [70] and experimental measurements [26] (in pp elastic scattering at $\sqrt{s}$ = 200 GeV in 2004, at RHIC), and [68] (in pp elastic scattering at $\sqrt{s}$ = 200 GeV in 2009, at RHIC). Therefore, the main contribution to A_N comes from the interference between the single photon exchange (Coulomb amplitude) with the hadronic amplitude, and Eq. (90) reduces to:

$$A_N \frac{d\sigma}{dt} = -\frac{8\pi}{s^2} \mathrm{Im}(\phi_5^{em} \phi_+^{had} + \phi_5^{had} \phi_+^{em}), \tag{121}$$

where $\phi_+ = (\phi_1 + \phi_3)/2$ are the helicity conserving amplitudes and ϕ_5 is the single helicity-flip amplitude. In the one-photon exchange approximation ϕ_+^{em} and ϕ_5^{em} are real and have well established expressions, as given in Eq. (100), so in order to give a theoretical prediction for A_N, one needs to know the hadronic amplitudes, [16]. The imaginary part of the largest hadronic amplitude ϕ_+^{had} is related at $t = 0$ to the total cross section σ_{tot} as given in Eq. (94) and the interference term between ϕ_5^{em} and ϕ_+ is most prominent at $t = -8\pi\alpha/\sigma_{tot} \equiv t_c$, [16]. What is left in Eq. (121) is the hadronic helicity flip amplitude ϕ_5^{had}, the existence and the magnitude of which at this energy and kinematic regime is not known. Previous measurements of A_N in the CNI region, from different experiments (including the measurement of A_N at 200 GeV, by the PP2PP experiment at RHIC), have been performed at different energy ranges and will be shown in the next subsection.

Given the above, the first interference term between the electromagnetic helicity-flip amplitude with the hadronic non helicity-flip amplitude (first term on the right side of Eq. (121)) can be calculated in QED (which means that A_N can be calculated in the absence of the hadronic helicity-flip amplitude ϕ_5^{had}), a measurement of A_N in the CNI region is a probe to a contribution of a second interference term between the electromagnetic non helicity-flip amplitude with a possible hadronic spin-flip amplitude, ϕ_5^{had}. The parametrization of ϕ_5^{had} is given in terms of ϕ_+^{had}, such as:

$$\phi_5^{had}(s,t) = \left(\frac{-t}{m}\right) r_5(s) \mathrm{Im}\phi_+^{had}(s,t), \tag{122}$$

where m is the proton mass and r_5 is a relative amplitude. As explained above, the presence of a hadronic helicity-flip amplitude modifies the QED calculation and the contribution of a hadronic helicity-flip amplitude to A_N, is described by the magnitude of the r_5-parameter.

Our main interest in this study is the measurement of A_N, whose main contribution comes from the interference of electromagnetic single helicity-flip amplitude ϕ_5 with the non helicity-flip amplitudes (as given in Eq. (121)), we will mainly focus on the asymptotic behavior of ϕ_5. The r_5-parameter can also be defined as:

$$r_5 = \mathrm{Re}\, r_5 + i\mathrm{Im}\, r_5 = \frac{m_p \phi_{flip}^{had}}{\sqrt{-t}\phi_{non-flip}^{had}}, \tag{123}$$

given also in Eq. (122). Therefore, the determination of the r_5-parameter is the measure of the hadronic spin-flip contribution to elastic pp scattering.

The asymmetry for the CNI region can be expressed as a ratio of a linear expression in t_c/t in the numerator and a quadratic expression for t_c/t in the denominator [71], and A_N can be parametrized in terms of the r_5 parameter, such as:

$$A_N = \frac{\sqrt{-t}}{m} \frac{[\kappa(1-\rho\,\delta) + 2(\delta\,\mathrm{Re}\,r_5 - \mathrm{Im}\,r_5)]\frac{t_c}{t} - 2(\mathrm{Re}\,r_5 - \rho\,\mathrm{Im}\,r_5)}{(\frac{t_c}{t})^2 - 2(\rho+\delta)\frac{t_c}{t} + (1+\rho^2)} \,. \tag{124}$$

In this formula $t_c = -8\pi\alpha/\sigma_{tot}$, κ is the anomalous magnetic moment of the proton, $\rho = \mathrm{Re}\phi_+/\mathrm{Im}\phi_+$ is the ratio of the real to imaginary parts of non-flip elastic amplitude, and δ is the relative phase between the Coulomb and hadronic amplitudes [16].

The Coulomb phase is small in the CNI region (≈ 0.02), getting smaller at larger-t and it has a slight effect on the position of the maximum peak in A_N:

$$\frac{t_{max}}{t_c} = \sqrt{3} + \frac{8}{\kappa}(\rho\mathrm{Im}\,r_5 - \mathrm{Re}\,r_5) - (\rho+\delta)\,, \tag{125}$$

where t_{max} is t value where A_N experiences its maximum. However, the effect of the phase δ is negligible in pp scattering, since it is multiplied by small amplitudes. The height of the peak is mainly sensitive to the unknown quantity $\mathrm{Im}[r_5]$, while the shape depends on $\mathrm{Re}[r_5]$. An $\mathrm{Im}[r_5]$ of $\pm$ 0.1, modifies A_N by about 11% and a large value of $\mathrm{Im}[r_5]$ generates a very large uncertainty on A_{max}, [16]. The asymmetry has a characteristic shape, which was first calculated by Schwinger [72] and other authors [16,21,32]. The interference between the electromagnetic single spin-flip and the hadronic non-flip amplitude gives rise to this asymmetry. Eq. (100) shows the value of ϕ_5^{em} calculated for one-photon exchange approximation and can be written also as:

$$\phi_5^{em} = \frac{\alpha\sqrt{s}}{\sqrt{|t|}} \frac{\mu_p - 1}{2m}\,, \tag{126}$$

where α is the fine structure constant and μ_p is the proton's total magnetic moment.

Overview of Measurements of the Transverse Single Spin Asymmetry A_N in the Coulomb Nuclear Interference (CNI) Region

The transverse single spin asymmetry (analyzing power) A_N has been extensively measured for pp elastic scattering. One of these measurements in the first measurement of A_N in the CNI region, performed by E704 experiment at Fermi National Accelerator Facility (Fermilab) [73], using a polarized proton beam on a fixed target

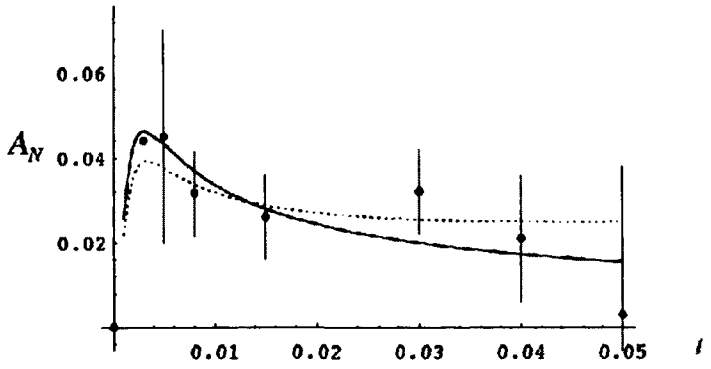

FIG. 15. The data points on A_N as a function of $-t$ in GeV/c. The solid curve is the best fit with the hadronic amplitude ϕ_5 constrained to be in phase with hadronic ϕ_+ and the dotted curve is the best fit without this constraint [16].

at a lab momentum $p_L = 200$ GeV/c and at the kinematic region where $-t$ from 1.5 $\times 10^{-3}$ (GeV/c)^2 to 5.0 $\times 10^{-3}$ (GeV/c)^2. The plot given in Fig. 15 shows the A_N results as a function of t, measured by the E704 experiment at a lab momentum p_L = 200 GeV/c. The two fits in the E704 data allow a non-zero r_5, the solid curve is the best fit with the constraint that ϕ_5 is in phase with ϕ_+. If the two amplitudes have the same asymptotic behaviour, they will have the same phase [16]. Fitting with this constraint results in an $|r_5| = 0.0 \pm 0.16$ from the fit, and fitting without the constraint results in $|r_5| = 0.2 \pm 0.3$ with a relative phase angle to ϕ_+ of 0.15 $\pm$ 0.27 rad [16].

The plot in Fig. 16 [73], shows results on the measurement of A_N as a function of $-t$ from E704 experiment at 200 GeV/c along with preliminary results from the same experiment at 185 GeV/c [75]. There are other data points on the same plot from polarized target experiments at different lab momenta: 300 and 100 GeV/c by Snyder *et. al.*, [76]; 176 $\pm$ 12 GeV/c by Corcoran *et. al.*, [77] and at 150 GeV/c by Fidecaro *et. al.*, [78].

Investigation of Polarized pp Scattering at Specific Momentum Transfer Squared $-t$ Regions

Several specific $-t$ regions are relevant to the measurement of different observables in the study of polarized pp scattering, [6]. In addition, information from different

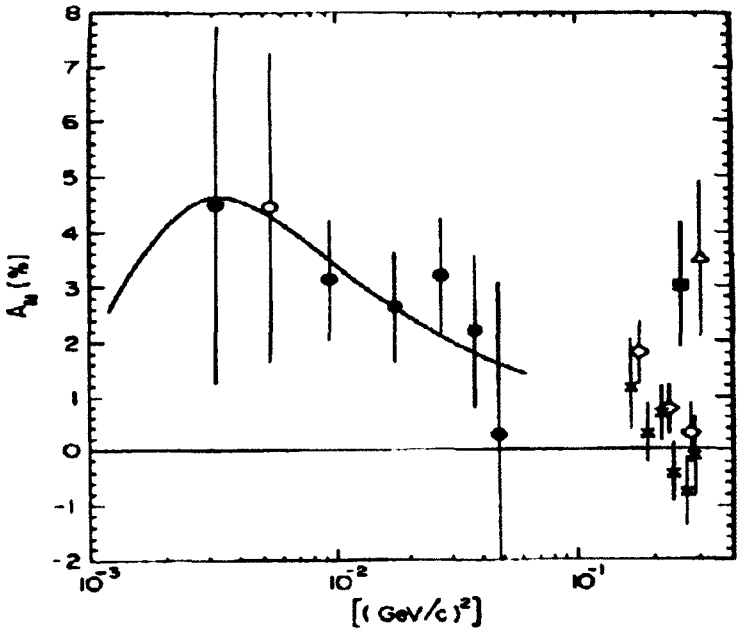

FIG. 16. A_N results for pp elastic scattering as a function of $-t$ [73]. The solid curve is the theoretical prediction [74] in the CNI-region. The data points represented by (o) are measured at 185 GeV/c [75] and the results those represented by (•) at 200 GeV/c [73]. The other data points: (×) are measured at lab momentum 300 GeV/c ($\sqrt{s} = 24$ GeV) and (◇) at 100 GeV/c [76], (△) at 176 ± 12 GeV/c [77], and (black-box) at 150 GeV/c [78] using a polarized target.

kinematic $-t$ regions helps us understand the t-dependence of the observables.

- Forward direction ($|t| \simeq 0$ region), is relevant to the measurement of the total cross section σ_{tot} and $\Delta\sigma_{\mathrm{T}}$
- Coulomb-Nuclear Interference (CNI) region, is relevant for the measurement of the analyzing power A_{N}, because this is the region of maximal interference between the electromagnetic and hadronic amplitudes, which results in a measurable asymmetry in pp scattering.
- Measuring in the small-t region (0.05 to 0.15 $(\mathrm{GeV}/c)^2$), where there is a pronounced lack of data (see Fig. 16), is important in order to understand the possible spin dependent amplitudes that survive at high energies even in the small-t region.
- A_{N} shows a unique structure in the region where the so called "diffractive dip" is observed, starting around $\sqrt{s} \approx 15$ GeV. This region can also be further explored by measuring the double spin correlation parameter A_{NN}, [6].
- The region of $|t| > 2$ $(\mathrm{GeV}/c)^2$ is unexplored and measurements in this region can help understand the hard regime spin effects, [6].

The A_{N} results presented by E704 experiment in 1993, showed for the first time that a theoretically predicted interference between the hadronic non-spin flip amplitude and the electromagnetic spin-flip amplitude is present at high energies in the four-momentum transfer squared region of 1.5×10^{-3} to 5.0×10^{-3} $(\mathrm{GeV}/c)^2$ [73]. A_{N} has been measured also at lower energy experiments: at lab momentum 10, 14 and 17.5 GeV/c [79], at 11.8 GeV/c [80], at 24 GeV/c [81] and at 45 GeV/c [82].

The following Table 3, lists the experiments that have contributed since 1966 to polarized pp elastic scattering data. The table gives information on the location (accelerator facility) of the experiment, the year of the experiment (in reverse-chronological order), the $\sqrt{s}$ and t ranges, the observables measured in each experiment and the corresponding reference. The table contains information from the summary made by [29] in 2001. In Table 3, AGS stands for Alternating Gradient Synchrotron accelerator at Brookhaven National Laboratory; SPS is the Super Proton Synchrotron accelerator at CERN; ZGS is the Zero-Gradient Synchrotron accelerator at Argonne National Laboratory and LRL is the Lawrence Radiation Laboratory in Berkeley, CA.

TABLE 3. Overview of experiments performed to measure polarized proton elastic scattering. P_0 indicates the polarization parameter measured at several designed experiments with polarized beam on a polarized target. The polarization parameter, P_0, in elastic scattering complements the differential cross section as a parameter which is sensitive to the spin dependence of the scattering amplitude [83].

Year	Collider Accelerator Facility (Exp.)	cms Energy $\sqrt{s}$ (GeV)	$\|t\|$ Range $(\mathrm{GeV}/c)^2$	Spin Dependent Observable	Ref.
2012	BNL (STAR)	200	0.003 - 0.035	A_N	[69]
2011	BNL (H-jet)	7.7, 21.7	0.002 - 0.008	A_N	[23]
2009	BNL (H-jet)	6.8, 13.7	0.001 - 0.032	A_N, A_{NN}	[22]
2007	BNL (STAR)	200	0.01 - 0.03	A_{NN}, A_{SS}	[26]
2006	BNL (H-jet)	13.7	0.001 - 0.032	A_N	[84]
2005	BNL (PP2PP)	200	0.01 - 0.03	A_N	[25]
1993	FNAL (E704)	19.4	0.0015 - 0.050	A_N	[73]
1989	AGS	5.3 - 6.2	0.3 - 4.7	A_N, A_{NN}	[85]
1989	FNAL (E704)	19.2	0.001 - 0.01	A_N	[75]
1981	CERN	7.1	0.7 - 5.0	P_0	[86]
1981	CERN SPS	200	0.5 - 4.0	P_0	[87]
1980	FNAL	6.3 - 19.7	0.6 - 1.0	P_0	[77]
1980	CERN SPS	17	0.4 - 3.0	P_0	[88]
1980	FNAL	14	0.15 - 1.10	P_0	[89]
1980	FNAL	24	0.15 - 2.0	P_0	[89]
1978	FNAL	14, 24	0.18 - 2.0	P_0	[76]
1978	CERN SPS	17.3	0.2 - 3.0	P_0	[90]
1978	CERN	7.1	0.1 - 0.9	P_0	[83]
1976	CERN	9.6	0.08 - 1.1	P_0	[82]
1974	ZGS	3.5 - 5.2	0.5 - 6.5	P_0	[91]
1971	CERN	4.7 - 6.1	0.1 - 2.9	P_0	[79]
1966	LRL	1.63 - 1.86		P_0	[92]
1966	LRL	2.3 - 3.78	0.1 - 1.0	P_0	[93]

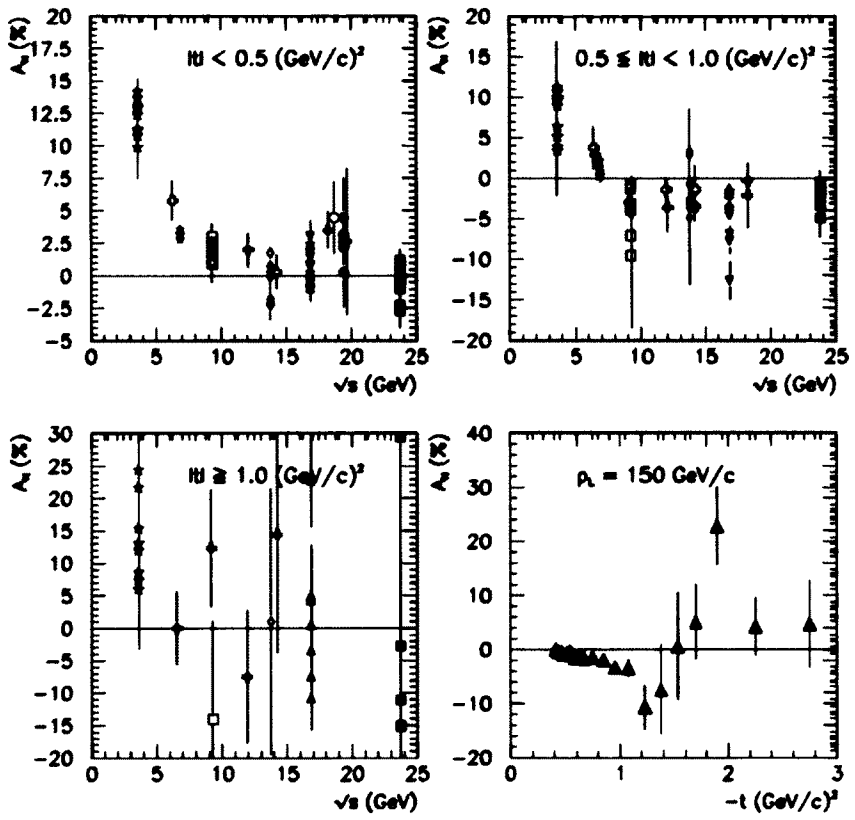

FIG. 17. A_N results for pp elastic scattering as a function of $\sqrt{s}$ at three different $|t|$ regions: ($|t| < 0.5$ (GeV/c)^2, $0.5 \leq |t| < 1.0$ (GeV/c)^2 and $|t| \geq 1.0$ (GeV/c)^2). The data points are measured in experiments using different incident proton beam with lab momentum spanning from 6 - 300 GeV/c [6].

Polarization measurements in elastic scattering have been performed up to 300 GeV/c ($\sqrt{s} = 24$ GeV), with polarized proton beam on a polarized fixed target, in different experiments [76,77,87,89,90] and at lower energies [79,82,83,91–93]. Figure 17 illustrates A_N as a function of center of mass energy $\sqrt{s}$ in three different $|t|$ regions [6], measured at several different experiments given in Table 3.

If we look at the A_N data at different energy and t ranges, we observe the following features.

- At small t values ($|t| \leq 0.5$ (GeV/c)^2, the analyzing power A_N is positive and decreasing as $\sim 1/\sqrt{s}$ up to $\sqrt{s} \approx 50$ GeV. At higher energies A_N shows a flattening.

- For $\sqrt{s} \geq 50$ GeV, A_N changes sign in the t range between 0.4 and 1.0 $(\text{GeV}/c)^2$, reaching a negative minimum. This is followed by a sharp zero-crossing (to the positive values) in the region of the diffractive dip of the differential cross section (around $|t| \approx 1.2$ $(\text{GeV}/c)^2$. Then, A_N most probably remains positive at larger $|t|$ values.

The features exhibited by A_N at large-t may indicate that the hadronic spin-flip contribution ϕ_5^{had} does not decrease as $1/\sqrt{s}$. It was suggested that at large $\sqrt{s}$, the diffractive scattering with the exchange of two pions could become important, an exchange mechanism which can cause a non-vanishing ϕ_5^{had} because one of the two pions can couple with spin-flip [6, 94]. In addition, ϕ_5^{had} may remain non-zero at high energies if the nucleon contains a dynamically enhanced compact diquark component [21].

If we look at more recent experiments dedicated to the measurement of A_N in the CNI region, we point out (mentioned before), the measurements by the PP2PP experiment at RHIC, at $\sqrt{s} = 200$ GeV but with limited statistics: on the measurement of A_N [25] and on the measurement of A_{NN} & A_{SS} [26].

Other experiments, performed at significantly lower energies include: the FNAL E704 experiment at $\sqrt{s} = 19.4$ GeV (mentioned in this section); high precision experiments with RHIC polarimeters (hydrogen-jet absolute polarimeter at RHIC): [84] using proton beam with momentum 100 GeV/c ($\sqrt{s} = 13.7$ GeV), [22] using proton beam with momentum 24 and 100 GeV/c ($\sqrt{s} = 6.8$ and 13.7 GeV, respectively) and [23] using proton beam with momentum 31 and 250 GeV/c ($\sqrt{s} = 7.7$ and 21.7 GeV, respectively). Figure 18 shows the measurement of the analyzing power A_N in pp elastic scattering using a polarized atomic hydrogen gas jet target and the RHIC proton beam from the three experiments. Similarly results from [23] are shown in Fig. 19 and 20, together with the measured r_5-parameter in each case.

The data from the measurement of A_N by the H-jet polarimeter at RHIC at 13.7 GeV (Fig. 18(a) and 18(c)) are well described by the CNI prediction, in which A_N is generated by the proton's anomalous magnetic moment alone and do not support the presence of a large hadronic spin-flip contribution, [84]. The A_N data at 6.8 GeV (Fig. 18(b)) indicate the presence of a non-zero hadronic spin-flip amplitude ϕ_5^{had} and suggest a significant energy dependence for this amplitude compared to the measurement at 13.7 GeV, [22]. In addition, Fig. 18(d) shows the measurement of the double spin asymmetry A_{NN} at both center of mass energies. The measured

A_{NN} data points are small and the data do not support a sizable double spin-flip amplitude ϕ_2^{had} at these energies, [22]. Finally, the A_N results shown in Fig. 20 are consistent with no hadronic helicity flip amplitude contribution within experimental 1σ uncertainty, while the A_N results shown in Fig. 19, require the presence of a hadronic helicity flip amplitude contribution at a ($\sim 2.5\ \sigma$) confidence level, [23].

To complete the reverse chronological order of this discussion, we finally introduce the results from the experiment which is the subject of this dissertation, high precision and very recent measurements from the STAR experiment at RHIC at $\sqrt{s} = 200$ GeV: on the measurement of A_N [69] (very recently published) and on the measurement of A_{NN} & A_{SS} [68].

The analyzing power has also been measured in proton-Carbon scattering at 6.4 GeV by the BNL AGS [95] (in the CNI region of momentum transfer $9.0 \cdot 10^{-3} < -t < 4.1 \cdot 10^{-2}$ (GeV/c)^2 with a 21.7 GeV/c polarized proton beam) and later by [96]. The usage of carbon target, as was pointed out by Kopeliovich and Trueman [97], has an important advantage of eliminating the contribution of the isovector Reggeons and thus allows one to probe the Pomeron spin-flip amplitude through A_N at medium energies [95]. A non-zero value of r_5 was obtained for the first time in p-C elastic scattering in the CNI region, at the given energy and t-range [95].

2.9 MEASUREMENT OF TRANSVERSE SPIN ASYMMETRIES A_N, A_{NN}, A_{SS} IN POLARIZED pp ELASTIC SCATTERING AT RHIC

In this section we will summarize the measurements of A_N, A_{NN} and A_{SS} in pp elastic scattering by the PP2PP experiment at RHIC at $\sqrt{s} = 200$ GeV. Bültmann *et al.*, performed the first measurement of the single spin analyzing power A_N at $\sqrt{s} = 200$ GeV and $0.01 \leq |t| \leq 0.03$ (GeV/c)^2, using polarized proton beams at RHIC [25]. The result on A_N and the measured r_5 parameter are shown in Fig. 21. The statistics of these measurements were limited.

The A_N result presented by the PP2PP collaboration in 2005, is about one standard deviation above the theoretical calculation which uses only the interference between electromagnetic spin-flip amplitude and hadronic non-flip amplitude. The difference could be explained by an additional contribution of a hadronic spin-flip amplitude [25]. Based on these results with limited statistics, Bültmann *et al.* conclude that the results are suggestive of a hadronic spin-flip term, but cannot definitely rule out the hypothesis that only hadronic non spin flip amplitudes contribute. After

PP2PP physics program was integrated with the STAR physics program at RHIC, the necessity and the strong motivation for a precise measurement of A_N at the energies available at RHIC (especially at $\sqrt{s} = 200$ GeV with improved statistics), motivated the STAR collaboration to perform a statistically significant measurement of A_N, and this was achieved during 2009 RHIC run. The A_N results from 2009 RHIC run by the STAR collaboration have been published very recently in [69].

The double spin asymmetries A_{NN} and A_{SS}, were also measured for the first time at $\sqrt{s} = 200$ GeV and $0.01 \leq |t| \leq 0.03$ $(\text{GeV}/c)^2$, by the PP2PP collaboration at RHIC. The measured asymmetries are consistent with zero and allow the estimation of the upper limits on the double helicity-flip amplitudes ϕ_2 and ϕ_4 at small $|t|$, as well as on the difference $\Delta\sigma_T$ between the total cross sections for transversely polarized protons with antiparallel and parallel spin orientations [26]. These measurements have been complemented by the RHIC 2009 run data. The analysis of these data to extract the double spin asymmetries has been carried out by the ITEP group at STAR and preliminary results have been presented by the STAR collaboration [68]. Preliminary results on the double spin asymmetries at $\sqrt{s} = 200$ GeV using RHIC Run09 data, shown in Fig. 22, show that the double spin effects are small and comparable with the luminosity normalization uncertainty [68]. Preliminary results agree with the hypothesis that only Pomeron exchange which contributes to spin non-flip amplitudes ϕ_1 and ϕ_3, survive at high energies [68].

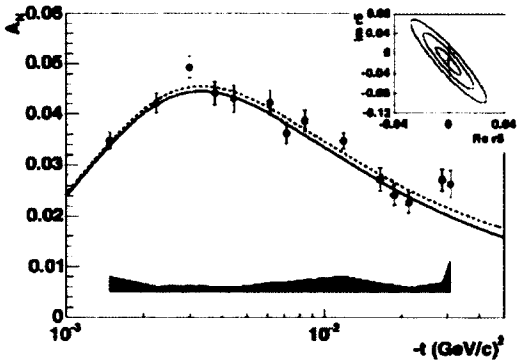

(a) A_N vs $-t$ at $\sqrt{s} = 13.7$ GeV (2006)

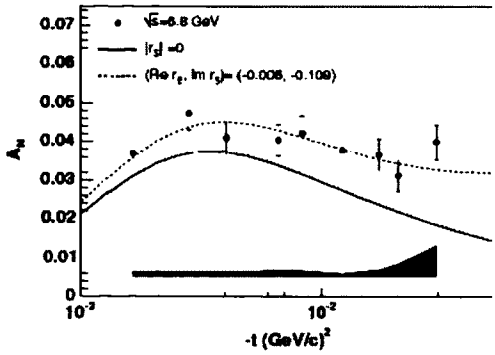

(b) A_N vs $-t$ at $\sqrt{s} = 6.8$ GeV

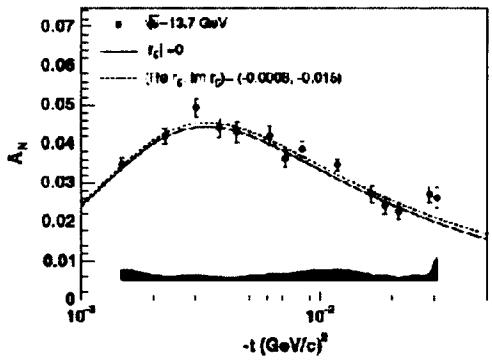

(c) A_N vs $-t$ at $\sqrt{s} = 13.7$ GeV (2009)

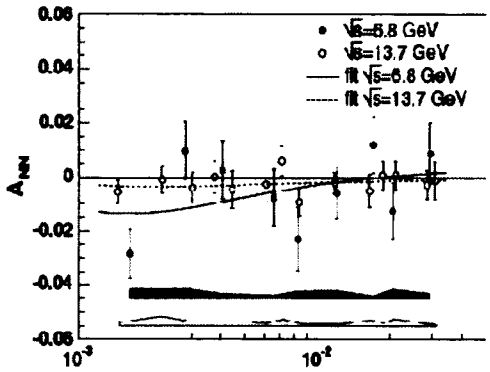

(d) A_{NN} vs $-t$ at $\sqrt{s} = 6.8$ and 13.7 GeV

FIG. 18. A_N as a function of $-t$ for $pp^\uparrow \to pp$ (a) at 13.7 GeV [84], the solid curve is the prediction of A_N with electromagnetic spin-flip only, the dashed curve is the fit to the data allowing a hadronic spin-flip contribution to A_N, the inset is the r_5 plot with the 1-, 2- and 3-σ confidence contours; (b) and (c) at 6.8 & 13.7 GeV (repeated), respectively, [22], the solid curve again corresponds to the QED prediction with no hadronic spin-flip contribution and the dashed curve allows this contribution, r_5 parameter is extracted from the best fit to the data; (d) A_N as a function of $-t$ at 6.8 GeV (filled circles) and 13.7 GeV (open circles), the solid curve is the fitting result for 6.8 GeV and the dashed curve for 13.7 GeV; valid for all the plots shown above: statistical errors are shown on the data points, the lower band represents the total systematic error.

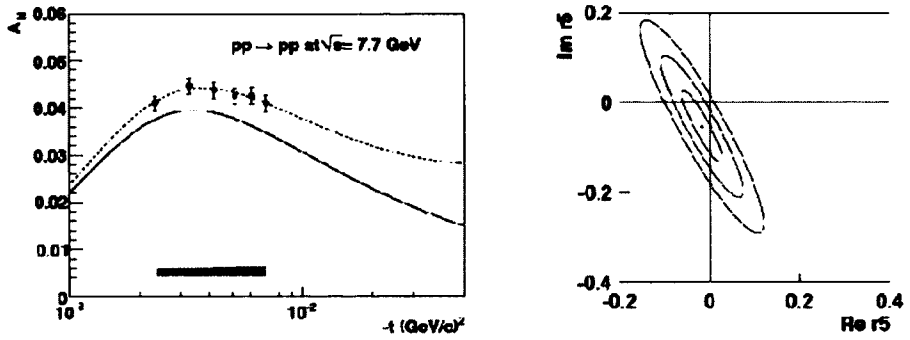

FIG. 19. A_N as a function of $-t$ for $pp^\uparrow \to pp$ at 7.7 GeV [23], statistical errors are shown on the data points, the lower band represents the total systematic error, solid curve is the prediction of A_N with electromagnetic spin-flip only, the dashed curve is the fit to the data allowing a hadronic spin-flip contribution to A_N, the r_5 plot with the 1-, 2- and 3-σ confidence contours is also shown.

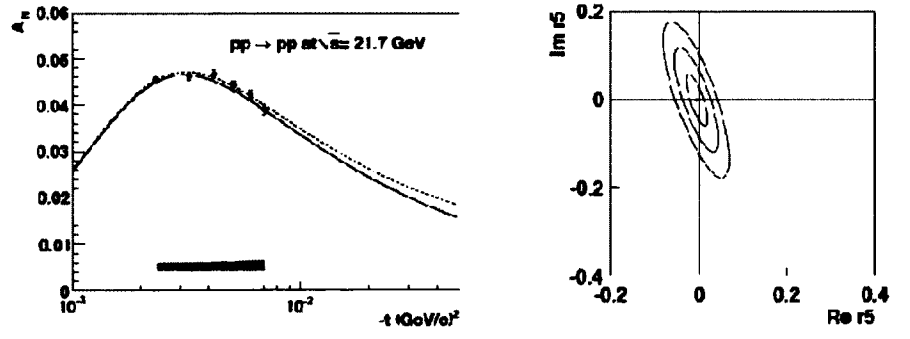

FIG. 20. A_N as a function of $-t$ for $pp^\uparrow \to pp$ at 21.7 GeV [23], the rest (details on the errors, solid and dashed curves, r_5 plot) are the same as in Fig. 19.

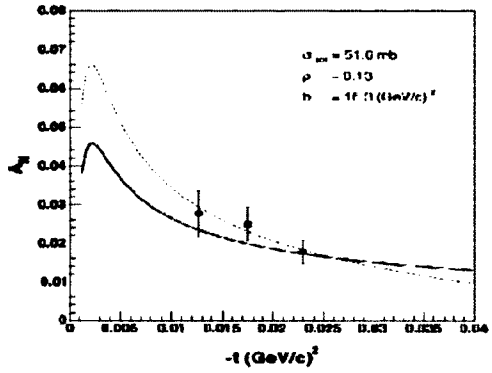

(a) A_N vs $-t$ at $\sqrt{s} = 200$ GeV (PP2PP)

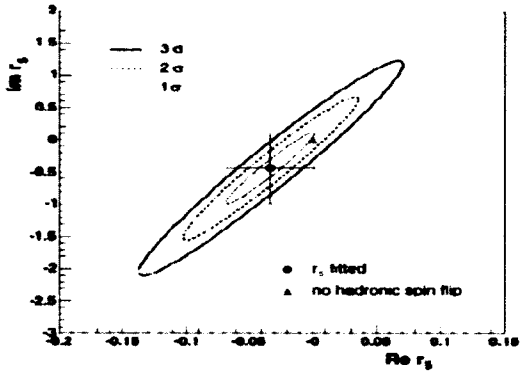

(b) r_5: $\mathrm{Im}r_5$ vs $\mathrm{Re}r_5$ (PP2PP)

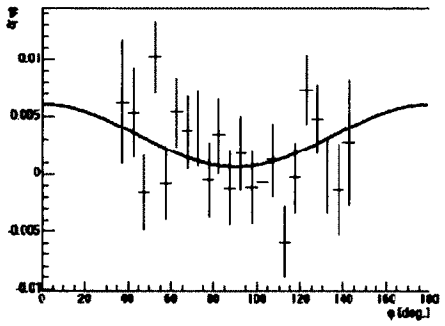

(c) Raw Double Spin Asymmetry vs ϕ (PP2PP)

FIG. 21. First measurement of A_N and the double spin asymmetries A_{NN} and A_{SS}, by the PP2PP collaboration at $\sqrt{s} = 200$ GeV, at RHIC. (a) A_N as a function of $-t$ for three t intervals. Vertical error bars show statistical errors. The solid curve corresponds to the theoretical calculations without hadronic spin-flip and the dashed curve represents the best r_5 fit [25]; (b) the measured r_5 parameter: full circles represent the fitted values of r_5 with contours corresponding to different confidence levels. The red triangle corresponds to no hadronic spin-flip; (c) the raw double spin asymmetry $\delta(\phi)$ measured in pp elastic scattering at $\sqrt{s} = 200$ GeV [26].

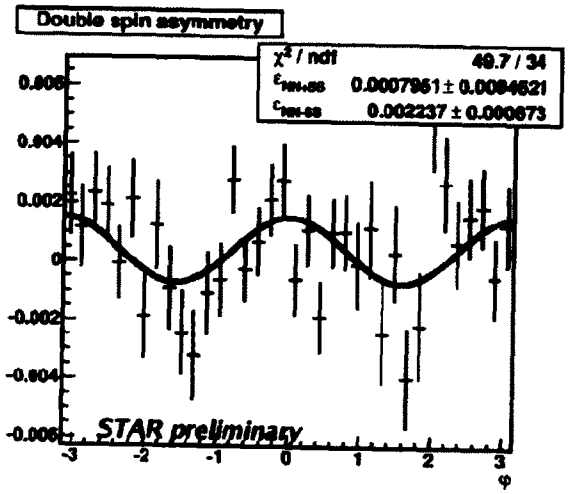

FIG. 22. Preliminary double spin asymmetry results using RHIC 2009 run data at $\sqrt{s} = 200$ GeV and $0.003 \leq |t| \leq 0.035$ $(\text{GeV}/c)^2$, by the STAR collaboration. The plots shows the raw asymmetries ϵ as a function of ϕ (in rad) [68].

CHAPTER 3

EXPERIMENTAL SETUP

3.1 THE RELATIVISTIC HEAVY ION COLLIDER (RHIC)

The Relativistic Heavy Ion Collider (RHIC) is located at Brookhaven National Laboratory (BNL). Figure 23 shows an aerial view of the BNL facility, located in Long Island, New York, USA.

The complete RHIC (see Fig. 24) facility is a complex of accelerators interconnected by beam transfer lines. The collider is located in a 3.8 km circumference tunnel. The main physics program of RHIC is to provide head-on collisions at energies up to 100 GeV/u per beam for heavy ions, like ^{197}Au, but the physics program also includes lighter ions all the way down to protons, including polarized protons [98]. RHIC is distinctive in the capability to collide spin polarized proton beams. Moreover, RHIC is known for its large versatility: the ability to collide a wide variety of atoms/particles (Au-Au, d-Au, Cu-Cu, polarized proton), with a high luminosity: reaching 10^{31} cm^{-2}s^{-1} in 200 GeV pp operation, in a wide and previously not accessible energy range: 50 GeV $\leq \sqrt{s} \leq$ 500 GeV, and with a high polarization for proton beams: achieving 70 % in 200 GeV pp operation.

The primary motivation for colliding heavy ions at ultra-relativistic energies is the creation of macroscopic volumes of nuclear matter at temperatures and energy densities high enough to induce a phase transition from hadronic matter to a confined plasma of quarks and gluons [98]. RHIC is presently the world's only polarized proton collider, therefore RHIC is unique in its capability to collide spin polarized protons, with a high average polarization per beam. RHIC started operation in 2000, consisting of five large experiments: BRAHMS (2 o'clock), PP2PP (2 o'clock), STAR (6 o'clock), PHENIX (8 o'clock) and PHOBOS (10 o'clock), (see Fig. 24). Presently there are only two physics experiments in operation, STAR and PHENIX. The physics program of the two experiments/collaborations consists of two main areas: Heavy-Ion and Spin-Physics programs. This is directly related to the main motivations that led to the construction of RHIC and the development of the capabilities that

FIG. 23. An aerial view of Brookhaven National Laboratory, Long Island, New York. A birds eye view of RHIC can be seen in the top left corner of the picture.

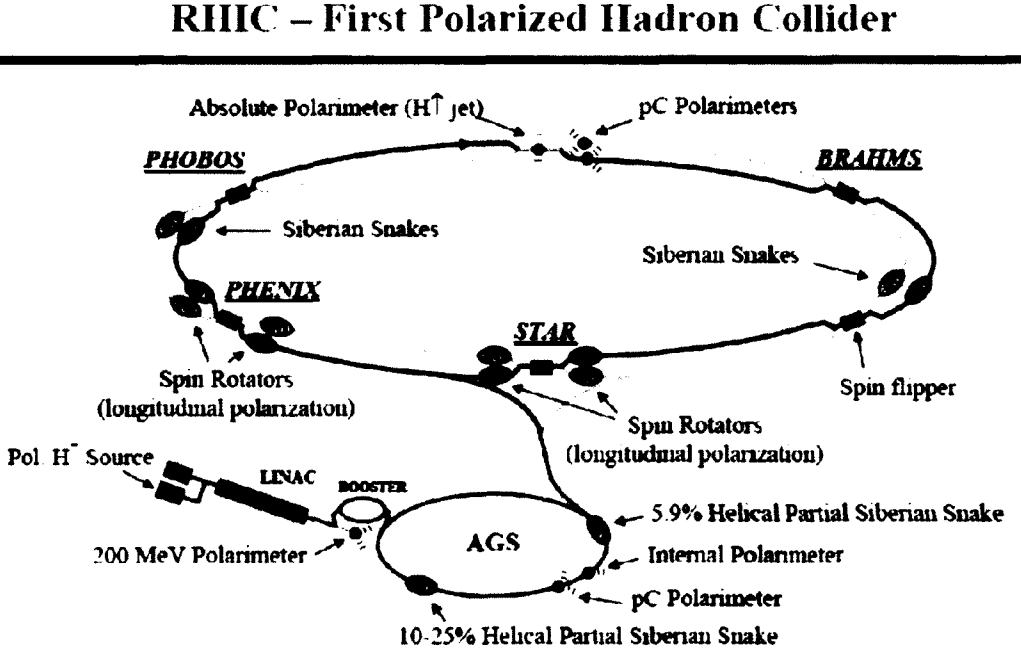

FIG. 24. Layout of Brookhaven National Laboratory accelerator complex, consisting of a LINAC, Booster, Alternating Gradient Synchrotron (AGS) which is the injector to RHIC and RHIC (north of AGS). The proton beam originates at the polarized hydrogen source and then follows these stages before being injected into RHIC.

RHIC possesses as a high-energy collider-accelerator facility. While in the heavy-ion program the experiments focus on the study of the properties of the quark-gluon plasma and the search for the QCD critical point, in the spin-physics program experiments are designed to study the proton's intrinsic properties (i.e proton spin), which has been a long standing puzzle in physics. The study of elastic and inelastic pp processes in the forward region are also part of the spin-physics program.

The STAR collaboration consists of 59 institutions from 12 countries, with 572 collaborators in total. The STAR physics program has three areas:

- Heavy-Ion Physics Program (Au-Au, Cu-Cu, d-Au, p-p), which focuses on studying the hot and dense medium properties created in high-energy (at 200 GeV top energy) heavy-ion collisions and the study of the pQCD regime. In the recent runs, STAR has been successful in performing a beam energy scan (BES), reaching as low as 5 GeV in Au-Au collisions. The motivation for the beam energy scan is the search for QCD critical point and the study of QCD phases (quark-gluon plasma, hadron gas, color superconductor).

- Forward Physics Program (p-p, d-Au), which focuses on the study of the low-x (Bjorken-x) medium properties and the non-perturbative regime of QCD. The physics program of PP2PP was incorporated with the forward physics program at STAR, and, as mentioned before, it focuses in the study of elastic and inelastic diffractive processes in pp.

- Polarized pp Physics Program (200 and 500 GeV), focuses on the study of the proton's intrinsic properties, i.e. the investigation of the proton's spin (1/2), as given by:
$$\frac{1}{2} = \frac{1}{2}\Delta\Sigma + \Delta G + L_q + L_g, \tag{127}$$
where $\Delta\Sigma$ is the contribution due to all quarks and anti-quarks within the proton, ΔG is the contribution due to gluons in the proton and L_q & L_g is the orbital angular momentum of the quarks and gluons, respectively.

A fundamental requirement of a collider is to operate over long periods of time with the beams stored at high energies. RHIC is composed of two identical quasi-circular intersecting storage rings (see Fig. 24), named Blue and Yellow. The two intersecting storage rings have individual transport magnets except in the intersection regions where the beams are brought into collision after passing through and

being bent by a common bending magnet. This configuration allows RHIC to collide identical particles such as protons. A detailed description of RHIC as a polarized proton collider will be given later in the next section. A unique feature of the program is to collide beams of different species at the same energy per nucleon. This is achieved by having two separate rings that can operate at two different magnetic field settings to maintain the necessary equal rotation frequencies. The beams are oriented to intersect at six locations. The collisions occur in the center of the interaction region (IR), where the beams are focused to a small spot and collide head-on. The IRs are spaced equidistant around the circumference and are separated by arc sections. One function of the IR optics is to bring the two counter-rotating beams, from separate beam pipes into a common beam-pipe, so that they can collide head-on at the intersection point (IP) [98].

3.1.1 RHIC AS A POLARIZED PROTON COLLIDER

In addition to the heavy ion collisions, RHIC has the capability to collide high-energy polarized proton beams and can achieve proton-proton collisions with both transversely and longitudinally polarized beams at $\sqrt{s}$ energies of up to 500 GeV. At present RHIC is the highest-energy polarized proton facility in the world.

An optically pumped polarized ion source (OPPIS) produces 10^{12} polarized protons per pulse. The protons pass through several stages of boosters before they reach the RHIC storage ring. After being produced at the source, protons are accelerated by a linear accelerator (LINAC) to 200 MeV and then by booster to 1.5 GeV (see Fig. 24). The booster then feeds the beam into the Alternating Gradient Synchrotron (AGS) where the proton beam is accelerated to 24 GeV. The AGS injects the proton beam into the RHIC storage ring over the AGS-to-RHIC Transfer Line (ATR). The proton beams are accelerated further to 100 GeV/c momentum.

Polarized Proton Beam Source at RHIC

The optically pumped polarized H^- ion source (OPPIS) at RHIC, was constructed at TRIUMF from the KEK OPPIS source [99]. The OPPIS technique was developed in the early 1980's and is based on charge-spin-transfer collisions between a proton in a low energy (2-5 keV) beam, produced in the electron cyclotron resonance (ECR) ion source and optically pumped alkali metal vapors [100]. At the RHIC OPPIS a pulsed laser is used to optically pump rubidium vapor to produce

polarized electrons. The polarized electrons are then picked up by the unpolarized ionized hydrogen gas, and a hyperfine interaction results in the transfer of polarization from the electron to the proton [101]. The goal of providing at least 0.5 mA H^- ion current with 80% polarization during a 300 μs pulse (corresponding to 9×10^{11} protons) and within a normalized emittance of 2π has been achieved [102]. The polarized H^- are stripped of their electrons and accelerated to 200 MeV using a Radio Frequency Quadrupole (RFQ) and the 200 MHz LINAC (Linear Accelerator) (see Fig. 24), before being injected in the Booster. Further acceleration to 1.5 GeV and capturing to a single bunch occurs in the AGS Booster. After being accelerated in the Booster, the single bunch of polarized protons is transferred to AGS, where it is accelerated to 24 GeV, before being injected in the RHIC rings. There are typically, up to 2×10^{11} protons in each filled beam bunch. The beam bunches are injected one at a time into the RHIC rings, allowing the configuration of the spin direction of each bunch independently. RHIC rings can have up to 112 of the 120 available RF buckets filled. The remaining 8 bunches are left unfilled, to provide an abort gap for the beam. At full RHIC design intensity, the bunches have a 2 ns duration and a 106 ns spacing between bunch centers [102]. Proton bunches are further accelerated to 100 GeV/c or 250 GeV/c, in the RHIC ring.

Acceleration and Storage of Polarized Proton Beams at RHIC

To achieve high energy polarized proton collisions, polarized beams first have to be accelerated and this requires an understanding of the evolution of the spin during acceleration and the tools to control it [102]. The evolution of the spin direction of a polarized proton beam, in external magnetic fields, that exist in a circular accelerator is governed by the Thomas-BMT equation [103]:

$$\frac{d\vec{P}}{dt} = -\left(\frac{e}{\gamma m}\right)[G\gamma\vec{B}_{\perp} + (1+G)\vec{B}_{\parallel} \times \vec{P}, \tag{128}$$

where the polarization vector $\vec{P}$ is expressed in the frame that moves with the particle, $G = 1.7928$ is the anomalous magnetic moment of the proton and $\gamma = E/m$. The $G\gamma$ factor gives the number of the spin precessions for every full revolution, a number which is also called the spin tune ν_{sp} [98,102]. During acceleration, a depolarizing resonance is crossed when the spin precession frequency equals the frequency of the spin-perturbing magnetic fields. There are two main sources of depolarization: *imperfection resonances*, driven by magnet errors and misalignments, and *intrinsic*

resonances, driven by the focusing fields [102]. When a polarized beam is accelerated through an isolated resonance, the final polarization can be calculated by [104]: $P_f/P_i = 2e^{\frac{\pi|\epsilon|^2}{2\alpha}} - 1$, where P_i and P_f are the polarizations before and after the resonance crossing, respectively, ϵ is the resonance strength obtained from the spin rotation of the driving fields, and α is the change of the spin tune per radian of the orbit angle [98,102].

Siberian Snakes and Spin Rotators

The introduction of magnetic configurations, named *Siberian Snakes* [105], was very beneficial to the acceleration and storage of polarized proton beams. Siberian Snakes correct for the depolarizing effects in the polarized proton beam caused by acceleration, and therefore serving to maintain the polarization of the proton beam at high energies. A Siberian Snake generates a 180° spin rotation about a horizontal axis and the spin direction remains unperturbed, as long as the spin rotation from the Siberian Snake is much larger than the spin rotation due to the resonance driving fields [102]. Two full Siberian Snakes were inserted on opposite sides of the RHIC lattice (at 3 and 9 o'clock locations), for each of the two counter-rotating rings (see Fig. 24). In addition to the Siberian Snakes, *spin rotator* magnets are located on each side of the two major interaction points (STAR and PHENIX, see Fig. 24), and serve to alter the spin orientation from vertical (transverse) to horizontal (longitudinal) plane at the collision points. Another magnetic component of the polarized beam project at RHIC, is the *spin flipper*, which is used for the manipulation of the spin orientation during a store. For lower energy synchrotrons, such as AGS at RHIC, which produces weaker depolarizing resonances, a partial snake is used. A partial snake rotates the spin by less than 180°. Two full Siberian Snakes, positioned on opposite sides of the two RHIC rings, are utilized to avoid depolarization from imperfection and intrinsic resonances, up to the top energy of 250 GeV/c [102].

Each Siberian Snake consists of four superconducting helical dipole magnets, which are capable of producing a central field of up to 4 T, which spirals around 360° over a length of $\approx$ 2.4 m [102]. Fig. 25 shows the proton spin direction being rotated as it passes through a full Siberian Snake.

The spin rotators rotate the polarization from the vertical to horizontal on one side of the IP, and restore it to the vertical direction on the other side [102]. Similar to Siberian Snakes, Spin Rotators consist also of helical dipole magnets, however, while the four helical dipole magnets of the Siberian Snake are right-handed, with

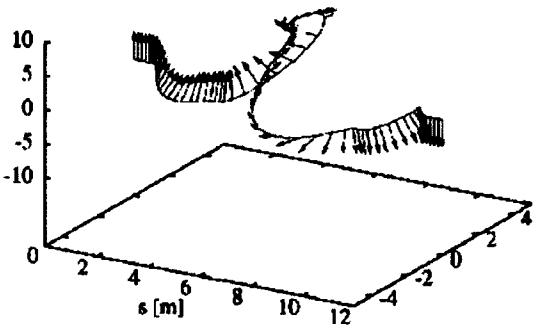

FIG. 25. Position and spin direction tracking for a proton as it passes through the four helical magnets of a Siberian Snake [98, 102]. The spin tracking shows the reversal of the vertical polarization. The three axes are in m.

the field at the end being vertical, for the Spin Rotators the helices alternate between right and left handedness (see Fig. 26), with the field at the end being horizontal.

RHIC Polarimetry: Beam Polarization Measurement Methods at RHIC

Precise knowledge of proton beam polarization is important for both STAR and PHENIX experiments. The physics program requires precision of beam polarimetry ~ 5 %. There are two main polarimeters at RHIC measuring proton beam polarization: the relative p-Carbon polarimeters (one per ring) and the absolute hydrogen-jet polarimeter, located at 12 o'clock at RHIC (see Fig. 24), and both are used "complementing each-other", to measure the polarization of the proton beam.

p-Carbon Polarimeter Two identical p-C polarimeters are positioned in the yellow and blue rings, in the straight beamline section at a distance from IP12 at RHIC. The approach of measuring the beam polarization is based on measuring the asymmetry in proton-Carbon elastic scattering in the Coulomb-Nuclear Interference (CNI) region [102]. RHIC p-C polarimeters are used for fast proton beam polarization measurements during a store, and require the knowledge of the analyzing power for a given beam momentum. Simultaneous measurement of the proton beam polarization using the absolute H-jet polarimeter at RHIC, provides the necessary calibration for the p-C polarimeters for a specific proton beam momentum. In this way, a relative measurement of the beam polarization in p-C elastic scattering is normalized by the absolute beam polarization measured in elastic $p + p$ scattering of a proton beam off a transversely polarized H-jet target.

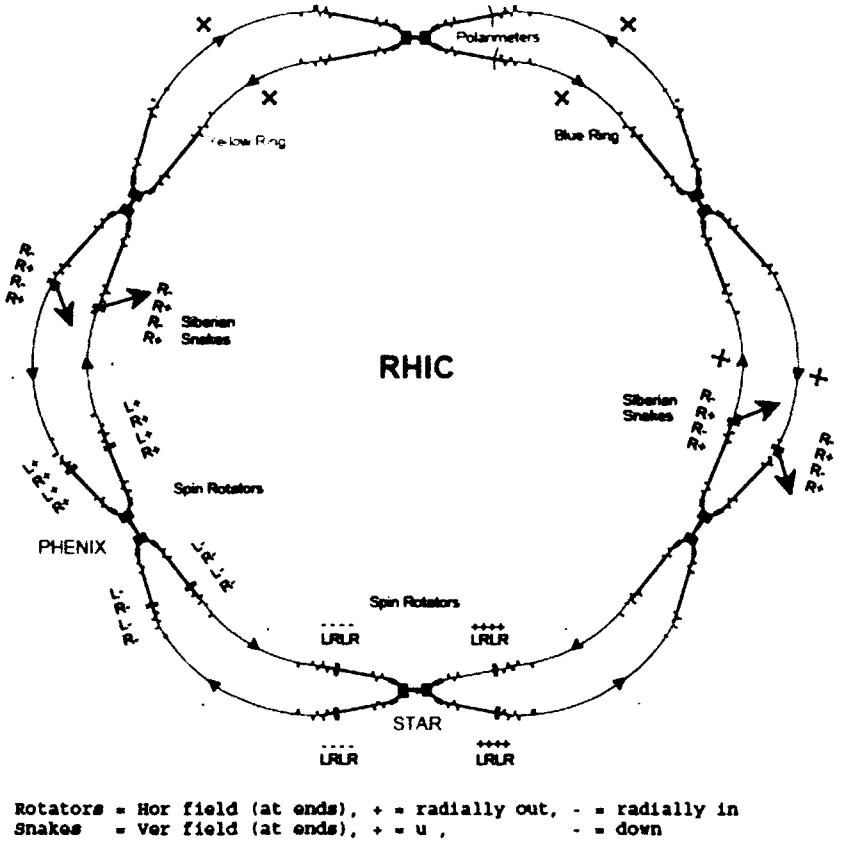

FIG. 26. View of RHIC with emphasized interaction regions, showing the location of Siberian Snakes and Spin Rotators, around STAR and PHENIX. The polarization directions around the rings and around the detectors for collisions with longitudinal polarization are also shown [102]. The handedness of the dipole magnets that constitute the Siberian Snakes and Spin Rotators is shown as L-left and R-right, handedness.

In general, the vertical beam polarization is measured by determining the left-right scattering asymmetry in the cross-section, using a reaction with a known analyzing power A_p [102]:

$$P_b = \frac{1}{A_p} \frac{N_L - N_R}{N_L + N_R}, \tag{129}$$

where P_b is the beam polarization, N_L and N_R are the number of particles scattered left and right, normalized by luminosity and A_p can be known from experiment or theory. Elastic scattering in the small-angle (small-t) CNI region is predicted to have a calculable analyzing power of about 4%, assuming negligible contribution from hadronic spin-flip, as well as large cross section over the whole RHIC range from 24 GeV/c to 250 GeV/c [32,71]. The analyzing power is given by [98,102]:

$$A_p(t) = \frac{Gt_0 t\sqrt{t}}{m_p(t^2 + {t_0}^2)}, \tag{130}$$

where $G = 1.7928$, the anomalous magnetic moment of the proton, m_p is the proton mass, and $t_0 = \frac{8\pi\alpha Z}{\sigma_{tot}}$ and Z the atomic number. The total cross section is only weakly energy dependent over the relevant energy range [98,102]. The calculated analyzing power for hydrogen target ($Z = 1$, $\sigma_{tot} = 35$ mb) and a carbon target ($Z = 6$, $\sigma_{tot} = 330$ mb [106]).

For p-C CNI at high energy (0.002 - 0.01 GeV^2), the scattering results in the proton scattering with a very small forward angle, and the carbon recoil with a very low kinetic energy (0.1 - 1 MeV). Since it is very impractical to measure the forward scattered proton, the identification of the elastic scattering relies only on the measurement of the carbon nuclei. Ultra-thin ribbon carbon targets, developed at Indiana University Cyclotron Facility (IUCF) [107], are being used in the p-C polarimeters at RHIC. The detectors are placed so that the carbon arrives between the passage of beam bunches, thus avoiding any prompt background [98]. The recoiling carbon ions are measured by six-silicon detectors located at 45°, 90° and 135° on each side of the beam and perpendicular to the beam direction, and at a distance of 15 cm away from the interaction point, see Fig. 28. Since, it is necessary to have both horizontal and vertical beam polarization profiles, separate targets are used, in order to scan the beam both vertically and horizontally [102]. Relative polarization measurements are fast, typically taking only a couple of minutes, and are performed periodically during the lifespan of a store. A typical RHIC physics store is 8-10 hours.

The silicon detector contains 12 (10 mm × 2 mm) strips, which are used to detect recoil carbon ions with kinetic energy $0.4 \leq \mathrm{E} \leq 0.9$ MeV [108]. The number

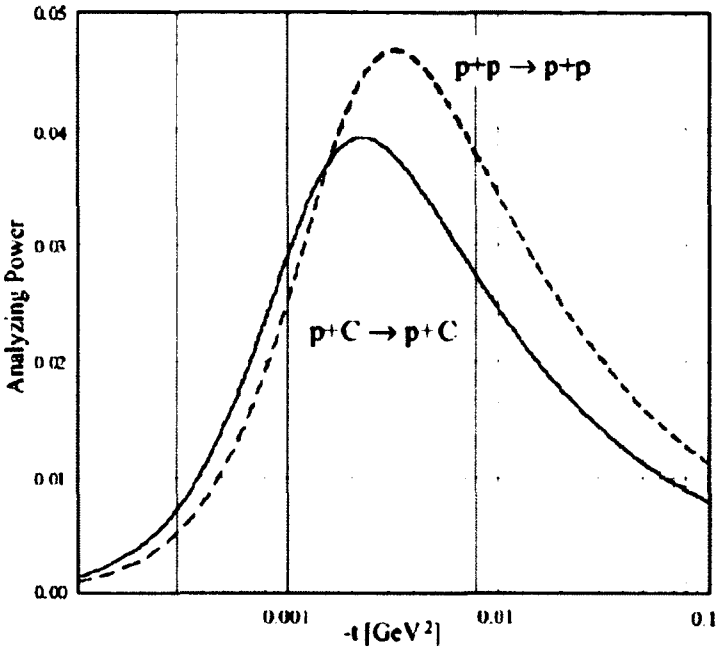

FIG. 27. Coulomb-nuclear interference analyzing power for pp and p-C scattering as a function of momentum transfer $-t$ [98].

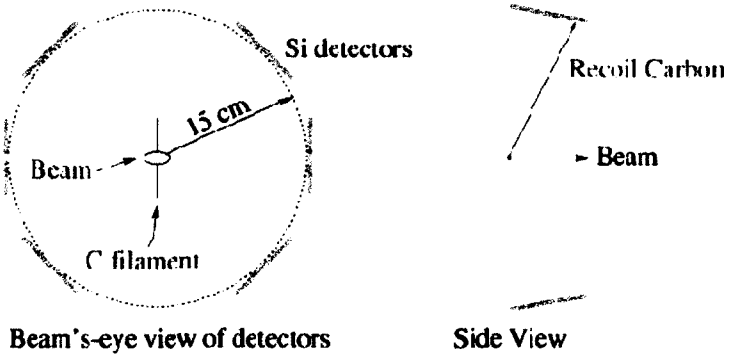

FIG. 28. Schematic layout of the p-C polarimeter at RHIC. The thin carbon ribbons are held in a target assembly, which is movable, thus positioning the target into the beam during the measurement. The silicon detectors are positioned perpendicular to the beam direction. The thin carbon ribbons used as targets are 6-8 $\mu g/cm^2$ in diameter, 10-20 μm wide and 2.5 cm in length [98].

of counts from p^+ and p^- bunches are measured for each strip, giving information on the scattering asymmetry. An averaged strip polarization P_B is measured by fitting the measured asymmetries A_i, for each silicon detector strip i, with respect to azimuthal angle, such as: $P_B(\phi) = \frac{A_i}{\bar{A}_N} = P_B \sin\phi$, where $\bar{A}_N$ is the weighted average analyzing power within the energy range [109]. Without normalization from the H-jet polarimeter, the RHIC p-C polarimeters measure the average beam polarization from multiple measurements with a relative uncertainty of about 10%.

The analyzing power has been measured in p-C CNI scattering, in the BNL AGS [95] with proton beam energy 21.7 GeV/c and [110]. Knowledge of the beam polarization from the polarized hydrogen jet target polarimeter was used in [110]. These measurements provided data to calibrate RHIC p-C polarimeter at the injection energy 24 GeV and at 100 GeV. Predicted properties of A_N (sizable analyzing power), the large cross section and the weak $\sqrt{s}$ dependence in the 24-250 GeV, makes this process ideal for beam polarization measurement [95, 111]. Simultaneous measurements in p-C and H-jet polarimeters, provide the calibration for p-C polarimeter. Fast p-C polarimeter measures possible polarization losses during the store duration [112].

In addition to the beam polarization measurement, the thin carbon target width compared to the beam size allows for measurement of the proton beam polarization profile. In a scanning mode of polarimeter operation the counting rate dependence on the target positions can be used for the beam polarization and transverse beam intensity profile measurements.

H-jet Polarimeter

The hydrogen-jet polarimeter at RHIC is located at 12 o'clock intersection point at RHIC, where it intersects both beams. A transversely polarized H-jet is produced by an Atomic Beam Source (ABS), in which the molecular hydrogen is dissociated by a radio frequency (RF) discharge [84]. Nuclear polarization of the atoms is obtained using two RF transitions that induce spin-flips in the hydrogen atoms [84]. The mean values for nuclear polarization of the atoms is $|P_\pm| = 0.958 \pm 0.001$ [113]. The H-jet travels in the vertical direction and intersects with only one of the RHIC polarized proton beams, while the other beam is displaced (see Fig. 29). The polarization of the target protons in the H-jet are measured with a Breit-Rabi polarimeter [115].

The detector system consists of six silicon strip detectors positioned 80 cm away, left and right of the intersection point, with strips oriented perpendicularly to the

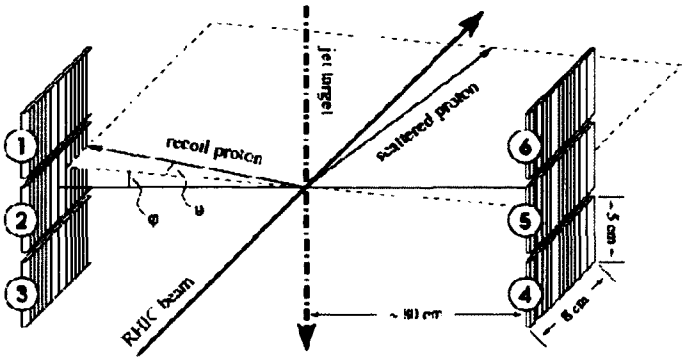

FIG. 29. Schematic layout of the H-jet polarimeter at RHIC. Six silicon strip detectors are placed one each side of the interaction point, with strips oriented perpendicular to the beamline [114]. The atomic hydrogen goes from the top to the bottom, and in routine operation, one for the two RHIC beams is displaced. Forward strips are used to measure the recoil proton from the interaction of the jet with one RHIC beam, and backward strips measure the recoil proton from the interaction with the other RHIC beam. The non-signal strips can be used to estimate the background [114].

beam direction. Two identical sets of 3 silicon strip detectors, 50×80 mm^2 were placed in vacuum on each side of the beam (see Fig. 29). Each detector is arranged in 16 channels. The detectors measure only the recoil protons from the interaction of the jet with the RHIC proton beam. Forward scattered protons are not detected, since their trajectory is too close to the beam direction.

After measuring the recoil protons, *pp* elastically scattered events are selected. Recoil protons from *pp* elastic scattering are identified by the scattering angle-kinetic energy correlation. The silicon detectors detect recoil protons with kinetic energies $0.6 \leq E \leq 17$ MeV [113]. Selection of *pp* elastic events, results in the measurement of the left-right asymmetry taking into account the jet polarization and averaging over the beam polarization. Combining the measured raw asymmetries ϵ_{target} and the known jet polarization P_{target}, provides the measurement of the analyzing power of the process, such as:

$$A_{\mathrm{N}} = \frac{\epsilon_{target}}{P_{target}}. \tag{131}$$

The reverse process measures the asymmetry taking into account the beam polarization direction and averaging over the jet polarization. The ratio of the measured raw asymmetries ϵ_{beam} and ϵ_{target}, and the known target polarization P_{target}, gives

the average beam polarization over the run:

$$P_{beam} = -\frac{\epsilon_{beam}(T_R)}{\epsilon_{target}(T_R)} P_{target}, \tag{132}$$

where ϵ are the observed asymmetries as a function of recoil energy T_R [113, 114]. The raw asymmetries are given by:

$$\epsilon = \frac{\sqrt{N_L^+ N_R^-} - \sqrt{N_R^+ N_L^-}}{\sqrt{N_L^+ N_R^-} + \sqrt{N_R^+ N_L^-}}, \tag{133}$$

where the contributions from different left-right detector acceptances and different luminosities in the measurements with up (+) and down (-) target polarization states to the asymmetry cancel [18]; N are the recoiled proton counts, scattered left and right denoted by $L(R)$, and $+(-)$ denote the beam polarization state.

The absolute polarization measurement requires data accumulation for about a day typically, thus measurement is performed during multiple physics stores. The relative beam polarization measurements from the p-C polarimeters are calibrated by the H-jet polarimeter measurements to an accuracy of about 5%.

The jet was first implemented in RHIC and collected first data in 2004, which provided a precise measurement of the analyzing power of pp elastic scattering in the CNI region with 100 GeV/c proton beam [84].

3.2 VERY-FORWARD DETECTORS AT STAR DETECTOR AT RHIC

The STAR experiment at RHIC is equipped with insertion devices (Roman Pots, RPs) that allow the detectors to be moved close to the beam in order to measure protons scattered in the forward direction (at very small scattering angles). The Roman pots were originally used by the PP2PP experiment, which started as a separate experiment and was one of the five experiments at RHIC between 2000 - 2007. The PP2PP experiment was designed to study pp elastic scattering in the forward direction. After beginning operation in 2000, RHIC had its first proton run in December 2001 - January 2002. PP2PP with its very-forward detectors was initially located on both sides of the interaction point (IP2), the BRAHMS experiment (see Fig. 24) at RHIC. PP2PP completed its first physics run in May 2003 and performed the first measurement of elastic scattering at $\sqrt{s} = 200$ GeV [24].

The very-forward proton detectors were then later relocated near IP6, the STAR experiment at RHIC (see Fig. 24) and thus the PP2PP physics program was integrated with the STAR experiment. The very-forward detectors are installed now

on either side of the interaction point at the STAR detector. The very-forward detectors are designed to study the dynamics and the spin-dependence in polarized proton-proton elastic scattering at a previously unexplored $\sqrt{s}$ energy range of 50 GeV $\leq \sqrt{s} \leq$ 500 GeV and four-momentum transfer squared of $4 \cdot 10^{-4} \leq |t| \leq 1.5$ $(\text{GeV}/c)^2$. The kinematic range can be divided into three regions (Coulomb, CNI and Hadronic), according to which interaction is dominant in each region. The three regions are listed below in increasing t order, with various **spin-averaged and spin-dependent observables** measurable in each region:

- Coulomb interaction region: $|t| \leq 10^{-3}$ $(\text{GeV}/c)^2$
  - Measure the total cross section σ_{tot} and access the imaginary part of the forward scattering amplitude by using the optical theorem (see Appendix A).
- Interference between Coulomb and hadronic interaction, the **CNI region**: $5 \cdot 10^{-4}(\text{GeV}/c)^2 \leq |t| \leq 0.12$ $(\text{GeV}/c)^2$
  - Measure and study the $\sqrt{s}$ dependence of the total σ_{tot} and elastic cross sections $d\sigma_{el}/dt$
  - Measure the ratio of real and imaginary part of the forward elastic scattering amplitude ρ (see Eq. (29)) and extract its real part by using the optical theorem (see Eq. (27)) and the measured σ_{tot}
  - **Spin-dependent observables**
    * By using polarized proton beams with transverse polarization: measure the transverse single spin asymmetry A_{N} and the double spin asymmetries A_{NN} and A_{SS}
    * By using polarized proton beams with longitudinal polarization: measure the double spin asymmetry A_{LL}
- Hadronic interaction region: $5 \cdot 10^{-3}(\text{GeV}/c)^2 \leq |t| \leq 1$ $(\text{GeV}/c)^2$
  - Measure the forward diffraction cone slope or the nuclear slope parameter B

3.2.1 ROMAN POTS AND SILICON DETECTORS

The use of Roman pots [116] in the detection of particles scattered in the very-forward direction in a collider experiment is a technique that first originated at the European Organization for Nuclear Research (CERN). The name Roman was chosen because this technique was first used by a CERN group from Rome in the early 1970's to study proton-proton collisions at CERN's intersecting storage rings (ISR). The CERN ISR was the world's first high-energy proton-proton collider and presently the Large Hadron Collider (LHC) at CERN is the most powerful hadron collider in the world, reaching a $\sqrt{s}$ energy of 14 TeV in proton-proton collisions. The Roman pot has the shape of a cylindrical vessel in which the detectors can be mounted. This is the reason that it is called a "pot". The pots are connected to the vacuum chamber of the collider by bellows tubes, which are compressed as the pots are pushed towards the particles circulating inside the vacuum chamber. In their retracted position, the Roman pots do not obstruct the beam, leaving the aperture of the vacuum chamber free for the beams during their injection and ramp. Once the beams are brought into collisions, the Roman pot is moved inside the beam-pipe as close as a few mm to the beam, without disturbing the stability of the circulating beams. Thus, the Roman pots are moved during operation, approaching the detectors close to the beam and enabling detection of forward scattered particles, while the detectors remain isolated from the beam vacuum.

In order to detect scattered protons at small-$|t|$, PP2PP developed its own version of Roman pots [117]. Figure 30 (a) and (b) show a picture of a Roman pot and a vertical Roman pot station in the RHIC tunnel, respectively. The Roman pots in the vertical RP station are positioned just above and below the outgoing beam-pipe. The window of the Roman pot is made of stainless steel with a thickness of 300 μm. The thin stainless steel is used to minimize the material through which the scattered proton passes, but must maintain its strength, preserving the beam pipe vacuum, in the event the proton beam is accidentally dumped directly into the pot [117]. As the interior of the pot is at atmospheric pressure and the exterior is exposed directly to the beam vacuum, the window frame serves as a window support to prevent the thin window from deforming into the beam [117].

The detector package/assembly mounted inside the RP, is composed of four silicon strip detectors, 2 $x-view$ (with horizontally oriented Si strips) and 2 $y-view$ (with vertically oriented Si strips) detectors. This configuration of the detectors allows the

(a)

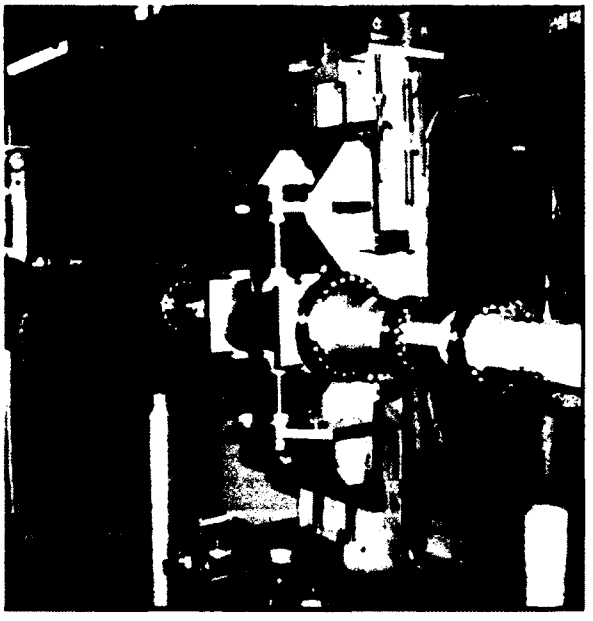

(b)

FIG. 30. (a) Roman Pots. The RP window frame and the stainless steel window (300 μm thick) is shown. The RP edge is machine channeled to allow a closer approach of the RP to the beam [117]; (b) a vertical RP station consisting of two RPs, above and below the outgoing beam-pipe.

measurement of the positions of the scattered protons in the transverse plane $(x-y)$ plane. Having two detector planes of the same kind in each RP, provides redundancy in measuring each coordinate. An assembled detector package is shown in Fig. 31 (a). Figure 31 (b) shows a detector package mounted inside the Roman pot. An 8 mm thick trigger scintillator, read out by two photomultiplier tubes, is mounted on each detector package.

Figure 32 (a) shows a picture of the four silicon detector boards that form a detector package and Figure 32 (b) shows a picture of an $x-$ *view* Si strip detector board. Detectors have a sensitive/active area of 79×48 mm^2 and a thickness of 400 μm. The trigger scintillator covers the sensitive area of the detectors. The edge of the detector closest to the beam was cut to within 500 μm of the first Si strip, in order to minimize the dead area and increase the low-$|t|$ acceptance [117].

Silicon Microstrip Detectors

Silicon strip detectors have been widely used in experimental particle physics as high-resolution particle trackers, becoming an essential part of the detector systems as a vertex tracker in the central region of the experiment. The particle tracking system requires a good position measurement resolution and the silicon microstrip detectors can have a position measurement resolution in the order of 5 μm, which is 10 times better than the resolution of other detectors such as wire chambers or scintillators. Silicon is the preferred material for high-precision tracking detectors, as well as for a wide range of radiation detectors, for a number of reasons [118]:

- A *condensed medium* is essential if position measurement precision less than 10 μm is required. For this reason, silicon and other solids are generally preferred

- Silicon is chosen among other solid state detection media, because silicon has a band gap of 1.1 eV, which is low enough for a minimum ionizing particle (MIP) to produce liberated electron-hole pairs (about 80 electron-hole pairs per micron of track length). Simultaneously the band gap of silicon is high enough to avoid very large dark current generation at room temperature (kT at room temperature is 0.026 eV).

- Silicon is a low-Z element ($Z = 14$), which is important for it's use in tracking detectors, where multiple scattering is of concern [118].

(a)

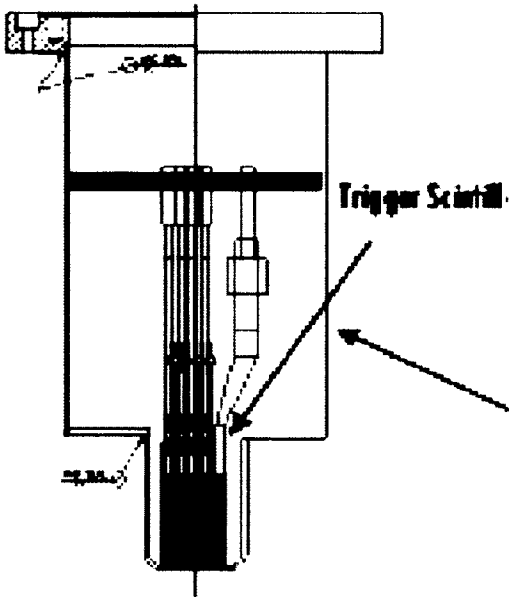

(b)

FIG. 31. (a) A detector package/assembly [117]; (b) detector assembly inserted in RP. A detector assembly/package consists of 4 Si detector boards (figure shows side-view of the detector package installed inside the RP). The triggering system for one detector package consists of a trigger scintillator connected to two photo-multiplier tubes (PMT). The 5^{th} plane (the right-most plane) represents the trigger scintillator connected to the PMTs.

(a)

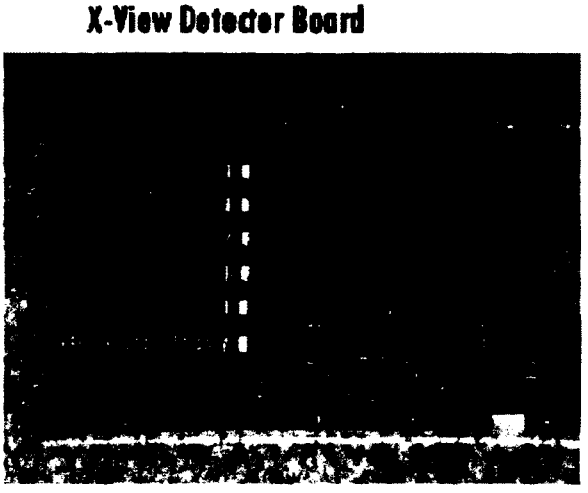

(b)

FIG. 32. (a) A disassembled silicon detector package consisting of four silicon detector boards, 2 $x-view$ and 2 $y-view$ detectors; (b) an x-*view* Si detector board. The silicon strips (horizontally oriented) are connected to 6 ADC readout chips, called SVXIIE [117].

- Furthermore, a vast integrated circuit (IC) technology has been developed for silicon.

- Silicon, which as a material is cheap and easy to find, at the same time brings unique combination of assets such as: the possibility of negative n-type (n-) and positive p-type (p+) doping, the possibility of selective growth of highly insulating layers (SiO_2 and Si_2N_3) and the possibility of using techniques which allow to feature sizes of $\sim$1 micro (and decreasing with time and IC technological developments).

  The silicon crystal can be made n-type or p-type by doping with atoms such as phosphorus or boron, respectively. The majority of the charge carriers are electrons in an n-type and holes in a p-type material. The number of the majority charge carriers, which depends on the doping concentration, determines the resistivity (conductivity) of the material.

These characteristics make it possible for the silicon detectors to be a part of the most sophisticated tracking systems where the ability to measure small dimensions is essential.

When conducting materials are brought in electrical contact with each other, charge flows from the high energy region to the low energy region until the same Fermi energy is established. This important rule applies also to n-type and p-type systems. In a $p-n$ junction of a semiconductor, such as silicon, electrons in the n-type silicon diffuse into the p-type silicon, leaving positively charged ions (donors) behind, while holes in the p-type silicon diffuse into n-type silicon, leaving negatively charged ions (acceptors) on the other side. This creates a *depletion region* inside the silicon, a region with no free charges, which can be used as a detection medium for ionizing particles passing through silicon. The ratio of the dopant concentrations on both sides is inversely proportional to the ratio of the depletion ranges at the two sides of the junction [118]. By applying a voltage difference across the junction, the previous equal Fermi levels are separated by an amount equal to the bias voltage.
A good detection region in silicon can be created by constructing a reverse biased $p-n$ junction with appropriate doping concentrations at each side of the $p-n$ junction. This is the basic idea of the silicon strip detectors, which is a series of $p-n$ junction diodes. A silicon microstrip detector is constructed by implementing thin strips of highly doped p-type silicon over an n-type silicon wafer [119]. All the p+ strips in

the silicon microstrip detector are connected to ground via resistors for biasing the detector. The silicon detectors used in our experiment use a general method for this purpose, the polysilicon resistors. The depth of the depletion region in the silicon bulk can be calculated by the formula:

$$d = (2\epsilon V(N_n + N_p)/eN_nN_p)^{1/2}, \tag{134}$$

where ϵ is the permitivity of silicon ($\epsilon = 11.7\epsilon_0$, $\epsilon_0 = 8.85 \times 10^{-18}$ F/μm), V is the bias voltage, N_n/N_p is the concentration of dopant atoms for n/p-type silicon. Since N_p is much larger than N_n in the case of silicon microstrip detectors, Eq. (134) can be written as:

$$d \approx (2\epsilon V/eN_n)^{1/2}, \tag{135}$$

which shows that the depletion depth from the junction point is directly proportional to the applied voltage difference across the junction until full depletion is reached.

When an ionizing particle enters the depletion region of silicon with enough energy, it creates electron-hole pairs. If a strong enough electric field is created the pairs will not recombine, but the holes will be collected by the $p+$ strips while the electrons end up at the backplane. Our aim is to determine the spatial coordinates of the ionizing particle which entered the silicon. The spatial resolution of the track followed by the ionizing particle depends on the distance between the adjacent $p+$ strips. Thus, in order to determine the spatial coordinates of the particle which passed through the silicon, first we need to determine the $p+$ strips which collected the holes that were created during this passage. The spacing between the $p+$ strips is called the *pitch*, an important parameter which determines the position measurement resolution of the silicon microstrip detector.

Figure 33 shows a cross sectional view of a silicon microstrip detector. The dimensions of individual parts in Fig. 33 are given in Table 4. The top surface of the silicon wafer is oxidized in a controlled manner to create a layer of silicon glass, SiO_2 (see Fig. 33) [119]. The silicon glass has a bandgap of 9 eV, which makes it an excellent insulator. Above the SiO_2 layer, aluminum strips run along the length of the $p+$ strips, forming a series of capacitors. The induced charge/current in the Al strip can be detected by the charge/current sensitive preamplifier, which is connected to the Al strips (see Fig. 33). This is an AC coupled silicon detector. The preamplifiers are implemented in the SVXIIE readout chips, which will be discussed later in this section.

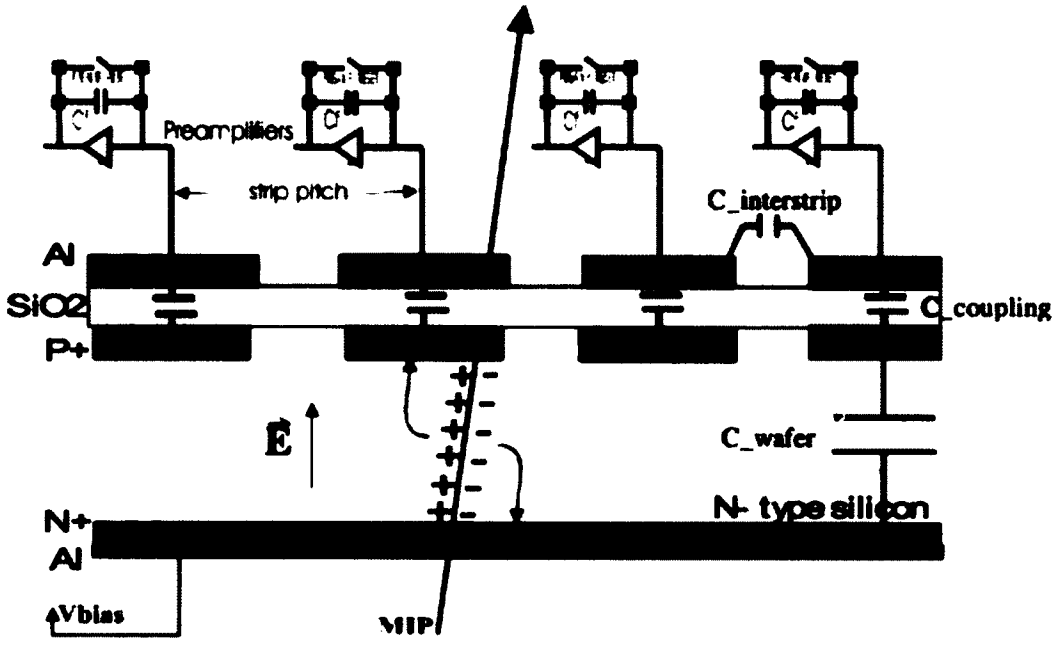

FIG. 33. Cross sectional view for a silicon microstrip detector [119].

The strip pitch is 100 μm resulting in a spatial precision of 100 μm / $\sqrt{12}$ = 28.8 μm, where $1/\sqrt{12}$ is the sigma of the uniform probability distribution. Ideally all the charge created in the vicinity of the strip would only be collected by that strip, however in reality the data shows (this will be discussed in detail in Chapter 6) that the charge is distributed among neighboring strips as well and thus clusters with strip number bigger than 1 are observed in the data. This effect of charge sharing among strips is considered carefully in the selection of hits in the silicon microstrip detector. Other factors related to the charge sharing, apart from the strip pitch, are the strip width and the angle of the trajectory of the ionizing particle. The $p+$ strip width for our detectors is 70 μm, so the gap between two adjacent strips is 30 μm. Although, the track trajectories of the particles are expected to be almost perpendicular to the detector plane, charge sharing between two adjacent strips is still possible.

Another important parameter in the silicon microstrip detector is the detector capacitance. The total capacitance depends on the thickness of the silicon bulk (400 μm in our case), the thickness of the oxide layer (100 nm), the length (typical length is 8 cm) and the width (70 μm) of the strips. There are two capacitors contributing

to the total detector capacitance: (1) the capacitor formed by the $n+$ backplane and $p+$ strip, which we refer to as C_{wafer} and (2) the capacitor formed by the $p+$ strip and Al strip, the coupling capacitance $C_{coupling}$. The total detector capacitance is the equivalent capacitance of both since to a good approximation, these two capacitors are connected in series. The first capacitor resembles a parallel plate capacitor, therefore the value of C_{wafer} can be calculated by:

$$C = \epsilon A/d, \tag{136}$$

where ϵ is the permitivity of silicon ($\epsilon = 11.7\epsilon_0$), A is the total strip area (8 cm $\times$ 70 μm) and d is the depletion depth, which depends on the applied bias voltage. Therefore, C_{wafer} depends on the wafer thickness and the depletion depth. The capacitance of the single $p+$ to backplane capacitor is expected to be around 600 pF/μm [119]. $C_{coupling}$ can also be calculated using Eq. (136), where the permitivity of silicon dioxide (SiO_2) is ($\epsilon = 4.4\epsilon_0$), the separation distance is 100 nm, giving a result of 2000 pF, which is much large than C_{wafer}. The bigger the coupling capacitance is the better the charge induction in the Al strip [119]. This capacitance is required to be much larger than the inter-strip capacitance in order to decouple the neighboring strips from each other [119].

When a charged particle passes through the silicon detector, energy of the particle will be lost mostly in the form of ionization. The quantum-mechanical description of the energy loss is given by the Bethe-Bloch formula (see Appendix F) [120]. For non-relativistic energies, the energy loss per distance dE/dx (also called *the stopping power*) decreases by c^2/v^2, where v is the velocity of the charged particle and c is the velocity of light in vacuum. For relativistic energies such as $v \geq 0.96c$, however, the dependence of dE/dx on energy can be considered almost constant. Energy loss per distance dE/dx for minimum ionizing particles (MIP) such as muon (μ), pion (π), proton (p) at the relativistic energies is almost the same, except the alpha (α) particle [120]. Energy loss of a MIP when passing through the silicon detector is a statistical process, which can be described by the Landau distribution. The average energy loss for a MIP in silicon is proportional to the distance the particle travels through the silicon.

TABLE 4. Parameters and their Dimensions of the Silicon Microstrip Detectors

Strip width	70 μm
Strip pitch (center to center)	100 μm
Resolution = Strip pitch/$\sqrt{12}$	$\sim$29 μm
SiO_2 layer	100 nm
Al width	72 μm
p^+ width	70 μm
Wafer thickness	400 μm
C_{wafer}	600 pF/μm depletion (1.7 pF for full depletion)
$C_{interstrip}$	2 nF
$C_{coupling}$	$\sim$2000 pF

Drawbacks of the Silicon Microstrip Detectors Used in Our Experiment

In this section the drawbacks and possible problems that can occur with the silicon microstrip detectors used in our experiment are listed.

- Radiation Damage

  The silicon detectors are located inside the RHIC tunnel, a high radiation zone which can cause change in the doping concentration in the silicon bulk, leading to an increase in the leakage current. Radiation can also increase the surface leakage current due to charge buildup in the surface layers.

- Unreliable Oxide Layer

  The oxide layer between $p+$ strips and Al strips can break if a voltage difference higher than 10 V is applied across it.

- Inter-strip Capacitance

  As mentioned earlier, the coupling capacitance should be kept much larger than the inter-strip capacitance to prevent fake signals from being observed on the neighbor strips of the strip which was hit by the particle.

- External Electric and Magnetic Fields

  External electric field of the accelerator environment can cause charge induction on the Al strips leading to surface charge currents. External magnetic field can cause unexpected deflections in the trajectory of the particle passing through the silicon detector, disturbing the spatial measurement precision. Because of this, the detectors should be protected from external fields.

- Edge-related Leakage Currents

  The silicon detectors used in our experiment are designed with a small cutting edge of 500 μm, which is the distance of the edge to the first strip closest to the beam. It is minimized in order to detect particles with scattering angles as small as possible. However, the cutting edge of the silicon can be a source of leakage current, which can affect nearby strips. To prevent this, a guard/bias ring is used around the strips to serve as a leakage current drain and minimize the inactive area.

For more details on the drawbacks refer to [119].

Silicon Detector Readout System

The silicon detectors are being readout by SVXIIE chips. The SVXII chip (earlier version) is a 128 channel device, developed by a collaboration of engineers at Fermilab and Lawrence Berkeley Laboratory (LBNL) [121]. The SVXII chip was designed to meet the silicon strip upgrade requirements for both CDF and D0 experiments at Fermilab. The SVXIIE chip features a 32-cell analog pipeline, programmable test patterns, downloadable settings for ADC ramp, pedestal, bandwidth and polarity [119]. The SVXII chip is designed for daisy chained operation with silicon strip detectors, to reduce the number of control and readout connections in a multichip system [121]. Figure 34 shows a simplified diagram of one of the 128 channels of electronics. The silicon strips/channels are wire-bonded to the SVXIIE chips, thus charge is received from the silicon strip detector via the input bond wire and integrated on a small feedback capacitor, Cf, which sets the gain of the input to be 5 mV/fC. The output of the preamplifier feeds the analog pipeline which has a maximum length (32 stages) set by the minimum interaction time and maximum required time delay [121]. The SVXII is designed to accept both positive and negative current input signals.

Control of the SVXII is handled by digital and bias pads, called MODE0, MODE1 and CHANGE-MODE, which are used to select one of the four possible operating modes (Initialize, Acquire, Digitize and Readout) for the SVXII during the Readout Mode [121]. Eight pads, called BUS0-7, are used to output address and data information from the SVXII during the Readout Mode [121]. Figure 35 shows a floorplan and pinout diagram of the SVXII chip. Starting from the left, the preamplifier section is followed by the analog pipeline section and the A/D section. The SVXIIE is a radiation hard chip, with its substrate at AVDD1 potential [121].

Although the SVXIIE is designed to be connected to read 128 channels, only 126 silicon strips/channels were connected to the chips in our detector setup, leaving the first and last silicon strip in each group of 128 strips disconnected. Since the first and last strips have offset pedestals (lower than other strips), they were excluded in order to optimize the readout of the SVXIIE chip. The readout system of all the detectors boards/planes was tested in the lab prior to installation and also after installation in the actual setup. During the testing of the detectors, important parameters of the readout system were set and the SVXIIE chips were programmed appropriately.
For more details on SVXIIE chips used in our experiment refer to [119].

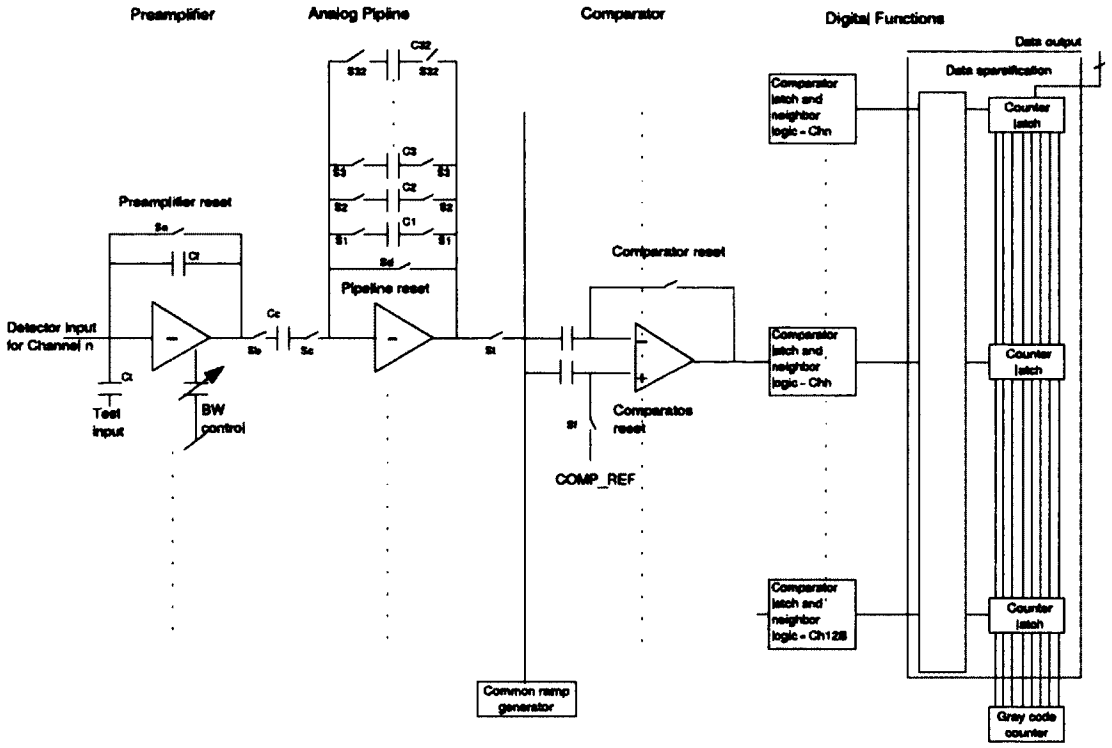

FIG. 34. Single Channel Block Diagram for SVXII chip [122].

3.3 MEASUREMENT TECHNIQUE

To detect scattered protons at small scattering angles, it is necessary to position the detectors where the scattered protons are well separated from the outgoing beam. For this reason the detectors are placed far from the interaction region (IR), where the beam and the scattered protons have passed through bending and focusing magnets. Each Roman pot station contains two Roman pots opposite to each other across the beam, with one detector package in each pot. A set of one vertical and one horizontal RP stations is located on each side of the IR, 55.5 and 58.5 m away from the IP, respectively, with the horizontal RP being closer to the IP. Figure 36 shows the location of the RPs for the experimental Phase I configuration. The RPs are located in the outgoing blue and yellow rings, equidistant from the IP and after the dipole magnets and quadrupole triplet magnets. The beams are separated into two beam pipes after they leave the first dipole magnet, then while passing through the second dipole magnet, their trajectory is bent, before entering the quadrupole triplet. In the

FIG. 35. Floorplan and pinout diagram of an SVXII chip. The inputs for 128 silicon strips are on the left hand side [121].

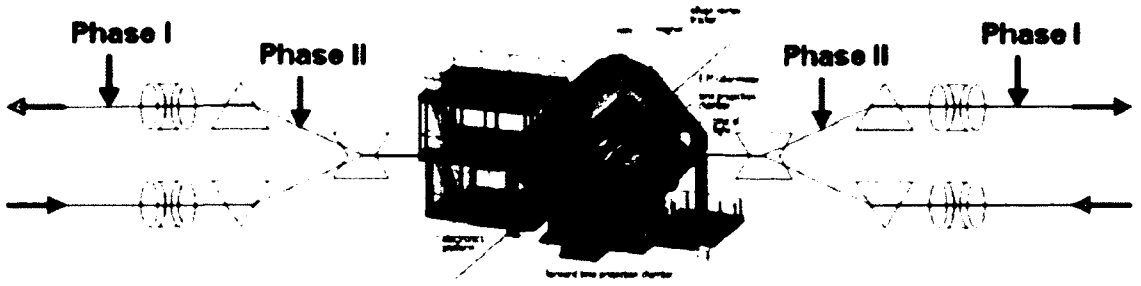

FIG. 36. Experimental Phase I: the RPs are located on both sides of the IP at the STAR detector (shown in the center), in the outgoing beam pipes and after two dipole magnets and the quadrupole triplet, in the RHIC tunnel. Experimental phase II is a future upgrade of the experiment, where new RPs are planned to be installed between the two dipole magnets on both sides of the IP.

planned experimental phase II configuration, new RPs will be installed between the two dipole magnets at a distance of $\sim$18 m from the IP. The phase II configuration will provide an increase of the high-$|t|$ acceptance.

Figure 37 shows the experimental layout for the phase I configuration in more details. Elastically scattered protons are detected in either collinear detector pair (elastic arm): A, B, C or D (see Fig. 37), (note: C and D arms are not shown in the Fig. 37). For an observer looking away from the IP at STAR towards the outgoing beam direction, the left/right RP of the horizontal RP station in the East of STAR (yellow beam) and the right/left RP of the horizontal RP station in the West of STAR (blue beam), form arms A/B, respectively. The top/bottom RP of the vertical RP station in the East and the bottom/top RP of the vertical RP station in the West, form arms C/D, respectively. This grouping of the RP stations and the detectors is used in the trigger logic for the elastic trigger, since the elastic trigger is based on the collinearity condition for elastic events. An elastic event implies that the two coordinates of the scattered protons, obtained from the silicon detectors on either side of the interaction point are coincident. Thus, the collinearity condition requires a collinear pair of detectors, one on each side of the IP, to be triggered simultaneously by the incident protons.

Measurement Method: The two protons collide at the IP in a local coordinate system at a vertical position y^* from the reference orbit and scatter with an angle θ_y^*. The scattered particles pass through various magnetic lenses (two dipole magnets DX

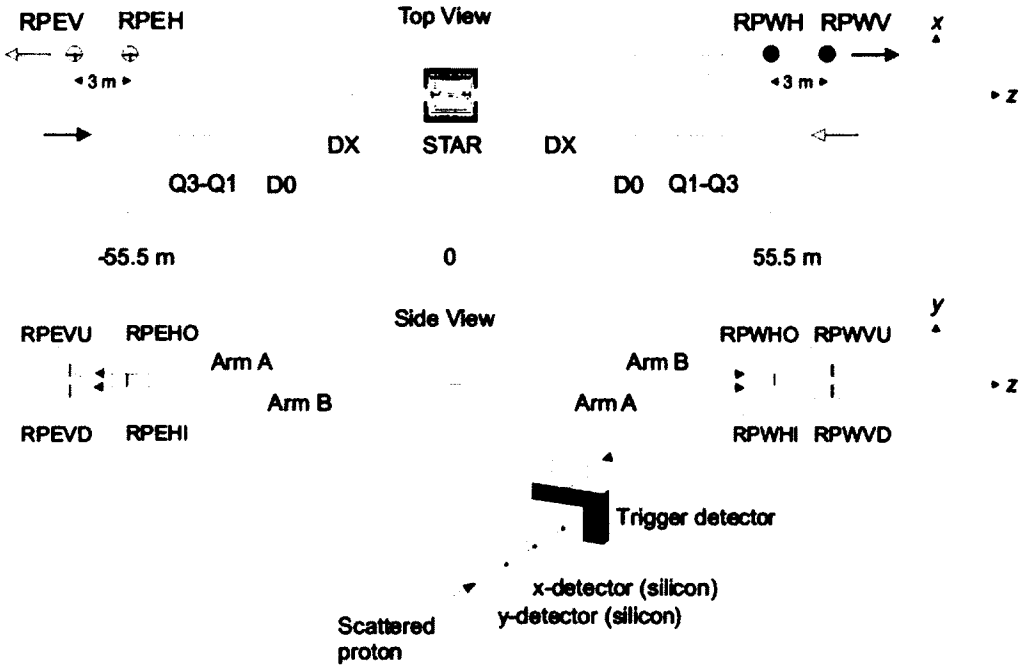

FIG. 37. Experimental Layout for Phase I. The RPs are located on both outgoing RHIC rings, Blue and Yellow. Two RP stations, one horizontal (55.5 m) and one vertical (58.5 m), with two RPs in each station, are located on both sides of the IP at STAR. Elastic scattering is detected in either collinear arm: A, B, C and D (C and D are not shown in the figure). The composition of the detector package placed in each RP (four Si strip detector planes and one trigger scintillator) is also shown.

and D0 and the focusing triplet Q1-Q3, see Fig. 37) of the accelerator lattice before they reach the detectors, which measure the positions of the scattered particles with respect to the reference orbit [6]. In order to measure the scattering angle of the protons, the scattering angle has to be larger than the angular spread/divergence of the beam at the collision point, which given by:

$$\sigma^*_{\theta_{x,y}} = \sqrt{\frac{\epsilon_N}{6\pi(\beta\gamma)\beta^*_{x,y}}}, \tag{137}$$

where $\beta\gamma = 106.8$, ϵ_N is the normalized emittance and $\beta^*_{x,y}$ is the betatron function at the IP. The betatron tune is the number of oscillations a particle makes in one revolution of the accelerator. Equation (137) shows that a large betatron function at the IP is required to minimize the angular spread of the beam. The betatron function determines also the size of the beam spot at the IP:

$$\sigma^*_{x,y} = \sqrt{\frac{\epsilon_N \beta^*_{x,y}}{6\pi(\beta\gamma)}}. \tag{138}$$

Therefore, special beam optics with $\beta^* = 22$ m were chosen to minimize the angular beam divergence at the IP [123]. Data taking with the phase I experimental setup and with this magnet configuration, however, requires special beam optics and a dedicated running time. In addition, the beam needs special scraping/collimation in order to lower its emittance, since the detectors need to be moved very close to the beam for data taking. The protons scattered at small scattering angles will follow trajectories determined by the beam transport magnets. The large β^* at the IP, infers a large beam size at IP, which lowers the luminosity for our run, but provides a small beam size at the detection point. Having a small beam size at the detection point allows us to approach the detectors close to the outgoing beam, in order to measure small scattering angles [117]. The luminosity (L) and emittance (ϵ_N) of the beam during 2009 RHIC run (Run09) are given in Table 7.

The protons scattered at small scattering angles will follow trajectories determined by the beam transport magnets. By using the known parameters of the accelerator lattice explained above, we can calculate the deflection y^* and the scattering angle θ^*_y of the scattered proton at the IP after measuring the deflection y and the angle θ_y at the detection point. To a good approximation, the equations relating these two sets of coordinates are:

$$y = a_{11}y^* + L^y_{eff}\theta^*_y, \quad (139)$$

$$\theta_y = a_{12}y^* + a_{22}\theta^*_y. \quad (140)$$

The coefficients (a_{11}, L^y_{eff}, a_{12} and a_{22}) are the transport matrix elements, which vary with z, the distance from the IR. The coefficients depend on the betatron function at the interaction point and the phase advance from the interaction point, Ψ, as follows:

$$\begin{aligned} a_{11} &= \sqrt{\frac{\beta(s)}{\beta^*}}(\cos\Psi + \alpha(s)^*\sin\Psi), \\ L_{eff} &= \sqrt{\beta^*\beta(s)}\sin\Psi. \end{aligned} \quad (141)$$

where $\beta^* = \beta(s=0)$ and $\alpha(s)$ is the derivative of the betatron function:

$$\alpha(s) = -\frac{1}{2}\frac{d\beta}{ds}. \quad (142)$$

The optimum condition of the experiment is to have a_{11} (the transport matrix element which magnifies the beam size at IP) as small as possible and L_{eff} (the transport matrix element which magnifies the scattering angle) as large as possible. The optics during the data taking period of the experiment is optimized such that these conditions are fulfilled. In this case the position and angles at the detection point are independent of the transverse beam position at the IP, which is not known precisely. This is called "parallel-point-focusing", or in other words, when this condition is fulfilled, all the parallel rays at the interaction point are focused to the same detection point. Thus, the coordinate of the scattered proton at the detection point can be approximated as: $y \approx L^y_{eff}\theta^*_y$. The optimum condition is achieved when $\sqrt{\beta\beta^*}$ is large and when the phase advance Ψ is the odd multiple of $\frac{\pi}{2}$, (see Eq. (141)).

The smallest measured scattering angle θ^*_{min} determines the smallest value of the four-momentum transfer squared:

$$t_{min} \sim \theta^*_{min} = \frac{d_{min}}{L_{eff}}, \quad (143)$$

where d_{min} is the minimum distance of approach to the beam and depends on the beam size at the detection point and d_0 is the dead space of the detector:

$$d_{min} = k\sigma_y + d_0, \quad (144)$$

where k is a constant that is optimized by beam scraping. The smallest four-momentum transfer squared t_{min} is reached by having β^* as large as possible and by reducing the k-factor and the emittance [6].

The phase II configuration (see Fig. 36) will not only provide an increase in high-$|t|$ acceptance, but will also allow running without requiring special running conditions. In this way the experiment can run simultaneously with the other STAR experiment, which normally operate at small-β^* below 1 m in order to reach a high luminosity.

3.3.1 EXPERIMENTAL LAYOUT DURING 2009 RHIC RUN

The STAR experiment with the Roman pots positioned in phase I configuration (see Fig. 36) had a successful data taking period during the RHIC 2009 run (Run09). In this section, I will give a detailed description of the detector system set-up and the numbering scheme during Run09. Firstly, I will define the coordinate system used in this experiment: the STAR coordinate system.

The STAR coordinate system, is defined as follows:

- **East of STAR or 5 o'clock (Yellow Beam)**

  Positive "X" is away from the center of RHIC

  Positive "Y" is up

  Positive "Z" points westward (Blue Beam)

- **West of STAR or 6 o'clock (Blue Beam)**

  Positive "X" is towards the center of RHIC

  Positive "Y" is up

  Positive "Z" points westward (Blue Beam)

The detector configuration and the numbering scheme used during 2009 RHIC run is given in Fig. 38.

During the RHIC 2009 run, eight Si detector packages were installed in eight RPs in the actual setup in the RHIC accelerator tunnel, (see Fig. 38). The detector packages are named either A or B according to their orientation. Each detector package was installed in one RP and connected to one readout sequencer board

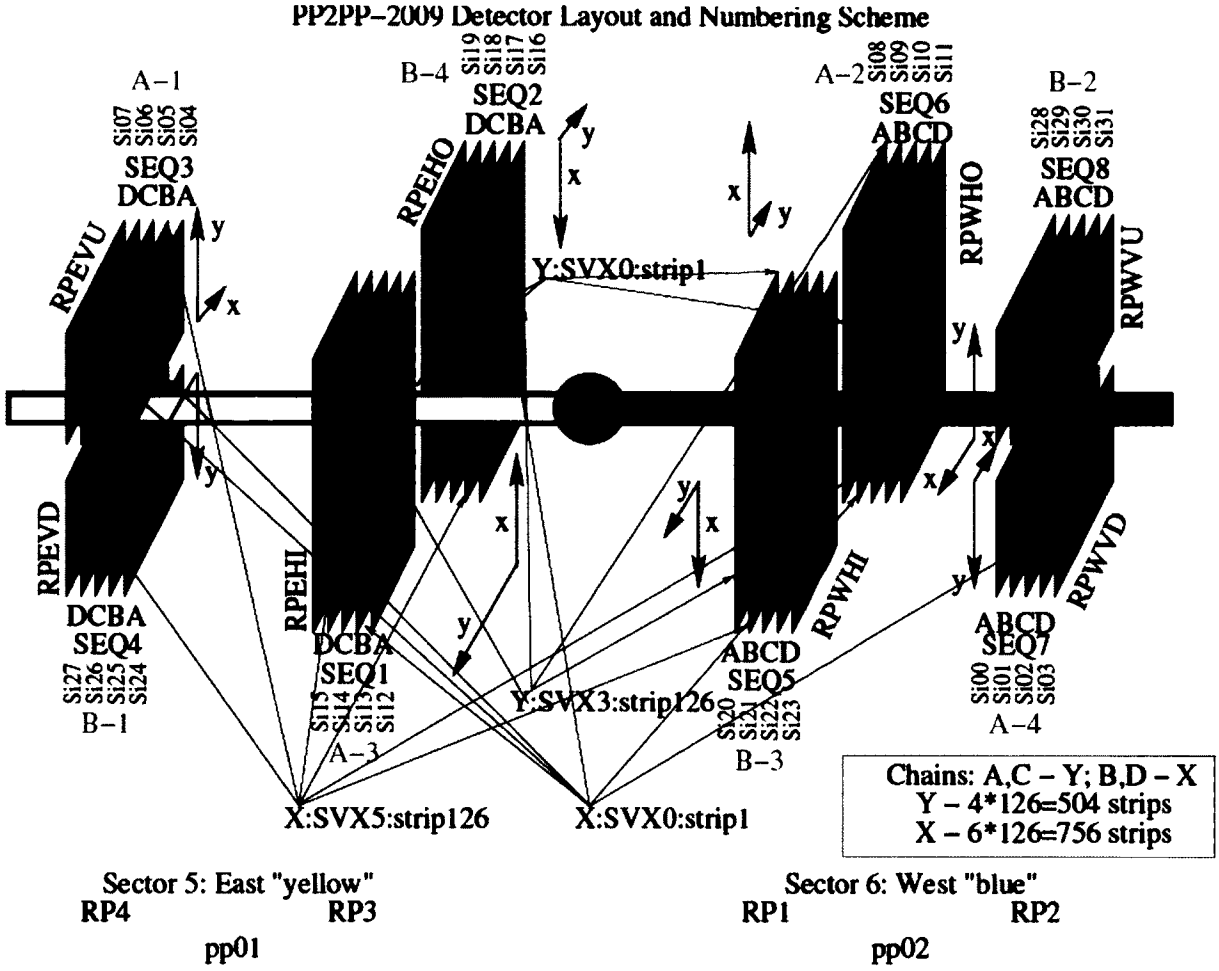

FIG. 38. Detector configuration and numbering scheme during RHIC 2009 run. There are 4 RP stations, 2 on each side of the IP at STAR: RP1 and RP2 in the West; RP3 and RP4 in the East. There are 8 detector packages consisting of 4 Si detector planes and inserted in each RP. Brown planes represent the Si detector boards/planes, blue planes represent the trigger scintillator attached behind the four Si detector boards in each detector assembly. There are 2 *y-view* (chains A and C) and 2 *x-view* (chains B and D) detectors in each detector assembly. The number of Si strips in each detector is given in the bottom-right legend. All detector packages and Si planes are numbered and labeled. The orientation of the Si strips in the x-y plane is also shown for each detector plane. The SVXIIE readout chips in each detector plane are labeled 0-5 for $x - view$ and 0-3 for $y - view$ detectors. The 1^{st} Si strip in a detector plane (important for survey and alignment) is the 1^{st} strip connected to SVXIIE-0 in each detector plane.

TABLE 5. Silicon detector installation map during RHIC 2009 run

Readout Sequencer	Detector Package Notation	Roman Pot Notation	Roman Pot Station
1	A-3	RPEHI	East Horizontal Inner
2	B-4	RPEHO	East Horizontal Outer
3	A-1	RPEVU	East Vertical Up
4	B-1	RPEVD	East Vertical Down
5	B-3	RPWHI	West Horizontal Inner
6	A-2	RPWHO	West Horizontal Outer
7	A-4	RPWVD	West Vertical Down
8	B-2	RPWVU	West Vertical Up

according to the the numbering scheme in the layout shown in Fig. 38 and the map given in Table 5.

There are two RP vessels in each RP station, vertical (up & down) and horizontal (inner & outer), with one Si detector assembly installed in each RP. For the horizontal RP stations, *Inner (Outer)* corresponds to *Left (Right)* RPs in the East (5 o' clock); and *Right (Left)* RPs in the West (6 o' clock), with respect to an observer looking away from the IP at STAR and towards the outgoing beam direction (+ve z in the West and $-$ve z in the East).

In each detector package, the 1^{st} and 3^{rd} detector planes (planes A & C) are *y-view* detectors, whereas 2^{nd} and 4^{th} planes (planes B & D) are *x-view* detectors. Thus, silicon strips/channels in planes A and C are parallel to each-other, but perpendicular to the silicon strips in planes B and D, and vice-versa. In addition, the silicon strips in horizontal RPs are perpendicular to the strips in vertical RPs, for the same plane (A, B, C, D). Each silicon micro-strip detector consists of either 512 individual Si strips, for *y-view* detectors (planes A & C), or 768 strips for *x-view* detectors (planes B & D). The Si strips are readout by 4 SVXIIE chips in a *y-view* detector plane and by 6 SVXIIE chips in a *x-view* detector plane. In total, 126 silicon strips are wire-bonded to one SVXIIE readout chip, (see Fig. 38), thus 504/756 out of 512/768 strips are wire-bonded to SVXIIE chips in a *y-view*/*x-view* detector plane, respectively.

The strip width is 70 μm, whereas the strip pitch/resolution, the distance between two silicon strips (center to center) is 105.0 μm for *x-view* detectors and 97.4 μm for *y-view* detectors.

Each detector plane (A, B, C, D) is used to measure either the x or y coordinate of the scattered particle, depending on the orientation of the Si strips. The detectors in all the packages follow the same order (*y-view*, *x-view*, *y-view*, *x-view*), (see Fig. 37). However, depending on the Roman pot in which the package is inserted (horizontal or vertical RP), the orientation of the strips in each plane is either vertical or horizontal in the $x-y$ plane. Table 6 gives a summary of the detector planes and the coordinates measured by each plane, in both horizontal and vertical RPs. On each side of the IP at STAR, 16 silicon detectors (8 *y-view* and 8 *x-view* detectors) were used to measure each coordinate, x and y.

Further details on the detector setup and infrastructure, can be found in Figures 101, 102 and 103 of Appendix D. The detector installation map and detailed infrastructure is shown for the East setup. Similar maps exist also for the West setup.

TABLE 6. Order of the detector planes and their measured coordinates in Horizontal and Vertical RPs

Detector Plane	Coordinate Measured in Horizontal RP	Coordinate Measured in Vertical RP
Plane A ($y-view$) 504 strips readout by 4 SVXIIE chips	x	y
Plane B ($x-view$) 756 strips readout by 6 SVXIIE chips	y	x
Plane C ($y-view$) 504 strips readout by 4 SVXIIE chips	x	y
Plane D ($x-view$) 756 strips readout by 6 SVXIIE chips	y	x

Stand Alone Sequencer boards (SAS) which are installed in a VME crate located in the tunnel near the Roman pots, are used to control SVXIIE chips. A detector package (4 Si detector planes) is connected to a SAS board (see Fig. 101 in Appendix D). The signals are sent via twisted pair differential cables, the use of which minimizes the noise during the signal transmission. The readout of SVXIIE chips from a detector package is then fed into the SAS FIFO, which is read by a MOTOROLA crate controller and sent to storage via Ethernet for offline process. The communication between the STAR counting house and the detector system in the tunnel is done via fiber optic cables.

CHAPTER 4

STUDY OF THE DETECTOR ACCEPTANCE USING SIMULATION OF THE TRANSPORT OF PROTONS IN THE RHIC BEAMLINE

4.1 DESCRIPTION OF THE SIMULATION METHOD

The main purpose of this simulation is the study of the acceptance and the kinematic range of the detector system used in this experiment. To accomplish this, we have simulated the transport of protons in the RHIC beamline from the interaction point (STAR IP) to the detection point (position of the Roman pots along the RHIC beamline). Simulations have been performed by using HECTOR, a fast simulator for the transport of particles in beamlines [124]. HECTOR computes the trajectories of particles in beamlines using information of the physical parameters of the beamline elements (dipole and quadrupole magnets, drift spaces etc.) that exist between the IP near the STAR detector and the very-forward detectors at about 60 m away from the IP, and through which the generated particles pass. Therefore, one of the requirements for the performance of this simulation is the knowledge of the actual physical parameters (magnetic field strength, beamline element's position in z-position along the beamline, length and apertures of the beamline elements, etc.).

Fig. 36 illustrates the experimental layout for two experimental phases. As mentioned also in Section 3.2, phase I is the present experimental layout (also the layout used in RHIC Run09), while phase II belongs to the future detector upgrade plans of the experiment at STAR. Our experiment is also referred to as *Physics with Tagged Forward Proton Detectors at STAR*, because it uses very-forward proton detectors (Roman Pots), to study pp elastic scattering in the very-forward region at STAR.

Simulation studies were done for the two phases of the experiment and the detector acceptance was studied in each scenario and for two beam momenta: 100 and 250 GeV/c in both scenarios. Results of the simulation study, which will be explained in

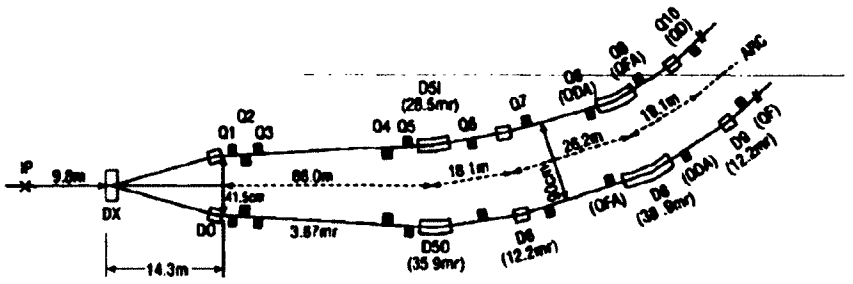

FIG. 39. Expanded layout of RHIC magnets from the IP to Q10 (from RHIC Configuration Manual [126]).

details in this chapter, can be found in conference proceedings [125]. Here, however, we will show results on the detector acceptance for the experimental phase I.

Fig. 37 shows the detector layout for the experimental phase I, with Roman pot detectors located at 55.5 m (horizontal RP station) and 58.5 m (vertical RP station), at each side of the STAR IP. The scattered protons pass through several drift spaces and other beamline elements before they reach the detectors: two dipole magnets (DX and D0, see Fig. 37) and a quadrupole triplet (Q1, Q2 and Q3). The dipole magnets are magnets for the path/trajectories of the beam and scattered protons in the horizontal direction, while the quadrupole magnets serve as focusing/defocusing elements for the particle trajectories. The Roman Pots are located bout 20 m downstream of the center of the third quadrupole magnet. Fig. 39 shows an expanded layout of RHIC magnets from the IP to Q10 of the RHIC beamline. Fig. 40 shows a simple layout of the magnets and drift spaces between IP6 at STAR and the RP location along the RHIC beamline. Fig. 40 illustrates only one side (i.e. East of IP), the other side (West) is similar.

4.1.1 SIMULATION METHOD

The HECTOR simulator [124] is based on a linear approach to the beamline optics, implementing transport matrices from the optical element magnetic effective length, and with correction factors on magnetic strength for particles with non nominal energy. HECTOR deals with the computation of the position and angle of the

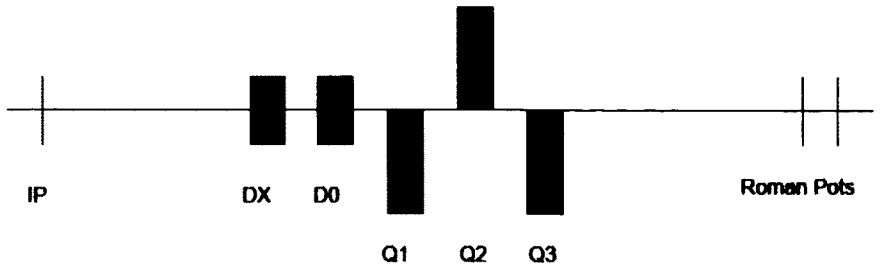

FIG. 40. Optical beamline elements (drift spaces and magnets: DX and D0 - dipole magnets and Q123 is the quadrupole triplet) between the IP and the RP location along the RHIC beamline. RP's are located at $\sim$ 60 m away from IP and the distance between center of Q3 (last quadrupole magnet) and the RP location is $\sim$ 20 m. Figure shows beamline elements only in one side of the (i.e. East of IP), West side looks similar.

beam particles, and the limiting aperture of the optical elements [124]. It is a program primarily dedicated to LHC beamlines, but it can be used for the transport of particles through generic beamlines. From the computational point of view, is has an object oriented structure, using the ROOT framework [127,128]. In forward physics, for example, HECTOR links the information on the measured position and angle of the particles in dedicated detectors (i.e. Roman Pots), located meters away from the IP, with the position and angles of the particles at the IP, by precisely calculating particle trajectory.

Trajectories of particles are computed using information of the physical parameters of the optical elements in the beamline. The content of this information (readout in the code) specifically is: name and type of the optical element (*drift* space; *dipole*: rectangular dipoles with a straight shape used in the straight sectors of the beamline and sector dipoles, which are bent to match the beam curved trajectory and used in the bending sections; *quadrupole* magnets focus the beam either vertically or horizontally; *kicker* magnets dedicated to produce the crossing angle at the IP, etc.), position and length in z, magnetic field strength for dipole, quadrupole fields and any multipole field effects, any kicker magnet effect, geometrical aperture shape of the element (circle, rectange, ellipse etc.) and aperture dimensions. This information is provided to us by the Collider-Accelerator (C-A) Department at BNL in a format that is also compatible to the MADX software [129,130]. We use this information to

construct the beamline, where each optical element is represented by a transport matrix M, and $M_{beamline}$ is the multiplication of the transport matrix of each element: $M_{beamline} = M_1 M_2 ..... M_n$, for n elements.

4.1.2 PROCEDURE AND INPUT PARAMETERS

In our simulation study we follow the general procedure and input parameters (beam parameters and detector geometry related parameters, for our case and for the experimental phase I setup) given below:

- Parametrize all beamline elements, as explained above. Construct beamline from IP to detector position (RP), specify beamline length: $L_{beamline} = 58.496$ m.

- Determine positions of detectors, detector characteristics and physical parameters, distance of approach of the detector to the beam.

  - Horizontal/Vertical RP station: $z = 55.496/58.496$ m, respectively.

  - Silicon detector area: 74×45 mm^2

  - Distance of approach of detector to the beam center: d_{min}. This depends on the Roman pot position with respect to the beam-pipe center. The Roman pot position relative to the beam-pipe center (assuming beam center is the center of the beam-pipe) can vary from a fully retracted RP position ($\sim$ 70 mm) to an inserted RP position (as close as 6 mm). Here one needs to take into account also the dead-space (d_0) between the bottom of the RP and the first silicon-strip position, which is $\sim$ 1.8 mm. So, depending on the beam position and beam width at the RP position, the first silicon strip can be as close as $\sim$ 10 mm to the center of the beam. During the actual experimental run, the distance of approach d_{min}, is determined by looking at the beam conditions during the run (specifically by observing the single event rate in the RP scintillation counters during the run while the Roman pot is inserted close to the beam for data taking). This will be explained in more details in Chapter 5. In general the minimum distance of approach is taken to be: $d_{min} = k\sigma_{x,y}(\text{RP}) + d_0$, where k is a constant optimized by beam collimation and $\sigma_{x,y}(\text{RP})$ is the beam size at the detection point (RP position).

- Determine beam parameters (the following parameters are given for our case):

  - Proton mass: $m_p = 0.938$ GeV

  - Proton charge: $q = +1e$

  - Beam momentum: $p_{beam} = 100$ GeV/c or 250 GeV/c

  - Beam energy divergence: $\sigma_{p_{beam}} = 0$ (for this simulation)

  - Beam position at IP: (x, y, z or s) = (0, 0, 0) m

  - Beam longitudinal dispersion: $\sigma_s = 0$ m

  - Beam lateral width (beam transverse size) at IP ($s = 0$): $\sigma_{x,y}(0) = 701.6$ μm for $p_{beam} = 100$ GeV/c and 265.3 μm for 250 GeV/c. This is calculated using Eq. (138), where β^* (the betatron function at IP) is 22 m (as required by the special beam tune for our experiment) and $\beta\gamma = 106.8$ for 100 GeV/c protons and 266.5 for 250 GeV/c protons.

  - Beam angular divergence/spread at IP: $\sigma_{\theta_{x,y}(0)} = 33.4$ μrad for 100 GeV/c and 35.4 μrad for 250 GeV/c, calculated similarly using Eq. (137). The horizontal and vertical emittances $\epsilon_{x,y} \approx 15\pi$ mm-mrad is used as input in Eq. (138) and Eq. (137). The emittance is constant along the orbit according to Liouville's theorem [131, 132].

  - Beam dispersion: $D = 0$ (for this simulation), so we assume that there are no off-momentum particles.

  - Beam crossing angle: $\theta_B = 0$ (we assume this for simplification, although in reality a beam crossing angle exists). We can also change this parameter and study the effect of the measured particle positions at the detection point on the beam crossing angle. A study to see the effect of a crossing angle was also done, for various possible crossing angles values: 3-, 4- and 5-$\sigma_{\theta_{x,y}(0)}$.

- Generate beam particles (protons) with randomized momentum-t in a given t-range (0 - 0.04 (GeV/c)^2) and ϕ (0 - 2π). The maximum value of t is determined by the known aperture just before the detectors (the aperture of the quadrupole magnets), and the minimum t value from the minimum distance of approach to the beam (d_{min}). Number of generated particles: $N = 2$M. Calculate other kinematic variables using the above:

  - Scattering angle: $\theta = \frac{\sqrt{t}}{p}$ from Eq. (20) for forward scattering.

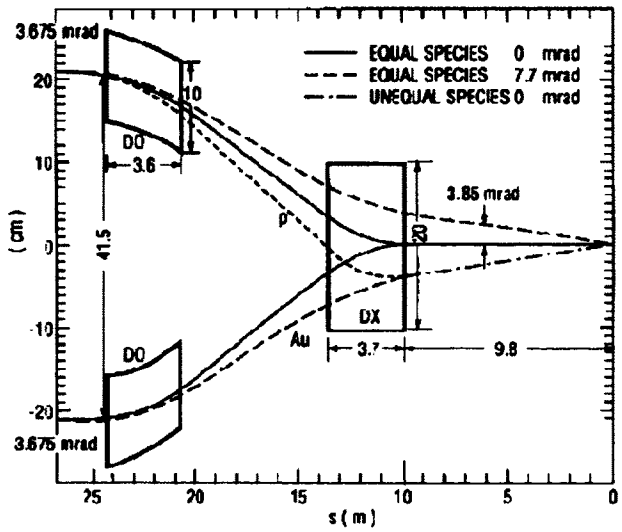

FIG. 41. Beam crossing geometry at one of RHIC IP's (magnetic lengths are shown). DX dipole magnet is common to both beams, D0 of inner and outer insertions are separately excited to accommodate variations in beam crossing angles, as well as collisions between unequal species [126]. Beam crossing angle can vary from 0 - 7.7 mrad [126].

- $\theta_x = N \times \theta \times \cos\phi$ and $\theta_y = N \times \theta \times \sin\phi$

- Each beam particle is then represented by a 6-component phase space vector $X = (x,\ \theta_x,\ y,\ \theta_y,\ E,\ 1)$, with horizontal and vertical coordinates and angles, E is the particle energy and 1 is just a factor used to add an angular kick on the particle momentum direction [124]. In our case we set the initial particles position and angles at the IP such as: $X(s = 0) = (0,\ \theta_x,\ 0,\ \theta_y)$.

- Propagate generated protons through the beamline. The propagation of a single particle through the constructed beamline (with n optical elements), is the *rotation* of the phase space vector by n optical elements matrices, such as:

$$X(s) = X(0)M_1M_2.....M_n\,. \tag{145}$$

- Compute the transverse position $(x,\ y)$ of the propagated protons at the detection point. This can be done in HECTOR.

- Study detector acceptance for proton positions (y vs x) and kinematic variables (t vs ϕ) etc.

In our case, the generated protons travel through the accelerator lattice consisting of drift space, two dipole and three quadrupole magnets, as shown in Fig. 40, before they reach the detectors. The trajectories of particles are limited by magnets' apertures and detector acceptance. When a particle is propagated through an optical element, its path is checked twice, at entrance at exit of the element, whether it is compatible with the element's acceptance or not [124]. If the particle does not pass through the element's acceptance, it is stopped and HECTOR provides the stopping element. The particle trajectory is calculated by using a transport matrix multiplication method given in Eq. (145). The whole beamline is modeled as a single transport matrix acting on each particle phase space vector X, assuming no intrabeam interactions [124].

In electromagnetism, the effect of an external electric ($\vec{E}$) and magnetic field ($\vec{B}$), on a charged particle with charge (q) and traveling with velocity ($\vec{v}$), is given by the Lorentz force: $\vec{F} = q(\vec{E} + \vec{v} \times \vec{B})$. The Taylor's expansion of the vertical component of magnetic field B_y, around its central value is:

$$\frac{e}{p}B_y(x) = \frac{e}{p}B_y + \frac{e}{p}\frac{\delta B_y}{\delta x}x + \frac{1}{2}\frac{e}{p}\frac{\delta^2 B_y}{\delta x^2}x^2 + ..., \tag{146}$$

where p is the momentum of the particle and e its charge [124]. The terms of this sum are interpreted as **dipolar**: ($\frac{1}{R} = \frac{e}{p}B_y$; **quadrupolar**: ($k = \frac{e}{p}\frac{\delta B_y}{\delta x}$; and sextupolar fields... In the co-moving coordinate system, neglecting small deviations ($x \ll R$, $y \ll R$) and small momentum loss ($\Delta p \ll p$), this leads to the following equations of motion for a for a particle traveling along the path s, through a magnetic element [131]:

$$\begin{aligned} x''(s) + \left(\frac{1}{R^2(s)} - k(s)\right)x(s) &= \frac{1}{R(s)}\frac{\Delta p}{p}, \\ y''(s) + k(s)y(s) &= 0. \end{aligned} \tag{147}$$

The transport matrices for various optical elements are given in [124, 131, 132]. The transport matrix for a horizontally focusing quadrupole ($k < 0$):

$$M_{QF} = \begin{pmatrix} \cos\Omega & \frac{1}{\sqrt{|k|}}\sin\Omega & 0 & 0 \\ -\sqrt{|k|}\sin\Omega & \cos\Omega & 0 & 0 \\ 0 & 0 & \cosh\Omega & \frac{1}{\sqrt{|k|}}\sinh\Omega \\ 0 & 0 & \sqrt{|k|}\sinh\Omega & \cosh\Omega \end{pmatrix}, \tag{148}$$

where $\Omega = \sqrt{|k|}s$ [131], and for a vertically focusing quadruple is given as [131]:

$$M_{QD} = \begin{pmatrix} \cosh\Omega & \frac{1}{\sqrt{|k|}}\sinh\Omega & 0 & 0 \\ -\sqrt{|k|}\sinh\Omega & \cosh\Omega & 0 & 0 \\ 0 & 0 & \cos\Omega & \frac{1}{\sqrt{|k|}}\sin\Omega \\ 0 & 0 & \sqrt{|k|}\sin\Omega & \cos\Omega \end{pmatrix}. \tag{149}$$

The transport matrices for a zero-field drift space ($k = 0$) and dipole magnet ($k = 0$, $R > 0$), are given below [131]:

$$M_{drift} = \begin{pmatrix} 1 & s & 0 & 0 \\ 0 & 1 & 0 & 0 \\ 0 & 0 & 1 & s \\ 0 & 0 & 0 & 0 \end{pmatrix}. \tag{150}$$

$$M_{dipole} = \begin{pmatrix} \cos\frac{s}{R} & R\sin\frac{s}{R} & 0 & 0 \\ -\frac{1}{R}\sin\frac{s}{R} & \cos\frac{s}{R} & 0 & 0 \\ 0 & 0 & 1 & s \\ 0 & 0 & 0 & 1 \end{pmatrix}, \tag{151}$$

[131]. The dispersion function can be defined from Eq. (147), for horizontal dipoles ($k = 0$), taking $\Delta p/p = 1$ [124]:

$$D''(s) + \frac{1}{R^2}D(s) = \frac{1}{R}. \tag{152}$$

The solution of this equation leads to a correction term for the deflection of off-momentum particles in the dipoles: $x_{off-mom.}(s) = x(s) + D(s)\frac{\Delta p}{p}$.

4.2 ACCEPTANCE OF THE DETECTOR SYSTEM, PHASE I - EXPERIMENTAL SETUP

$p = 100$ GeV/c and $\beta^* = 21$ m

Fig. 42 shows in detail the trajectories of 100 GeV/c beam and scattered protons, computed for a sector of the RHIC beamline (West and up to 80 m away from the IP at STAR). The trajectory of the scattered particles is actually the term $\theta L_{eff}[x, y]$ from Eq. (140), neglecting the first term (the term dependent on transport matrix element a_{11}. This plot illustrates the optimization of the optics for our experiment (as explained also in Chapter 3, using large-β^* to minimize the angular beam divergence at IP (remember Eq. (137). The matrix elements are also optimized such that a_{11} is as small as possible at the RP location (60 m) and L_{eff} is as large as possible, in order to achieve *parallel-to-point focusing* as accurately as possible, meaning the (x, y) position of the scattered protons at the RP, depends almost only on their scattering angles and is nearly independent to the transverse position at the IP.

The purpose of displaying Fig. 42 is to show the optimization of the beam optics required for phase I, and also to illustrate an example of the trajectories of 100 GeV/c

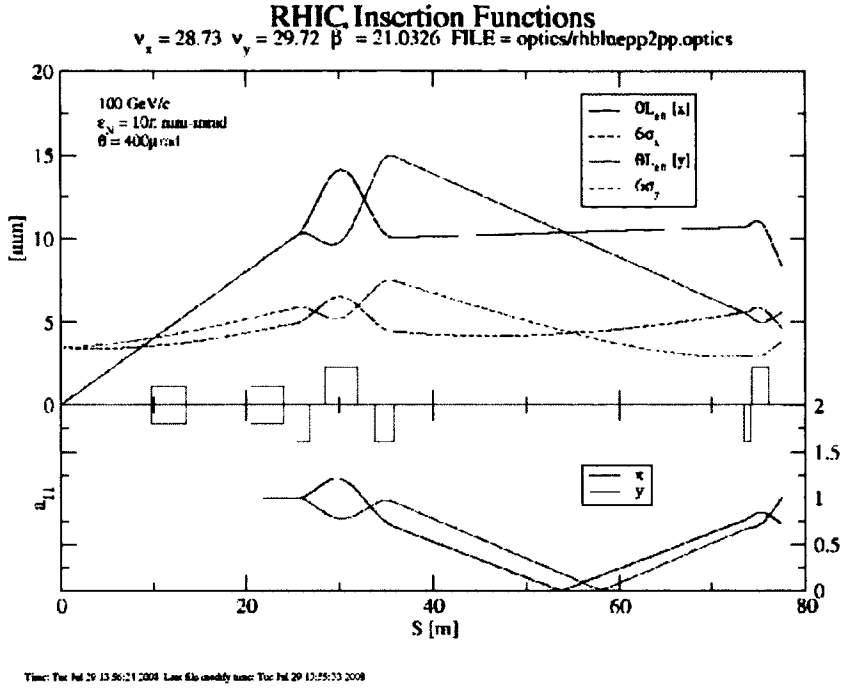

FIG. 42. Trajectories of 100 GeV/c beam particles (dashed line) and scattered particles (solid line), computed for a sector of the RHIC beamline (West and up to 80 m away from the IP at STAR). The betatron function at the IP ($\beta^* \approx 21$ m), the special beam tune required for experimental Phase I setup. The plot has two different axes: horizontal axis is in mm, showing the trajectory in x and y for both beam and scattered particles, while the vertical axis is the $z(s)$ position in m. Red and black refer to y and x coordinates of the particles, respectively. The beamline elements: two dipole and a quadrupole triple are shown in cyan. Trajectory of the 6σ of the beam (dashed line) is shown, including the focusing and defocusing effects on the beam particles. The beam emittance of the beam is taken to be $\epsilon = 10\pi$ mm-mrad. The trajectory of the scattered particles is also shown for a particle scattered with a scattering angle $\theta = 400$ μrad. The deflecting effect of the dipole magnets on the trajectories is not shown in the plot, as it is purposefully removed in the software used to produce the plot. The magnitude of the matrix element $a_{11}(x, y)$ is also shown in the figure (the graph below 0), where $a_{11}(x, y)$ is optimized to be as small as possible at the RP location (60 m). Figure courtesy of S. Tepikian from the C-A Dept. at BNL.

protons from the IP to the RP location. It can be seen in Fig. 42, that the Roman pots are located at a position where the scattered protons are well separated from beam protons, which is needed to allow the Roman pots to be moved close to the scattered beam particles, without coming very close to the outgoing beam particles, while the RP is inserted inside the accelerator beampipe.

After propagating generated protons and computing their trajectories and transverse positions (x, y) through the constructed beamline, as described in the simulation procedure above, we can study the acceptance of the detector system with the given detector specifications. Fig. 43, shows the computed (y vs x) coordinates of the protons at two RP locations (55.496 and 58.496 m, horizontal and vertical RP stations respectively). Every point in the plot corresponds to a particle with specific x and y coordinates, computed at the detection point. The elliptical shape of the plot is due to the different focusing in x and y by the quadrupoles. The outer edges are limited mostly by the apertures of the quadrupole magnets. The simulated acceptance shows that we have full acceptance in azimuthal space ϕ, which is important for the measurement of spin-dependent observables. It can also be seen very clearly in Fig. 43 that there are overlapping regions between the horizontal and vertical detectors (shown darker in the plot). The overlapping regions are important for detector alignment studies.

Fig. 44 shows the acceptance as a function of $|t|$. There is a region in $|t|$, where the acceptance is independent of $|t|$, this is the region of 100 % and flat/constant acceptance: $0.003 \leq |t| \leq 0.02$ (GeV/c)^2.

$p = 250$ GeV/c and $\beta^* = 7.5$ m

Fig. 45 shows the simulated acceptance for 250 GeV/c protons (thus $\sqrt{s} = 500$ GeV). In this case a different beam tune is used, $\beta^* = 7.5$ m. Fig. 45(a) shows the geometrical acceptance and Fig. 45, the acceptance as a function of $|t|$. Higher $|t|$ acceptance is extended to 0.2 (GeV/c)^2. The region of 100 % and flat/constant acceptance in this case is about: $0.06 \leq |t| \leq 0.145$ (GeV/c)^2.

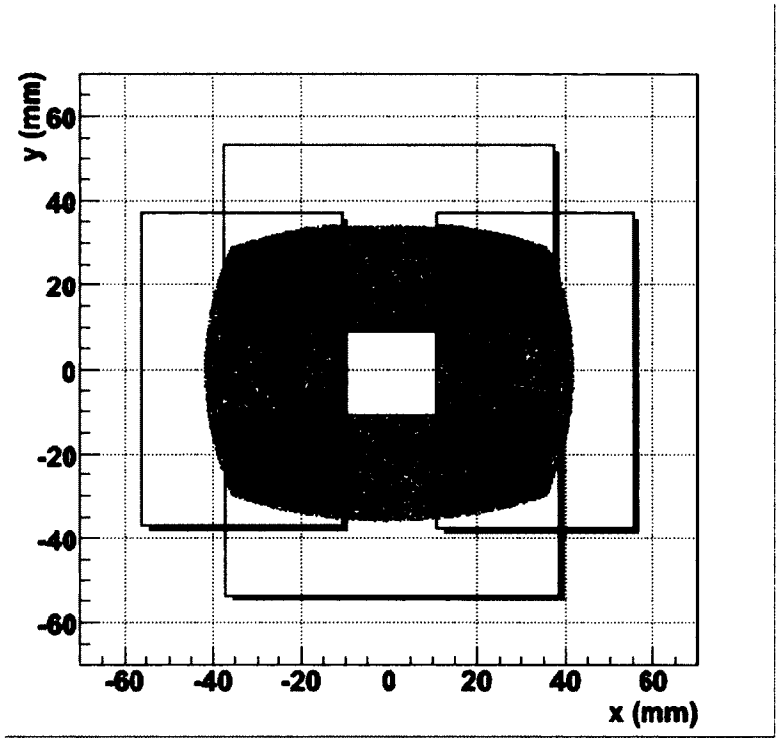

FIG. 43. The geometrical acceptance: coordinates y vs x (mm) of 100 GeV/c protons at the RP location, for Phase I ($\beta^* = 21$ m). The outer boundaries are limited by the apertures of the quadrupoles, the vertical coordinate is limited by the width of the detector (37 mm). The inner boundaries are related with the minimum distance of approach of the beam d_{min}, relative to the beam center. d_{min} in this case was set to 15 mm. The detectors are shown by red rectangles: horizontal (inner and outer) and vertical (up and down). The vertical RP station is 3 m away from the horizontal RP station, with the horizontal station being closer to IP for an observer looking away from the IP and towards the RP location. The overlapping regions of the detectors are shown in darker black.

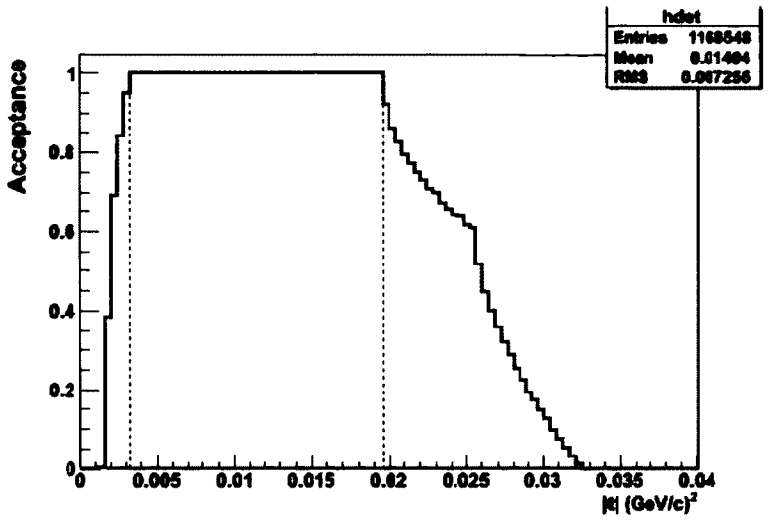

FIG. 44. Normalized number of particles (acceptance) plotted as a function of $|t|$ for 100 GeV/c protons and for Phase I. The region of 100 % and flat acceptance is indicated in the plot.

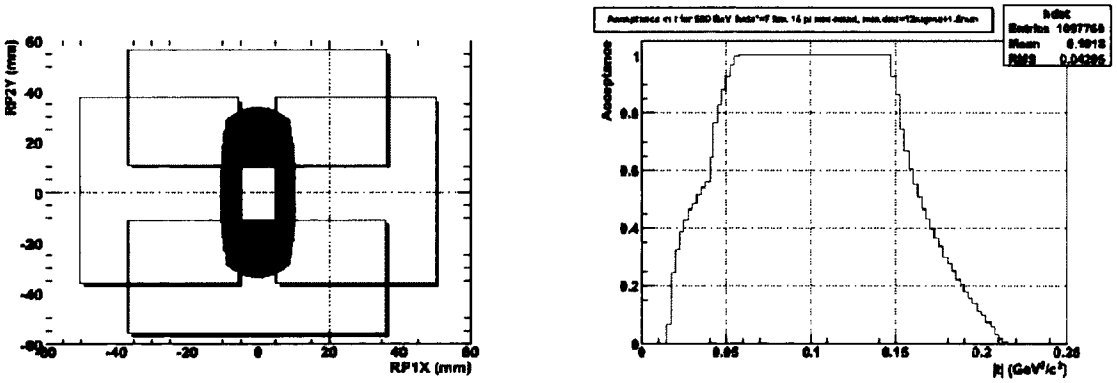

(a) Geometrical Acceptance: y vs x in mm

(b) Acceptance as a function of t

FIG. 45. Acceptance for 250 GeV/c protons, for Phase I and with $\beta^* = 7.5$ m: (a) y vs x in mm, and (b) acceptance as a function of $|t|$. Note: in (a) horizontal RPs are insterted twice a close to the center, compared to vertical RPs.

CHAPTER 5

DATA COLLECTION DURING RHIC 2009 RUN

5.1 RUNNING CONDITIONS DURING DATA COLLECTION

During the second half of RHIC Run09, the Relativistic Heavy Ion Collider (RHIC) provided polarized proton collisions at the STAR and PHENIX interaction points [133]. The spin orientation of both proton beams at the collision points was controlled by helical spin rotators, and physics data were taken with different orientations of the beam polarization [133]. The final week of the run was devoted to the polarized proton-proton elastic scattering experiment at RHIC, originally named PP2PP and now part of the STAR experiment.

During Run09, the STAR collaboration was able to record a total of 33 million elastic triggers. The data were taken during four dedicated RHIC stores between June 30 and July 4, 2009 with special beam optics of $\beta^* = 22$ m. The luminosity was $\mathcal{L} \approx 2{\cdot}10^{29}\text{cm}^{-2}\text{s}^{-1}$. The data were collected during 46 runs and the closest approach of the first Si strip to the center of the beam pipe was ~ 10 mm. The four momentum transfer squared t range covered during Run09 was $0.003 \leq |t| \leq 0.035$ $(\text{GeV}/c)^2$.

The main objective of this data analysis is the measurement of the transverse single spin asymmetry A_N in the elastic scattering of two transversely polarized protons at $\sqrt{s} = 200$ GeV. Measurement of A_N in the CNI region and at the high energy range available at RHIC will help us attain a better understanding of the spin-dependence of the diffractive processes and the involved exchange mechanisms.

A summary of the running conditions, i.e. beam parameters, during Run09 is given in Table 7.

The runs taken during Run09 are listed in Fig. 104 in Appendix D, according to Ref. [134]. The run list given in Appendix D provides information on several important running conditions, such as: run number; starting and stopping date and time of each run; duration of the run; number of events taken in each run; number and fraction of elastic events for each run; run type/comment; store number and RP position (Pos) for each run. Note that not all the runs taken during Run09 are physics

TABLE 7. Beam parameters and other running conditions during Run09

Parameter	Symbol	Value
Beam Momentum	p	100 GeV/c
Beam Polarization (Blue)	P_B	0.60
Beam Polarization (Yellow)	P_Y	0.62
Fill Pattern (No. of Bunches/Ring, Blue×Yellow)		120 × 120
No. of Filled Bunches/Ring, Blue×Yellow (after excluding the abort gap in the fill pattern)		90 × 90
No. of Colliding Pairs		64
No. of Bunches with Both Beams Polarized		64
No. of Bunches with Polarization Pattern either ↑↑, ↓↓, ↑↓ or ↓↑ for P_B and P_Y, respectively		16
No. of Events with Polarization Pattern (for P_B and P_Y, respectively)	↑↑	5,310,345
No. of Events with Polarization Pattern	↓↓	5,346,003
No. of Events with Polarization Pattern	↑↓	5,439,282
No. of Events with Polarization Pattern	↓↑	5,648,314
No. of Protons/Bunch (Beam Intensity)	I_{beam}	$5{\cdot}10^{10}$ protons/bunch
Beam Emittance	ϵ_N	15π mm mrad
Betatron Function at IP	$\beta^*_{x,y}$	22 m
Beam Lateral Width at IP	$\sigma^*_{x,y}$	701.62 μm
Beam Angular Divergence at IP	$\sigma^*_{\theta_x,\theta_y}$	33.36 μrad
Closest Approach of the first Si strip to the center of beam-pipe	d_{min}	$\sim$ 10 mm $\approx$ 12 σ_{beam}

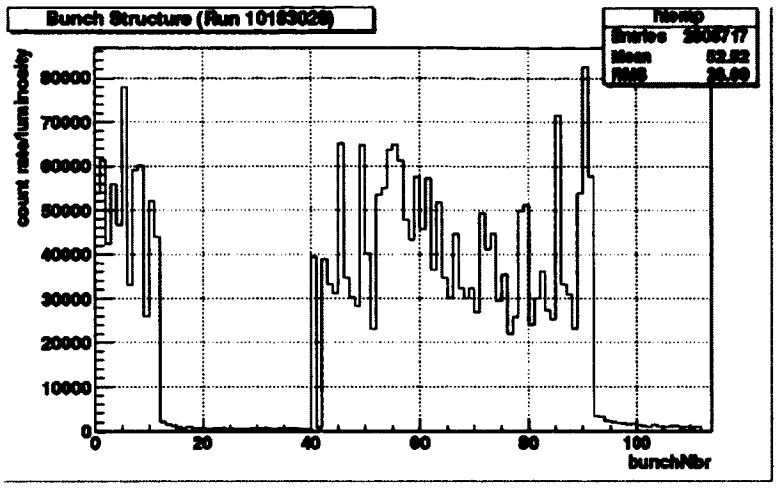

FIG. 46. Bunch structure for run 10183028, showing the number of scattering events as a function of bunch number.

runs, only 13 out of 17 RP positions correspond to physics runs and more than one run was taken with the RPs inserted close to the beam at certain RP positions (this corresponds to one RP Pos in the run list in Appendix D). This set of physics runs is used for data analysis. Figure 105, also in Appendix D, provides a list of the RP positions for each run together with information on the: run number; starting and stopping date and time for each run; RP position; distance of approach (mm) of each RP to the RHIC accelerator beamline center. The distance of approach of the RP to the center of the beamline during the run was measured by using a device called Linear Variable Differential Transformer (LVDT).

The 4 RHIC stores during data collection (11020, 11026, 11030, 11032) had the same bunch structure for both counter-circulating beams, Blue and Yellow (90 $\times$ 90), respectively. Figure 46 shows the bunch numbers for a typical run, here run 10183028.

Events coming from the collision of the first 7 bunches were excluded from the analysis, because the timing of these bunches corresponded to the time when the pre-amplifier of the SVX readout chip of the silicon detectors was resetting. The preamplifier must be reset once per revolution of the proton beam. After the reset, it takes a short amount of time for the preamplifier output to settle. The resetting occurred during the collision of bunches 1-7. Thus, another bunch number was introduced after the exclusion of the first 7 bunches of the beams (bunch numbers: 1-7)

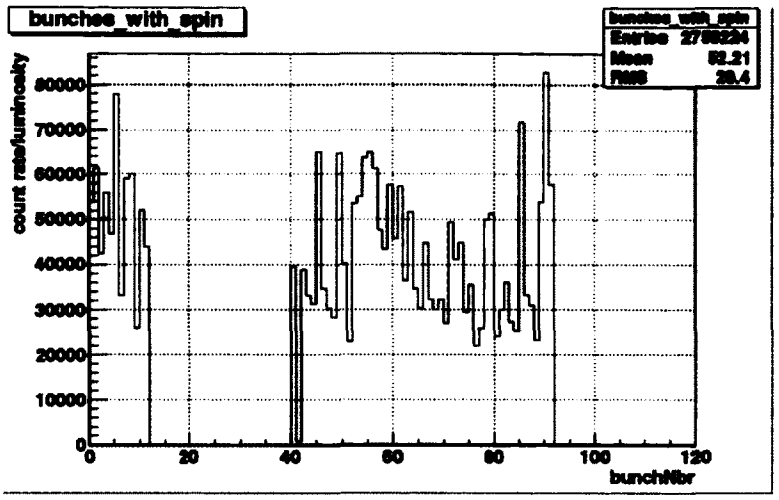

FIG. 47. Bunches with spin for run 10183028, spin orientation is transverse, either positive (up) ↑ or negative (down) ↓.

due to the RP data acquisition system.

To provide an abort gap for the beams, 30 out of 120 bunches are purposefully left unfilled (see Fig. 46). If we look at the polarization of the bunches we see that only 64 out of the 90 bunches per beam provide bunch combinations where both Blue and Yellow beams are polarized, (see Fig. 47). Thus, only 64 out of 90 bunches have usable polarization pattern for both beams. This includes four bunch combinations (all possible spin direction combinations): 16 ↑↑, 16 ↓↓, 16 ↑↓, 16 ↓↑, for Blue and Yellow beams, (see Table 7). The number of events coming from collisions of each of these bunch combinations is also given in Table 7. The polarization direction of every RHIC bunch is determined by the spin-flip control system in the polarized ion source [112], and every single pulse is accelerated and becomes a RHIC bunch with a specific polarity: ↑ (+) or ↓ or (-). Selected patterns of spin direction sequences are loaded into the rings. Having all possible spin direction combinations for colliding bunches enhances the systematic error control greatly. The polarization pattern for the Blue beam was: -+-++-+-..., and for the Yellow beam was: ++−++−..., with 90/90 bunches for Blue/Yellow. The polarization measurement during the run was performed by the CNI Polarimeter group at RHIC, refer to the analysis note given in [135].

Figure 48 and 49, show the bunch numbers for the four spin combinations for Blue and Yellow beams: ↑ ↑, ↓ ↓, ↑ ↓, ↓ ↑.

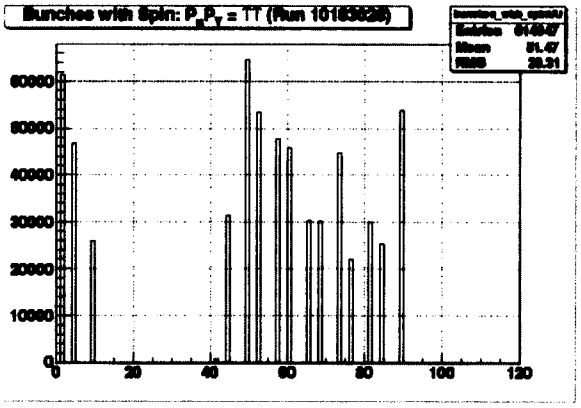

(a)

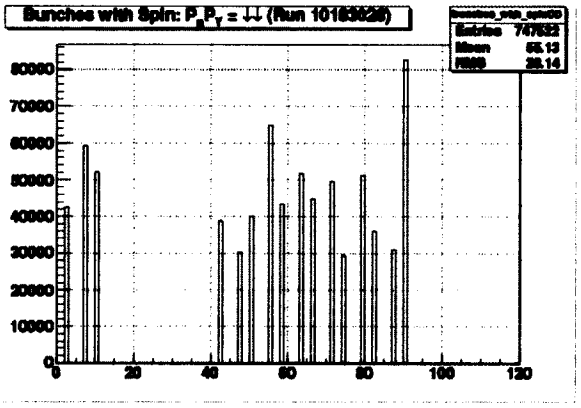

(b)

FIG. 48. Bunches with spin orientation: (a) ↑ ↑ (b) ↓ ↓, for run 10183028.

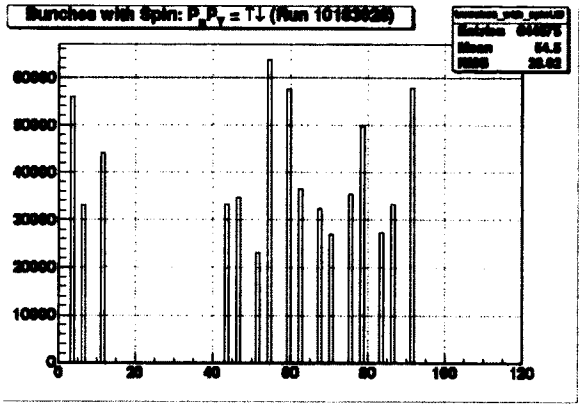

(a)

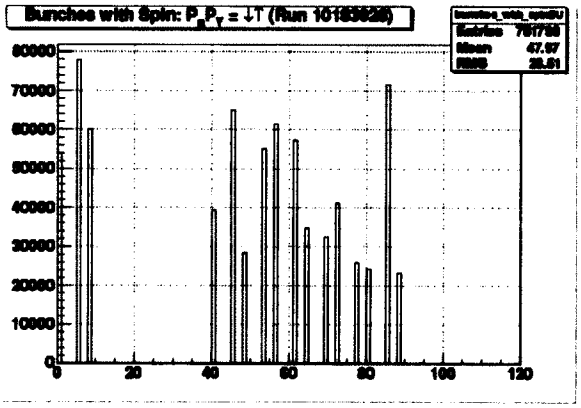

(b)

FIG. 49. Bunches with spin orientation: (a) $\uparrow \downarrow$ (b) $\downarrow \uparrow$, for run 10183028.

The transverse single spin asymmetry A_N is defined as the left-right cross section asymmetry with respect to transversely polarized beams. With the available bunch combinations given above, various asymmetries could be built:

1. We can measure an asymmetry using $\uparrow\uparrow$ and $\downarrow\downarrow$ bunch combinations. This includes 32 bunch combinations out of 64 colliding bunches with both beams polarized. In this case the measured asymmetry is proportional to the sum of the Blue and Yellow beams' polarization values, $P_b + P_y$.

2. Another asymmetry can be measured when we consider one beam polarized and we do not look at the polarization of the other beam, or we consider the other beam unpolarized. For example we consider the Blue beam to be polarized and the Yellow beam to be unpolarized and vice-versa.

   In this case, there are 45 out of 90 colliding bunches when the spin orientation of the Blue/Yellow beam bunches is positive and the spin orientation of the Yellow/Blue beam bunches is either positive, negative or zero; 45 bunches when the spin orientation of the Blue/Yellow beam bunches is negative and the spin orientation of the Yellow/Blue beam bunches is either positive, negative or zero. One could measure a transverse single spin asymmetry in this case, but the measured asymmetry is proportional to the polarization value of one beam only, P_b or P_y, rather than the sum of Blue and Yellow beams' polarization values as in the first case.

3. We can also use the opposite bunch spin combinations: $\uparrow\downarrow$ and $\downarrow\uparrow$. This again includes 32 bunch combinations out of 64 bunches when both beams are polarized. In this case, the measured asymmetry is proportional to the difference of the Blue and Yellow beams' polarization values, $P_b - P_y$. The difference in the polarization values should be very small, close to zero, leading to a small measurable asymmetry in this case. In other words, the measurement of an asymmetry in this case can be used as a systematics check for the asymmetry measurement.

In order to reduce the background from the beam halo, the beam was scraped during the run by using beam collimators. The Roman pots were positioned at the closest position allowed by the beam envelope, depending on the beam conditions. The single event rates measured by the scintillator counters of our detectors were

monitored while the RP was being moved close to the beam. The RP was moved slowly, ~10 mm each time and the single event rates were constantly checked.

As the RP is moved close to the beam, the distance of the RP relative to the beam center decreases, allowing the detection of particles scattered at small scattering angles, or small momentum transfer t. As t decreases, approaching $|t| \sim 10^{-4}$ $(\mathrm{GeV}/c)^2$ or less, the Coulomb amplitude starts to dominate the differential elastic cross-section and the cross-section increases as $1/t^2$. The approach of the RPs to the beam halo and maybe the fast increase of the cross-section due to the dominance of the Coulomb amplitude at small-t (if RPs move close enough to reach the Coulomb region), makes the singles rates in the scintillator counters increase quickly as the RP is moving closer to the beam. Because of the limited trigger rate of the data acquisition system, the RP movement was stopped by the operator whenever the single event rate reached the maximum allowed rate ~ 30 kHz. In this way the RP was moved to the limit of the rates, assuring that the RP was positioned to the closest distance possible relative to the center of the outgoing beam, without approaching the Coulomb region.

Since the beam conditions (i.e. position of the beam center) are different for different stores/fills, the position of the RPs and thus the distance of approach of the detectors with respect to the center of the beam-pipe, changed from one store/fill to the other. Considering the position of all the Roman pots, there are 13 different RP positions during the 4 stores, (see Appendix D). At least one of the Roman pots were moved to a closer position during the same store, whenever the beam envelope allowed this approach.

5.1.1 BEAM PARAMETERS

The luminosity of the beam can be calculated using the following expression:

$$L = \frac{3}{2}\frac{\mu}{\beta^*}(\beta\gamma)\frac{N_B N^2}{\epsilon}, \tag{153}$$

where μ is the revolution frequency, β^* is the betatron function at the IP, $\gamma = 106.8$ for 100 GeV protons, N_B is the number of bunches per beam, N is the number of protons per bunch or the beam intensity and ϵ is the beam emittance. Given the conditions of our experiment: $\mu = 78.4$ kHz, $\beta^* = 22$ m, $\beta\gamma = 106.8$, $N_B = 64$ colliding bunch pairs, $N = 5{\cdot}10^{10}$ protons/bunch, $\epsilon = 15\pi$ mm mrad, therefore we get for the luminosity of our run is $L = 1.9 \times 10^{29}\ cm^{-2}s^{-1}$.

TABLE 8. Polarization Values and Errors during Run09

Stores	Blue Beam	Error	Yellow Beam	Error
	P_b	(stat. + syst.)	P_y	(stat. + syst.)
11020	0.6234	0.0516	0.6211	0.0712
11026	0.5477	0.0511	0.5900	0.0484
11030	0.6199	0.0531	0.6438	0.0508
11032	0.6186	0.0540	0.6178	0.0480

TABLE 9. Sum and Difference of Polarization Values and Errors during Run09

Stores	Sum	Difference	Error
	$P_b + P_y$	P_b - P_y	(stat. + syst.)
11020	1.2445	0.0023	0.0879
11026	1.1377	-0.0423	0.0703
11030	1.2637	-0.0239	0.0735
11032	1.2364	0.0008	0.0722

Beam Polarization

The beam polarization values for Run09 run can be found in [135] and [136]. The polarization values and errors (including statistical and systematic), for the Blue and Yellow beams and for each RHIC store/fill during Run09 are given in Table 8. The sum and difference of the polarization values of the two beams P_b and P_y are given in Table 9. The statistical and systematic errors for each beam and for the individual stores are added in quadrature.

The overall luminosity weighed average polarization values for the 4 RHIC stores during Run09 (sum, difference of P_b and P_y and the respective errors) were calculated as:

$$\left\langle P_b + P_y \right\rangle = \frac{\Sigma(P_b + P_y) \times L_i}{\Sigma L_i} = 1.224, \tag{154}$$

$$\delta^2_{P_b+P_y}(stat. + syst.) = \frac{\Sigma\delta_i^2(P_b + P_y) \times L_i^2}{(\Sigma L_i)^2} = 0.0383, \tag{155}$$

$$\left\langle P_b - P_y \right\rangle = \frac{\Sigma(P_b - P_y) \times L_i}{\Sigma L_i} = -0.0157, \tag{156}$$

$$\delta^2_{P_b-P_y}(stat. + syst.) = \frac{\Sigma\delta_i^2(P_b - P_y) \times L_i^2}{(\Sigma L_i)^2} = 0.0383, \tag{157}$$

where L_i is the luminosity for each store i.

In addition to the above mentioned statistical and systematic errors of the polarization values, there was a global error in the measurement of the polarization, $\delta_{P_b+P_y}(\text{global})/\langle P_b + P_y\rangle = 4.4\%$. After adding the global polarization error, the total polarization error $\delta_{P_b+P_y}(\text{total})/\langle P_b + P_y\rangle = 5.4\%$.

5.2 TRANSPORT MATRIX

In order to describe the transport of beam particles in a beamline, first each beam particle is represented by a 6-component phase-space vector, such as $X = (x, x', y, y', E, 1)$, where (x, x') are the horizontal and (y, y') are the vertical coordinates and angles, respectively; E is the particle energy and the sixth component is a factor used to add an angular kick on the particle momentum direction. Each optical element in the beamline (dipole or quadrupole magnet, drift space etc.), is represented by a transport matrix. Refer to Ref. [132] and [131] for definitions of the transport matrices of different optical elements used in particle accelerators. The beamline from one point to another along the z axis (or as commonly used in accelerator physics along s, where s = 0 is at the interaction point), can be modeled as a single transport matrix acting on each particle phase space vector, assuming there are no intra-beam interactions. The single transport matrix is the multiplication of the transport matrices of each optical element which make up a particular segment along the beamline or the whole beamline. In general, for n optical elements in the

beamline, the propagation of a single particle through the beamline is the *rotation* of the phase space vector by n transport matrices as given in Eq. (158).

$$X(s) = \underbrace{M_1 M_2 ... M_n}_{M_{beam-line}} X(0). \tag{158}$$

The whole beamline can be represented by the multiplication of each transport matrix, where $M_{beam-line}$ is the product of the multiplication.

The full, 6×6 matrix of the particle transport can be decomposed into blocks as given in Eq. (159).

$$M_{units} = \begin{pmatrix} A & A & 0 & 0 & D & K \\ A & A & 0 & 0 & D & K \\ 0 & 0 & B & B & 0 & K \\ 0 & 0 & B & B & 0 & K \\ 0 & 0 & 0 & 0 & 1 & 0 \\ 0 & 0 & 0 & 0 & 0 & 1 \end{pmatrix},$$

$$= \begin{pmatrix} 1 & \text{m} & 1 & \text{m} & \text{m/GeV} & 1 \\ 1/\text{m} & 1 & 1/\text{m} & 1 & 1/\text{GeV} & 1 \\ 1 & \text{m} & 1 & \text{m} & \text{m/GeV} & 1 \\ 1/\text{m} & 1 & 1/\text{m} & 1 & 1/\text{GeV} & 1 \\ \text{GeV/m} & \text{GeV} & \text{GeV/m} & \text{GeV} & 1 & 1 \\ 1 & 1 & 1 & 1 & 1 & 1 \end{pmatrix}, \tag{159}$$

where A and B blocks (2×2 matrices) refer to the action (focusing, defocusing, drift) on horizontal and vertical coordinates and angles of particles, respectively; D terms reflect the dispersion effects of the dipole magnets on off-momentum particles and K factors are the angular action of kickers. The diagonal terms are equal to 0 in this description of the full transport matrix.

The full 6×6 transport matrix calculated for the special running conditions during Run09 is given below:

Blue Transfer Matrices:

"RP" at 55.49553423					
-0.09132371863	25.25660678	-0.003407342595	0.07645145495	0	-0.083472914
-0.03964361056	0.01373531561	-0.0001382548495	0.00566210853	0	0.004625655462
-0.003294203268	-0.1001110115	0.1043509155	24.75980174	0	0.002785759922
0.0001857690455	0.008293503463	-0.04305702299	-0.6331964563	0	-3.340383325e-05
0.003732007221	-0.1179551283	-8.915908038e-05	-0.00176313181	1	0.007538433453
0	0	0	0	0	1
"RP" at 58.49552823					
-0.2102543124	25.29781264	-0.003822106314	0.09343774656	0	-0.06970129271
-0.03964361056	0.01373531561	-0.0001382548495	0.00566210853	0	0.004625655462
-0.002736897246	-0.07523055083	-0.02481989511	22.86021617	0	0.002950183901
0.0001857690455	0.008293503463	-0.04305702299	-0.6331964563	0	-3.340383325e-05
0.003736231542	-0.1179543801	-0.000100538927	-0.001931294249	1	0.007800908246
0	0	0	0	0	1

Yellow Transfer Matrices:

"RP" at 55.49553525					
-0.09038891985	25.30270237	-0.0001006373282	-0.1086595919	0	0.08506090227
-0.03957787452	0.01587988506	7.33399047e-05	-0.002158444287	0	-0.00457448534
0.0001727273093	0.05167789227	0.1061795437	24.80043304	0	-9.877115174e-05
-0.000169938049	-0.003448997213	-0.04302630665	-0.6317527953	0	-1.662777594e-05
-0.003779992848	0.1170987983	1.179328201e-05	-0.0002058859334	1	0.00753116186
0	0	0	0	0	1
"RP" at 58.49552925					
-0.2091223059	25.35034193	0.0001193819458	-0.1151349118	0	0.07150878975
-0.03957787452	0.01587988506	7.33399047e-05	-0.002158444287	0	-0.00457448534
-0.0003370858179	0.04133092133	-0.0228991181	22.90517845	0	-0.0001783223269
-0.000169938049	-0.003448997213	-0.04302630665	-0.6317527953	0	-1.662777594e-05
-0.003786768132	0.1171016211	1.30823485e-05	-0.000187512901	1	0.007793349465
0	0	0	0	0	1

Notice that in reality the diagonal terms are not equal to zero, however, they are small.

5.3 OVERVIEW OF THE COLLECTED DATA SAMPLE

The following graphs show the total number of elastic triggers collected during the four days of data taking from June 30 - July 4, 2009, (see Fig. 50). The pattern in the graph resembles an inclined ladder with four steps, which correspond to the four RHIC stores and the time between the stores, when the data taking was stopped. The graph in Fig. 51 shows the number of elastic triggers taken with RPs inserted at different distances, as close as $\sim$ 6 mm to the beam center.

The total number of triggers ($N^{tot}_{triggers}$) is $\sim$72 M triggers, recorded at a rate of

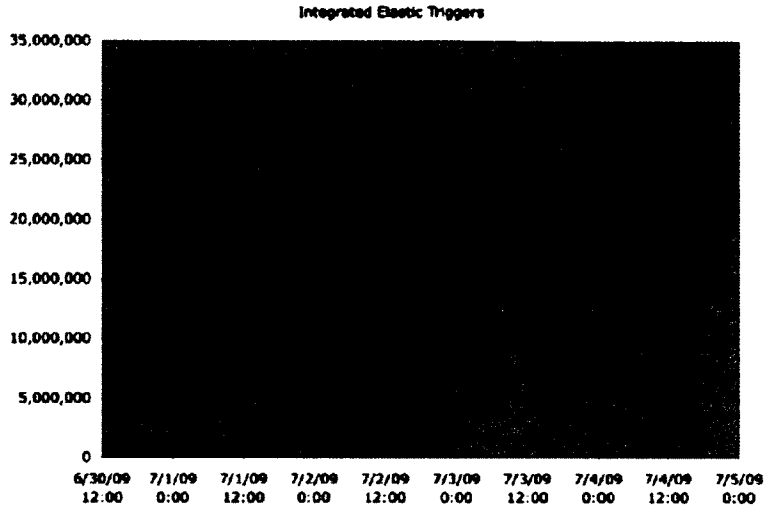

FIG. 50. Integrated number of elastic triggers during Run09. The steps in the graph correspond to the time between the four RHIC stores/fills during Run09, when there was no beam circulating at RHIC and data taking was stopped. Figure courtesy of S. Bültmann.

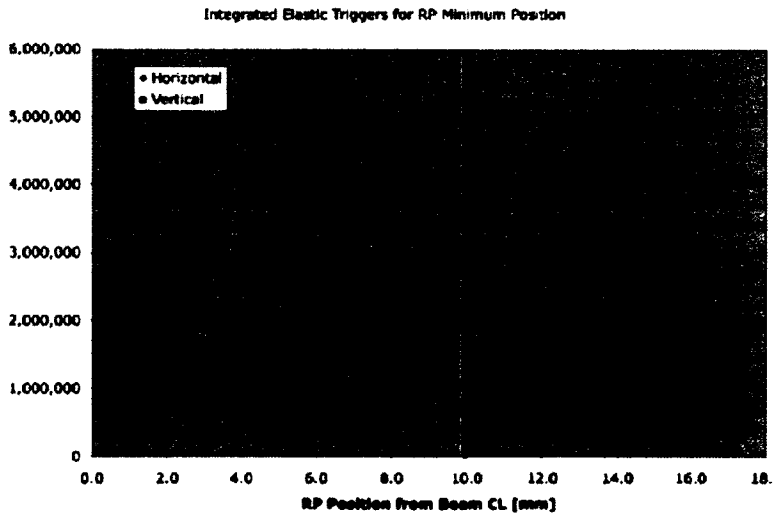

FIG. 51. Integrated number of elastic triggers for RP minimum position, during Run09. Figure courtesy of S. Bültmann.

~660 Hz and during a total period of 34 hrs and 50 min. Among these, the total number of elastic triggers ($N^{el}_{triggers}$) is ~33 M, about 46% of $N^{tot}_{triggers}$. The elastic trigger rate was ~350 Hz.

5.4 ACCEPTANCE DURING RUN09

We have studied the acceptance of the RP system, for each RP position during Run09, using the simulator program HECTOR (as described in Chapter 4). The acceptance for all RP positions (see Appendix D) is given in [137]. Fig. 52(a) and 52(b) shows the minimum-t reached by the silicon detectors for all RP positions during Run09, based on vertical and horizontal RP positions, respectively. The minimum-t is calculated from the minimum distance of approach of the detector to the beam (d_{min}) such as:

$$|t_{min}| = p^2\theta^2 \approx p^2 \left(\frac{d_{min}}{25\,\mathrm{m}}\right)^2, \tag{160}$$

where 25 m is the approximate value of one of the transport matrix element, the magnification of the scattering angle, also referred to as the effective length or L_{eff} (see the transport matrix in Section 5.2). As explained also in Chapter 4, d_{min} depends on the beam size at the detection point, such as: $d_{min} = k\sigma_D + d_0$, where d_0 is the dead-space between the bottom of RP and the first silicon strip. d_0 is usually taken to be 1.8 mm, and is included in the calculation of the minimum-t. It should be mentioned that, what is shown in Fig. 52(a) and Fig. 52(b) is an estimate. Analysis of elastic events (Chapter 6), will give exact information of the minimum-t reached during Run09. Fig. 52(c) and 52(d) show the geometrical acceptance and acceptance as a function of t, for RP Position 2 during Run09. The ellipses shown in Fig. 52(c), indicate the min-, max-t values and scattering angles reached during the run set in Run09 RP Position 2.

5.5 ALIGNMENT OF THE SILICON DETECTORS

Precise knowledge of the alignment of the detectors is required in this experiment. The preliminary alignment was done by surveying the detector package in the lab after being assembled. The detector packages were surveyed again in their installed position in the RHIC tunnel at the end of 2009 RHIC run. The final alignment (Local Alignment) was done by using elastic events in the overlapping regions of the

horizontal and vertical RPs. However, this was followed by a study (Global Alignment) based on the collinearity of the elastic events and Monte-Carlo simulations of the acceptance boundaries. The acceptance boundaries of the detectors are limited by the apertures of the quadrupole magnets positioned in front of the RPs in the outgoing RHIC rings. The study of the acceptance boundaries was used to further constrain the geometry and to finalize the alignment of the silicon detectors.

When the detector packages are installed in the RP, they are sled inside the RP by using two rails and fixed in place by screws. The rails inside the RP, on which the detector packages slide in, define the plane perpendicular to the beam pipe central axis. The position of the detectors inside the RP may be slightly tilted in the $x - y$ plane. The survey of the detector packages in the actual setup enabled us to measure the angle of tilt of the detectors in the $x - y$ plane. The information provided by the survey of the detector packages, both in the lab and in the actual setup during the experiment, was used to calculate the position of the 1^{st} silicon strip/channel in each Si detector plane, relative to the RHIC beamline center. The position of the 1^{st} silicon strip relative to the beamline center in the actual setup during the run, is needed to translate the measured coordinate of the scattered particles at the detection point from silicon strip/channel# notation to $x - y$ coordinates relative to the beamline center.

5.5.1 SURVEY ALIGNMENT

All the detector packages were surveyed in the lab (table-top setup) in 2003. Two detector packages, A-1 (installed in RPEVU) and A-2 (installed in RPWHO), were reassembled in March 2009 before installation in the RHIC tunnel. After completion of RHIC 2009 run, all the detector packages were surveyed in the actual setup in the RHIC tunnel and also resurveyed in the lab setup to also correct for the survey of the two packages that were reassembled before the run.

Initial Survey of the Detectors in the Lab Setup

Figure 53 shows a detector package being surveyed in the lab (table-top setup). The table-top survey of the detectors performed in the lab provides information on the positions of the two survey points on the package (the tooling balls), with respect to a previously established reference point on the package, shown by the centering pin in Fig. 53. Refer to [138] for a detailed explanation on the steps followed during

the initial survey of the detectors in the lab. Four cross points on each corner of the silicon detector plane were made by lithography on the silicon during manufacturing. The positions of these four points with respect to the strips are known precisely and their distances to the centering pin were measured for each detector plane before assembly. These measurements provide the positions of the 1^{st} silicon strip/channel on each plane with respect to the centering pin. By combining these measurements with the positions of the tooling balls with respect to the centering pin on each detector package, we can calculate the positions of the tooling balls with respect to the 1^{st} silicon strip/channel on each plane.

Survey of the Detectors in the RHIC tunnel

The survey of the detector packages in the actual setup in the RHIC tunnel was performed in August 2009, after the run. During the survey, the RHIC or local coordinate system was used. The RHIC coordinate system is defined as follows:

- **East of STAR or 5 o'clock (Yellow Beam)**
  - Negative "X" is away from the center of RHIC
  - Positive "Y" is up
  - "Z" origin is the insertion point for O05Q03 (the marker which defines the center of the 3^{rd} quadrupole magnet downstream of IP6 at RHIC and towards East, Q03, located $\sim$ 34.780 m away from IP6) and positive "Z" is towards O05Q04 (the marker which defines the center of the 4^{th} quadrupole magnet downstream of IP6 at RHIC and towards East, Q04, located after Q03 when looking away from IP6 and towards East)
- **West of STAR or 6 o'clock (Blue Beam)**
  - Negative "X" is towards the center of RHIC
  - Positive "Y" is up
  - "Z" origin is the insertion point for O06Q03 (the marker which defines the center of the 3^{rd} quadrupole magnet downstream of IP6 at RHIC and towards West, Q03, located $\sim$ 34.780 m away from IP6 at RHIC) and positive "Z" is towards O06Q04 (the marker which defines the center of the 4^{th} quadrupole magnet downstream of IP6 at RHIC and towards West,

Q04, located after after Q03 when looking away from IP6 and towards West)

During the survey, the Roman pots were positioned at their fully retracted position ($\sim$ 70 mm) and then moved to 16 different positions relative to the beamline center from their fully retracted position. Measurements of the positions of the tooling balls in each RP were performed at each RP position. The RP displacement was measured by using a position measuring device, Linear Variable Differential Transformer (LVDT). We will use this notation "LVDT position" to refer to the RP position relative to the beamline center. The LVDT positions during the survey were chosen to be close, but not exactly the same, to the LVDT positions of the RPs during the run. The two furthest LVDT positions during survey were $\sim$ 70 mm and the next 15 LVDT positions varied from $\sim$ 20 mm to as close as $\sim$ 6 mm from the beamline center. Thus, in order to eliminate any possible small change in position of the RP when moved to different LVDT positions, the survey information for the two furthest LVDT positions was not used because of the large difference ($\sim$50 mm) between these positions and the other 15 LVDT positions. Another reason of the exclusion of the two furthest LVDT positions during survey is to use survey LVDT positions that are closer to the LVDT positions of the RPs during the run.

The coordinates of the tooling balls relative to the beamline center were measured at a precision of 30 μm. The survey in the actual setup provides (x, y, z) coordinates of the tooling balls on each detector package relative to the beamline center for 15 different RP positions (LVDT positions).

Angles of Tilt of the Detector Packages in $x - y$ Plane

The survey information in the actual setup was first used to calculate the angles of tilt of the detector packages in the $x - y$ plane, as positioned inside the RP during the run. The sign convention for the tilt angle, for an observer looking away from the IP and towards the 1^{st} silicon detector plane is *positive for clockwise* and *negative for counter-clockwise.* Initially the tilt angle of all the detector packages is calculated when the RP is at the fully retracted LVDT position. Refer to [138] for a detailed explanation on this calculation. Then, the same calculation was repeated for the other RP positions. Since the orientation of the detector package inside the RP does not change when the RP is moved (up-down) or (left-right) to a different LVDT

position, it is expected that the tilt angle of the detector package in the $x-y$ plane remains constant for different LVDT positions. After calculation of the tilt angles of each detector package for all the LVDT positions during survey, it was observed that the standard deviation between the measurements of the tilt angle of the same detector package for different LVDT positions was small, in the order of $\sim 10^{-5}$ [138]. The final calculated tilt angle of the detector package is the average of the angles calculated for each LVDT position:

$$\alpha_{tilt}^{package}(in\ the\ x-y\ plane) = \frac{\sum_i \alpha_{tilt}^{package}(i)}{\sum_i (i)}, \tag{161}$$

where i = LVDT-position.

Each detector plane can be slightly tilted relative to the package itself in the $x-y$ plane. This angle is also added to the calculated tilt angle of the detector package. Thus, for each detector package and plane:

$$\alpha_{tilt}^{plane}(in\ the\ x-y\ plane) = \alpha_{tilt}^{package}(in\ the\ x-y\ plane) + \beta_{tilt}^{plane}, \tag{162}$$

where β_{tilt}^{plane} is the tilt angle of each detector plane relative the the detector package in the $x-y$ plane. Since each plane in the same detector package may be tilted slightly differently relative to the package, the final calculated tilt angle for each of the four planes in one package is slightly different. Table 10 gives a summary of the final calculated tilt angles of all the detector planes.

1^{st} Silicon Strip/Channel Position Calculation

By combining the information provided by the survey performed in the actual setup, (*position of the tooling balls relative to the beamline center*) and the tabletop setup (*position of the tooling balls relative to the* 1^{st} *silicon strip*), we can calculate the position of the 1^{st} silicon strip/channel in each detector plane relative to the beamline center. The angle of tilt of the planes is taken into account in the calculation of the 1^{st} Si strip position, to include the tilt/rotation of the silicon strips in the $x-y$ plane.

The SVX readout chips in each detector plane are labeled 0 - 5 for $x-view$ and 0 - 3 for $y-view$ detectors. *Definition of the* 1^{st} *Si strip/channel:* The 1^{st} Si strip/channel in each detector plane is the 1^{st} Si strip connected to SVX0 in each detector plane. We will use (x_0, y_0) notation to refer to the (x, y) coordinates of the

TABLE 10. Calculated final tilt angle for all detector planes in the $x - y$ plane.

	Plane A Tilt Angle (mrad)	Plane B Tilt Angle (mrad)	Plane C Tilt Angle (mrad)	Plane D Tilt Angle (mrad)
RPEHI	1.803	1.803	1.903	1.903
RPEHO	-0.659	-0.659	-0.759	-0.659
RPEVU	0.366	0.566	0.466	0.466
RPEVD	-2.041	-2.041	-2.041	-2.041
RPWHI	-0.896	-0.996	-0.896	-0.796
RPWHO	0.607	0.507	0.507	0.607
RPWVD	1.320	1.420	1.420	1.220
RPWVU	-2.472	-2.472	-2.472	-2.572

opposite edge (edge closer to the beam) of the 1^{st} Si strip connected to SVX0 (see Fig. 38).

Firstly, the positions of the 1^{st} strip in each plane, relative to the beamline center (either x_0 or y_0 depending on the coordinate measured by each plane), (see Table 6), were calculated for the furthest LVDT position. Refer to [138] for an example and a detailed explanation on this calculation. Then, the same calculation was repeated for the other LVDT positions during survey. The two furthest LVDT positions were again excluded from this calculation, since they differ from the other survey LVDT positions and the LVDT positions during the run by ~50 mm. The final calculated positions, x_0 (y_0) of the edge of the 1^{st} silicon strip connected to SVX0 in each detector plane is the average of all the x_0 (y_0) calculated for each RP position during survey, (see Eq. (163)).

$$x_0(y_0)(1^{st}\ Si\ strip) = \frac{\sum_i x_0(y_0)(i)}{\sum_i (i)}, \tag{163}$$

where i = LVDT-position.

For planes A and C in each detector package, the calculated y_0 for vertical RPs and x_0 for horizontal RPs was compared to the LVDT position of the RP during survey. The plot in Fig. 54 (a) shows the linear relation between the calculated x_0 for RPEHI plane-A and the LVDT position of RPEHI during survey. This relation is needed to get the 1^{st} silicon strip positions during the run, knowing the LVDT positions of the Roman pots during the run. For planes B and D in each detector package, the calculated x_0 for vertical RPs and y_0 for horizontal RPs is the same for all the RP positions during survey. This measurement will be used directly to refer to the x_0 (vertical RPs) and y_0 (horizontal RPs) of the 1^{st} silicon strip in a particular Roman pot during the run. The plot in Fig. 54 (b) shows the calculated y_0 for RPEHI (detector package A3) plane-B and for 13 different RP positions of RPEHI during survey.

The calculated positions x_0 (y_0) of the 1^{st} silicon strip in all the detector planes and their relation with the LVDT positions of the RPs are given in Table 11. For planes A & C, one can use the given linear relation between the calculated x_0 (y_0) and the LVDT position for each run# during Run09 to get the x_0 (y_0) of the 1^{st} silicon strip during the run. For planes B & D, the calculated x_0 (y_0) is the same for all the runs.

TABLE 11. Calculated 1^{st} silicon strip/channel positions x_0 (y_0) in each detector plane during Run09. For planes A & C, one can use the given relation between the calculated x_0 (y_0) and the LVDT position for each run# during Run09 to get x_0 (y_0) of the 1^{st} silicon strip during the run. For planes B & D, the calculated x_0 (y_0) is the same for all the runs.

Roman Pot	Plane A (mm)	Plane B (mm)
RPEHI	x_0 = (1.001*LVDT + 1.619)*(-1)	y_0 = -39.287
RPEHO	x_0 = 1.016*LVDT + 3.096	y_0 = 39.635
RPEVU	y_0 = 1.013*LVDT + 2.645	x_0 = -39.017
RPEVD	y_0 = (1.001*LVDT + 2.076)*(-1)	x_0 = 40.745
RPWHI	x_0 = (0.992*LVDT + 1.885)*(-1)	y_0 = 39.188
RPWHO	x_0 = 0.997*LVDT + 2.993	y_0 = -38.621
RPWVD	y_0 = (1.005*LVDT + 2.178)*(-1)	x_0 = -40.530
RPWVU	y_0 = 0.989*LVDT + 3.733	x_0 = 40.064
Roman Pot	Plane C (mm)	Plane D (mm)
RPEHI	x_0 = (1.001*LVDT + 1.638)*(-1)	y_0 = -39.323
RPEHO	x_0 = 1.016*LVDT + 3.096	y_0 = 39.635
RPEVU	y_0 = 1.013*LVDT + 2.670	x_0 = -38.989
RPEVD	y_0 = (1.001*LVDT + 2.080)*(-1)	x_0 = 40.742
RPWHI	x_0 = (0.992*LVDT + 1.887)*(-1)	y_0 = 39.250
RPWHO	x_0 = (0.997*LVDT + 2.976)	y_0 = -38.651
RPWVD	y_0 = (1.005*LVDT + 2.197)*(-1)	x_0 = -40.470
RPWVU	y_0 = 0.989*LVDT + 3.735	x_0 = 40.030

The LVDT positions of each RP during RHIC 2009 run, given in Appendix D, were used together with the equations given in Table 11, to get the positions x_0 (y_0) coordinates of the 1^{st} silicon strip in all the detector planes during the run. The 1^{st} silicon strip positions for each RP position that correspond to only physics runs are given in Appendix E.

In this section, the survey and the initial alignment of the silicon detectors was explained. The maximum measured tilt angle is ~2 mrad and each detector plane in the same detector package has a slightly different tilt angle. Given the dimensions of the detector plane (area covered by the Si strips) to be 79 × 48 mm, the difference in the $x(y)$ coordinates between the two edges of the same Si strip is ~ 158 μm and 96 μm, respectively. Considering that the strip pitch of the Si detectors is 97.4 μm for $x - view$ detectors and 105 μm for y-view detectors, the impact of the tilt angle on the change in coordinates $x(y)$ is on the order of or slightly bigger (by ~53 μm) than the strip pitch. To summarize, the preliminary alignment involved using the survey information to calculate the position of the 1^{st} silicon strip/channel in each Si detector plane, relative to the beamline center for the RP positions during the run. This is needed to translate the measured coordinates of the scattered particle at the detection point, from silicon strip/channel# to positions (x, y) with respect to the beamline center.

5.5.2 LOCAL ALIGNMENT

Corrections were introduced to the survey alignment by a study carried out by I. Alekseev *et al.* at ITEP. The study [139], made use of the selected elastic events which fall in the overlapping regions between the vertical and horizontal RPs (see Fig. 43 for an example), to understand the relative alignment between vertical and horizontal detectors. The study is described in details in [139]. The survey alignment, explained in the previous section, provides knowledge of the 1^{st} silicon strip position (x and y coordinates) with respect to the center of the beampipe, assuming the beam itself is centered with respect to the center of the beampipe and that the beam crossing angle at the IP is zero. However, the position of the beam at the detection point may be shifted from the center and the beam crossing angle at IP may be non-zero. These factors contribute to the uncertainties in the alignment of the silicon detectors, which is crucial in this experiment.

The purpose of the ITEP group study is to use the elastically scattered proton tracks detected in the overlapping regions of the detectors to find constraints on the alignment of the silicon detectors relative to each other, and also to use selected elastic events to understand the overall/global alignment of the detectors. Elastic events are characterized by the collinearity condition, requiring a simultaneous hit of the scattered proton on a collinear pair of detectors positioned on opposite sides of the interaction region, i.e. East and West of the STAR IP. The selection process for elastic events will be discussed in Chapter 6.

The study of relative/local alignment by I. Alekseev *et al.*, is based on the fact that there are four overlapping regions between RPs in each side of the IP (eight in total), with silicon detectors measuring x and y coordinates of the scattered protons. Therefore, in terms of relative alignment, there are 16 unknown shifts between the detectors (8-x and 8-y shifts) [139]. By looking at the differences of the x and y coordinates of the protons in the detectors in one of the overlapping regions, for example (RPEVU - RPEHI), we can form two equations, such as: $\delta x = x_{EVU}$ - x_{EHI} and $\delta y = y_{EVU}$ - y_{EHI}. For 8 overlapping regions (4 on each side of the IP, see Fig. 43), we then have 16 equations in total, four equations for each side of the IP and for each coordinate (x/y). Since we are measuring relative alignment, we assume that three out of four of these equations (for each side of the IP and for each coordinate) are independent, resulting in only two unknown shifts for each side of the IP, and thus four unknown shifts out of the initial 16. Using the collinearity of the elastic events, $\delta x = x_{East}$ - x_{West} and $\delta y = y_{East}$ - y_{West}, we are then left with only two unknowns, I. Alekseev *et al.* [139]. In the study, it is also assumed that the errors associated with the survey alignment, the survey errors of the positions measurements, are not correlated. A simplified (2×2) form of the transport matrix is used for the purposes of this study, taking into account the fact that the beam size at the IP is small and the transport matrix elements that magnify the beam size at the IP are also small (see Eq. (140)), these terms are neglected in the transport matrix equations, and only the relation between the coordinate at the RP and the angles at the IP is used. It is also assumed that the RPs were no tilted.

By using the relation between the coordinates at the RP and the angles at the IP, given by the transport equation in their simplified form, I. Alekseev *et al.* calculated the positions of the scattered protons (detected simultaneously in the overlapping regions between vertical and horizontal RPs) in the horizontal RP, projected from

TABLE 12. Local/Relative Alignment Corrections for the Survey Alignment in (mm) + corrections due to kicker magnets, also in (mm).

RP	Plane A	Plane B	Plane C	Plane D
EHI	-0.95	-0.75	-0.95	-0.75
EHO	-0.77	-0.15	-0.77	-0.15
EVU	-0.22	0.14	-0.22	0.14
EVD	-0.42	-1.51	-0.42	-1.51
WHI	-0.10	0.86	-0.10	0.86
WHO	-0.11	1.32	-0.11	1.32
WVD	1.90	-0.21	1.90	-0.21
WVU	1.77	-0.27	1.77	-0.27

their measured positions in the vertical RP, i.e. EVU-EHI overlapping region and x-coordinate, we have: $T^{EVU^{-1}} \cdot (x)^{EVU}_{measured} = (\theta_x)_{IP}$ and similarly, $T^{EHI} \cdot \theta_{IP} = x^{EHI}_{projected}$, and combining the two we obtain:

$$(x)^{H}_{projected} = T^{H} \cdot T^{V-1} \cdot (x)^{V}_{measured}, \tag{164}$$

which is similar for the y coordinate, resulting in x and y positions of the scattered protons in the horizontal RP station, calculated from their positions in the vertical RP station. The projected positions provided by this method are then compared to the measured positions in the horizontal RPs and differences are calculated: $\delta x_{shift} = x^{EHI}_{calculated} - x^{EHI}_{measured}$. This was done for every run during Run09, where Roman pots were moved to different positions. The set of shifts obtained in this way for each coordinate and side, are then forced to a minimization so that the average shift from the survey position is zero [139]. The precision of the method used is about 0.1 mm. This results in a set of corrections to the survey alignment, given in Table 12 [139], (note: planes A and C measure x coordinates in horizontal RPs and planes B and D measure y coordinate, and vice-versa for vertical RPs).

Continuing the study, I. Alekseev *et al.* introduced another set of corrections after taking into account the effect of the kickers magnets on the protons trajectories. These corrections are also included in the corrections given in Table 12. By studying the differences in the measured angles of elastic events East and West of the IP, $\delta\theta_x$(East-West) and $\delta\theta_y$(East-West), a global/overall shift of 0.30 mm in x and -0.07

mm in y was calculated and it is applicable to all RPs [139].

5.5.3 GLOBAL ALIGNMENT

After introducing the corrections from the local alignment study, where corrections were calculated with respect to a common reference point in the East and another reference point in the West, the measured scattering angle difference distributions of selected elastic events $\delta\theta_x$(East-West) and $\delta\theta_y$(East-West) were examined and they were found to be non-zero [140]. Therefore, a final correction was applied to align the RP system with respect to the position of the un-scattered beam at the detection point, which is also referred to as $t = 0$ trajectory, refer to the global alignment study performed by W. Guryn [140]. As given by the transport matrix equations 140, the position at the detection point (x_D, y_D) depends on the position of the collision point (x_0, y_0) and on the proton's outgoing angle at the IP, where the latter includes the scattering angle (θ_x, θ_y) and the unknown beam crossing angle (θ_x^B, θ_y^B) [140]. To calculate the correction, W. Guryn studied the measured (x, y) distributions of elastic events at the RP and by observing the edges of the distributions, it was noticed that the distribution was not centered for the East RPs and a correction of x = 2.5 mm and y = -1.5 mm was necessary [140]. No correction was found for the West RPs.

All the above corrections, resulted from the local and global alignment studies, were added to the positions from the survey alignment and corrected positions were used in data analysis. The overall uncertainty of the alignment correction is estimated to be about 0.4 mm [140], which will be taken into account for the calculation of the systematic errors in the determination of t.

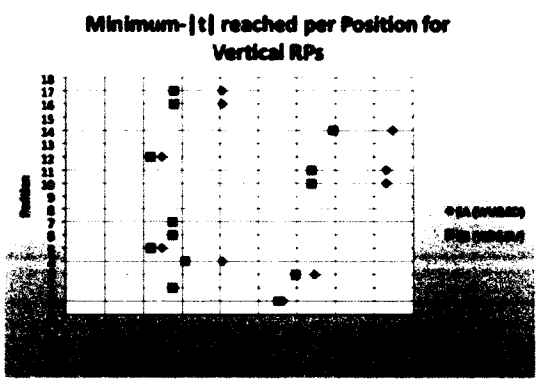

(a) Min.-t per RP position (Vertical RP's)

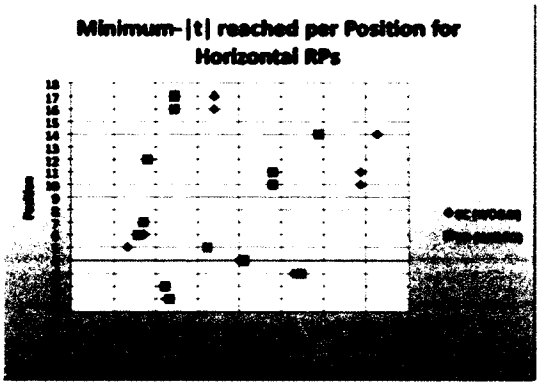

(b) Min.-t per RP position (Horizontal RP's)

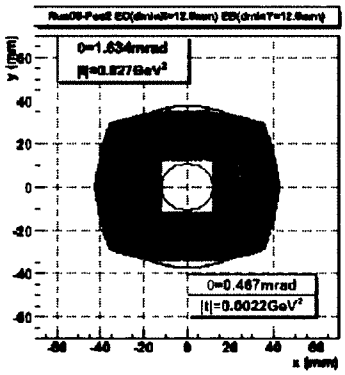

(c) y vs x in mm for RP Pos-2

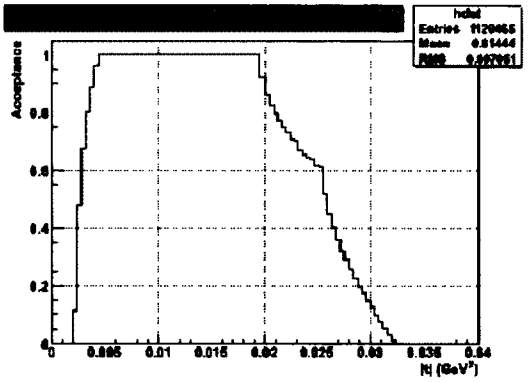

(d) Acceptance as a function of t for RP Pos-2

FIG. 52. Minimum-t reached by detectors in (a) Vertical RPs: West Up/Down and East Down/Up, EA and EB elastic arms, respectively; (b) Horizontal RPs: West Outer/Inner and East Inner/Outer, EC and ED elastic arms, respectively; for each RP position during Run09 (as given in Appendix D). Minimum-t was calculated from the minimum distance of approach of the RP to the center of the beam (+ the dead space from the bottom of RP to the silicon detector); (c) y vs x acceptance for RP Position 2 during Run09, min-t and max-t values and angles are indicated by ellipses; (d) Acceptance in t for RP Position 2 during Run09.

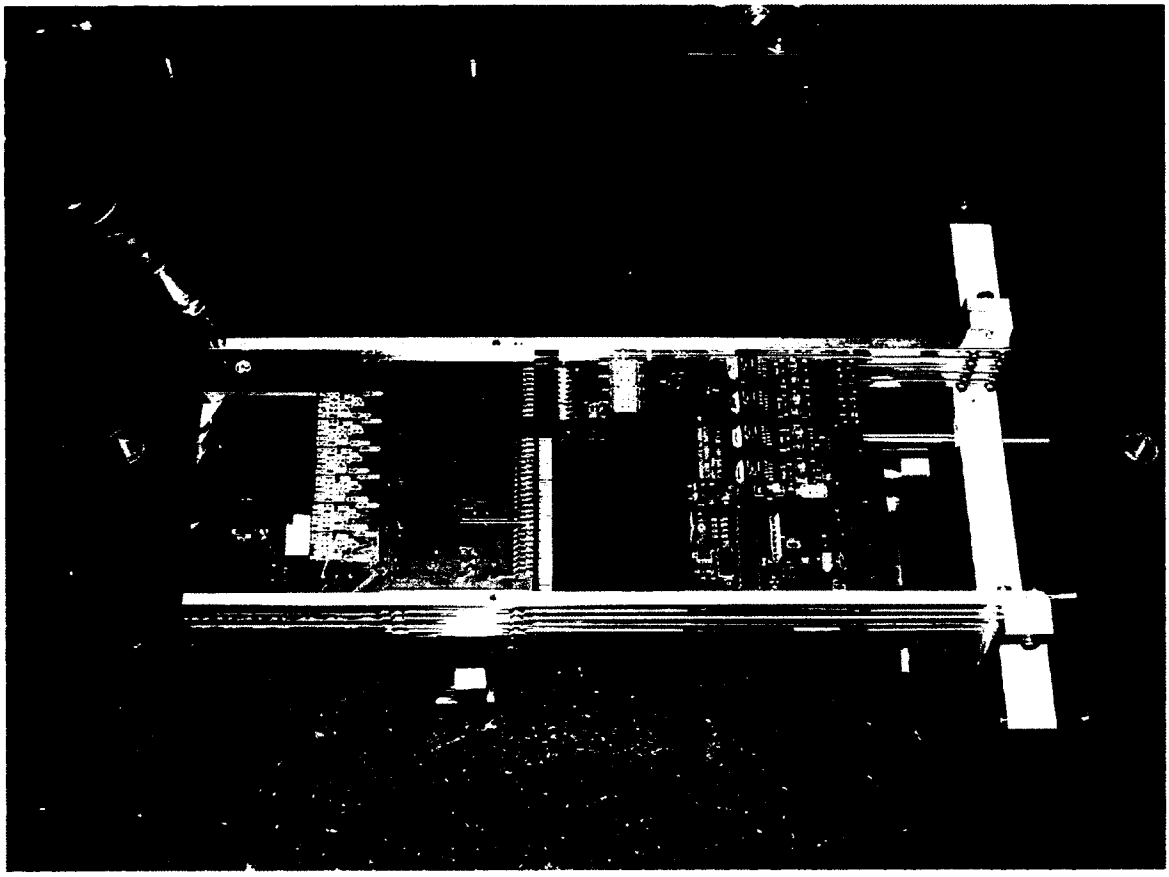

FIG. 53. A detector package being surveyed in the lab (table-top setup). The centering pin and reference point or point (0,0) on the detector package is shown (top-left corner). Two tooling balls, used as survey points during the survey of the detector package, are also shown (top and bottom right corners).

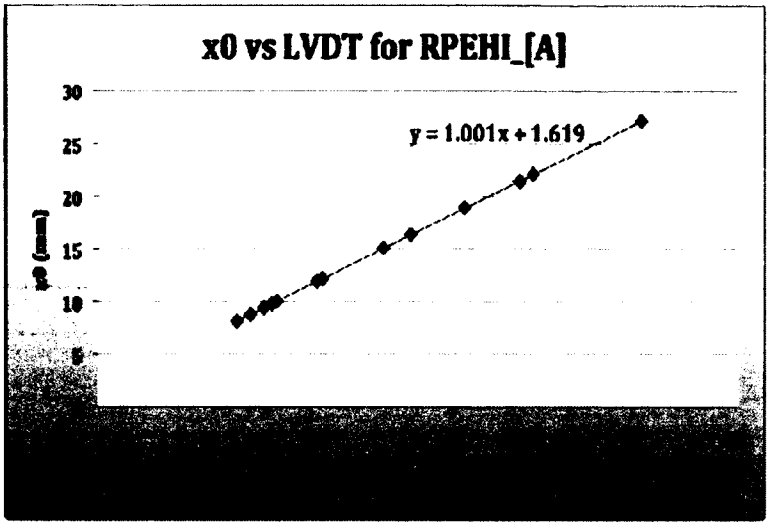

(a)

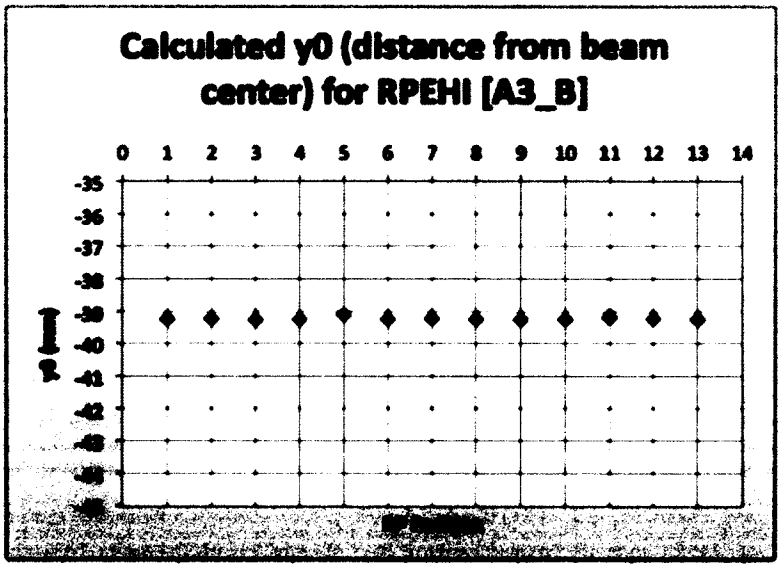

(b)

FIG. 54. (a) Calculated x_0 of the 1^{st} silicon strip in RPEHI plane-A vs the LVDT position of RPEHI during survey; (b) calculated y_0 of the 1^{st} silicon strip in RPEHI plane-B for 13 different RP positions during survey.

CHAPTER 6

DATA ANALYSIS

6.1 DATA SAMPLE

In the previous chapter, the data collection process and the conditions during Run09 are discussed. The conditions include the special setup of the RHIC accelerator (special beam optics with $\beta^* = 22$ m) and the beam conditions during Run09. The collected data contains information about both elastic and central production processes in pp scattering, (see Fig. 1 (a) and (c)). These scattering processes are distinguished by the triggering criteria that characterize each process. An elastic event requires two coincident proton hits in a collinear pair of detectors on both sides of the STAR IP. A central production event, however, requires the detection of a central mass in the central system of the STAR detector, as well as two proton hits in a pair of detectors on both sides of the IP. The triggering criteria for elastic events will be described in more details later in this chapter.

During Run09 we accumulated about 33 million elastic triggers with transversely polarized proton beams at $\sqrt{s} = 200$ GeV. The collected data are first stored in a raw data format in the STAR data storage system. All the runs taken during Run09 are listed in Appendix D. The Roman pots were positioned at different distances close to the beam and several runs were taken with the RPs at a certain RP position. There were 13 different RP positions during 4 RHIC stores. The physics runs (46 runs in total) can thus be grouped in 13 sets according to the RP position referred to as "Pos" in Appendix D. The 13 sets, also grouped in 4 main groups according to the RHIC store/fill they correspond to, are shown in Table 13.

The diversity of the RP positions provides an overall kinematic coverage in $|t|$, during the run of $0.003 \leq |t| \leq 0.035$ $(\mathrm{GeV}/c)^2$, which includes the CNI region, crucial for the measurement of the transverse single spin asymmetry A_N. After analyzing the scattered proton data sample, we obtain a data set of 20 million elastically scattered proton pairs or elastic events. In this chapter we will describe the analysis process in detail.

TABLE 13. Physics runs per RP position and RHIC store/fill during Run09

Store #	RP Position (see Appendix D)	Physics Run #
11020	1	10181085, 10181086, 10182001, 10182002, 10182004, 10182005, 10182006
	2	10182015, 10182016, 10182021, 10182025
11026	3	10183013, 10183014, 10183015, 10183016, 10183017
	4	10183018, 10183020, 10183021
	5	10183027, 10183028
	6	10183034
	7	10183035, 10183037, 10183038
11030	10	10184016, 10184017, 10184018, 10184019, 10184020, 10184021
	11	10184030, 10184031, 10184032, 10184033
11032	12	10185001, 10185002, 10185003
	14	10185004, 10185005, 10185006
	16	10185016
	17	10185018, 10185019, 10185020, 10185023

6.2 SELECTION OF ELASTIC EVENTS

To calculate the transverse single spin asymmetry in elastic scattering (A_N), the raw data first needs to pass through a selection process of elastic events. At the end of this selection process we obtain a sample of elastic events that can be used for further analysis and for the calculation of physics observables. In this section I am going to discuss in details the selection criteria and the cuts that were applied to the data sample, and, in general, the process that was followed during data analysis.

The raw data with particle hits in the detector system, was first converted to a standard format used in STAR, μDST format [141]. The raw data was processed into μDST format by using a package called *St_pp2pp_Maker*, written by K. Yip of Brookhaven National Laboratory [142]. This package has been included in the standard reconstruction chain in STAR. The following main steps are followed in order to select the sample of elastic events and to use this sample in the calculation of A_N:

1. Pre-selection of proton hits from the raw data. This step also includes reformatting the raw data into *StEvent* format, as required by the standard μDST format.

2. Selection of proton hits from the set of data stored in μDST format. This step also includes reformatting the data stored in μDST format into initial ROOT data files [127] and [128].

3. Selection of elastic events and track reconstruction from the data set stored in ROOT files.

4. Assigning kinematic parameters, momentum transfer squared-t and azimuthal angle ϕ to the selected elastic events.

5. Calculation of the raw asymmetries (various combinations).

6. Calculation of A_N.

7. Comparison of the measured A_N with the theoretical model.

The following terms need to be defined before continuing with the explanation of the selection criteria for proton hits and elastic events.

Definitions:

- **Hit**

  When a proton hits the silicon detector, it deposits energy while passing through the material with a thickness of 400 μm for each silicon detector plane, and charge is accumulated. The dE/dx of the proton hit passing through matter, can be calculated by the $Bethe - Bloch$ formula, an expression used for energy loss calculations of charged particles passing through matter [120]. Refer to Appendix F for the calculation of the energy loss of a proton which passes through a Si detector plane, where the parameters that describe the material through which the proton passes are the parameters of the detector system used in our experiment. After passing through the four silicon detector planes, the proton is detected by the scintillator and an event is triggered in case the respective scintillation counter on the other side of the IP also triggers. A triggered event produces an ADC (Analog to Digital Converter) signal read out in the silicon strips, which is digitized from the silicon strips by the SVXIIE chips. An SVXIIE chip is connected to 126 Si strips and there are 4(6) chips for $y - view(x - view)$ planes. The digitized signal for each strip/channel in a given Si detector plane is stored. A valid hit is defined as a recorded signal with energy deposited (ADC value) of at least 5 σ above the pedestal-per-channel value:

  Valid hit/Si strip with energy ADC $\geq$ Pedestal per strip/channel + $5\sigma_{pedestal}$

  Pedestals are charges collected by the connected capacitors in the SVXIIE readout chips. When we measure pedestals, we measure the channel readout when there is no trigger or signal. The electronic noise is defined as the RMS value of the ADC distribution. ADC value and distribution is a measure of the energy deposited in the silicon.

- **Cluster**

  An elastically scattered proton detected by the silicon detector may deposit its energy in several neighboring Si strips of the ***hit strip***. A cluster is a set

of consecutive strips with an ADC read out value above a certain threshold. Below, we will define three important parameters which we use to describe a cluster:

- **Cluster Length (L_{cls})** is the number of consecutive strips in a cluster. While analyzing the data it was decided that L_{cls} cannot be bigger than 5, so clusters with length > 5 are rejected. The reason for this cut will be explained later in this section.
- **Cluster Energy (E_{cls})**

  Energy value of a cluster is an ADC value required to be above a certain threshold, where the threshold depends on cluster size/length. A threshold depending on the cluster length is applied to the total charge of the cluster, while wider clusters are rejected. The energy threshold of clusters with different size/length was determined and can be found in Ref. [143].
- **Cluster Position (Pos_{cls})**

  The position of a cluster is the energy deposit weighted average of the position of each strip that make up the cluster:

$$\bar{x} = \frac{\sum x_i E_i}{\sum E_i}, \tag{165}$$

  where x_i is the strip position of cluster i and E_i is its ADC readout value.
- **Number of Clusters in one Si Detector Plane (N_{cls}^{plane})**

  It was observed that a detector plane can have multiple detected clusters per event. If the number of detected clusters is relatively big, this may indicate that the hit is not related to a real event. Thus, a cut is applied to the number of clusters detected in one plane, such as:

  max. number of clusters in one Si detector plane (N_{cls}^{plane}) ≤ 5.

- **Track**

At least one cluster detected in detector planes A/C or B/D in each RP form a track. Planes A(B) and C(D) measure the $y(x)$-position of clusters in vertical RPs and $x(y)$-position of clusters in horizontal RPs.

Cluster Matching

The position of the clusters measured in planes A(B) and C(D) is matched, meaning that the difference between the two clusters' positions, coming from

the same event, in the two silicon detector planes which measure the same coordinate, is required to be within a certain distance. This distance was decided to be not bigger than 2 *strip pitch*. So, for example, if $x_1(y_1)$ and $x_2(y_2)$ are the $x(y)$ positions measured in the two $x-view$ ($y-view$) planes, respectively, then the position difference of the detected clusters in these two planes, coming from the same event, is: $\Delta x = |x_1 - x_2| \leq 2 \cdot (105\ \mu\text{m})$ and $\Delta y = |y_1 - y_2| \leq 2 \cdot (97.4\ \mu\text{m})$. After matching the clusters in this way, an average value of the cluster position is calculated.

- **Elastic Event**

  Elastic trigger condition requires that a collinear pair of detectors on both sides of the IP are triggered simultaneously. An elastic event fulfills this trigger condition and the **Collinearity Condition** which will be discussed later. There are four collinear detector pairs in our system, which form four elastic arms, categorized in two groups according to the RP location:

  - Two Horizontal Arms:

    East Horizontal Inner (EHI) - West Horizontal Outer (WHO)
    East Horizontal Outer (EHO) - West Horizontal Inner (WHI)

  - Two Vertical Arms:

    East Vertical Up (EVU) - West Vertical Down (WVD)
    East Vertical Down (EVD) - West Vertical Up (WVU)

6.2.1 SILICON HIT SELECTION

STEP 1. Pre-selection of proton hits from the raw data

In the first step, the data go through an initial selection process. The signal measured in the readout system of the detectors is proportional to the energy deposited in the silicon due to a detected proton hit. So, firstly we look at the energy distributions of the proton hits. The measured energy distributions have to be differentiated from any possible electronic noise/background in the readout. For this, pedestal mean values and distributions for each Si strip/channel were identified while the detectors were tested. The pedestal value for each channel was stored into the calibration database under the name *pp2ppPedestal*. This information was used to

calibrate the detectors readout system and pre-select the proton hits from the raw data into μDST format.

STEP 2. Selection of proton hits from the set of data stored in μDST format

Conversion of the data from μDST format to initial ROOT files was done by a short analysis code, written by Ivan Koralt of Old Dominion University. The data stored in the initial ROOT files (pre-selected from μDST format) contains information on cluster level, after the clusters are selected with proper number of clusters per plane, cluster length and energy: $N_{cls}^{plane} \leq 5$; $L_{cls} \leq 5$ and $E_{cls} >$ ADC threshold based on L_{cls}.

Figure 55 (a) and (b) show the number of clusters detected in chain/plane A of the detector package installed in RPEHI and the overall number of clusters for run 10183028, respectively. The number of clusters detected in one plane is usually less than 5. The remaining number of events after excluding the planes with more than 5 clusters per event, resulted in an average fraction of 99.88% of all clusters in a plane [143].

Figure 56 (a) and (b) show the distribution of the length/size (# of strips) of clusters detected in plane A of EHI and the overall length of clusters for run 10183028, respectively. It is expected that the trajectories of particles scattered at small scattering angles are close to perpendicular to the silicon detector planes. This means that when a scattered proton hits the silicon plane, most probably it hits on one silicon strip (which has a width of 70 μm) or between two silicon strips, depositing its energy on at least one silicon strip. This limits the cluster size/length and thus the number of strips with measured deposited energy. Data shows that the widest clusters coming from real events with perpendicular trajectories are not wider than 4 strips and that clusters with size/length of 1 are the most common. Clusters with size 2 can happen if the particle hits between two silicon strips. Clusters of size 3 and bigger are suspicious and their origin is unclear. Various factors for the occurrence of these cases could be: (a) Si strips/channels may measure an image charge from the neighbor strip, in particular when the energy deposit is very large, or (b) the signal could be due to the detection of a delta ray which might have been produced in the scattering process. A delta ray can be defined as a recoil particle produced by secondary ionization. A delta ray can be characterized as a fast electron that is

produced after an energetic charged particle (proton in our case) interacts with the atoms of the material it is passing through.

Pedestal and Noise Analysis

Prior to installation of the detector packages in the RPs, all the silicon detector planes were tested in the lab. While testing, several hardware problems with the detectors were determined and fixed. In addition, a detailed pedestal and noise study was performed for all the detector planes prior to installation in the RPs. Pedestal distributions can also be used to represent the electronic noise/background. Thus, pedestal and noise study serves to determine the signal to noise ratio of a particular detector, which in turn is important for the calibration of the detector's readout system.

After installation of the detector packages in the RPs in the RHIC tunnel and also during Run09, we took several pedestal runs to test our detectors in the actual setup. To calibrate the SVXIIE readout for the hits in the silicon detector, we need to determine the mean value and the width ($\sigma_{pedestal}$) of the pedestal distribution. The pedestal distribution for a silicon strip/channel follows a Gaussian distribution.

The plots given in Fig. 57 show the pedestal distributions, pedestal mean values in Fig. 57 (a) and pedestal-σ in Fig. 57 (b), for a particular pedestal run during Run09. The four distributions represent the pedestals measured for each SVXIIE chip (126 Si strips/channels are wire bonded to each SVXIIE chip) in the four Si detector planes that make up a detector assembly, planes A and C (4 SVXIIE chips) and planes B and D (6 SVXIIE chips).

The main source of the noise measured in SVXIIE is the silicon micro-strip detector. What we measure is the total noise, which has two sources, the "*white noise*" σ_w and the "*common mode noise*" σ_k, [144] and [145]. The later, σ_k is the σ of the pedestal distribution for each SVXIIE chip. The common mode noise can be defined as [144]:

$$\sigma_k^2 = \sum_{i=1}^{N} a_{ik}^2/N - \left(\sum_{i=1}^{N} a_{ik}/N\right)^2, \tag{166}$$

where $a_{ik} = \sum_{j=1}^{126} \mathrm{ADC}_{ijk}/126$ and ADC_{ijk} is the number of ADC counts in SVX k, strip j and event i. a_{ik} is the average value of ADC counts for the strips in SVX k and event i and N is the number of events. The study of the channel noise and gain of the silicon detectors used in this experiment, which is given in [144], shows that

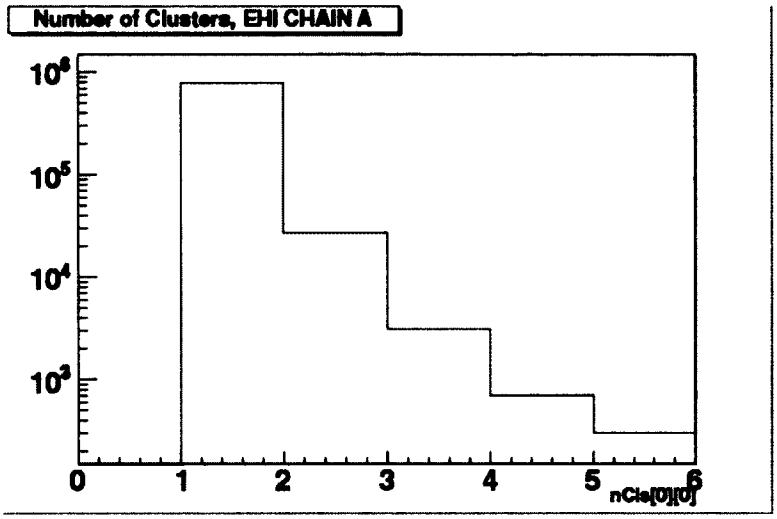

(a)

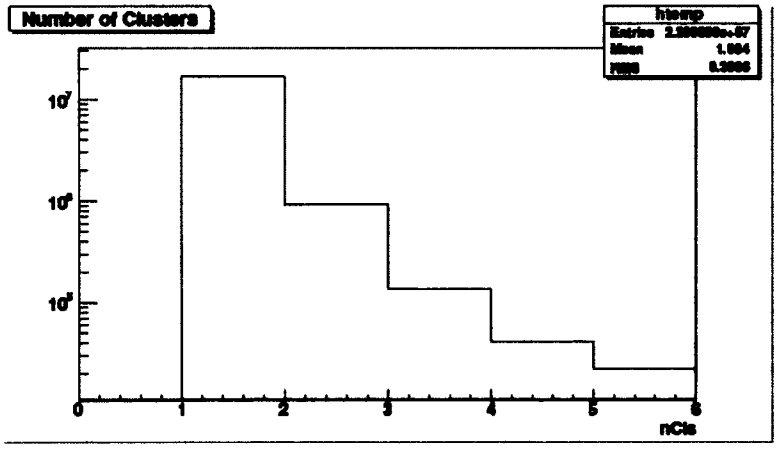

(b)

FIG. 55. Distribution of the number of clusters (defined as *nCls* on the plot): (a) detected in EHI plane A, for run 10183028 and (b) overall for run 10183028.

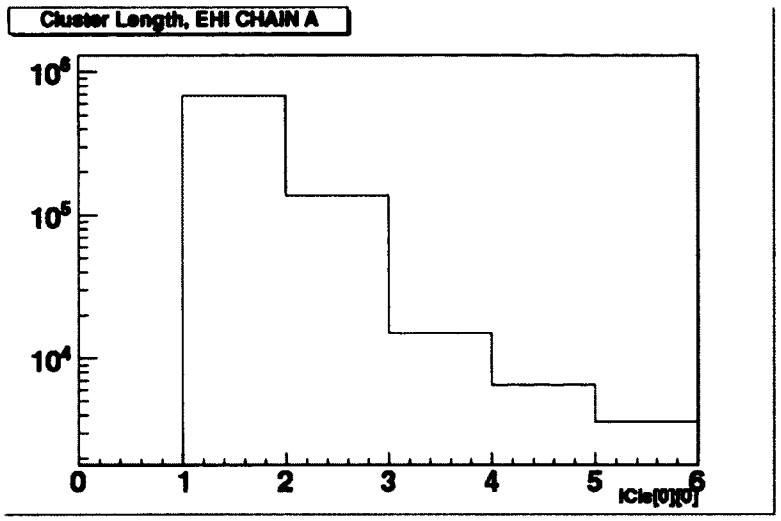

(a)

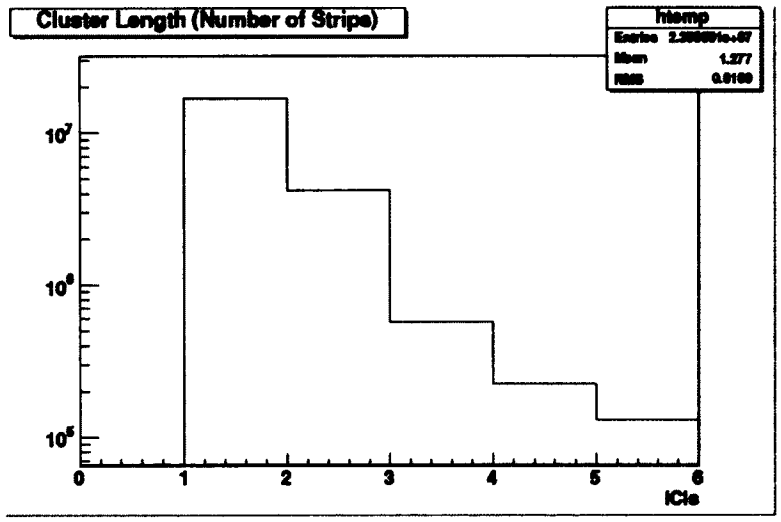

(b)

FIG. 56. Distribution of the size/length (# of strips) of clusters (defined as *lCls* on the plot): (a) detected in EHI plane A, for run 10183028 and (b) overall for run 10183028. Plots show that clusters of length = 1 are most common and the length does not exceed 5.

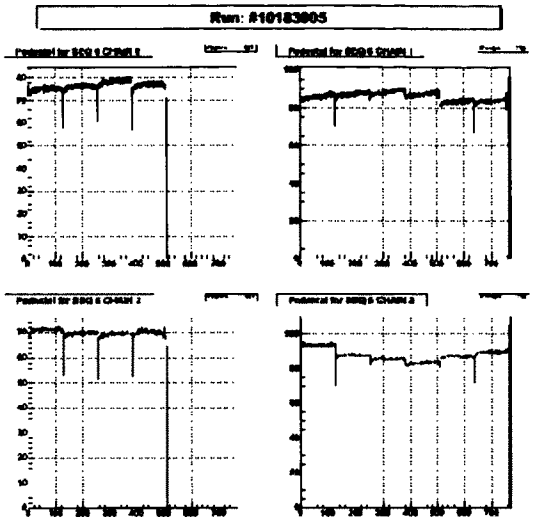

(a) Pedestal vs strip number

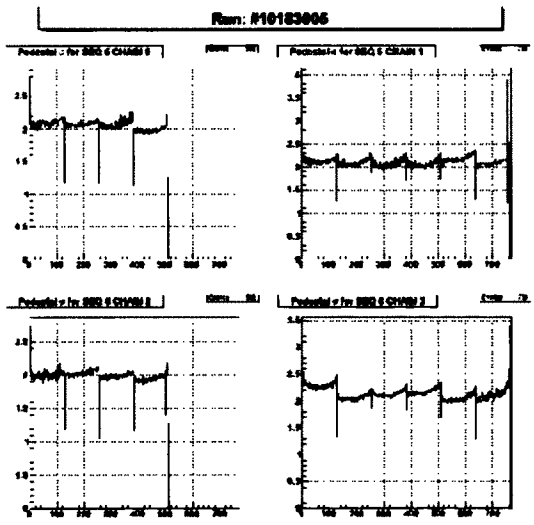

(b) Pedestal σ vs strip number

FIG. 57. (a) Pedestals and (b) pedestal-σ vs strip number for Si detector planes A: $y-view$ (4 SVXIIE chips), B: $x-view$ (6 SVXIIE chips), C: $y-view$ (4 SVXIIE chips), D: $x-view$ (6 SVXIIE chips) detectors, in the detector package connected to readout sequencer (SEQ 6), see Table 5, for run 10183005 during Run09. Plots courtesy of K. Yip.

the RMS value of the pedestal distribution for the one detector plane (4 or 6 SVX), is approximately equal to the RMS values for each of the pedestal distributions of each SVX. This indicates that the common mode noise fluctuations are correlated across the detector and not just within one SVX chip [144]. The study also concludes that there are no bunch related noise effects.

The white noise is an intrinsic noise (thus uncorrelated) in the SVXIIE chip for each Si strip/channel connected to the chip. The white noise may be caused by the thermal properties of the chip and the capacitance of the connected silicon detector. The total noise is the sum of the squares of common mode noise and white noise:

$$\sigma_{tot}^2 = \sigma_w^2 + \sigma_k^2. \tag{167}$$

A study performed on the same Si detectors in 2003, [145] showed that the typical white noise σ_w for an $x-view/y-view$ detector is about 1.7/2 ADC counts, the total noise σ_{tot} about 2.3/2.5 ADC and the common mode noise σ_k is about 1.5/1.5 ADC counts. Note that the $y-view$ detector has higher white noise than the $x-view$ detector, as expected, since the $y-view$ detector has higher capacitance due to its longer strip length [145]. In practice, the common mode noise can be subtracted from the total noise, in order to improve signal to noise performance. However, during these studies it was decided that this procedure was not necessary, since the typical signal is usually large enough.

A small measured σ_{tot}, see Fig. 57 (b), indicates small noise in the readout. The normal range for σ_{tot} is $\sim$ 2 - 2.5. The pedestal distributions of all the detectors were measured during the tests and pedestal runs and the σ of the pedestal distributions of all Si channels was determined. The σ_{tot} of the pedestal distributions measured after installing the detectors at RHIC was observed to be slightly higher than those measured in the lab, the difference is $\sim$ 0.5 - 1σ.

It was observed that most of the channels have total noise in the range of 2 - 3 ADC counts, with no SVX showing anomalous behavior. This indicates that the chips were working properly and that there was no strip with leakage current large enough to affect detector performance. Shifts in the pedestal occur mainly in groups of 126 channels (1 SVX chip), as expected. This is due to the process variations in the manufacturing of the SVX chips [145].

Moreover, it was observed that some Si strips have higher noise than the surrounding strips. These strips were marked as inefficient channels. The strip number and

positions of the inefficient channels were determined and excluded from the analysis. There are three main cases of inefficient channels:

(a) The Si strip might be an edge strip in the Si detector and the edge strips have low pedestal and signal, which makes them inefficient when running in the sparse mode (a feature in which only channels above a preset threshold are readout). To take care of these channels a cut is made to remove 3 strips from the edge in every silicon detector plane.

(b) The Si strip may just be a noisy strip.

(c) The Si strip may be a dead strip and this might cause the neighbor strips to be noisy, since the strips are capacitively coupled.

(d) The Si strip may be located in the center of the Si detector plane, which can be considered as a hot region when the detector is approached very close to the beam.

Cases (b) and (c) constitute only 5 dead/noisy strips out of ~14,000 active strips, where the number of active strips is generally limited by the acceptance. The detector system of the 2009 run setup had 100% acceptance and all the Si strips were activated during the run. The dead/noisy strips therefore constituted only ~0.04% of the total number of active strips, which is negligible. Case (d) is usually observed in the vertical RPs for the runs that there were moved very close to the beam ~6 mm close. This observation indicates that the shape of the beam resembles an ellipse (beam envelope is usually described as "pancake" shaped), with the longer axis in the vertical plane. These strips that fall in these so called "hot regions" are taken care of by *fiducial cuts*, which will be explained later in this chapter.

Energy Threshold for a Valid Proton Hit

Figure 58 shows the energy distribution of the clusters in EHI plane A. The energy distribution follows a Landau distribution (see Fig. 58). The lower peak in Fig. 58 is the pedestal distribution.

Figure 59 shows the energy distributions of the clusters detected in all RPs (top plots - East RPs and bottom plots - West RPs). The first small peak in the plots represent the pedestal distribution, which is removed by requiring that the ADC

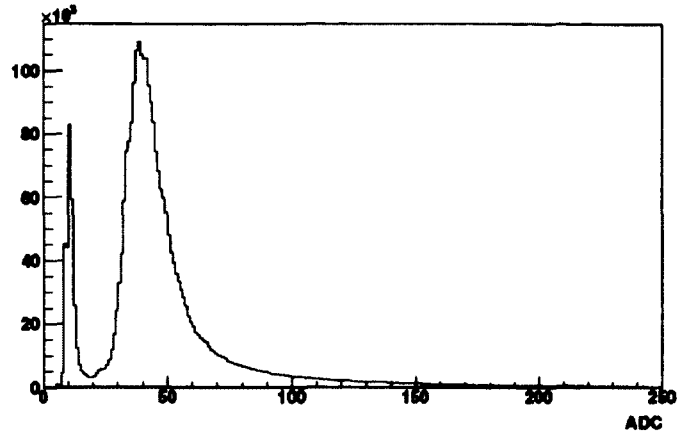

FIG. 58. Energy distribution (defined as *eCls* on the plot) of the clusters detected in EHI plane A, for run 10183028. The horizontal axis is in ADC units. The pedestal peak (first peak) is also shown. Figure courtesy of I. Koralt.

readout of each Si channel to be: ADC $\geq$ Pedestal per strip/channel + $5\sigma_{pedestal}$, as explained above in the definition of a valid hit.

Energy Threshold Dependence on Cluster Length

The analysis given in Ref. [144] showed that 3 σ and 4 σ cuts of the pedestal distribution left some noise hits, while a 5 σ cut eliminates most of the noise without eliminating any of the signal. However, a constant ADC cut (based on cluster size) is also needed to eliminate the rest of the noise/background. Table 14 gives a list of the energy threshold for different cluster size and for each RP/detector package. For more details on the determination of the energy threshold for each RP refer to analysis note given in Ref. [143]. The energy distribution depends on cluster size and tends to shift to higher energy ranges with size [143]. The energy threshold values given in Table 14 are used to select the detected clusters with size of 1, 2, 3, 4 or 5 strips in the Si detector. Clusters with size bigger than 5 are rejected. Figure 60 shows the energy distribution of clusters detected in EHI dependence on cluster length.

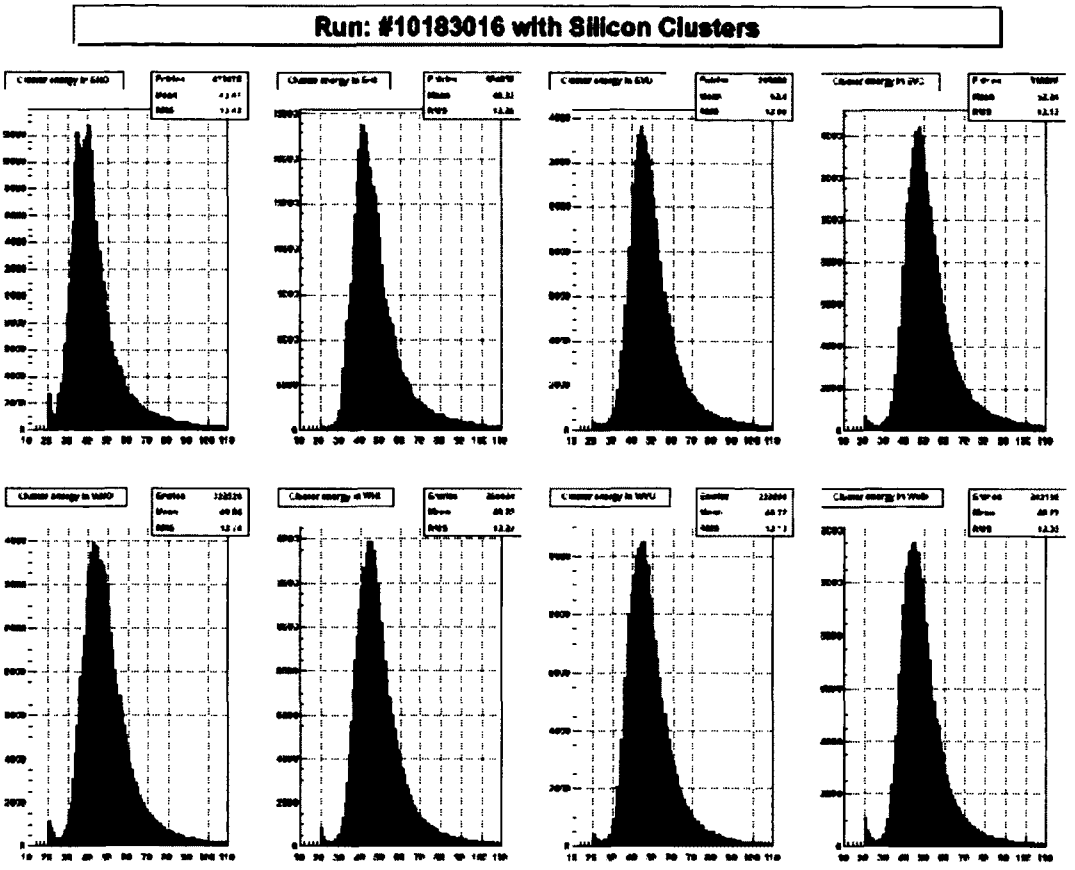

FIG. 59. Energy distribution (defined as *eCls* on the plot) of the clusters detected in all RPs (namely from right to left and top to bottom: EHO, EHI, EVU, EVD, WHO, WHI, WVU, WVD) for run 10183016. The horizontal axis is in ADC units. The first small peak represents the pedestal distribution. Plot courtesy of K. Yip.

TABLE 14. Energy threshold based for different Cluster Size/Length and for each RP (refer to [143])

RP/L_{cls}	EHI	EHO	EVU	EVD	WHI	WHO	WVD	WVU
1	19	18	18	19	20	23	21	19
2	27	24	28	28	27	29	29	25
3	49	45	48	50	50	53	46	46
4 or 5	65	60	69	70	60	64	60	59

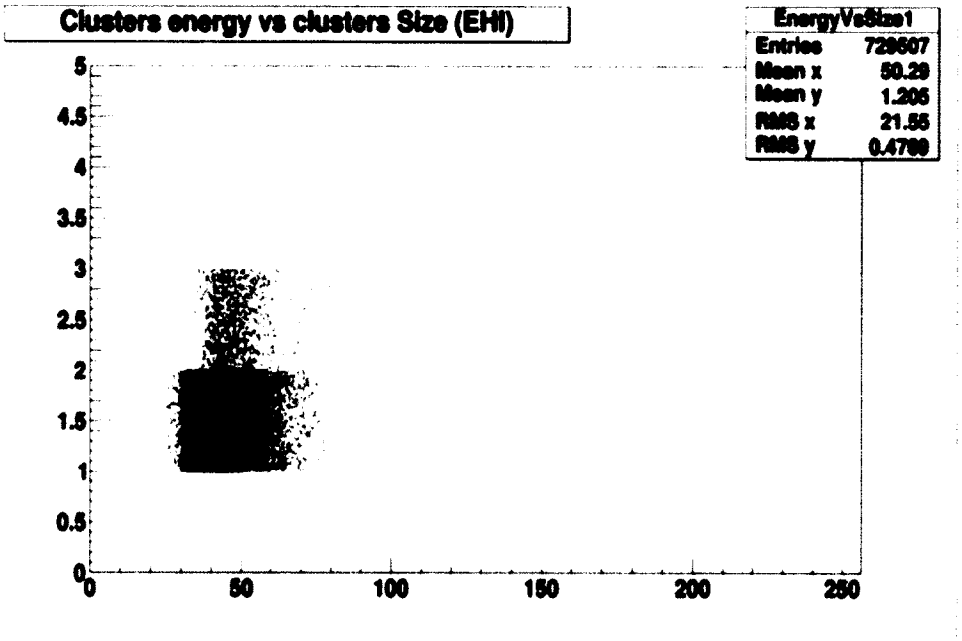

Cluster length ($lcls$) vs cluster energy ($eCls$) for EHI

FIG. 60. Energy distribution dependence on cluster length for EHI for a typical run during Run09.

6.2.2 SELECTION CRITERIA FOR TRACK RECONSTRUCTION

In the first and second steps of the analysis, an initial selection of the data is performed. At the end of this initial selection we obtain a set of hits/clusters of the scattered protons in the Si detectors with "proper" number of clusters in a detector plane, cluster length and energy, according to the cuts explained in the previous section. This set of data is stored in ROOT files and will be used in the track reconstruction logarithms and further selection of elastic events.

STEP 3. Selection of elastic events and track reconstruction from the data set stored in ROOT files.

Measurement of elastic scattering does not require the measurement of the momenta of the scattered protons, however, this analysis necessitates a good characterization of an elastic event. First, hits/clusters of the elastically scattered protons in the silicon detector are selected. Next, the coordinates/positions of the selected clusters are calculated, using also the information of the positions of the detectors in the STAR coordinate system, which is determined from the survey and alignment of the detectors. The clusters are further selected by cluster matching algorithms for one RP (4 detector planes) and one elastic arm (2 collinear pair of detectors across IP). This will be explained later in this section in detail. In the final step of the characterization of an elastic event, the positions of the selected clusters are used together with the transport equations to calculate the scattering angles of the detected scattered protons. The scattering angles are then used in the reconstruction of the elastic events and calculation of physics parameters, such as four momentum transfer squared t and azimuthal angle ϕ. The final step of the analysis is to use the selected elastic events, to calculate physics observables, i.e. spin-dependent and spin-averaged observables. For spin asymmetry measurements, most of the systematics related to the detectors, i.e. geometrical acceptance and efficiencies, cancel out. Systematics related to the bunch polarization does not cancel out in the asymmetry calculation and therefore needs to be determined.

Elastic Trigger Condition

The elastic trigger during the run was the first bit of the trigger index, with TriggerId 250101. The elastic trigger bit requires that there is a detected proton

TABLE 15. Elastic Trigger Components/Arms

Definition of Elastic Arms	Elastic Arm
EA (Elastic Trigger A - vertical)	EA = WVU and EVD
EB (Elastic Trigger B - vertical)	EB = WVD and EVU
EC (Elastic Trigger C - horizontal)	EC = WHO and EHI
ED (Elastic Trigger D - horizontal)	ED = WHI and EHO

TABLE 16. Forbidden Components

Definition of Forbidden Components	Combinations
EVF (East Vertical Forbidden)	EVF = EVU and EVD
EHF (East Horizontal Forbidden)	EHF = EHI and EHO
WVF (West Vertical Forbidden)	WVF = WVU and WVD
WHF (West Horizontal Forbidden)	WHF = WHI and WHO

in a collinear pair of detectors in the East and West of the STAR IP, i.e. vertical RPs (West UP - East DOWN and vice-versa) and horizontal RPs (West Inner - East Outer and vice-versa). There is one trigger scintillator/counter in each RP, read out by two PMTs. Hence, the STAR trigger system receives 16 signals from PMTs in the Roman Pots. Both amplitude and timing information of each of the 16 PMTs is recorded. The ADC threshold for the trigger counters was determined and set to be equal to 5. The range for the TAC (Time to Analog Converter) signal of the trigger counters was determined to be $100 \leq$ TAC signal ≤ 1700. For the elastic trigger definition, we make basic combinations of the trigger signal as an "OR" of the two PMTs of the same counter, i.e. RPEVU1 or RPEVU2, refer to [146]. Elastic trigger components/arms are defined as in Table 15. Forbidden combinations of RPs are defined as in Table 16. Hence, elastic trigger requires that at least one of the elastic arms (EA, EB, EC and ED) is triggered simultaneously and not (WVF, WHF, EVF or EHF).

Before proceeding with cluster matching, we check if the selected clusters correspond to the identified inefficient (bad/hot) channels. Only 5 out of 14,000 active strips were identified as inefficient channels. Data coming from inefficient channels is rejected.

Cluster Matching

Planes A(B) and C(D) in one Si detector package, measure the same coordinate, respectively. Therefore, the positions of clusters measured in plane A(B) and C(D) can be compared and matched. The distance between the positions of clusters originated from the same event and measured in planes A(B) and C(D), respectively, was required to be less than or equal to twice the strip pitch. So, in order to match a pair of clusters detected in planes which measure the same coordinate, they must have a position difference of $\Delta x = |x_1 - x_2| \leq 2 \cdot$ *strip pitch*. The same applies for the planes which measure the y coordinate of the particles. Strip pitch depends on plane type, 97.4 μm for $x - view$ and 105.0 μm for $y - view$ planes. After the clusters detected by the pair of detector planes, which measure the same coordinate (redundant detector planes), are matched with this condition, an average value for the cluster position is calculated from the positions of clusters in each plane.

Different cases of the number of clusters detected in planes A(B) and C(D) are observed in the data and can be summarized as shown in Table 17. At least one cluster in planes A/C or B/D is required to form a *track*. The most probable case was observed to be case 4 in Table 17, when only one cluster is detected on the pair of planes which measure the same coordinate. For case 2, when there is one cluster in one plane (for ex. plane A) and none in the other plane (for ex. plane C), we use the existing cluster (the one in plane A in this example) to form a track. For case 3, when there is more than one cluster in one plane and none in the other plane, no track is formed. For cases 5 and 6 in Table 17, when there is more than one cluster in either plane or in both planes, respectively, we examine the closest clusters in the A/C or B/D planes and calculate the average value of the matched cluster position.

We can look at case 4 (one cluster in both planes A(C) or B(D)) more closely and use this case to check the alignment of the redundant planes with respect to each other. Figure 61 shows the measured distance of the clusters detected in RPEHO - planes A and C, which measure the x coordinate, for a typical run. The plot shows that the distance between the detected clusters is ~ 0.1 mm. The distributions of the

TABLE 17. Cluster Matching Case Summary

Case	N_{cls} (plane A or B)	N_{cls} (plane C or D)	Average Value of Pos_{cls}
1	0	0	NA
2	0	1	use second plane only
	1	0	use first plane only
3	0	>1	NA
	>1	0	
4	1	1	use both planes
5	1	>1	use closest clusters on both planes
	>1	1	
6	>1	>1	use closest clusters on both planes

distances of clusters (case 4 in Table 17), were plotted and examined for all RPs and all runs during Run09. The mean of the distributions corresponds to the distance between the redundant planes in each RP, which is given in Table 18. This distance, which shows the geometrical misalignment of the redundant planes is corrected for before finding the closest clusters in the cluster matching procedure.

After cluster selection and matching we obtain a set of (x,y) positions for the selected tracks in each RP. The next step is to check RP combinations on each side of the IP, East and West, and to reconstruct elastic events by using the collinearity condition. The collinearity condition requires that tracks on each side of the IP are collinear in order to be combined and form an *elastic event*. Collinear pairs of detectors form four elastic arms, as shown also in the elastic trigger condition given in Table 15. For elastic events selection purposes we categorized the elastic arms as shown in Table 19.

First of all, using the algorithm given in Table 17, we form various combinations between two RPs in an elastic arm, for each arm. There are eight detector planes in one elastic arm, four of which are measuring one coordinate (x,y) and two of the four planes correspond to one RP and give one average value of the track after cluster matching in the particular RP. Therefore, we have two average values for each coordinate of the measured clusters across IP, $x_{ave}(East)$, $x_{ave}(West)$, $y_{ave}(East)$, and $y_{ave}(West)$. The data shows that the most probable cluster number combination

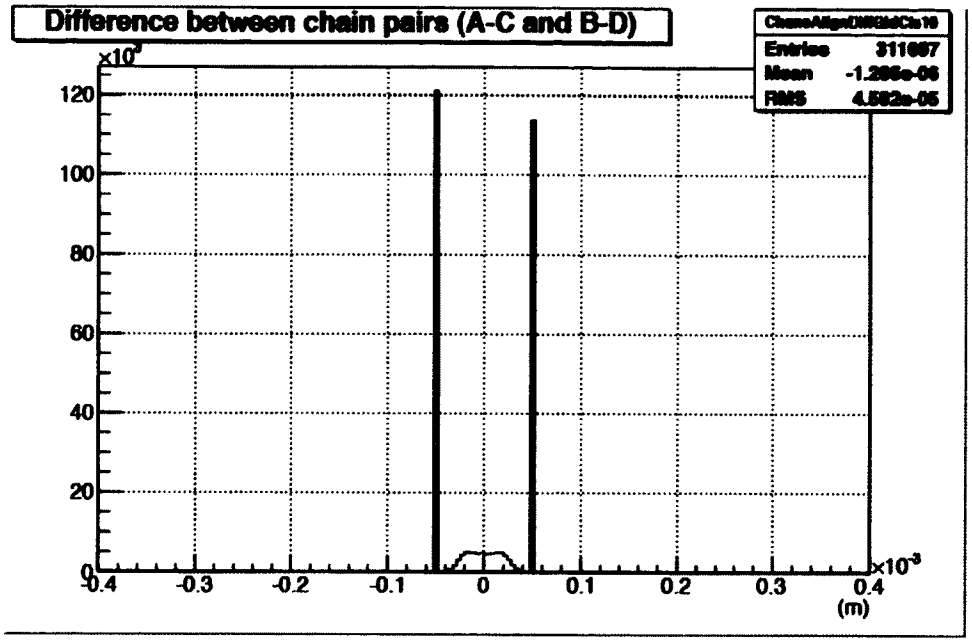

FIG. 61. Distribution of the distance (in m) between clusters in planes A and C, for RPEHO and run 10183028.

TABLE 18. Offset between redundant planes, A(C) and B(D), in each RP

RP	[A-C] (m)	[B-D] (m)
EHI	1.658E-5	4.092E-5
EHO	-1.415E-6	-4.609E-5
EVU	-2.848E-5	-3.382E-5
EVD	7.213E-6	3.991E-8
WHI	-3.523E-6	-6.329E-5
WHO	-1.854E-5	3.000E-5
WVD	6.532E-6	-6.132E-5
WVU	-1.520E-6	4.098E-5

TABLE 19. Elastic Arms

Arm #	Elastic Arm
0	EA = EHI and WHO
1	EB = EHO and WHI
2	EC = EVU and WVD
3	ED = EVD and WVU

across the IP is when there is one cluster in each of the eight planes that form the elastic arm. This combination of tracks forms what we call a *golden event*. We used the sample of golden events to plot distributions of the difference between (x,y) positions of matched clusters/tracks in each elastic arm, for each run separately. Figure 62 shows the difference in x-positions (Δx in m) of tracks measured in Arm 0: EHI - WHO for a typical run. The plot is fit with a Gaussian function. The mean of the distributions for each elastic arm and for all the runs, was used to determine the collinearity offset between RPs in each arm and for each run during Run09. The collinearity needs to be studied and determined for each run, since the beam may be centered differently for different RHIC stores/fills. A study of the Δx and Δy distributions of each elastic arm shows that the beam might have shifted by several 100 μm also during the same store. The reason for this may be the change in the magnet strength of the quadrupole magnets during the store.

STEP 4. Assigning kinematic parameters, momentum transfer squared-t and azimuthal angle ϕ to the selected elastic events.

In this analysis step we need to make use of the beam transport to calculate kinematic parameters, i.e. polar and azimuthal scattering angles θ and ϕ from the measured and selected positions of elastic events. In order to calculate the momentum transfer squared-t, we first need to calculate the polar scattering angle θ of the elastic events. The polar, azimuthal angles and momentum transfer squared-t are defined

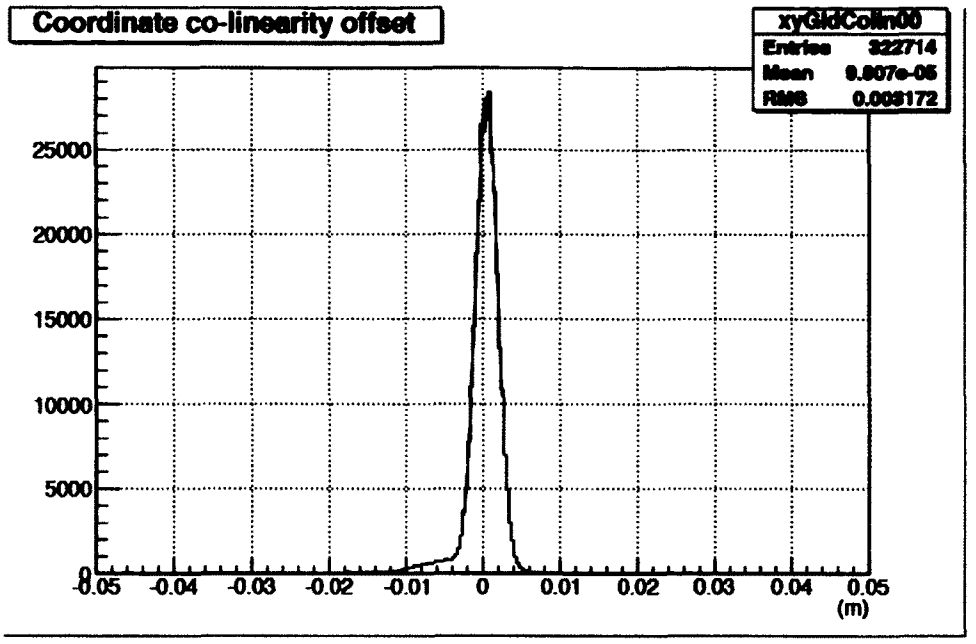

FIG. 62. Distribution of the difference in x-positions of tracks (in m) for a golden event in Arm 0: EHI - WHO.

as given in Eq. (168):

$$\begin{aligned}
\theta_x &= \vec{P}_x/\vec{P}, \\
\theta_y &= \vec{P}_y/\vec{P}, \\
\theta &= \sqrt{\theta_x^2+\theta_y^2}, \\
\cos\theta &= \vec{P}_z/\vec{P}, \\
\phi &= \tan^{-1}(\theta_y/\theta_x), \\
\text{For } |p| = |p'| \text{ (see Eqs. 15 \& 19) } t &= -2p^2(1-\cos\theta) = -4p^2\sin^2\frac{\theta}{2}, \\
\text{For small}-\theta \; t &\approx -p^2\theta^2,
\end{aligned} \tag{168}$$

where $p = 100.2$ GeV/c.

Each beam particle is represented by a phase-space vector $X = (x, \theta_x, y, \theta_y)$ of coordinates and angles in the transverse plane. Each optical element in the RHIC beamline from the IP (z = 0) at STAR to the RP location (z = 55.5 and 58.5 m), (namely two dipole, three quadrupole magnets and drift spaces), is represented by a transport matrix by which the vector X is multiplied, see Eq. (158) in Section 5.2.

Beam Transport Equations

Equation (158) in Section 5.2 can explicitly be expressed as:

$$\begin{bmatrix} x \\ \theta_x \\ y \\ \theta_y \end{bmatrix}^d = \begin{pmatrix} a_{11} & a_{12} & a_{13} & a_{14} \\ a_{21} & a_{22} & a_{23} & a_{24} \\ a_{31} & a_{32} & a_{33} & a_{34} \\ a_{41} & a_{42} & a_{43} & a_{44} \end{pmatrix} \begin{bmatrix} x \\ \theta_x \\ y \\ \theta_y \end{bmatrix}^* , \tag{169}$$

where a_{12} and a_{34} correspond to the *effective length* in x and y: L^x_{eff} and L^y_{eff}, $()^*$ are the positions and scattering angles at the IP and $()^d$ are the positions and angles measured at the detection point.

Equation (169) shows that the beam transport is used to correlate positions and angles of beam protons along the beamline. Since the scattering angles of the elastically scattered protons are small, the scattered protons stay within the beampipe of the accelerator and also follow trajectories determined the beam transport magnets. Therefore, the trajectories of the scattered protons can be described by the same set of equations, as follows:

$$\begin{aligned} x^d &= a_{11} \cdot x_0 + L^x_{eff} \cdot \theta_x{}^* + a_{13} \cdot y_0 + a_{14} \cdot \theta_y{}^*, \\ \theta_x{}^d &= a_{21} \cdot x_0 + a_{22} \cdot \theta_x{}^* + a_{23} \cdot y_0 + a_{24} \cdot \theta_y{}^*, \\ y^d &= a_{31} \cdot x_0 + a_{32} \cdot \theta_x{}^* + a_{33} \cdot y_0 + L^y_{eff} \cdot \theta_y{}^*, \\ \theta_y{}^d &= a_{41} \cdot x_0 + a_{42} \cdot \theta_x{}^* + a_{43} \cdot y_0 + a_{44} \cdot \theta_y{}^*. \end{aligned} \tag{170}$$

where x_0 and y_0 are the positions at the IP (vertex).

Solving for the scattering angles at the vertex, we obtain the following equations:

$$\begin{aligned} \theta^*_x &= \frac{1}{L^x_{eff} - \frac{a_{14}a_{32}}{L^y_{eff}}} \\ &\times \left[x^d - \frac{a_{14}}{L^y_{eff}} \cdot y^d + \left(\frac{a_{14}a_{31}}{L^y_{eff}} - a_{11} \right) \cdot x_0 + \left(\frac{a_{14}a_{33}}{L^y_{eff}} - a_{13} \right) \cdot y_0 \right], \\ \theta^*_y &= \frac{1}{L^y_{eff} - \frac{a_{32}a_{14}}{L^x_{eff}}} \\ &\times \left[y^d - \frac{a_{32}}{L^x_{eff}} \cdot x^d + \left(\frac{a_{32}a_{13}}{L^x_{eff}} - a_{33} \right) \cdot y_0 + \left(\frac{a_{32}a_{11}}{L^x_{eff}} - a_{31} \right) \cdot x_0 \right]. \end{aligned} \tag{171}$$

The full transport matrix (6 × 6) for Run09 and the values of the transport matrix elements are given in Section 5.2. For example, the transport matrix (4 × 4)

for the West Horizontal RP is given in Eq. (172).

$$M = \begin{bmatrix} a_{11} & L^x_{eff} & a_{13} & a_{14} \\ a_{21} & a_{22} & a_{23} & a_{24} \\ a_{31} & a_{32} & a_{33} & L^y_{eff} \\ a_{41} & a_{42} & a_{43} & a_{44} \end{bmatrix},$$

$$= \begin{bmatrix} -0.0913 & 25.2566\,\mathrm{m} & -0.0034 & 0.0765\,\mathrm{m} \\ -0.0396\,\mathrm{m}^{-1} & 0.0137 & -0.0001\,\mathrm{m}^{-1} & 0.0057 \\ -0.0033 & -0.1001\,\mathrm{m} & 0.1044 & 24.7598\,\mathrm{m} \\ 0.0002\,\mathrm{m}^{-1} & 0.0083 & -0.0431\,\mathrm{m}^{-1} & -0.6332 \end{bmatrix}. \quad (172)$$

After inputting the values of the transport matrix elements in Eq. (171) we obtain the following equations for the scattering angles at the IP for each beam and RP station, where B = Blue beam, Y = Yellow beam, H = Horizontal-RP, V = Vertical-RP:

$$\begin{aligned}
\theta^*_x(B,H) \times \mathrm{m} &= 0.03959 \cdot x^d - 0.0001223 \cdot y^d + 0.003615 \cdot x_0 + 0.0001477 \cdot y_0, \\
\theta^*_y(B,H) \times \mathrm{m} &= 0.04039 \cdot y^d + 0.0001601 \cdot x^d - 0.004214 \cdot y_0 + 0.0001477 \cdot x_0, \\
\theta^*_x(B,V) \times \mathrm{m} &= 0.03953 \cdot x^d - 0.0001616 \cdot y^d + 0.008311 \cdot x_0 + 0.0001471 \cdot y_0, \\
\theta^*_y(B,V) \times \mathrm{m} &= 0.04374 \cdot y^d + 0.0001301 \cdot x^d + 0.001086 \cdot y_0 + 0.0001471 \cdot x_0, \\
\theta^*_x(Y,H) \times \mathrm{m} &= -0.03952 \cdot x^d - 0.0001732 \cdot y^d - 0.003572 \cdot x_0 + 0.0001477 \cdot y_0, \\
\theta^*_y(Y,H) \times \mathrm{m} &= -0.04032 \cdot y^d - 0.0000824 \cdot x^d + 0.004281 \cdot y_0 - 0.0000144 \cdot x_0, \\
\theta^*_x(Y,V) \times \mathrm{m} &= -0.03945 \cdot x^d + 0.0001938 \cdot y^d - 0.008249 \cdot x_0 - 0.0000002 \cdot y_0, \\
\theta^*_y(Y,V) \times \mathrm{m} &= -0.04366 \cdot y^d - 0.0000712 \cdot x^d - 0.000999 \cdot y_0 - 0.0000002 \cdot x_0.
\end{aligned} \quad (173)$$

The dominating term in the transport matrix is the magnification of the scattering angle, or $L^{x,y}_{eff}$ in Eq. (170). The values of $L^{x,y}_{eff}$ are in the range of 22-26 m, see Section 5.2. The coefficients which magnify the beam position at the vertex (x_0 and y_0) are minimized in the case of "parallel-to-point focusing". This is achieved by the optimization of the beam optics for this experiment. Equation (172) shows that the values of a_{11} and a_{13} are small, -0.0913 and -0.0034, respectively. Therefore, for the case of parallel-to-point-focusing and in the absence of $x - y$ mixing terms, the Eq. (170) can be simplified to the form given in Eq. (174). However, this simplified form

was not used in the analysis.

$$\begin{aligned} x^d &\approx L^x_{eff} \cdot \theta^*_x \rightarrow \theta^*_x \approx x^d / L^x_{eff}, \\ y^d &\approx L^y_{eff} \cdot \theta^*_y \rightarrow \theta^*_y \approx y^d / L^y_{eff}. \end{aligned} \tag{174}$$

Scattering Angle θ and t Reconstruction

The scattering angles θ^*_x and θ^*_y are calculated using (4×4) transport matrix as given in Eq. (172) and by taking $x_0 = y_0 = 0$, since they are expected to be small. By using Eq. (173) and the measured positions of the scattered particles, we calculate the scattering angles in the transverse plane, for each side of the IP and each RP station.

Collinearity Condition

After calculating the scattering angles for detected elastic events on both sides of the IP and for each RP station, we impose a collinearity condition on the measured angles of the elastic events. The collinearity condition is parametrized by introducing a parameter χ^2, and requiring χ^2 to be less than or equal to 9, as given in Eq. (175):

$$\chi^2 = \left(\frac{\delta\theta_x - \delta\bar{\theta}_x}{\sigma_{\theta_x}} \right)^2 + \left(\frac{\delta\theta_y - \delta\bar{\theta}_y}{\sigma_{\theta_y}} \right)^2 \leq 9, \tag{175}$$

where $\delta\theta_{x,y} = \theta_{x,y}(West) - \theta_{x,y}(East)$. Therefore, in order to calculate $\delta\theta_{x,y}$ we histogram the difference between the measured scattering angles in East and West of the IP, for each elastic arm (given in Table 19) and for each run separately. The histograms $\delta\theta_{x,y}$ are then fitted by a Gaussian function and the mean ($\delta\bar{\theta}_x$ and $\delta\bar{\theta}_y$) and the rms values (σ_{θ_x} and σ_{θ_y}) of the distributions are determined.

Figure 63 shows the χ^2 distribution for EHI-WHO elastic arm and for a typical run. The solid black line shows the boundary when $\chi^2 = 9$.

The plots given in Fig. 64 and Fig. 65 show the measured x and y positions of the scattered protons horizontal and vertical RPs, respectively, for a typical run and for $\chi^2 \leq 18$. The inner boundaries of the distributions are determined by the distance of approach of the detectors close to the beam. The outer boundaries are determined by the apertures of the quadrupole magnets located before the detectors along the beamline from IP (both East and West) to the RP location.

Some visible characteristics are observed in the transverse position distributions given in Fig. 64 and Fig. 65. The bands (regions in the distributions with less events)

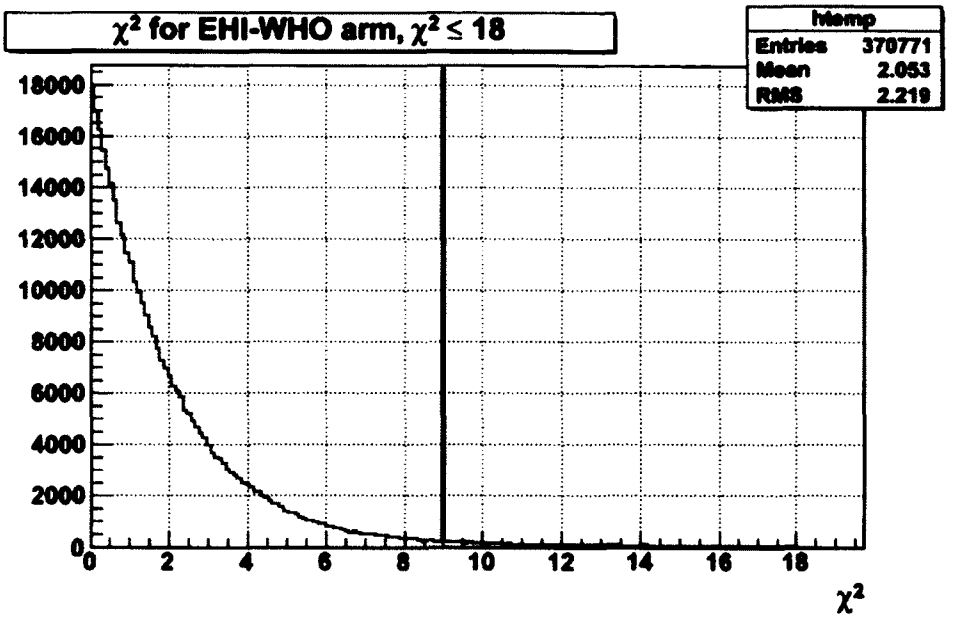

FIG. 63. χ^2 distribution for EHI-WHO arm and run 10183028.

visible in both vertical and horizontal RPs are an example of the characteristics seen in the data, which is common for all the runs. The horizontal bands in horizontal RPs (are not very visible on the plots, see Fig. 64), are most probably caused by a trigger bias effect. An event/track which passes through the horizontal RP and then hits the stainless steel frame of the vertical RP may produce secondary tracks, which may hit both vertical RPs simultaneously, causing a trigger veto as defined in the elastic trigger definition (see Table 16). This causes the trigger bias which in turn is manifested as the bands/shadows seen in the data. The vertical bands/shadows visible in the vertical RPs (see Fig. 64, more easily visible than the horizontal bands in horizontal RPs) have two causes. One cause is the same as above, the trigger bias effect and the other cause is the shadowing of the frames of the horizontal-RPs, which are 3 m in front of the vertical RPs in the RHIC tunnel, when looking away from the IP at STAR.

The measured transverse positions of the scattered protons were used to calculate the scattering angles (θ_x and θ_y) for each RP station. Calculated scattering angles for run 10183028 and $\chi^2 \leq 18$ are shown in Fig. 66 and Fig. 67.

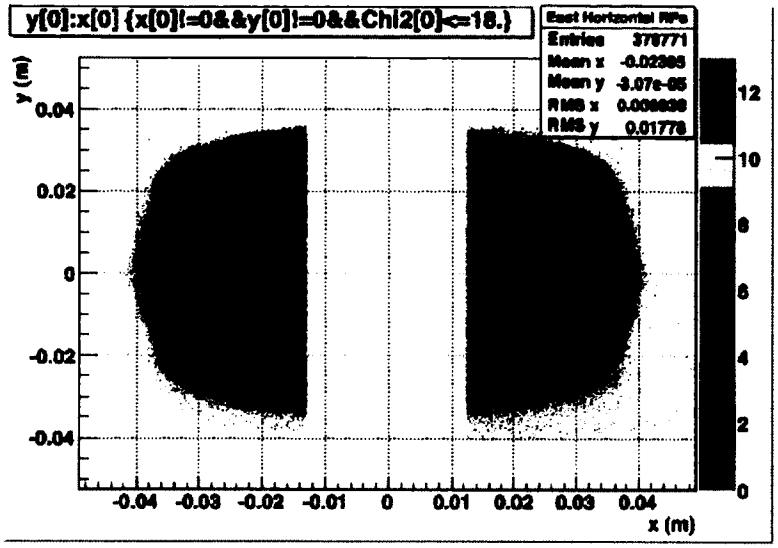

(a)

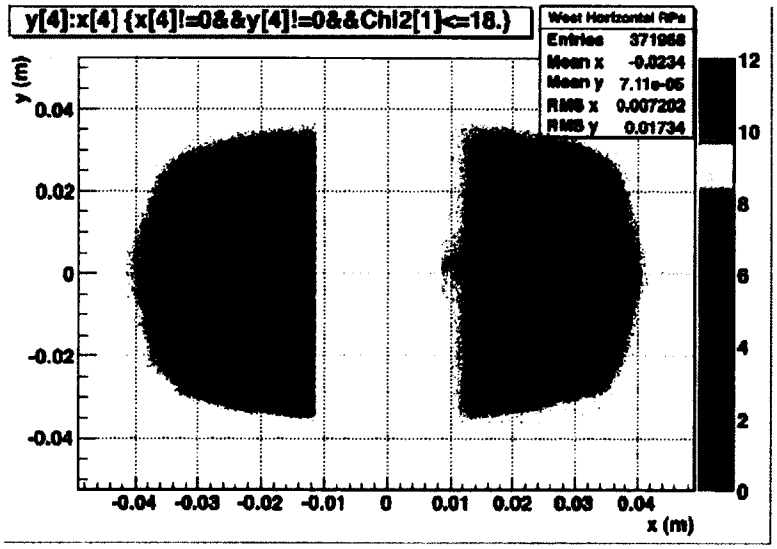

(b)

FIG. 64. Measured x and y positions of scattered protons in Horizontal RPs: (a) East Horizontal RPs and (b) West Horizontal RPs, for run 10183028 and $\chi^2 \leq 18$.

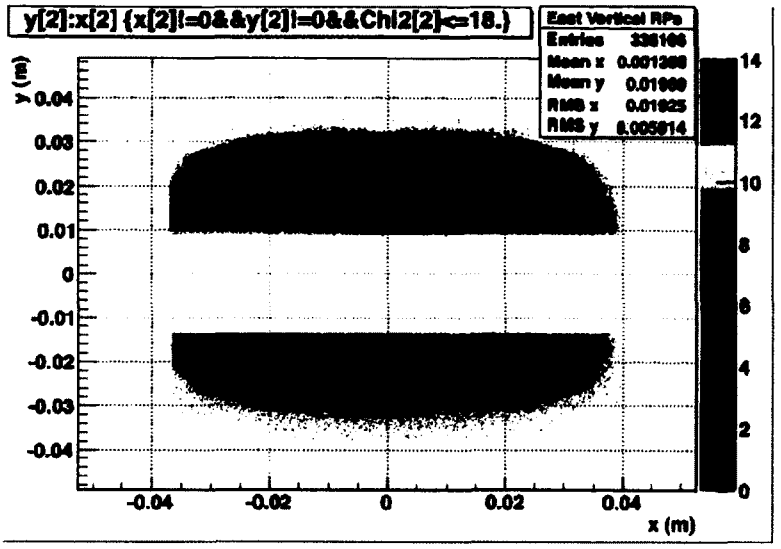

(a)

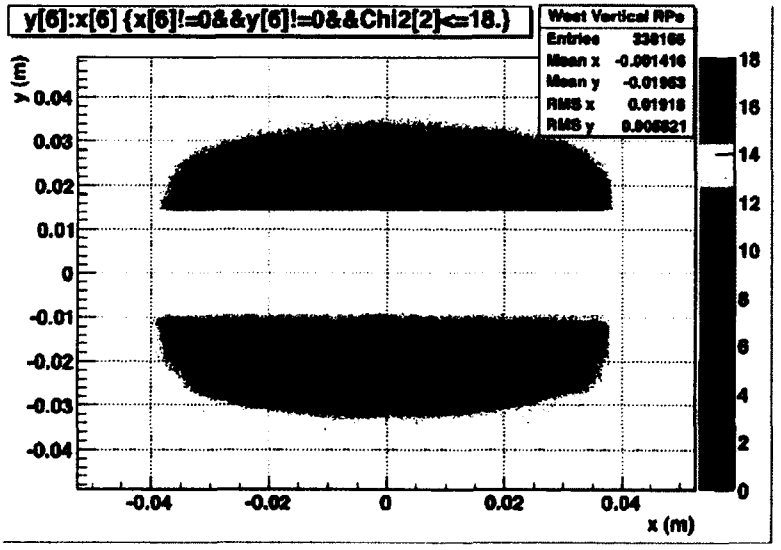

(b)

FIG. 65. Measured x and y positions of scattered protons in Vertical RPs: (a) East Vertical RPs and (b) West Vertical RPs, for run 10183028 and $\chi^2 \leq 18$.

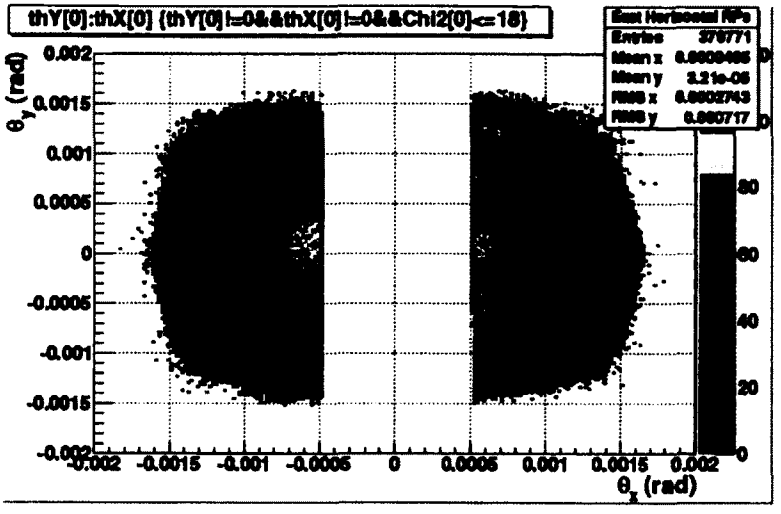

(a)

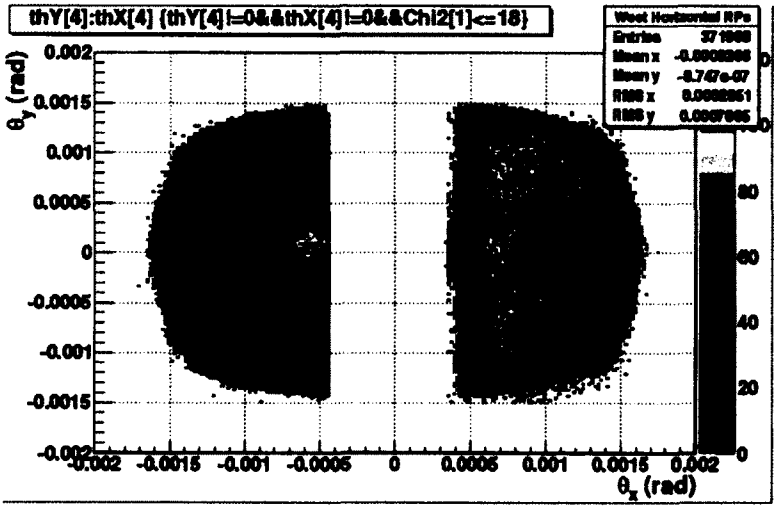

(b)

FIG. 66. Calculated scattering angles (θ_x and θ_y) of protons in Horizontal RPs: (a) East Horizontal RPs and (b) West Horizontal RPs, for run 10183028 and $\chi^2 \leq 18$.

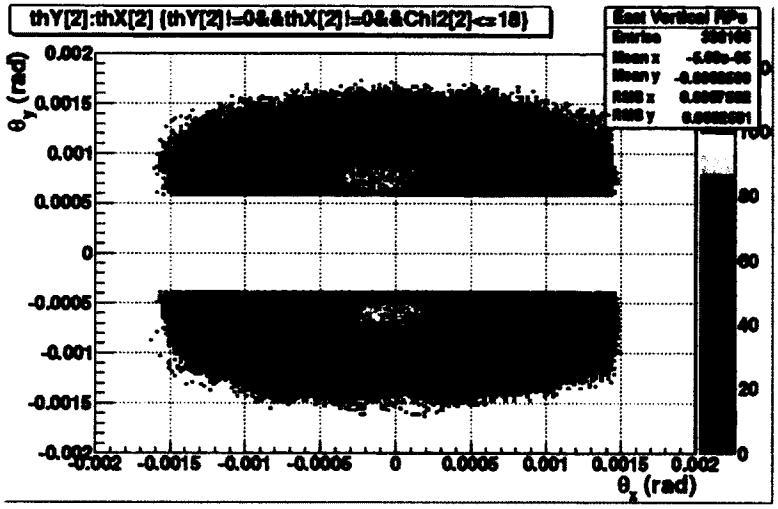

(a)

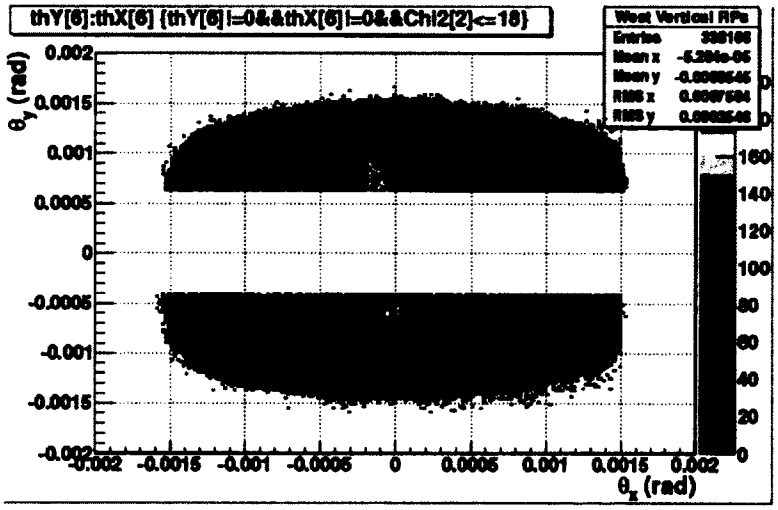

(b)

FIG. 67. Calculated scattering angles (θ_x and θ_y) of protons in Vertical RPs: (a) East Vertical RPs and (b) West Vertical RPs, for run 10183028 and $\chi^2 \leq 18$.

The plots given in Fig. 68 show $\delta\theta_y$ vs $\delta\theta_x$ distributions of scattering angles for various χ^2 cuts, for a pair of collinear detectors (EHI-WHO elastic arm) and for run 10183028.

Figures 69 and 70 show $\delta\theta_x$ and $\delta\theta_y$ distributions for horizontal elastic arms and vertical elastic arms, respectively, for run 10183028 and $\chi^2 \leq 9$. The distributions are fitted using a Gaussian function. The mean and σ of the distributions are extracted from the fit.

In the above figures, measured positions and angles of scattered particles were shown for each RP station. To reconstruct elastic events we need to "match", by using the collinearity condition, positions and angles of collinear detector pairs with respect to the IP (elastic arms as shown in Table 19). The plots given in Fig. 71 and Fig. 72 show measured positions of scattered protons in each Horizontal Elastic Arm and Vertical Elastic Arm, respectively, for run 10183028 and $\chi^2 \leq 9$. Likewise, the plots given in Fig. 73 and Fig. 74 show measured angles of scattered protons in each Horizontal Elastic Arm and Vertical Elastic Arm, respectively, also for run 10183028 and $\chi^2 \leq 9$.

Elastic Events Selection Table

Table 20 gives the total number of events processed in 46 runs and the number of events after each major selection criteria: elastic trigger; cluster matching and co-linearity condition.

TABLE 20. Elastic Event Selection Table

Total number of events processed (in 46 runs)	58,068,295
Total number of elastic/scintillator triggers	32,729,261 ~44% less than total # of events
Total number of events after matching	25,195,897 ~23% less than total # of elastic triggers
Total number of elastic events (after $\chi^2 \leq 9$ co-linearity cut)	22,130,570 ~12% less than total # of "matched" events
Total number of "golden" events	18,452,103 ~83% of all selected elastic events

6.3 EFFICIENCY OF THE SILICON STRIP DETECTORS

The efficiency of all the silicon detector planes used during data taking was studied and determined. The optimization of selection cuts, such as the minimum energy threshold E_{min} and the maximum number of clusters per plane is important since it directly affects the efficiency of the silicon detectors. The determination of optimal cuts improves the signal to noise ratio, which in turn improves the efficiency of the detectors.

Method

Before determining the efficiency of the silicon detectors used in Run09, first the inefficient silicon strips/channels (noisy/dead strips) were determined and excluded from analysis. Overall, it was found from this analysis that only five out of 14,000 active silicon strips/channels were to be marked as noisy/dead channels. The exclusion of the inefficient channels is not very critical since there are two redundant planes (two planes measuring the same coordinate in each detector package). Apart from excluding the determined inefficient channels, the first edge strip in the first and third detector plane in each detector package was also excluded from analysis. The reason for this is because the edge strips in this planes have lower gain than the other strips.

The method (algorithm) used for studying the efficiency of the silicon detectors is shown in Fig. 75. For example (see Fig. 75), in order to determine the efficiency of silicon detector plane A in the East, we select events when there is a cluster in each of the seven other detector planes which make up an elastic arm (collinear detectors with respect to IP). Transverse positions of selected clusters (x, y) are determined and matched in each pair of detector planes which measure the same coordinate (A-C and B-D). Selected clusters in these pair of detector planes are matched requiring that their position minus the geometric offset between the planes is within two strip pitch distance. Average values of the matched cluster positions are calculated using cluster positions from the detectors on each side of the IP. Then, scattering angles are calculated using measured cluster positions and transport matrix coefficients. Scattering angles from collinear detector pairs with respect to IP are then compared. This is done by first plotting distributions of the difference of scattering angles ($\delta\theta_x$ and $\delta\theta_y$ distributions), fitting them with a Gaussian function and determining the

mean value and σ of the distributions. Events that fall within 3σ of the $\delta\theta_x$ and $\delta\theta_y$ distributions are selected for further use in the efficiency study. The next step is to look for detected clusters in the 8^{th} plane (plane A in Fig. 75), when there is a cluster in each of the seven other planes in one particular elastic arm. The same procedure is followed for the other planes in the same elastic arm and for other elastic arms. Two parallel studies of the detector efficiencies were performed using Run09 data, from I. Koralt and T. Obrebski, see Ref. [143] for the later.

Result

According to the study by T. Obrebski, see Ref. [143], the plane efficiency after determination of the optimal cluster selection cuts, oscillates between 99.1 % and 99.8 %. It was also shown in the same study that the plane efficiency improved by 0.1 % after optimization of selection cuts, such as minimum cluster energy threshold E_{min} and accepted maximum number of clusters per plane. In the study performed by I. Koralt, the overall plane efficiency was determined to be above 99 % after the exclusion on the inefficient and edge silicon strips/channels. Figure 76 shows the determined inefficiency of all the detector planes for run 10183028 in the study performed by I. Koralt. More details on the performance of the silicon detectors during RHIC Run09 can be found in [147].

Figure 77 shows the efficiencies of all detector planes after the determination of optimal cuts in the study given in [143].

6.4 SELECTED ELASTIC EVENT DISTRIBUTIONS

6.4.1 SCATTERING ANGLES

The plots given in Fig. 78 show the measured scattering angles distributions (average θ_y vs average θ_x) for each elastic arm (Figures 78(a), 78(b), 78(c) and 78(d)) and for all arms together (Fig. 78(e)), for all the runs during Run09.

6.4.2 t VS ϕ DISTRIBUTIONS

Using the measured scattering angles and Eq. (168) we can calculate the azimuthal angle ϕ and the four-momentum transfer squared-t of the reconstructed elastic events. Calculated Mandelstam-t distributions and azimuthal angle ϕ for

each elastic arm and all runs are given in Fig. 79 and Fig. 80. The plots given in Fig. 81 show t vs ϕ distributions for each elastic arm (Figures 81(a), 81(b), 81(c) and 81(d)) and all elastic arms together (Fig. 81(e)), for all runs during Run09.

6.5 BACKGROUND AND FIDUCIAL CUTS

Backgrounds affecting the data are due to several factors: beam halo particles (since the detectors are moved close to the beam for data taking), products of beam-beam and beam-gas interactions and detector noise. The detector noise was taken into account and minimized by applying appropriate pedestal and energy cuts during the elastic event selection process. The inefficient silicon strips/channels were identified and excluded from the analysis, providing an excellent ($> 99\%$) silicon plane efficiency. The collinearity condition used in the identification of elastic events (elastic trigger) and the elastic event selection process was chosen in order to minimize the non-linear background affecting the elastic events. The collinearity condition of $\chi^2 \leq 9$ eliminates ≈ 12 % of the total number of elastic events. In addition to the collinearity condition, fiducial cuts were applied in certain areas of the detectors to remove the so-called "hot" regions. Hot regions are areas in the detectors with considerably more events than the other parts of the same detector. The fiducial cut removes the events detected in these areas. The "hot" regions are observed usually in the center of the vertical-RPs, see Fig. 65. These regions are the lowest acceptance boundaries of the detectors, where the detector approaches the beam and thus are most probably caused by beam-halo events (tail of the outgoing beam). For data analysis purposes we will define the azimuthal angle ϕ as follows:

- East of STAR (Yellow Beam)

  $\phi = 0 \rightarrow$ Center of RPEHI

  Proceeding counterclockwise:

  $\phi = \pi/2 \rightarrow$ Center of RPEVD

  $\phi = \pi \rightarrow$ Center of RPEHO

  $\phi = 3\pi/2$ or $-\pi/2 \rightarrow$ Center of RPEVU

- West of STAR (Blue Beam)

  $\phi = 0 \rightarrow$ Center of RPWHO

Proceeding clockwise:

$\phi = \pi/2 \rightarrow$ Center of RPWVU

$\phi = \pi \rightarrow$ Center of RPWHI

$\phi = 3\pi/2$ or $-\pi/2 \rightarrow$ Center of RPWVD

- Elastic Arms

$-\pi/2 \leq \phi \leq \pi/2 \rightarrow$ EHI - WHO arm (see Fig. 81(a))

$-\pi \leq \phi \leq \pi \rightarrow$ EHO - WHI arm (see Fig. 81(b))

$-\pi \leq \phi \leq 0 \rightarrow$ EVU - WVD arm (see Fig. 81(c))

$0 \leq \phi \leq \pi \rightarrow$ EVD - WVU arm (see Fig. 81(c))

The center of the vertical RPs is the region where the azimuthal angle $\phi = \pm \pi/2$, the region where the "hot" spots are observed. These events may dilute the asymmetry and are rejected.

6.5.1 IDENTIFICATION OF FIDUCIAL CUT REGION

To determine the fiducial cut region, all the x and y distributions of the events in all RPs were studied carefully for all runs during Run09. Figure 65 shows the transverse position distribution (y vs x) in East and West Vertical RPs for run 10183028 and collinearity condition $\chi^2 \leq 18$. The "hot" spot region can be easily seen in the central region of the plots, especially in Fig. 65 (b). The "hot" spot region is reduced after imposing a tighter collinearity condition of $\chi^2 \leq 9$ (see Fig. 82, as the number of events overall is reduced by $\approx 3\%$ for run 10183028.

For each run during Run09, we determined the x and y coordinates of the "hot" spot by studying the measured x and y distributions. A fiducial cut in form of a square cut for the exclusion of the "hot" spot, was applied to the data for each run, where the δ_x and δ_y lengths of the square-cut were determined by examining the x and y distributions of the events in each detector and for each run. The intensity of the hot spot is bigger for the runs when the detectors were positioned very close to the beam, implying that the hot spot is caused by the beam halo particles. The position of the hot spot changes primarily from one RP position to the other and is the same for the group of runs in the same RP position (see Appendix D). The plots given in Fig. 83 show the measured x and y positions in RPWVU, for run 10185018,

TABLE 21. Elastic Event Selection Table after Fiducial Cuts

Total number of elastic events (after $\chi^2 \leq 9$ co-linearity cut)	22,130,570 ~12% less than total # of "matched" events
Total number of elastic events (after Fiducial Cuts for hotspot exclusion)	21,803,644 ~1.5% less than $\chi^2 \leq 9$ case

before (see Fig. 83(a)), after applying the collinearity cut (see Fig. 83(b)) and after the fiducial cut (see Fig. 83(c)).

Table 21 summarizes the number of events after the collinearity cut $\chi^2 \leq 9$ and fiducial cuts and is an addition to Table 20.

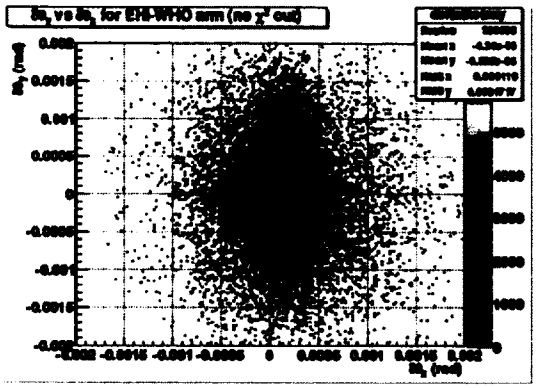

(a) $\delta\theta_y$ vs $\delta\theta_x$ in EHI-WHO arm (no χ^2 cut)

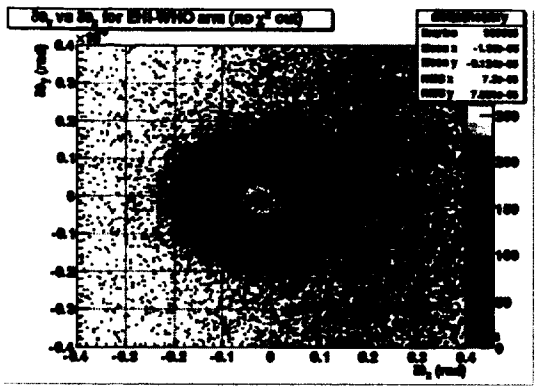

(b) $\delta\theta_y$ vs $\delta\theta_x$ in EHI-WHO arm (no χ^2 cut, zoomed)

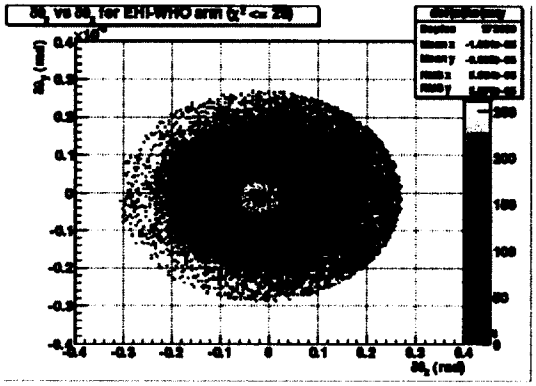

(c) $\delta\theta_y$ vs $\delta\theta_x$ in EHI-WHO arm ($\chi^2 \leq 25$)

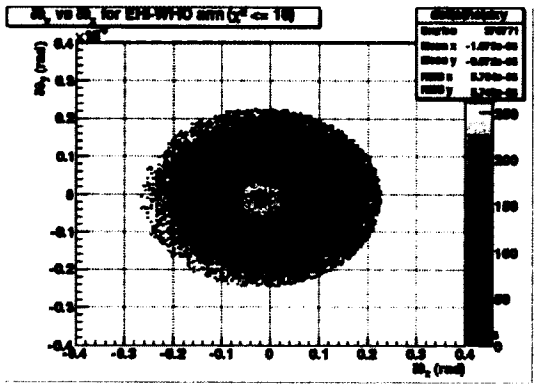

(d) $\delta\theta_y$ vs $\delta\theta_x$ in EHI-WHO arm ($\chi^2 \leq 18$)

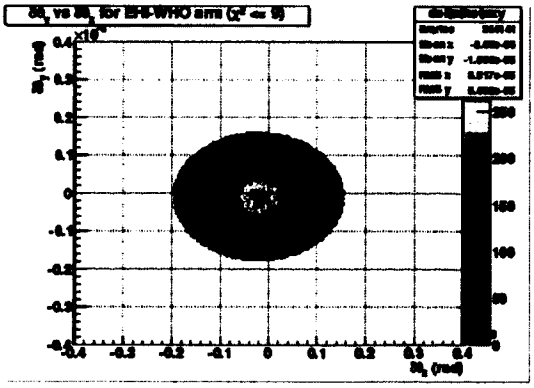

(e) $\delta\theta_y$ vs $\delta\theta_x$ in EHI-WHO arm ($\chi^2 \leq 9$)

FIG. 68. $\delta\theta_y$ vs $\delta\theta_x$ in EHI-WHO elastic arm for various χ^2 cuts: (a) no χ^2 cut; (b) no χ^2 cut and zoomed; (c) $\chi^2 \leq 25$; (d) $\chi^2 \leq 18$ and (e) $\chi^2 \leq 9$, for run 10183028.

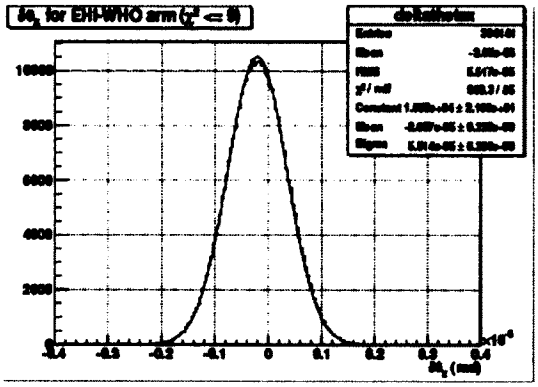

(a) $\delta\theta_x$ in EHI-WHO arm

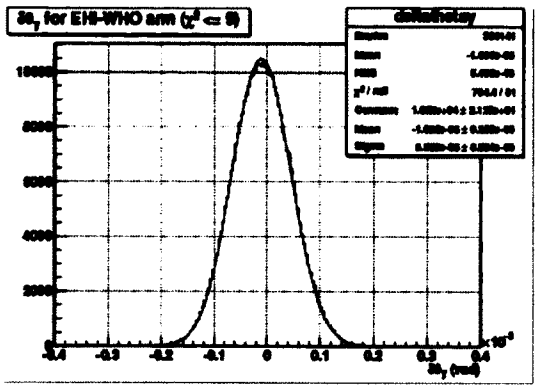

(b) $\delta\theta_y$ in EHO-WHI arm

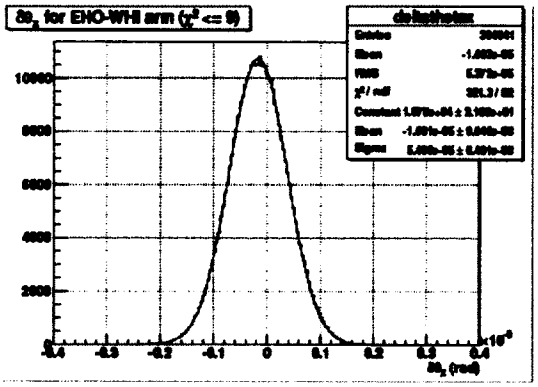

(c) $\delta\theta_x$ in EHO-WHI arm

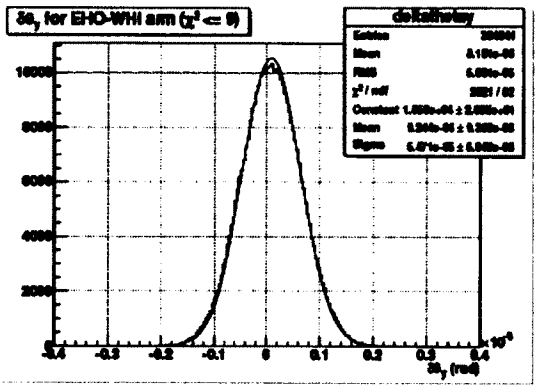

(d) $\delta\theta_y$ in EHO-WHI arm

FIG. 69. $\delta\theta_x$ and $\delta\theta_y$ in Horizontal Elastic Arms: (a) $\delta\theta_x$ in EHI-WHO; (b) $\delta\theta_y$ in EHI-WHO; (c) $\delta\theta_x$ in EHO-WHI and (d) $\delta\theta_y$ in EHO-WHI elastic arm, for run 10183028 and $\chi^2 \leq 9$.

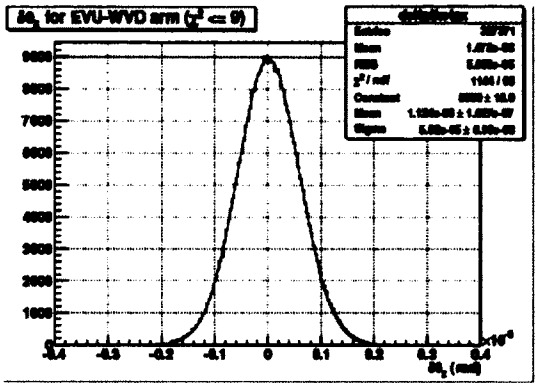

(a) $\delta\theta_x$ in EVU-WVD arm

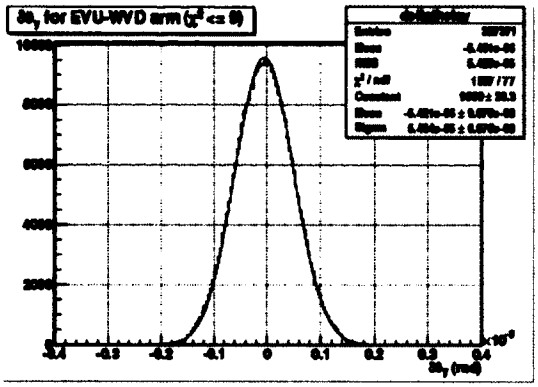

(b) $\delta\theta_y$ in EVU-WVD arm

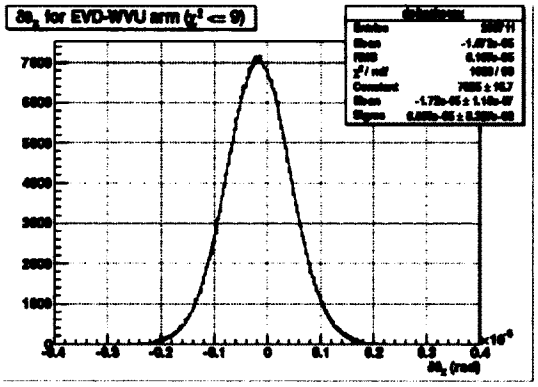

(c) $\delta\theta_x$ in EVD-WVU arm

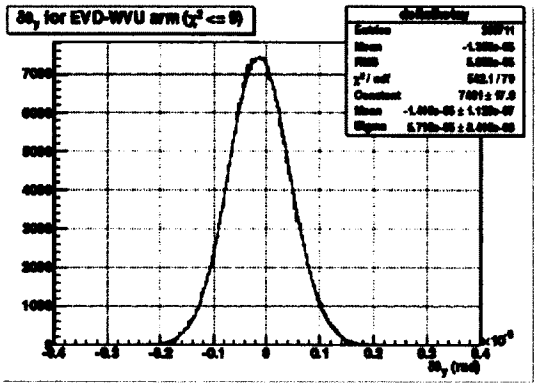

(d) $\delta\theta_y$ in EVD-WVU arm

FIG. 70. $\delta\theta_x$ and $\delta\theta_y$ in Vertical Elastic Arms: (a) $\delta\theta_x$ in EVU-WVD; (b) $\delta\theta_y$ in EVU-WVD; (c) $\delta\theta_x$ in EVD-WVU and (d) $\delta\theta_y$ in EVD-WVU elastic arm, for run 10183028 and $\chi^2 \leq 9$.

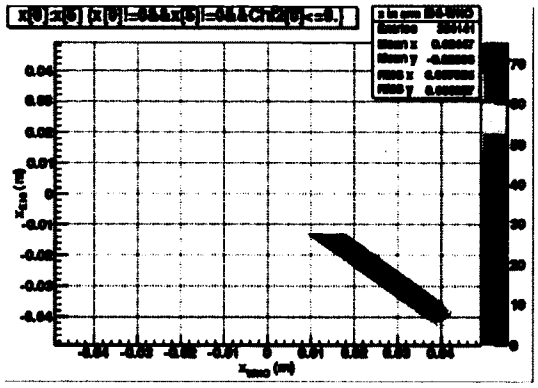

(a) x-position in EHI-WHO arm

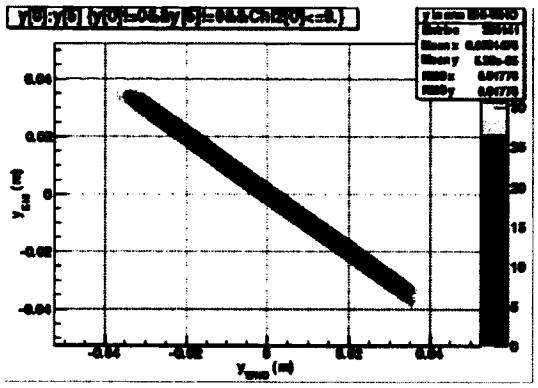

(b) y-position in EHI-WHO arm

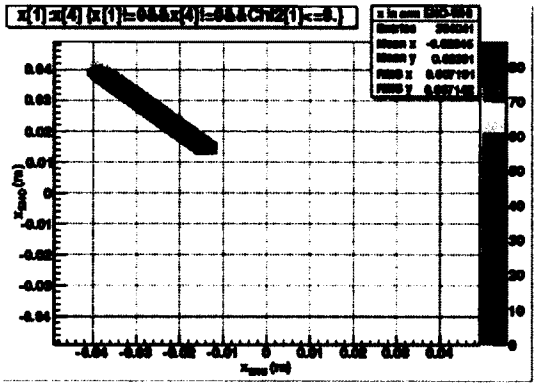

(c) x-position in EHO-WHI arm

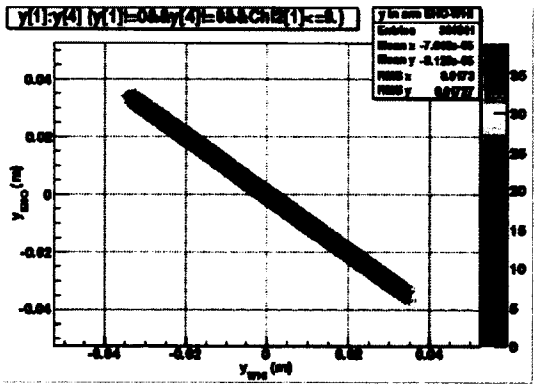

(d) y-position in EHO-WHI arm

FIG. 71. Measured x and y positions of scattered protons in Horizontal Elastic Arms: (a) x-position in EHI-WHO; (b) y-position in EHI-WHO; (c) x-position in EHO-WHI and (d) y-position in EHO-WHI elastic arm, for run 10183028 and $\chi^2 \leq 9$.

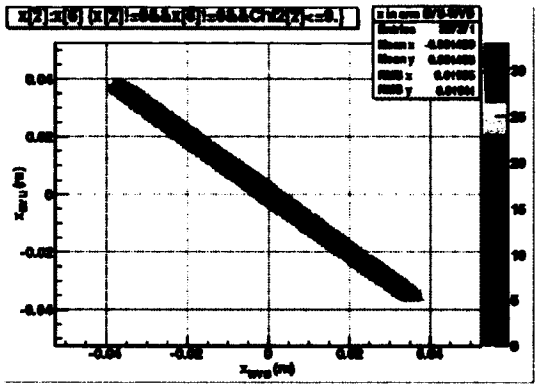

(a) x-position in EVU-WVD arm

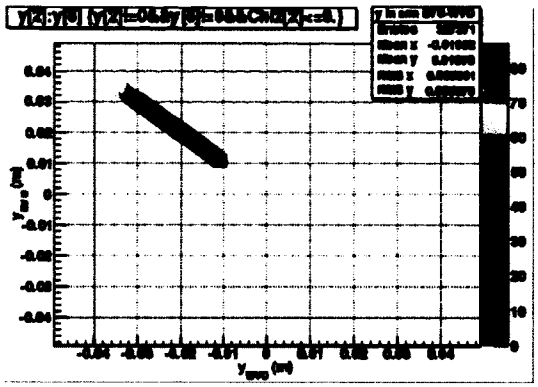

(b) y-position in EVU-WVD arm

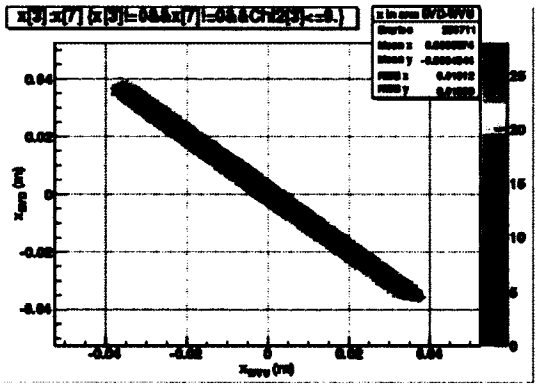

(c) x-position in EVD-WVU arm

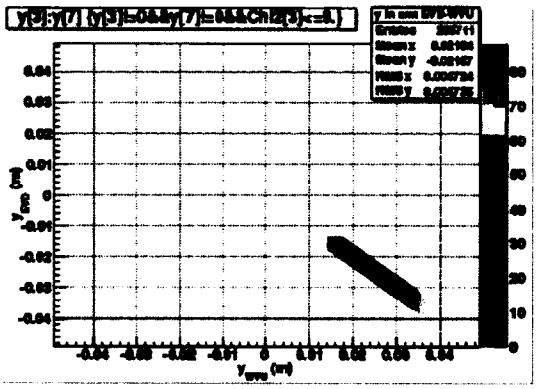

(d) y-position in EVD-WVU arm

FIG. 72. Measured x and y positions of scattered protons in Vertical Elastic Arms: (a) x-position in EVU-WVD; (b) y-position in EVU-WVD; (c) x-position in EVD-WVU and (d) y-position in EVD-WVU elastic arm, for run 10183028 and $\chi^2 \leq 9$.

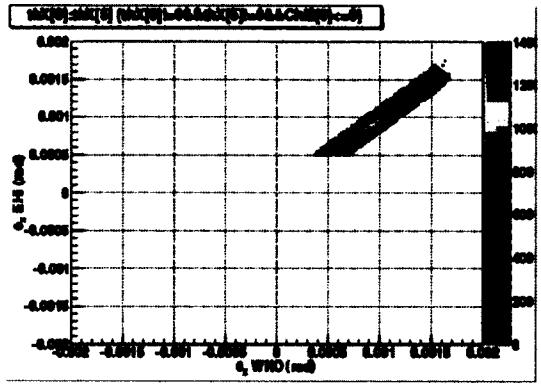

(a) θ_x in EHI-WHO arm

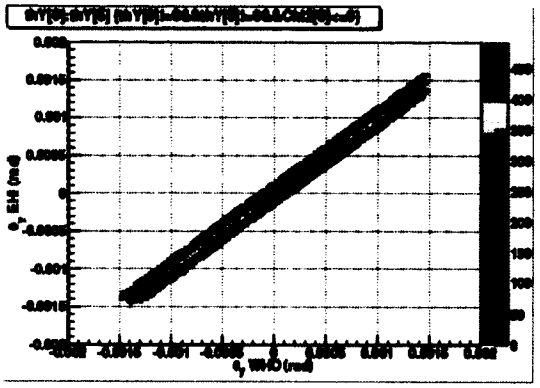

(b) θ_y in EHI-WHO arm

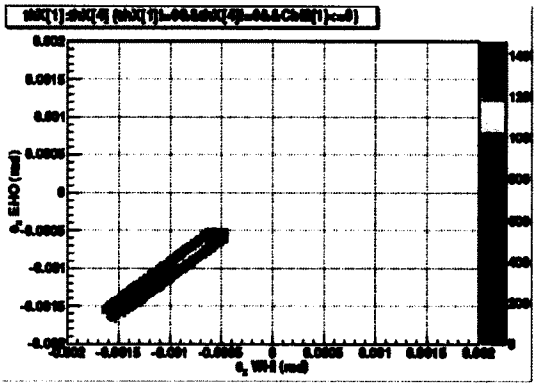

(c) θ_x in EHO-WHI arm

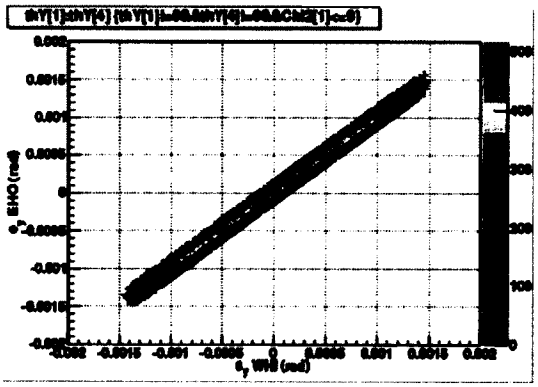

(d) θ_y in EHO-WHI arm

FIG. 73. Measured θ_x and θ_y angles of scattered protons in Horizontal Elastic Arms: (a) θ_x in EHI-WHO; (b) θ_y in EHI-WHO; (c) θ_x in EHO-WHI and (d) θ_y in EHO-WHI elastic arm, for run 10183028 and $\chi^2 \leq 9$.

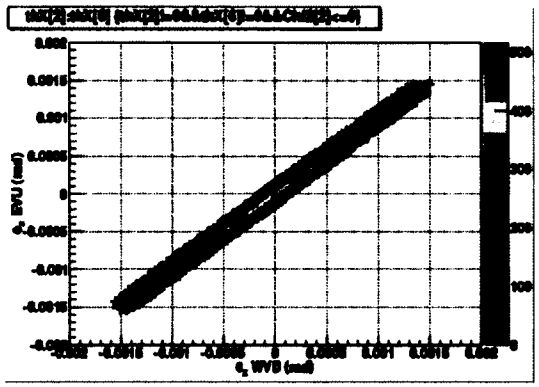

(a) θ_x in EVU-WVD arm

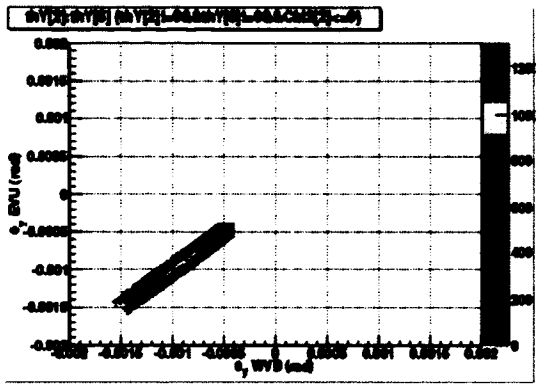

(b) θ_y in EVU-WVD arm

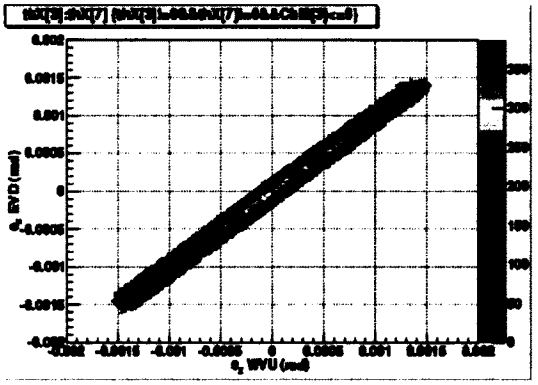

(c) θ_x in EVD-WVU arm

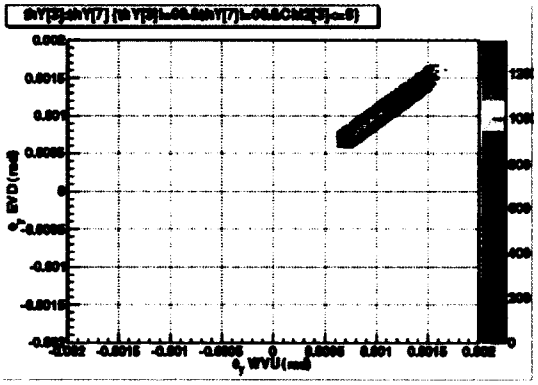

(d) θ_y in EVD-WVU arm

FIG. 74. Measured θ_x and θ_y angles of scattered protons in Vertical Elastic Arms: (a) θ_x in EVU-WVD; (b) θ_y in EVU-WVD; (c) θ_x in EVD-WVU and (d) θ_y in EVD-WVU elastic arm, for run 10183028 and $\chi^2 \leq 9$.

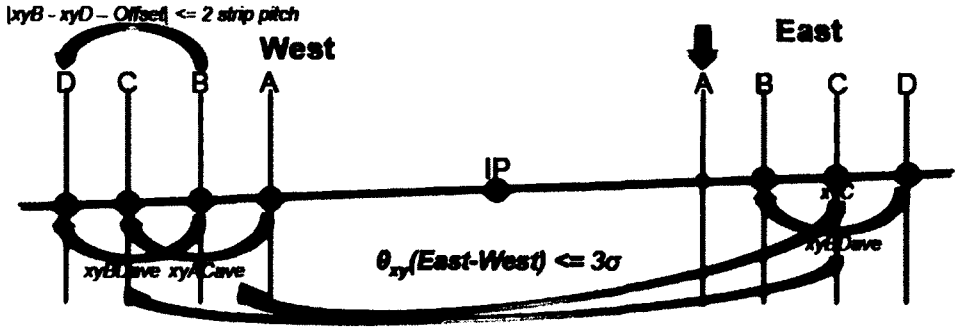

FIG. 75. The method used for studying and determining the efficiency of the silicon detectors. The method of determining the efficiency of one silicon plane in an elastic arm (consisting of 8 silicon planes, 4 planes on each side of the IP), when there is a hit in the other 7 silicon planes of the same elastic arm, is explained in Section 6.3.

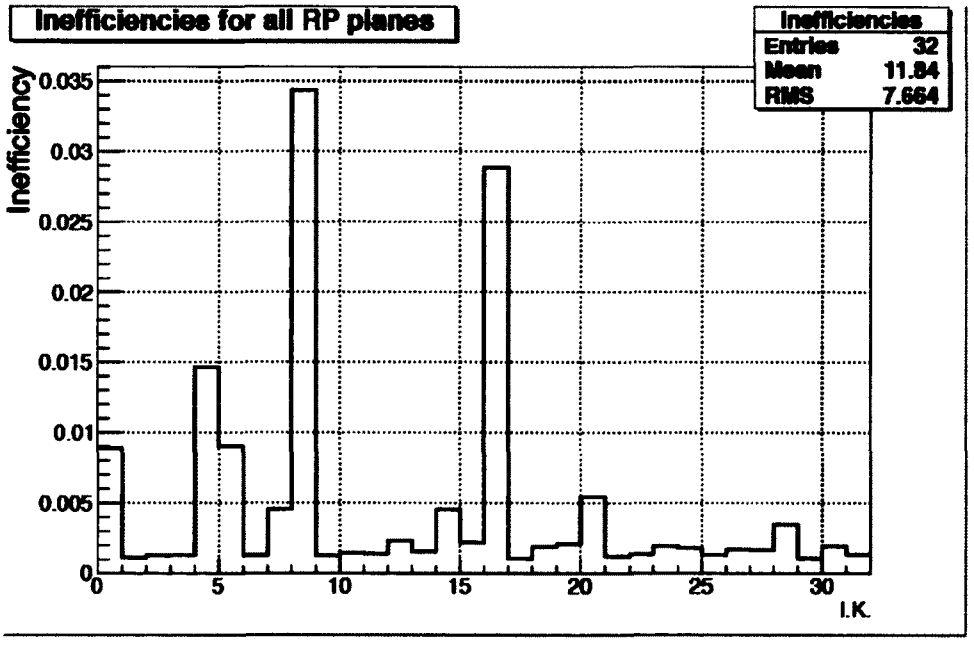

FIG. 76. Inefficiency distribution of all detector planes for run 10183028. Four detector planes in each RP, order of RPs in the plot from left to right: EHI, EHO, EVU, EVD, WHI, WHO, WVD and WVU (plot courtesy of I. Koralt).

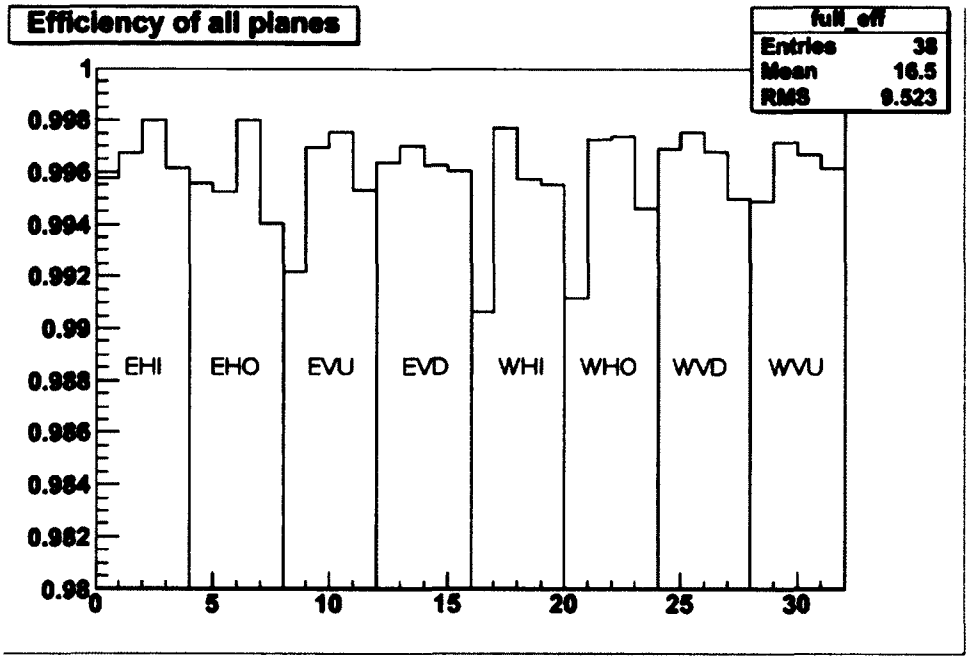

FIG. 77. Efficiency of all detector planes. Four detector planes in each RP, order of RPs in the plot from left to right: EHI, EHO, EVU, EVD, WHI, WHO, WVD and WVU (plot courtesy of T. Obrebski).

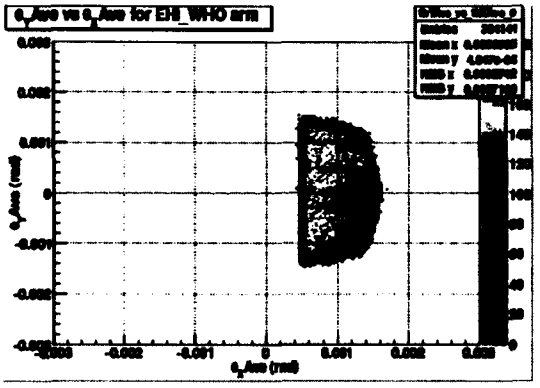

(a) θ_y^{ave} vs θ_x^{ave} in EHI-WHO arm ($\chi^2 \leq 9$)

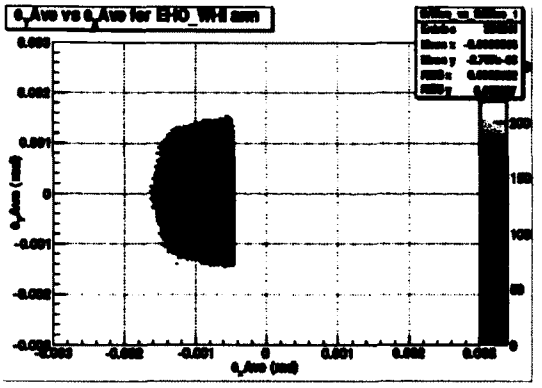

(b) θ_y^{ave} vs θ_x^{ave} in EHO-WHI arm ($\chi^2 \leq 9$)

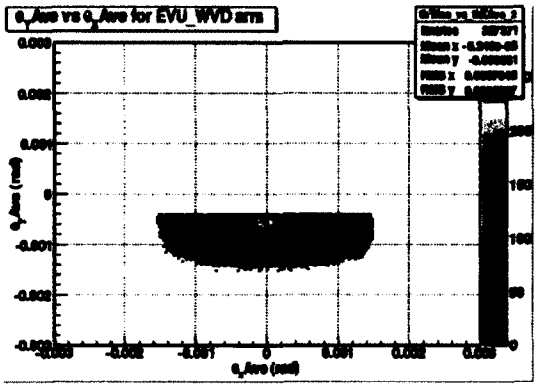

(c) θ_y^{ave} vs θ_x^{ave} in EVU-WVD arm ($\chi^2 \leq 9$)

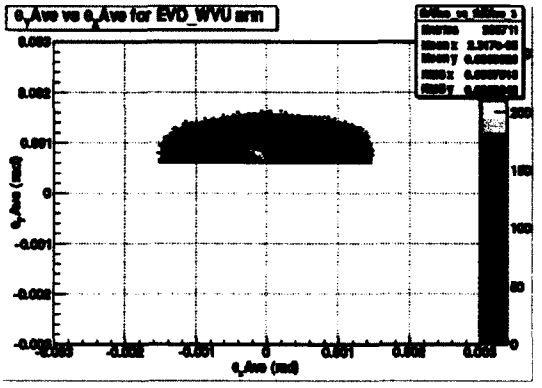

(d) θ_y^{ave} vs θ_x^{ave} in EVD-WVU arm ($\chi^2 \leq 9$)

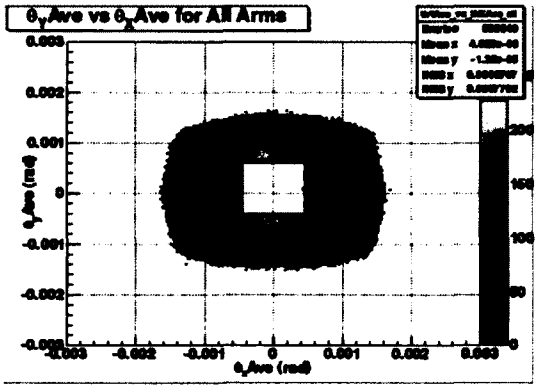

(e) θ_y^{ave} vs θ_x^{ave} in all arms ($\chi^2 \leq 9$)

FIG. 78. θ_y^{ave} vs θ_x^{ave} in elastic arms: (a) EHI-WHO; (b) EHO-WHI; (c) EVU-WVD; (d) EVD-WVU and (e) all arms together, for $\chi^2 \leq 9$ and run 10183028.

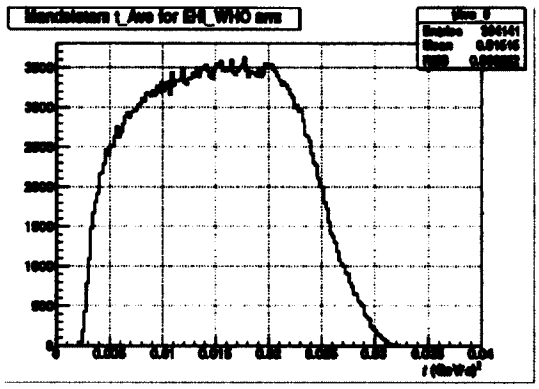

(a) t_{ave} in EHI-WHO arm ($\chi^2 \leq 9$)

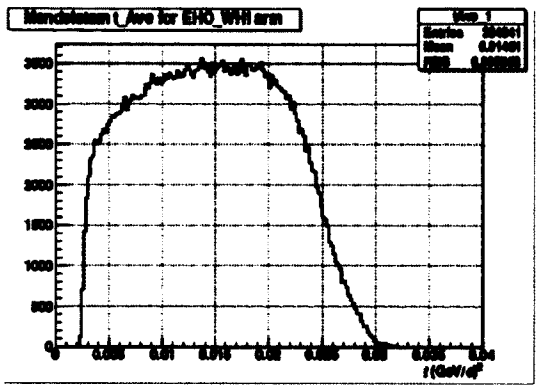

(b) t_{ave} in EHO-WHI arm ($\chi^2 \leq 9$)

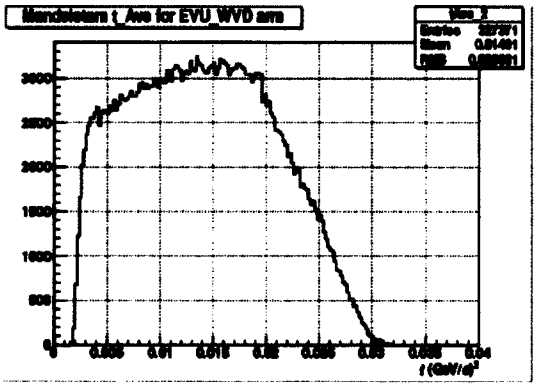

(c) t_{ave} in EVU-WVD arm ($\chi^2 \leq 9$)

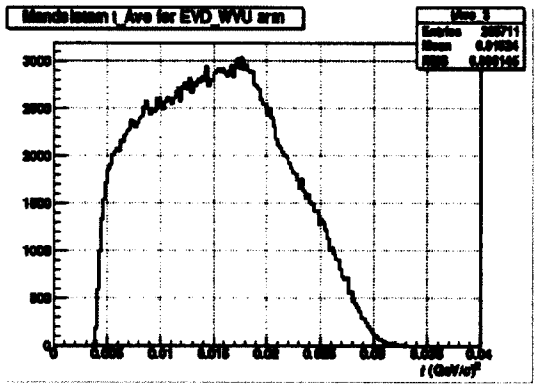

(d) t_{ave} in EVD-WVU arm ($\chi^2 \leq 9$)

FIG. 79. Mandelstam-t_{ave} distributions in elastic arms: (a) EHI-WHO; (b) EHO-WHI; (c) EVU-WVD; (d) EVD-WVU, for $\chi^2 \leq 9$ and run 10183028.

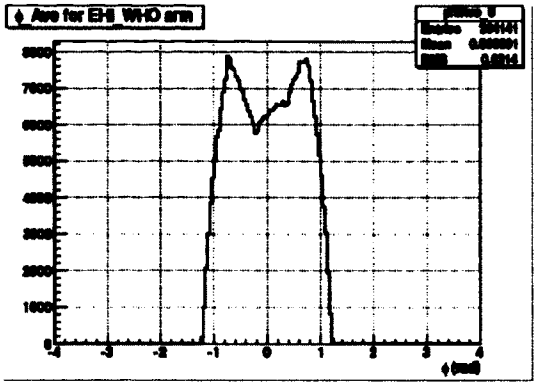

(a) ϕ_{ave} in EHI-WHO arm ($\chi^2 \leq 9$)

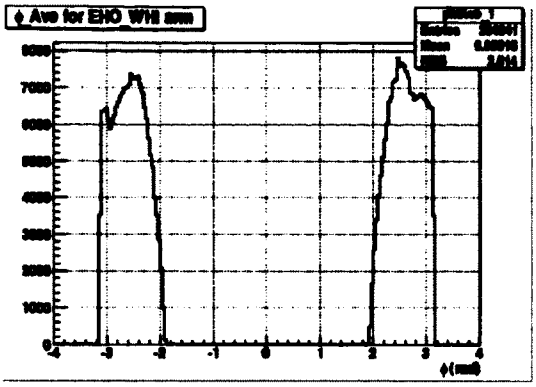

(b) ϕ_{ave} in EHO-WHI arm ($\chi^2 \leq 9$)

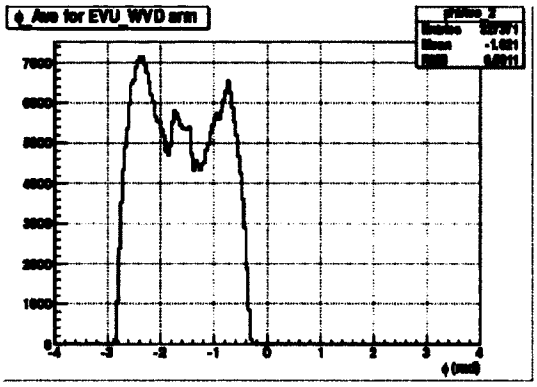

(c) ϕ_{ave} in EVU-WVD arm ($\chi^2 \leq 9$)

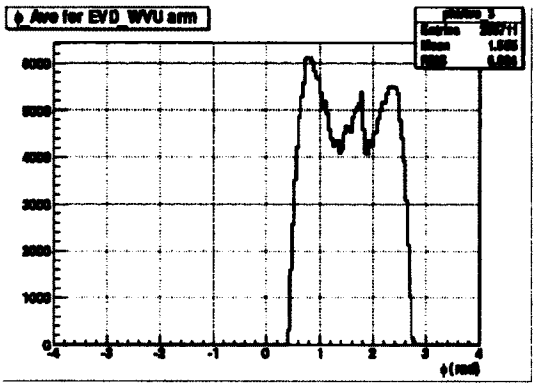

(d) ϕ_{ave} in EVD-WVU arm ($\chi^2 \leq 9$)

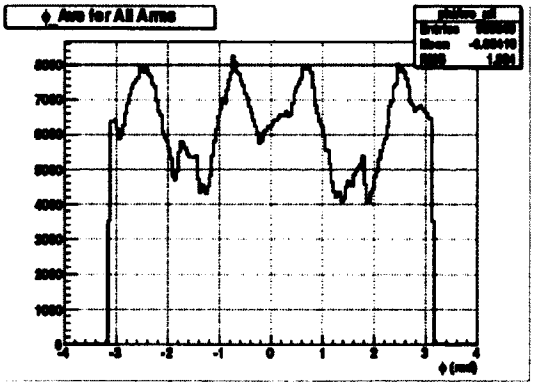

(e) ϕ_{ave} in all arms ($\chi^2 \leq 9$)

FIG. 80. ϕ_{ave} distributions in elastic arms: (a) EHI-WHO; (b) EHO-WHI; (c) EVU-WVD; (d) EVD-WVU and (e) all arms together, for $\chi^2 \leq 9$ and run 10183028.

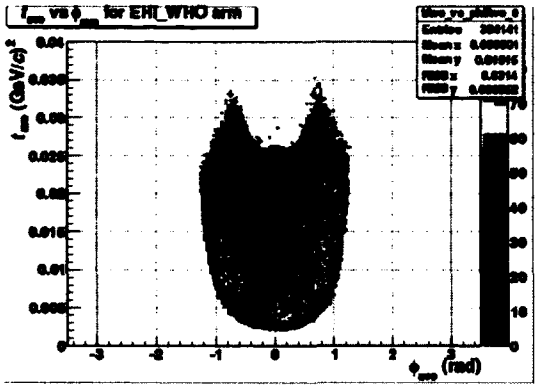

(a) t vs ϕ in EHI-WHO arm ($\chi^2 \leq 9$)

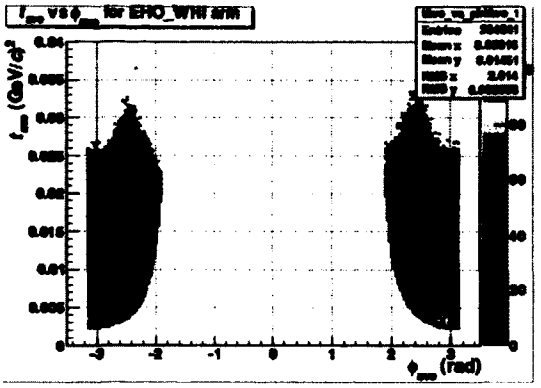

(b) t vs ϕ in EHO-WHI arm ($\chi^2 \leq 9$)

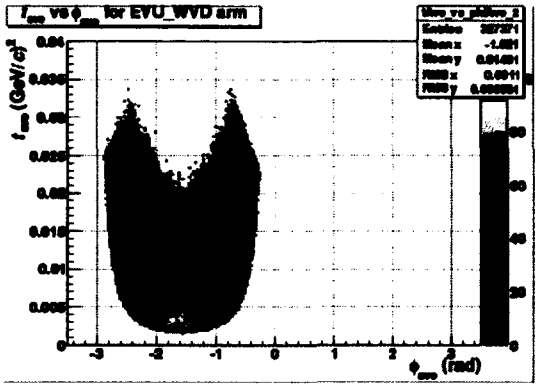

(c) t vs ϕ in EVU-WVD arm ($\chi^2 \leq 9$)

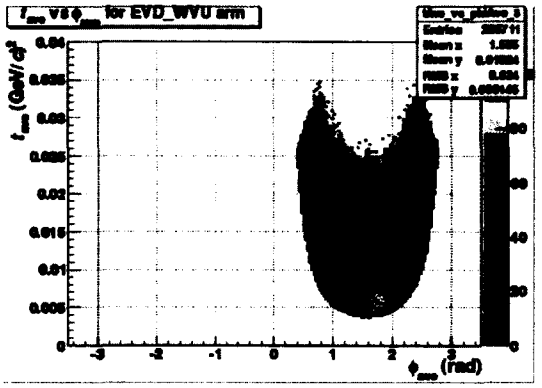

(d) t vs ϕ in EVD-WVU arm ($\chi^2 \leq 9$)

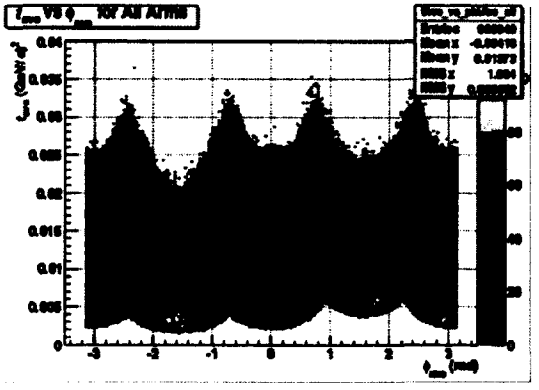

(e) t vs ϕ in all arms ($\chi^2 \leq 9$)

FIG. 81. t vs ϕ in elastic arms: (a) EHI-WHO; (b) EHO-WHI; (c) EVU-WVD; (d) EVD-WVU and (e) all arms together, for $\chi^2 \leq 9$ and run 10183028.

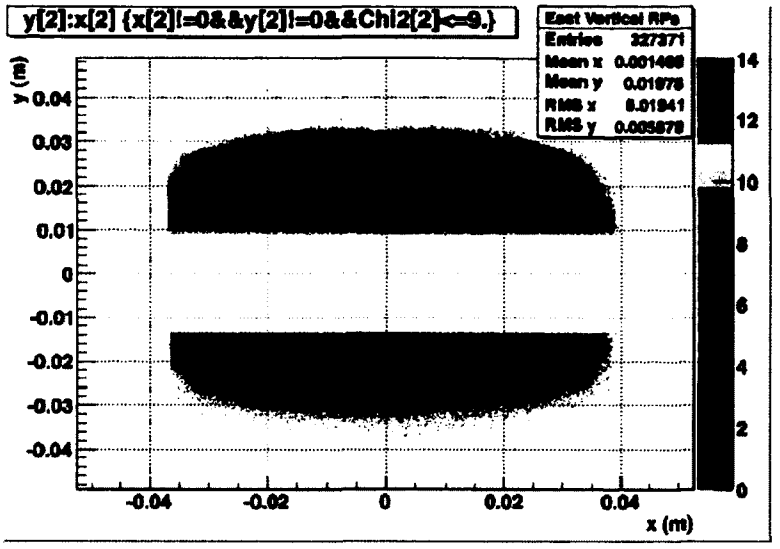

(a)

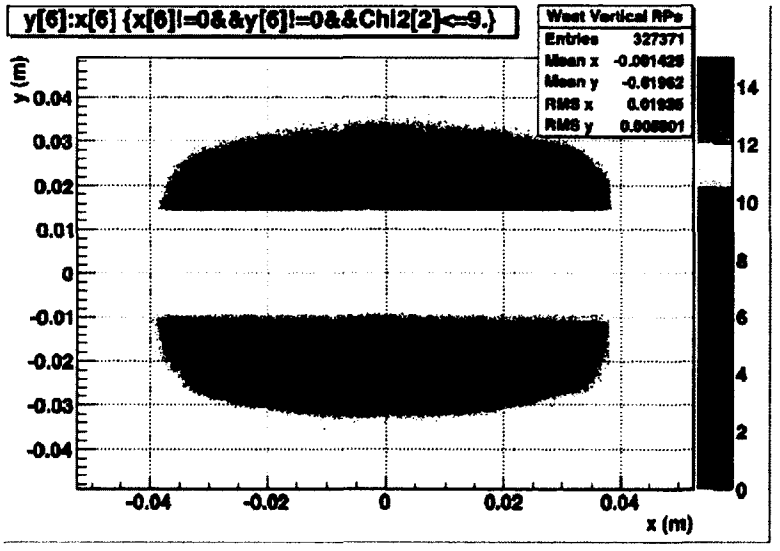

(b)

FIG. 82. Measured x and y positions of scattered protons in Vertical RPs: (a) East Vertical RPs and (b) West Vertical RPs, for run 10183028 and $\chi^2 \leq 9$. Compare with Fig. 65 to see the effect of the collinearity condition on the "hot" spot region.

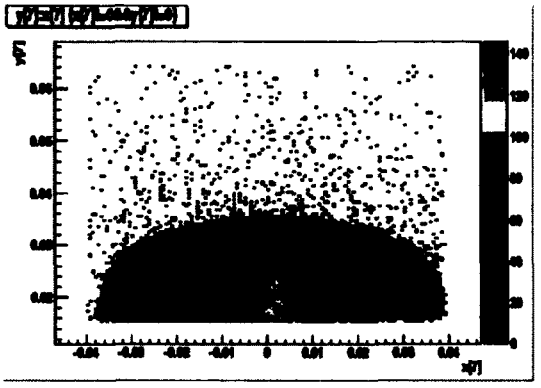

(a) Measured y vs x positions in WVU for run 10185018 (before χ^2 and fiducial cut)

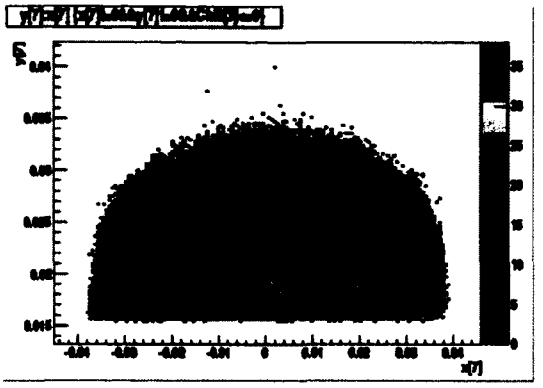

(b) Measured y vs x positions in WVU for run 10185018 (after $\chi^2 \leq 9$ collinearity cut)

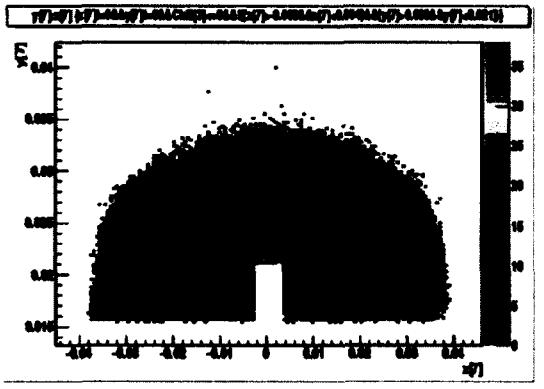

(c) Measured y vs x positions in WVU for run 10185018 (after collinearity and fiducial cut)

FIG. 83. Measured x and y positions in WVU before and after collinearity cut $\chi^2 \leq 9$ and fiducial cut, for run 10185018. The fiducial cut applied to the data, is a "square" cut in x and y, as shown in (c). The (x, y) coordinates of the cut are determined by examining the measured y vs x distributions for each RP and run during Run09. Regions in the RPs with considerably more events than the other regions, also called "hot spots" are excluded by the fiducial cut. The "hot spots" are observed mainly in vertical RPs and may be caused by the proximity of the RPs to the beam.

CHAPTER 7

RESULTS ON TRANSVERSE SINGLE SPIN ASYMMETRY A_N

7.1 CALCULATION OF THE RAW ASYMMETRY

In this chapter, I will explain how the raw asymmetries and the transverse single spin asymmetry are calculated using the selected elastic events (**STEP 5 of the analysis procedure given in Section 6.2**). For asymmetry analysis purposes, we group the runs in four main groups according to the RHIC fill/store number during Run09: 11020, 11026, 11030 and 11032 (see Table 13). Each store needs to be analyzed separately while calculating asymmetries since the polarization values of the two beams are slightly different for different stores.

7.1.1 BUNCH POLARIZATION PATTERN

During Run09, all possible polarization patterns of the Blue and Yellow beams were available, see Section 5.1. We can thus use the Blue and Yellow beam bunches with polarization pattern: $\uparrow\uparrow$, $\downarrow\downarrow$, $\uparrow\downarrow$ or $\downarrow\uparrow$ for P_B and P_Y, respectively, to build various asymmetries. We can use the so called "square-root formula" [18] to calculate the raw asymmetries ϵ_1, ϵ_2, ϵ_3 if we consider both beams (Blue and Yellow) to be polarized, and ϵ^B, ϵ^Y if we consider one beam polarized (Blue/Yellow) and the other unpolarized (Yellow/Blue), as given in Eq. (180) (see Eq. (117) in Section 2.8 for the derivation).

$$\epsilon = \frac{\sqrt{N_L^{++}N_R^{--}} - \sqrt{N_R^{++}N_L^{--}}}{\sqrt{N_L^{++}N_R^{--}} + \sqrt{N_R^{++}N_L^{--}}}, \tag{176}$$

$$\epsilon_1 = \frac{\sqrt{N^{++}(\phi)N^{--}(\pi-\phi)} - \sqrt{N^{++}(\pi-\phi)N^{--}(\phi)}}{\sqrt{N^{++}(\phi)N^{--}(\pi-\phi)} + \sqrt{N^{++}(\pi-\phi)N^{--}(\phi)}}, \tag{177}$$

$$= \frac{A_{\rm N}(P_b + P_y)\cos\phi}{1 + P_b P_y(A_{\rm NN}\cos^2\phi + A_{\rm SS}\sin^2\phi)},$$

$$\epsilon_2 = \frac{\sqrt{N^{++}(\phi)N^{--}(\pi+\phi)} - \sqrt{N^{++}(\pi+\phi)N^{--}(\phi)}}{\sqrt{N^{++}(\phi)N^{--}(\pi+\phi)} + \sqrt{N^{++}(\pi+\phi)N^{--}(\phi)}}, \tag{178}$$

$$= \frac{A_{\rm N}(P_b + P_y)\cos\phi}{1 + P_b P_y(A_{\rm NN}\cos^2\phi + A_{\rm SS}\sin^2\phi)},$$

$$\epsilon_3 = \frac{\sqrt{N^{+-}(\phi)N^{-+}(\pi-\phi)} - \sqrt{N^{+-}(\pi-\phi)N^{-+}(\phi)}}{\sqrt{N^{+-}(\phi)N^{--}(\pi-\phi)} + \sqrt{N^{++}(\pi-\phi)N^{--}(\phi)}}, \tag{179}$$

$$= \frac{A_N(P_b - P_y)\cos\phi}{1 - P_b P_y(A_{\rm NN}\cos^2\phi + A_{\rm SS}\sin^2\phi)},$$

where ϵ_1, ϵ_2 and ϵ_3 are the "raw asymmetries" for $(\uparrow\uparrow,\downarrow\downarrow)$ and $(\uparrow\downarrow,\downarrow\uparrow)$ spin combinations, N^{ij} are the unnormalized counts with $+$ for $\uparrow$ and $-$ for $\downarrow$ spin orientation and L and R stand for left and right in azimuthal space, respectively. The transverse single spin asymmetry $A_{\rm N}$ is defined as the left - right cross-section asymmetry with respect to the transversely polarized beams, see Eq. (176). N_L can be viewed as $N(\phi)$ and N_R as $N(\pi-\phi)$, in Eq. (177). Equations (177) and (178) represent two slightly different formulas for calculating the raw asymmetry ϵ with $\uparrow\uparrow$ and $\downarrow\downarrow$ spin combinations. The first formula, which we will call the $(\pi$ - $\phi)$ case for convenience, will be mainly used to measure the transverse single spin asymmetry in this experiment. However, the later formula, Eq. (178) is more appropriate to use while calculating the raw asymmetry if the spin of the beam particles are not exactly vertically polarized, but there is a spin-tilt from the vertical direction. We will call this case the $(\pi + \phi)$ case, and use it as a systematics check in this experiment.

The $A_{\rm NN}$ and $A_{\rm SS}$ terms are the transverse double spin asymmetries and P_b and P_y are the polarizations of the Blue and Yellow beams, respectively. $A_{\rm NN}$ is defined as the cross-section asymmetry in proton-proton scattering, with spin orientations parallel and anti-parallel with respect to the unit vector $\hat{n}$, normal to the scattering

plane. A_{SS} is defined analogously for both fully polarized beams along the unit vector $\hat{s}$ in the scattering plane and normal to the beam. A_{NN} and A_{SS} are predicted [17] and measured by PP2PP collaboration at $\sqrt{s} = 200$ GeV to be very small, [26]. This puts a constraint to the term $P_b P_y (A_{NN} \cos^2\phi + A_{SS} \sin^2\phi) \leq 0.002$, thus it can be safely neglected compared to 1, in the calculation of the single spin asymmetry.

The asymmetry ϵ_1 and ϵ_2 are proportional to the sum of the polarization values of the two beams, $(P_b + P_y)$. The asymmetry ϵ_3, on the other hand, is proportional to the difference of the two polarization values, $(P_b - P_y)$, and thus it is expected to be close to 0 or small, since the polarization values of the two beams are very close to each other. Any difference in the polarization values of the two beams may be due to beams being transported by two different sets of magnets, and thus the depolarizing effects on the beams may be different.

$$\epsilon^B = \frac{\sqrt{N_B^+(\phi)N_B^-(\pi-\phi)} - \sqrt{N_B^+(\pi-\phi)N_B^-(\phi)}}{\sqrt{N_B^+(\phi)N_B^-(\pi-\phi)} + \sqrt{N_B^+(\pi-\phi)N_B^-(\phi)}}, \tag{180}$$

$$= A_N P_b \cos\phi,$$

$$\epsilon^Y = \frac{\sqrt{N_Y^+(\phi)N_Y^-(\pi-\phi)} - \sqrt{N_Y^+(\pi-\phi)N_Y^-(\phi)}}{\sqrt{N_Y^+(\phi)N_Y^-(\pi-\phi)} + \sqrt{N_Y^+(\pi-\phi)N_Y^-(\phi)}}, \tag{181}$$

$$= A_N P_y \cos\phi,$$

where the term $P_b P_y (A_{NN} \cos^2\phi + A_{SS} \sin^2\phi)$, see Eq. (177), is zero when one beam is considered polarized and the other unpolarized.

We can also measure several other asymmetries, i.e. when we consider one beam to be polarized and the other unpolarized, see Eq. (182). In this case, ϵ^B, Eq. (180), is proportional to P_b only and ϵ^Y, Eq. (181), is proportional to P_y. If one compares ϵ_1 with ϵ^B or ϵ^Y, one would expect that:

$$\frac{\epsilon_1}{\epsilon^B} \approx \frac{\epsilon_1}{\epsilon^Y} \approx 2. \tag{182}$$

7.1.2 t and ϕ BIN SIZE SELECTION

For the measurement of the transverse single spin asymmetry A_N we divided the covered t-range 0.003 GeV/c^2 $\leq |t| \leq$ 0.035 GeV/c^2 into 5 t bins, as follows:

1. $-t < 0.005$ GeV/c^2

2. 0.005 GeV/$c^2 \leq -t < 0.01$ GeV/c^2

3. 0.01 GeV/$c^2 \leq -t < 0.015$ GeV/c^2

4. 0.015 GeV/$c^2 \leq -t < 0.02$ GeV/c^2

5. $-t \geq 0.02$ GeV/c^2

Subsequently, in each t-bin we subdivide the ϕ distributions into 36 bins of 10° per bin. Now, we can proceed using the square-root formula to calculate the raw asymmetries for each case in Eq. (180) and (182), then divide by appropriate polarization values to obtain the various asymmetries mentioned above.

7.2 CALCULATION OF THE TRANSVERSE SINGLE SPIN ASYMMETRY $\epsilon(\phi)/(P_B + P_Y)$

STEP 6. Calculation of $\epsilon(\phi)/(P_b + P_y)$

By using Equations (180) and (182), we can calculate the various raw asymmetries ϵ given in the previous Section 7.1. The next analysis step is to divide the calculated raw asymmetries with the appropriate polarization values, in order to achieve $\epsilon(\phi)/(P_b + P_y)$ values. In the following sections we will present results on $\epsilon(\phi)/(P_b + P_y)$ and raw asymmetries as a function of azimuthal angle ϕ (various asymmetries) in 5 t-bins and also in the combined-t range, for the (π - ϕ) and (π + ϕ) cases. The measured raw asymmetries ϵ for $\uparrow\uparrow$ and $\downarrow\downarrow$ spin combinations are fit with a cos-function, cos(ϕ) in (π - ϕ) case and cos($\phi + \delta\phi$) in (π + ϕ) case. The different fitting function used in (π + ϕ) case, including the additional parameter $\delta\phi$ in the fit, takes into account the possible tilt of the spin direction from the vertical direction. The raw asymmetries for $\uparrow\downarrow$ and $\downarrow\uparrow$ spin combinations are measured with a linear function in ϕ, again allowing an additional parameter in the fit for the (π + ϕ) case.

7.2.1 (π - ϕ) CASE

$\epsilon(\phi)/(P_b + P_y)$ vs ϕ for separate t-bins, $\uparrow\uparrow$ and $\downarrow\downarrow$ Spin Combinations

The plots given in Fig. 84 show $\epsilon(\phi)/(P_b + P_y)$ as a function of ϕ, for $\uparrow\uparrow$ and $\downarrow\downarrow$ spin combinations and (π - ϕ) case, thus calculated using Eq. (177) for 5 separate t-bins and combined-t range.

Raw Asymmetry vs ϕ for separate t-bins, $\uparrow\downarrow$ and $\downarrow\uparrow$ Spin Combinations

The plots given in Fig. 85 show raw asymmetry $\epsilon(\phi)\sim(P_b - P_y)$ as a function of ϕ, for $\uparrow\downarrow$ and $\downarrow\uparrow$ spin combinations and (π - ϕ) case, calculated using Eq. (179) for 5 separate t-bins and combined-t range.

$\epsilon(\phi)/(P_b + P_y)$ vs ϕ (Assuming: Blue/Yellow beam polarized only) for separate t-bins, $\uparrow$ and $\downarrow$ Spin Orientations

The plots given in Figs. 86 and 87 show $\epsilon(\phi)/(P_b+P_y)$ as a function of ϕ for the one beam polarized case (assuming Blue and Yellow beam polarized only, respectively), for $\uparrow$ and $\downarrow$ spin orientations and (π - ϕ) case, thus calculated using Eq. (180) and Eq. (181), respectively, for 5 separate t-bins and combined-t range.

7.2.2 (π + ϕ) CASE

$\epsilon(\phi)/(P_b + P_y)$ vs ϕ for separate t-bins, $\uparrow\uparrow$ and $\downarrow\downarrow$ Spin Combinations

The plots given in Fig. 88 show $\epsilon(\phi)/(P_b + P_y)$ as a function of ϕ, for $\uparrow\uparrow$ and $\downarrow\downarrow$ spin combinations and (π + ϕ) case, thus calculated using Eq. (178) for 5 separate t-bins and combined-t range.

Raw Asymmetry vs ϕ for separate t-bins, $\uparrow\downarrow$ and $\downarrow\uparrow$ Spin Combinations

The plots given in Fig. 89 show raw asymmetry $\epsilon(\phi)\sim(P_b - P_y)$ as a function of ϕ, for $\uparrow\downarrow$ and $\downarrow\uparrow$ spin combinations and (π + ϕ) case.

$\epsilon(\phi)/(P_b + P_y)$ vs ϕ (Assuming: Blue/Yellow beam polarized only) for separate t-bins, $\uparrow$ and $\downarrow$ Spin Orientations and $(\pi + \phi)$ case

The plots given in Fig. 90 and Fig. 91 show $\epsilon(\phi)/(P_b + P_y)$ as a function of ϕ for the One Beam Polarized Case (assuming Blue and Yellow beam polarized only, respectively), for $\uparrow$ and $\downarrow$ spin orientations and $(\pi + \phi)$ case, thus calculated using Eq. (180) and Eq. (181), respectively, for 5 separate t-bins and combined-t range.

There is a general trend shown in the asymmetry plots given in following figures (Fig. 84, 86, 87, 88, 90 and 91), the maximum asymmetry is observed in the horizontal plane (at azimuthal angle $\phi \leq 0$ according to our chosen coordinate system). The asymmetry drops to 0 in the vertical plane (Vertical RPs, $\phi = \pi/2$ and $-\pi/2$).

The measured asymmetry for $\uparrow\downarrow$ and $\downarrow\uparrow$ spin combinations (False Asymmetry) is very small or 0 as expected, since this asymmetry is proportional to the difference of the polarization values of the two beams $(P_b - P_y)$, (see Fig. 85, 89).

To check for the relation given in Eq. (184), the difference in the measured asymmetry between the "One Beam Polarized" and "Both Beams Polarized" cases, we can look at the asymmetry plots given in Fig. 92(a) and Fig. 92(b), and compare to Fig 92(c), for $(\pi$ - $\phi)$ case. Look at Fig. 93(a) and Fig. 93(b) and compare to Fig 92(c), for $(\pi + \phi)$ case.

After inspecting the plots, we can calculate the following ratios of asymmetries for the cases given above:

$$\begin{array}{lcll} & (\pi - \phi) & Case & \\ \dfrac{\epsilon_1}{\epsilon^B} & = & \dfrac{0.02743}{0.01351} \approx 2.03, & \\ \dfrac{\epsilon_1}{\epsilon^Y} & = & \dfrac{0.02743}{0.01412} \approx 1.94. & (183) \end{array}$$

$$\begin{array}{lcll} & (\pi + \phi) & Case & \\ \dfrac{\epsilon_1}{\epsilon^B} & = & \dfrac{0.02776}{0.01373} \approx 2.02, & \\ \dfrac{\epsilon_1}{\epsilon^Y} & = & \dfrac{0.02743}{0.01425} \approx 1.92. & (184) \end{array}$$

7.2.3 $\epsilon(\phi)/(P_B + P_Y)$ DEPENDENCE on t

Table 22 summarizes the A_N results for 5 $-t$ bins, for $(\pi$ - $\phi)$ case, given in Fig. 84 and for $(\pi + \phi)$ case given in Fig. 88. The $-t$ range, number of events in each

TABLE 22. A_N values in 5 $-t$-ranges and corresponding statistical uncertainties, for both (π - ϕ) and (π + ϕ) cases and "both beams polarized with ↑↑ and ↓↓ spin combinations of bunches per beam".

$-t$ range (GeV/c)^2	< 0.005	0.005 - 0.01	0.01 - 0.015	0.015 - 0.02	> 0.02
No. of Events	494710	2175468	2848620	2872958	2566903
$\langle -t \rangle$ (GeV/c)^2	0.0039	0.0077	0.0125	0.0175	0.0233
δt (GeV/c)^2 (stat.)	9.8E-07	6.6E-07	7.3E-07	8.6E-07	1.0E-07
(π - ϕ) Case					
A_N	0.0402	0.0300	0.0226	0.0197	0.0170
δA_N (stat.)	0.0019	0.0009	0.0008	0.0008	0.0008
(π + ϕ) Case					
A_N	0.0411	0.0303	0.0230	0.0198	0.0172
δA_N (stat.)	0.0021	0.0009	0.0008	0.0008	0.0008
$\delta\phi$ (degree)	-6.908	-6.374	-9.173	-6.478	-8.053
stat. error on $\delta\phi$ (degree)	5.813	2.043	2.154	2.473	3.440

range and the mean $-t$ value for each bin is shown. Statistical errors for t andA_N are also given. Statistical errors for t are negligible.

The uncertainty in the t-scale is mostly due to the beam angular divergence. To calculate how the uncertainty in the t-scale from the angular beam divergence we can start from using the expression for the momentum transfer squared t, given in Eq. (168).

$$-t = p^2\theta^2. \tag{185}$$

Taking the first derivative with respect to θ, the uncertainty on t due to beam angular divergence is then:

$$\delta(-t) = 2p \times \sqrt{-t} \times \delta(\theta), \tag{186}$$

where the beam momentum $p = 100.2$ GeV/c and $\delta(\theta) = 54$ μrad based on the study of the elastic event distributions $\delta(\theta)$, calculated as a weighted average (all runs) of the σ of the $\delta(\theta)$ distribution of each elastic arm, see Fig. 94. This gives a value for $\delta(t)$ due to the beam angular divergence:

$$\delta(t) \approx 0.011 \times \sqrt{-t}. \tag{187}$$

TABLE 23. A_N values in 5 $-t$-ranges and corresponding statistical uncertainties, for (π - ϕ), "both beams polarized" and "one beam polarized" cases.

$-t$ range (GeV/c)^2	< 0.005	0.005 - 0.01	0.01 - 0.015	0.015 - 0.02	> 0.02
No. of Events	494710	2175468	2848620	2872958	2566903
Both Beams Pol.					
A_N	0.0402	0.0300	0.0226	0.0197	0.0170
δA_N (stat.)	0.0019	0.0009	0.0008	0.0008	0.0008
No. of Events	984073	4322717	5654199	5704735	5094463
Blue Beam Pol.					
A_N	0.0423	0.0294	0.0228	0.0204	0.0165
δA_N (stat.)	0.0014	0.0007	0.0006	0.0006	0.0006
No. of Events	983076	4319604	5650932	5701495	5092295
Yellow Beam Pol.					
A_N	0.0388	0.0312	0.0228	0.0193	0.0177
δA_N (stat.)	0.0014	0.0007	0.0006	0.0006	0.0006

The uncertainty in t for the data sample (number of events = N) used in the calculation of the single spin asymmetry (thus events coming from collision of bunches with $\uparrow\uparrow$ and $\downarrow\downarrow$ spin combinations), was calculated using $\delta(-t) \approx \frac{0.011 \times \sqrt{t}}{\sqrt{N}}$ (GeV/c)^2, for each t-bin. These results are given in the 4^{th} row of Table 22.

Table 23 summarizes the results of the A_N values and the corresponding statistical uncertainties per each t-bin, for cases when polarization of both is considered and the case when one beam (blue/yellow) is considered polarized and the other one "unpolarized" and for (π - ϕ) case. The number of events in each t-bin for the "one beam polarized" case is twice as large as the number of events for the "both beams polarized" case, thus the statistical error associated with the A_N values in each t-bin is smaller in the former case compared to the later. The A_N values in both cases is about the same, as expected.

7.2.4 COMPARISON WITH THE THEORETICAL MODEL

The plots given in Fig. 95 present A_N dependence on four-momentum transfer squared t, for the (π - ϕ) and (π + ϕ) cases. There are five data points (red in Fig. 95(a) and green in Fig. 95(b)), representing the A_N for 5 $-t$-bins for each case. The solid curve (blue in Fig. 95(a) and green in Fig. 95(b)) is the best fit to the data.

The dotted curve is the theoretical calculation in the absence of the hadronic spin-flip amplitude.

It has been shown in Eq. (177) that the single spin asymmetry A_N depends also on the double spin asymmetries A_{NN} and A_{SS}. However, it has been theoretically shown [17] and experimentally determined by the PP2PP collaboration at RHIC [25], that the contribution of the two double spin-flip hadronic amplitudes ϕ_2^{had} and ϕ_4^{had} to the single spin asymmetry A_N is small. The main contribution to A_N is given in terms of the helicity amplitudes ϕ and mainly the interference between the electromagnetic spin-flip amplitude (ϕ_5^{em*}) and hadronic non-flip amplitude (ϕ_+^{had}), as shown in Eq. (188). The second term is the interference between the electromagnetic non-flip amplitude (ϕ_5^{em}) and a possible hadronic spin-flip amplitude (ϕ_+^{had*}), if the later exists in the Pomeron exchange mechanism. The hadronic spin-flip amplitude (ϕ_5^{had}) is usually expressed in terms of (ϕ_+^{had}) as: $\phi_5^{had}(s,t) = (\sqrt{-t}/\mathrm{m}) \cdot r_5(s) \cdot \mathrm{Im}\phi_+^{had}(s,t)$, where m is the proton mass. A contribution from the hadronic spin-flip amplitude to elastic scattering is parametrized by the relative amplitude r_5, see Eq. (189).

$$A_N \frac{d\sigma}{dt} = -\frac{8\pi}{s^2} \mathrm{Im}(\phi_5^{em*}\phi_+^{had} + \phi_5^{had*}\phi_+^{em}), \tag{188}$$

where $\phi_+ = (\phi_1 + \phi_3)/2$ and ϕ_1, ϕ_3 are the spin non-flip helicity amplitudes.

$$r_5 = \frac{m_p \phi_5^{had*}}{\sqrt{-t}\mathrm{Im}\phi_+^{had}}. \tag{189}$$

The data presented in Fig. 95 is fitted using the formula given in Eq. (190), where the r_5 value ($\mathrm{Im}(r_5)$ and $\mathrm{Re}(r_5)$ parameters) are left as free parameters in the fitting function in order to extract their values from the best fit to the data.

$$A_N = \frac{\sqrt{-t}}{m} \frac{[\kappa(1-\rho\,\delta) + 2(\delta\,\mathrm{Re}\,r_5 - \mathrm{Im}\,r_5)]\frac{t_c}{t} - 2(\mathrm{Re}\,r_5 - \rho\,\mathrm{Im}\,r_5)}{(\frac{t_c}{t})^2 - 2(\rho+\delta)\frac{t_c}{t} + (1+\rho^2)}. \tag{190}$$

In this formula $t_c = -8\pi\alpha/\sigma_{tot}$, κ is the anomalous magnetic moment of the proton, $\rho = \mathrm{Re}\phi_+/\mathrm{Im}\phi_+$ is the ratio of the real to imaginary parts of non-flip elastic amplitude, and δ is the relative phase between the Coulomb and hadronic amplitudes [16]:

$$\delta = \alpha \ln \frac{2}{|t|(B + 8/\Lambda^2)} - \alpha\,\gamma, \tag{191}$$

where B is the slope of the forward peak in elastic scattering, α is the fine structure constant, Euler's constant $\gamma = 0.5772$ and $\Lambda^2 = 0.71\ \mathrm{GeV/c^2}$.

TABLE 24. False asymmetry results or $\epsilon_N \sim P_b - P_y$ for $(\pi - \phi)$ and $(\pi + \phi)$ cases.

$-t$ range $(\mathrm{GeV}/c)^2$	< 0.005	0.005 - 0.01	0.01 - 0.015	0.015 - 0.02	> 0.02
Both Beams Pol. ($\uparrow\downarrow$ & $\downarrow\uparrow$)					
$(\pi - \phi)$ Case					
$\epsilon_N \sim P_b - P_y$	0.0022	-0.0010	-0.0004	0.0005	-0.0009
$\delta\epsilon_N$ (stat.)	0.0016	0.0007	0.0006	0.0006	0.0006
$(\pi + \phi)$ Case					
$\epsilon_N \sim P_b - P_y$	-0.0004	-0.0021	-0.0015	-0.0003	0.0004
$\delta\epsilon_N$ (stat.)	0.0003	0.0018	0.0007	0.0006	0.0006
$\delta\phi$	0.0001	-2.6E-05	1.3E-05	1.3E-05	6.1E-07
stat. error on $\delta\phi$	6.0E-05	1.5E-05	1.2E-05	1.2E-05	1.6E-05

TABLE 25. r_5 Values extracted from the fit of the A_N dependence on t plots for various asymmetry cases.

	$P_b + P_y$ $(\pi$ - $\phi)$	$P_b + P_y$ $(\pi + \phi)$	P_b $(\pi$ - $\phi)$	P_y $(\pi$ - $\phi)$
Re[r_5]	0.0016	6.6E-05	0.0009	0.0003
δRe[r_5] (stat.)	0.0021	0.0021	0.0015	0.0015
Im[r_5]	0.0065	-0.0085	-0.0110	0.0051
δIm[r_5] (stat.)	0.0350	0.0359	0.0248	0.0247

Table 24 summarizes the false asymmetry or the asymmetry calculated using $\uparrow\downarrow$ & $\downarrow\uparrow$ spin combinations. The false asymmetry is proportional to $P_b - P_y$, and thus it is expected to be small. Finally, the real and imaginary parts of the r_5 parameter extracted from the A_N dependence on t plots for various asymmetry cases, are presented in Table 25.

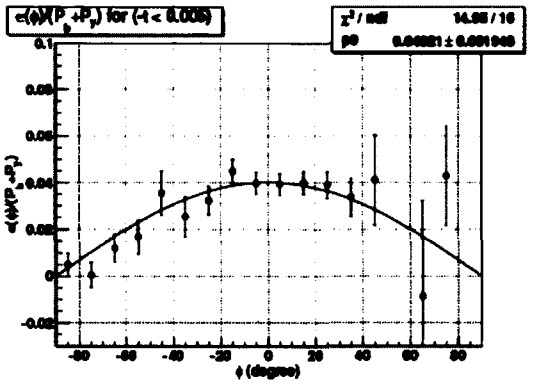

(a) $\epsilon(\phi)/(P_b + P_y)$ for -t < 0.005 GeV/c^2

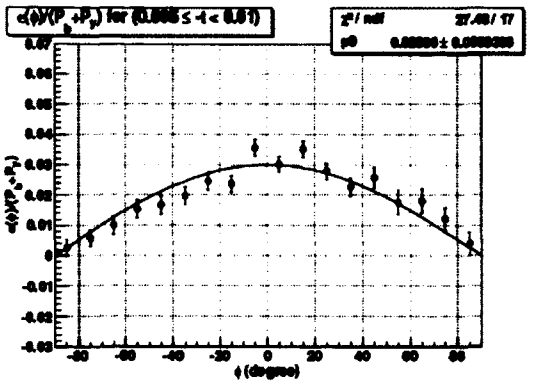

(b) $\epsilon(\phi)/(P_b+P_y)$ for 0.005 $\leq$ -t < 0.01 GeV/c^2

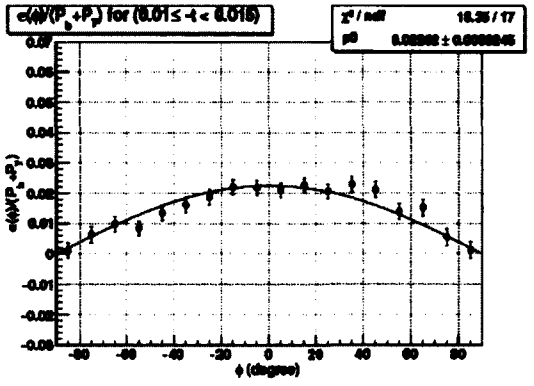

(c) $\epsilon(\phi)/(P_b+P_y)$ for 0.01 $\leq$ -t < 0.015 GeV/c^2

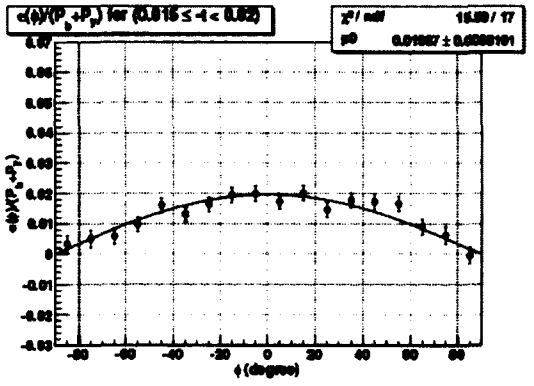

(d) $\epsilon(\phi)/(P_b+P_y)$ for 0.015 $\leq$ -t < 0.02 GeV/c^2

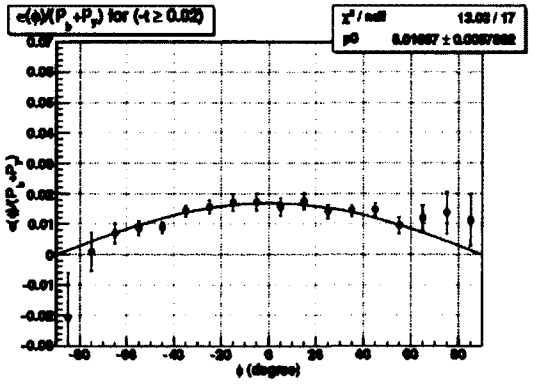

(e) $\epsilon(\phi)/(P_b + P_y)$ for -t $\geq$ 0.02 GeV/c^2

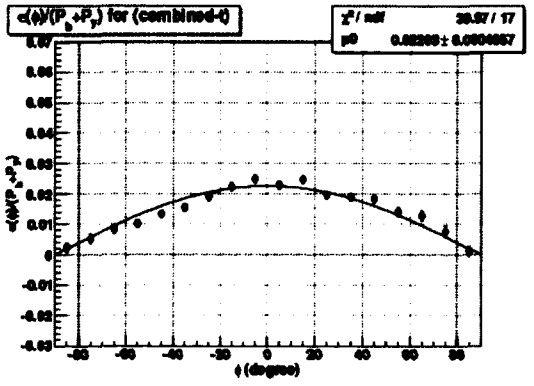

(f) $\epsilon(\phi)/(P_b + P_y)$ for combined-t range

FIG. 84. Asymmetry $\epsilon(\phi)/(P_b + P_y)$ as a function of ϕ, for $\uparrow\uparrow$ and $\downarrow\downarrow$ spin combinations and (π - ϕ) case, for 5 t-bins (a - e) and combined-t range (f).

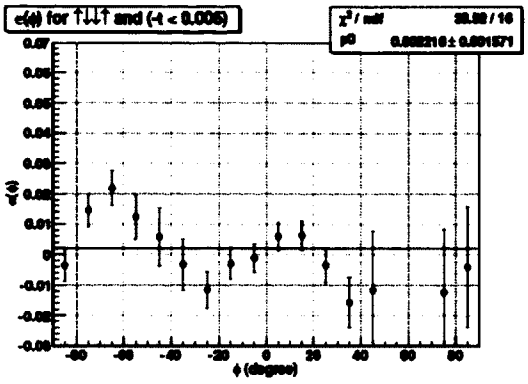

(a) $\epsilon(\phi)\sim(P_b - P_y)$ for $-t < 0.005$ GeV/c^2

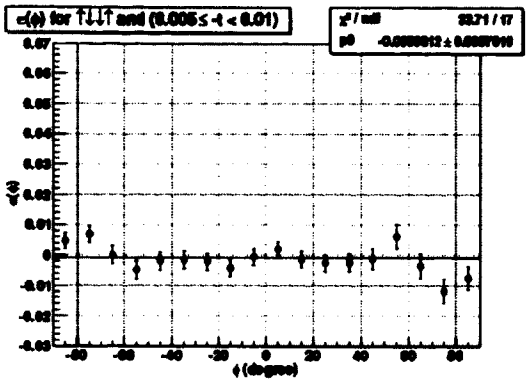

(b) $\epsilon(\phi)\sim(P_b - P_y)$ for $0.005 \leq -t < 0.01$ GeV/c^2

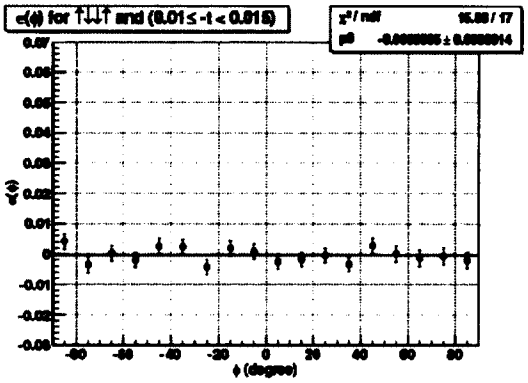

(c) $\epsilon(\phi)\sim(P_b - P_y)$ for $0.01 \leq -t < 0.015$ GeV/c^2

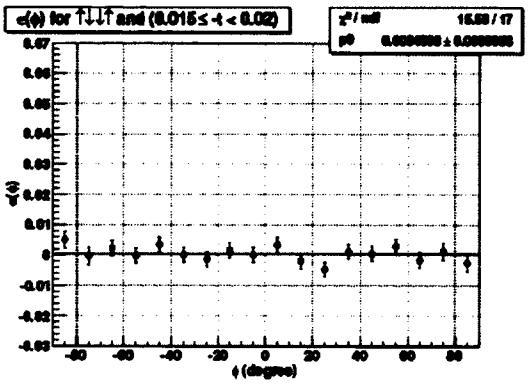

(d) $\epsilon(\phi)\sim(P_b - P_y)$ for $0.015 \leq -t < 0.02$ GeV/c^2

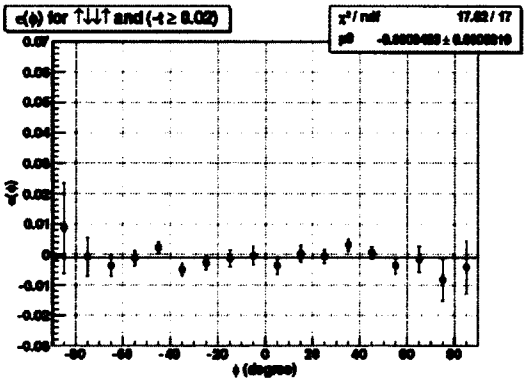

(e) $\epsilon(\phi)\sim(P_b - P_y)$ for $-t \geq 0.02$ GeV/c^2

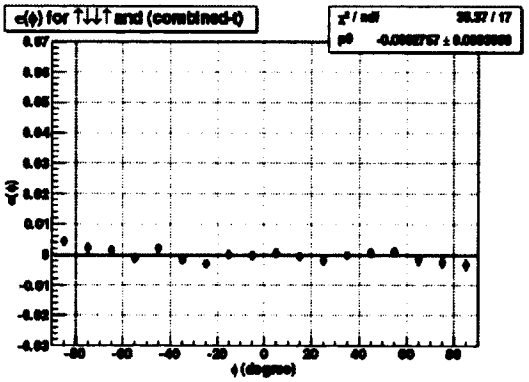

(f) $\epsilon(\phi)\sim(P_b - P_y)$ for combined-t range

FIG. 85. Asymmetry $\epsilon(\phi)\sim(P_b - P_y)$ as a function of ϕ, for $\uparrow\downarrow$ and $\downarrow\uparrow$ spin combinations and (π - ϕ) case, for 5 t-bins (a - e) and combined-t range (f).

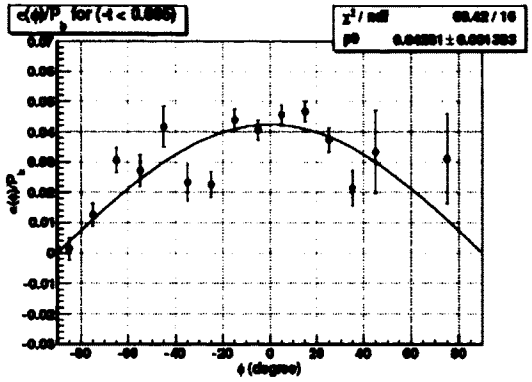

(a) $\epsilon(\phi)/P_b$ for -t < 0.005 GeV/c^2

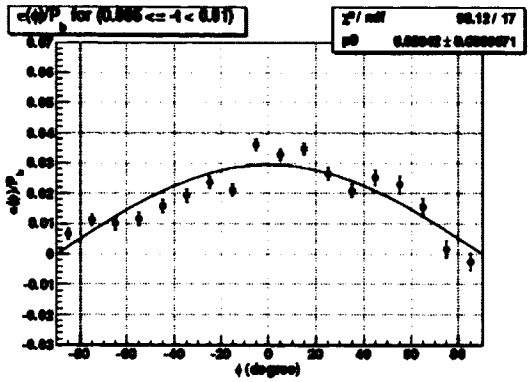

(b) $\epsilon(\phi)/P_b$ for 0.005 ≤ -t < 0.01 GeV/c^2

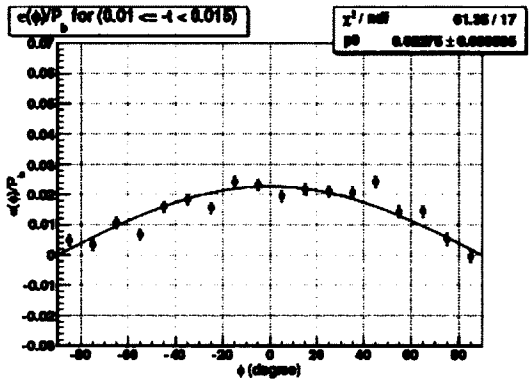

(c) $\epsilon(\phi)/P_b$ for 0.01 ≤ -t < 0.015 GeV/c^2

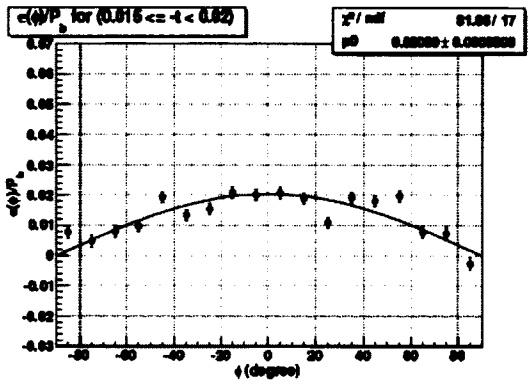

(d) $\epsilon(\phi)/P_b$ for 0.015 ≤ -t < 0.02 GeV/c^2

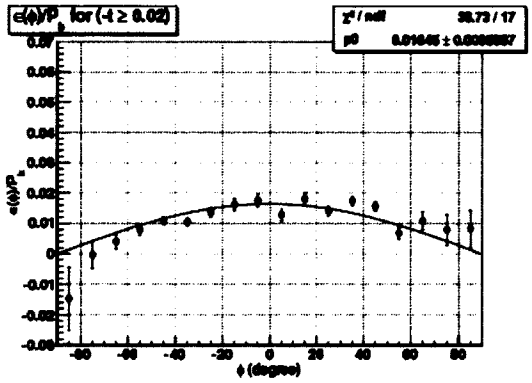

(e) $\epsilon(\phi)/P_b$ for -t ≥ 0.02 GeV/c^2

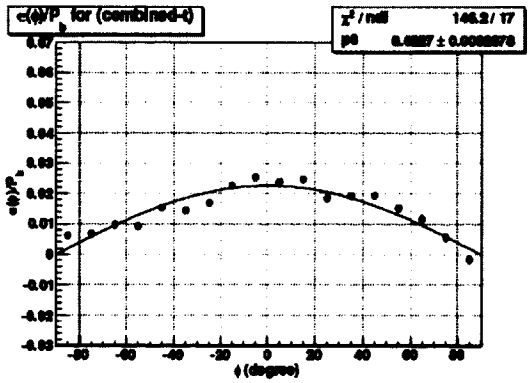

(f) $\epsilon(\phi)/P_b$ for combined-t range

FIG. 86. Asymmetry $\epsilon(\phi)/P_b$ as a function of ϕ ("Blue beam polarized only" case), for ↑ and ↓ spin combinations and (π - ϕ) case, for 5 t-bins (a - e) and combined-t range (f).

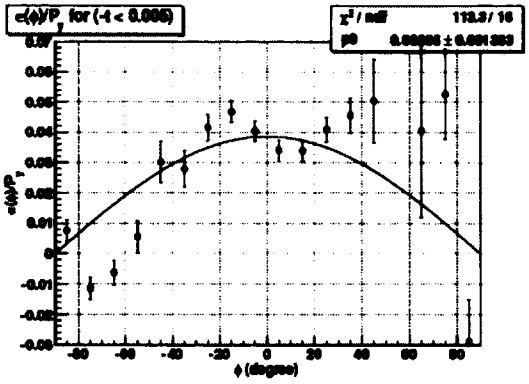

(a) $\epsilon(\phi)/P_y$ for -t < 0.005 GeV/c^2

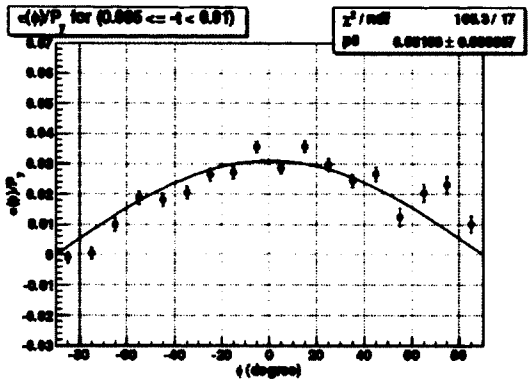

(b) $\epsilon(\phi)/P_y$ for 0.005 ≤ -t < 0.01 GeV/c^2

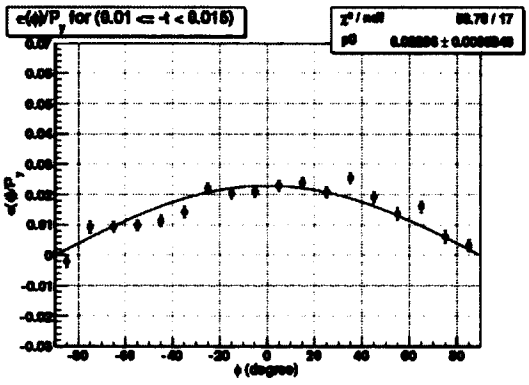

(c) $\epsilon(\phi)/P_y$) for 0.01 ≤ -t < 0.015 GeV/c^2

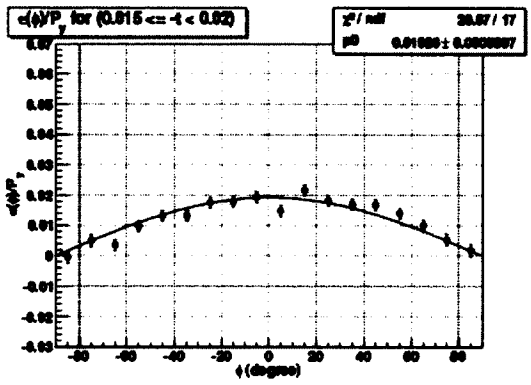

(d) $\epsilon(\phi)/P_y$ for 0.015 ≤ -t < 0.02 GeV/c^2

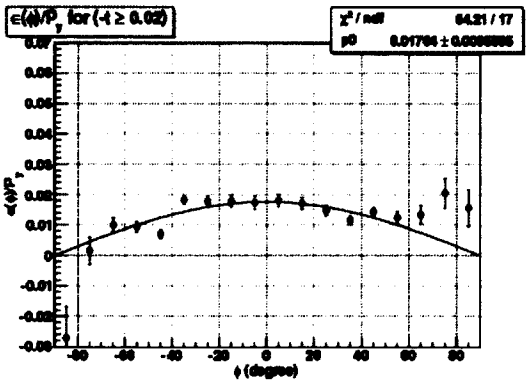

(e) $\epsilon(\phi)/P_y$ for -t ≥ 0.02 GeV/c^2

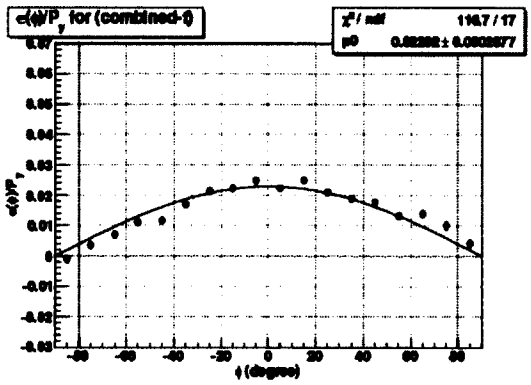

(f) $\epsilon(\phi)/P_y$ for combined-t range

FIG. 87. Asymmetry $\epsilon(\phi)/P_y$ as a function of ϕ ("Yellow beam polarized only" case), for ↑ and ↓ spin combinations and (π - ϕ) case, for 5 t-bins (a - e) and combined-t range (f).

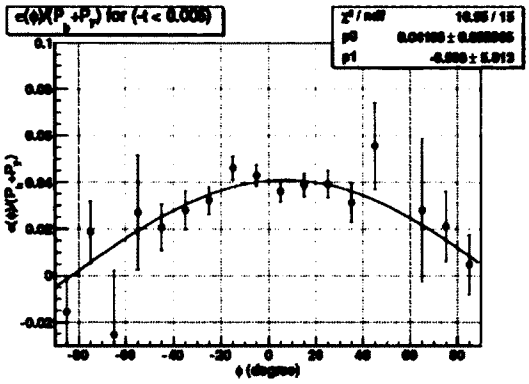

(a) $\epsilon(\phi)/(P_b + P_y)$ for -t < 0.005 GeV/c^2

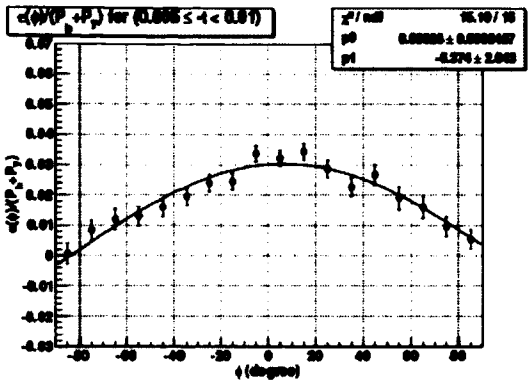

(b) $\epsilon(\phi)/(P_b+P_y)$ for 0.005 $\leq$ -t < 0.01 GeV/c^2

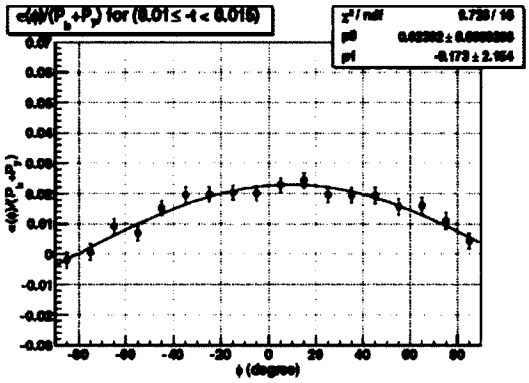

(c) $\epsilon(\phi)/(P_b+P_y)$ for 0.01 $\leq$ -t < 0.015 GeV/c^2

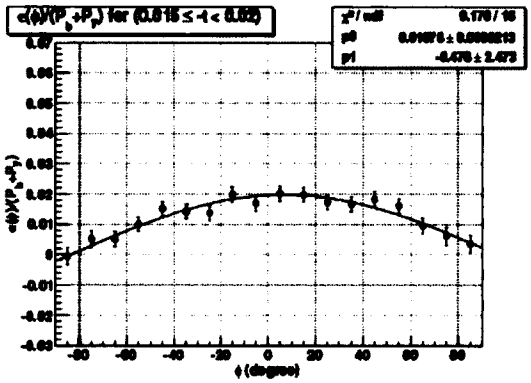

(d) $\epsilon(\phi)/(P_b+P_y)$ for 0.015 $\leq$ -t < 0.02 GeV/c^2

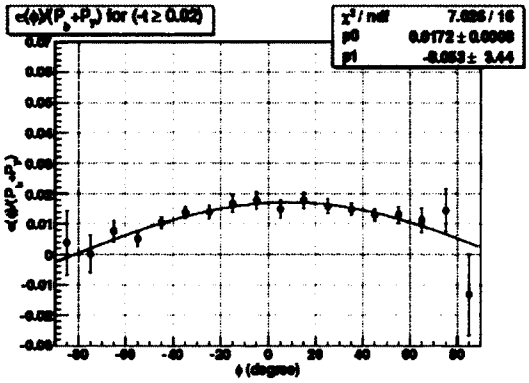

(e) $\epsilon(\phi)/(P_b + P_y)$ for -t $\geq$ 0.02 GeV/c^2

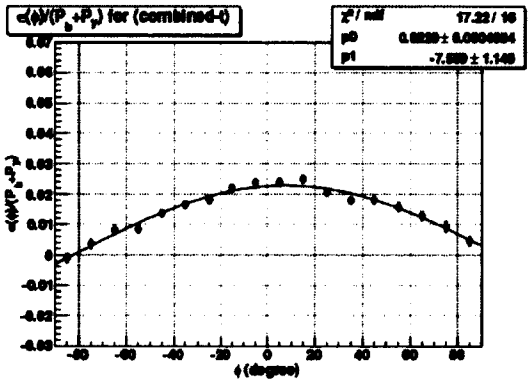

(f) $\epsilon(\phi)/(P_b + P_y)$ for combined-t range

FIG. 88. Asymmetry $\epsilon(\phi)/(P_b + P_y)$ as a function of ϕ, for $\uparrow\uparrow$ and $\downarrow\downarrow$ spin combinations and $(\pi + \phi)$ case, for 5 t-bins (a - e) and combined-t range (f).

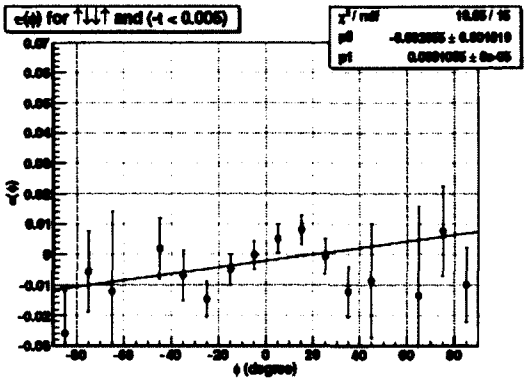

(a) $\epsilon(\phi)\sim(P_b - P_y)$ for -t < 0.005 GeV/c^2

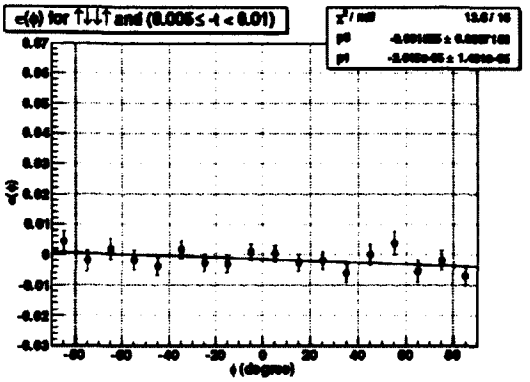

(b) $\epsilon(\phi)\sim(P_b - P_y)$ for 0.005 $\leq$ -t < 0.01 GeV/c^2

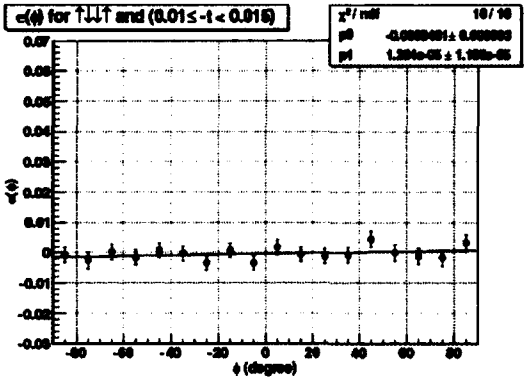

(c) $\epsilon(\phi)\sim(P_b - P_y)$ for 0.01 $\leq$ -t < 0.015 GeV/c^2

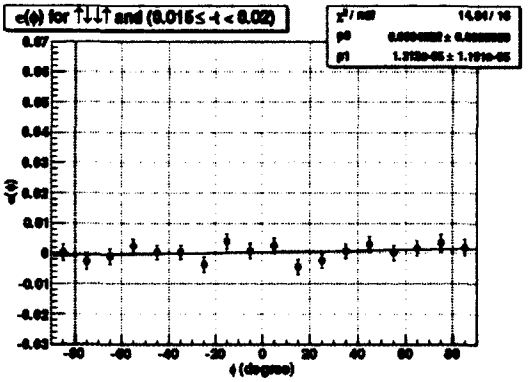

(d) $\epsilon(\phi)\sim(P_b - P_y)$ for 0.015 $\leq$ -t < 0.02 GeV/c^2

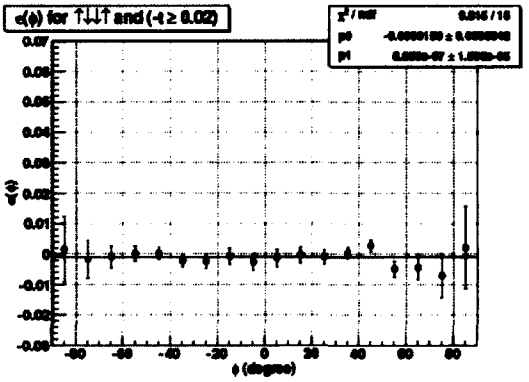

(e) $\epsilon(\phi)\sim(P_b - P_y)$ for -t $\geq$ 0.02 GeV/c^2

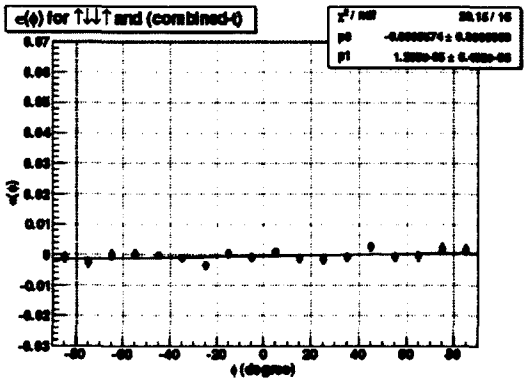

(f) $\epsilon(\phi)\sim(P_b - P_y)$ for combined-t range

FIG. 89. Asymmetry $\epsilon(\phi)\sim(P_b - P_y)$ as a function of ϕ, for $\uparrow\downarrow$ and $\downarrow\uparrow$ spin combinations and $(\pi + \phi)$ case, for 5 t-bins (a - e) and combined-t range (f).

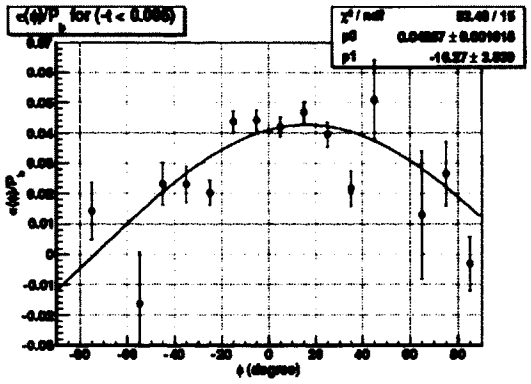

(a) $\epsilon(\phi)/P_b$ for -t < 0.005 GeV/c^2

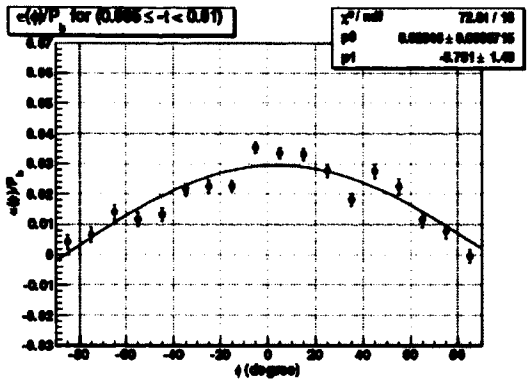

(b) $\epsilon(\phi)/P_b$ for 0.005 ≤ -t < 0.01 GeV/c^2

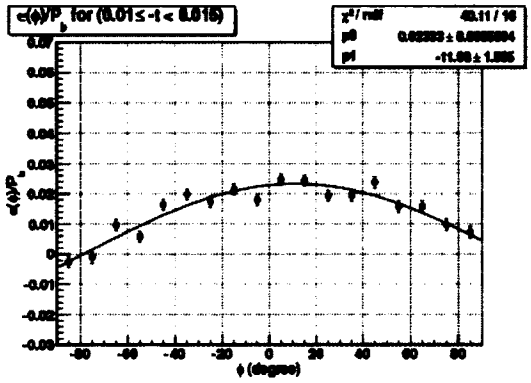

(c) $\epsilon(\phi)/P_b$ for 0.01 ≤ -t < 0.015 GeV/c^2

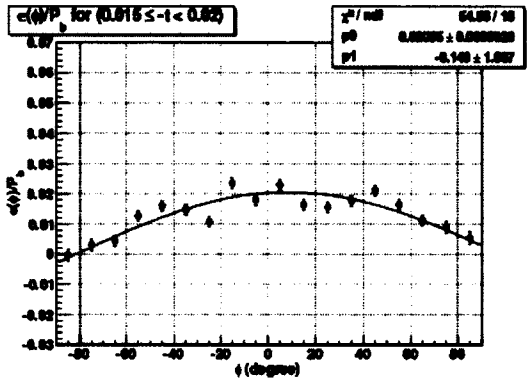

(d) $\epsilon(\phi)/P_b$ for 0.015 ≤ -t < 0.02 GeV/c^2

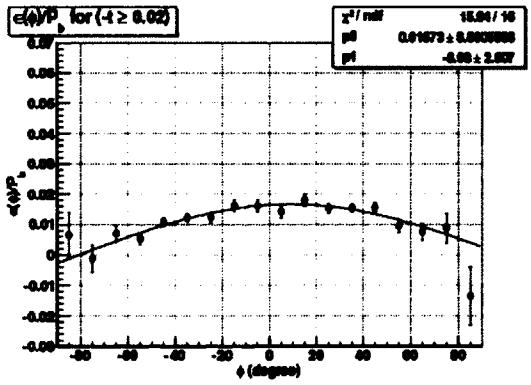

(e) $\epsilon(\phi)/P_b$ for -t ≥ 0.02 GeV/c^2

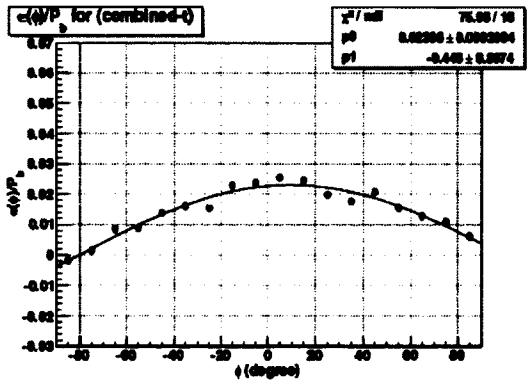

(f) $\epsilon(\phi)/P_b$ for combined-t range

FIG. 90. Asymmetry $\epsilon(\phi)/P_b$ ("Blue beam polarized only" case), for ↑ and ↓ spin orientations and ($\pi + \phi$) case, for 5 t-bins (a - e) and combined-t range (f).

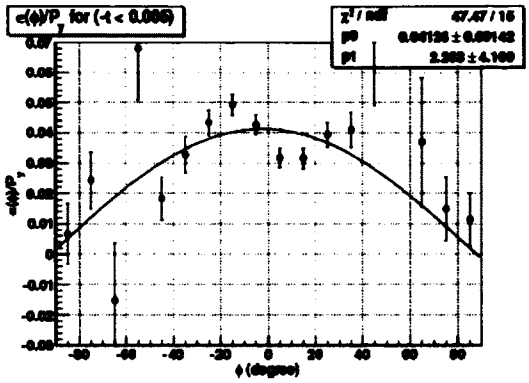

(a) $\epsilon(\phi)/P_y$ for -t < 0.005 GeV/c^2

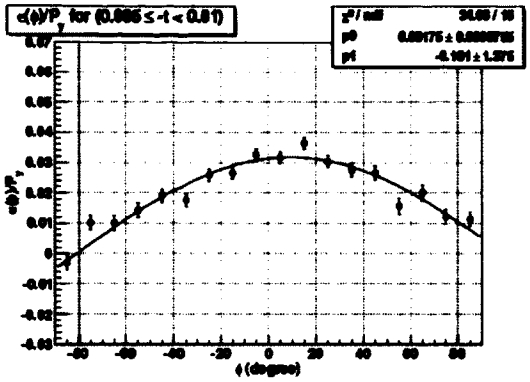

(b) $\epsilon(\phi)/P_y$ for 0.005 ≤ -t < 0.01 GeV/c^2

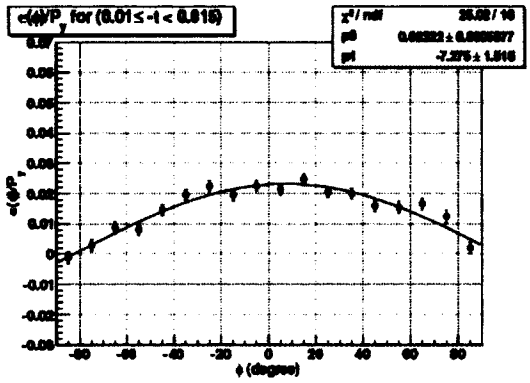

(c) $\epsilon(\phi)/P_y$ for 0.01 ≤ -t < 0.015 GeV/c^2

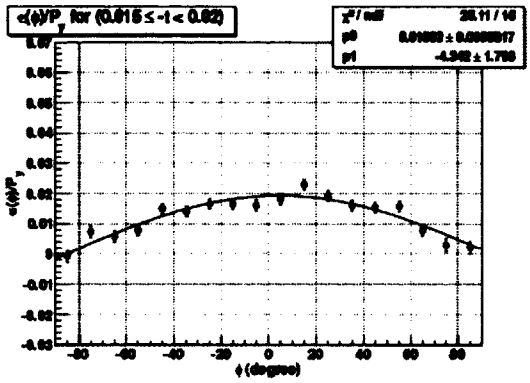

(d) $\epsilon(\phi)/P_y$ for 0.015 ≤ -t < 0.02 GeV/c^2

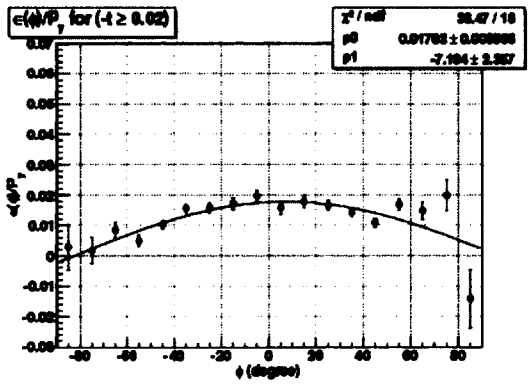

(e) $\epsilon(\phi)/P_y$ for -t ≥ 0.02 GeV/c^2

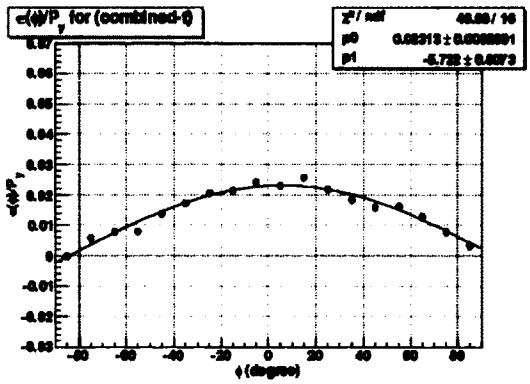

(f) $\epsilon(\phi)/P_y$ for combined-t range

FIG. 91. Asymmetry $\epsilon(\phi)/P_y$ ("Yellow beam polarized only" case), for ↑ and ↓ spin orientations and ($\pi + \phi$) case, for 5 t-bins (a - e) and combined-t range (f).

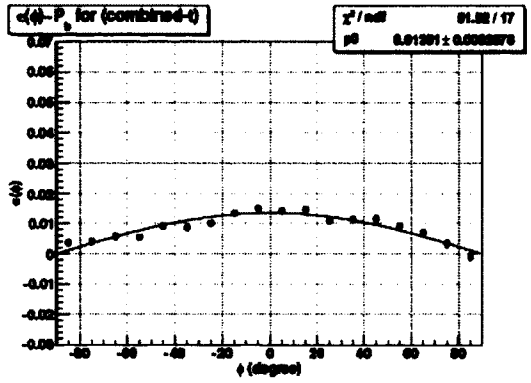

(a) $\epsilon(\phi)\sim P_b$, combined-t range for (π - ϕ) case

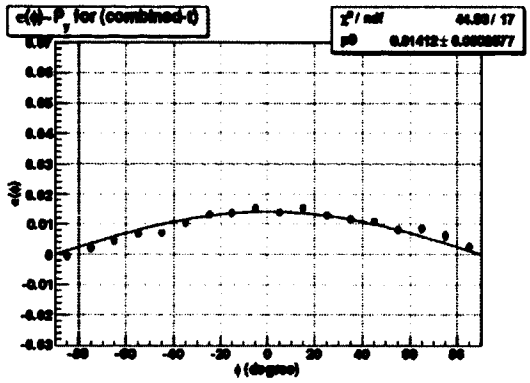

(b) $\epsilon(\phi)\sim P_y$, combined-t range for (π - ϕ) case

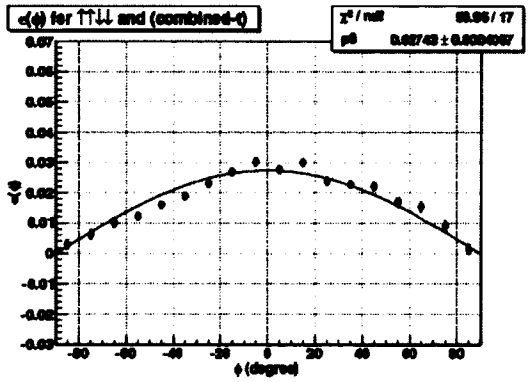

(c) $\epsilon(\phi)\sim P_b + P_y$, combined-$t$ range for (π - ϕ) case

FIG. 92. Asymmetry $\epsilon(\phi)\sim$P$_b$ ("Blue beam polarized only" case), $\epsilon(\phi)\sim$P$_y$ ("Yellow beam polarized only" case) and $\epsilon(\phi)\sim P_b + P_y$ ("Both Beams Polarized" Case), for combined-t range and (π - ϕ) case.

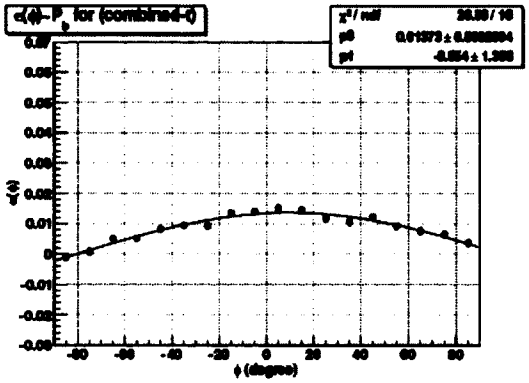

(a) $\epsilon(\phi)\sim P_b$, combined-t range for $(\pi + \phi)$ case

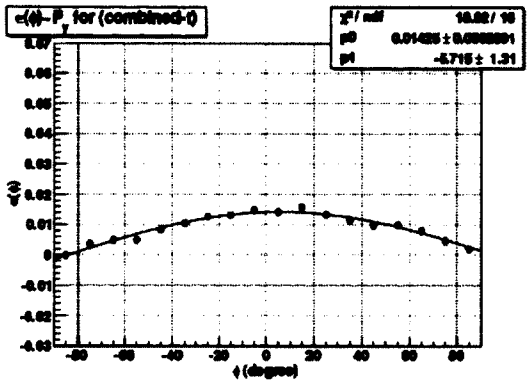

(b) $\epsilon(\phi)\sim P_y$, combined-t range for $(\pi + \phi)$ case

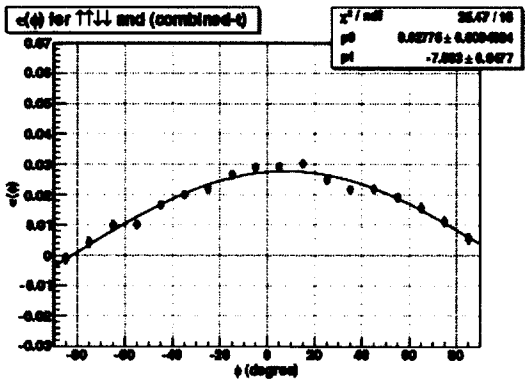

(c) $\epsilon(\phi)\sim P_b + P_y$, combined-$t$ range for $(\pi + \phi)$ case

FIG. 93. Asymmetry $\epsilon(\phi)\sim$P$_b$ ("Blue beam polarized only" case), $\epsilon(\phi)\sim$P$_y$ ("Yellow beam polarized only" case) and $\epsilon(\phi)\sim P_b + P_y$ ("Both Beams Polarized" case), for combined-t range and $(\pi + \phi)$ case.

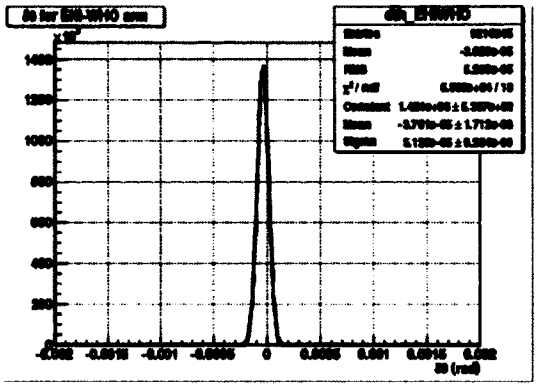

(a) $\delta\theta$ in EHI-WHO arm

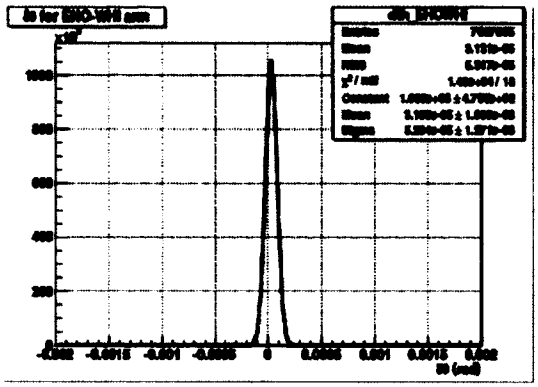

(b) $\delta\theta$ in EHO-WHI arm

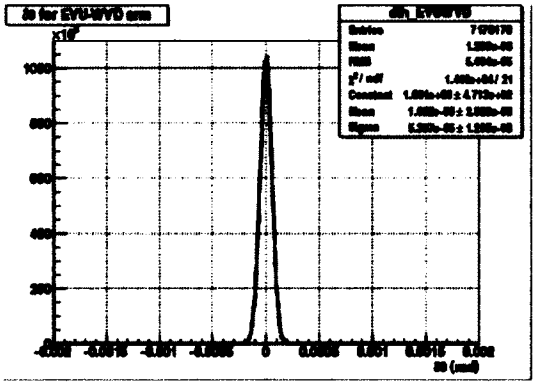

(c) $\delta\theta$ in EVU-WVD arm

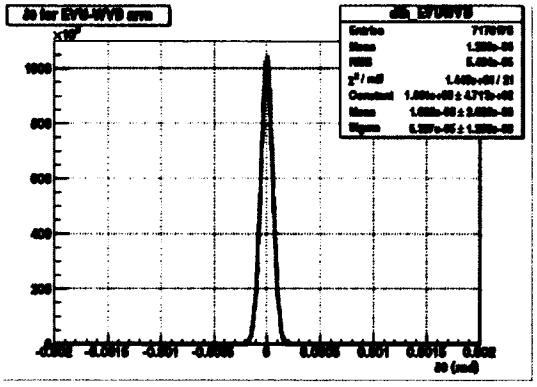

(d) $\delta\theta$ in EHI-WHO arm

FIG. 94. $\delta\theta$ in Horizontal Elastic Arms: (a) $\delta\theta$ in EHI-WHO; (b) $\delta\theta$ in EHO-WHI, and Vertical Elastic Arms: (c) $\delta\theta$ in EVU-WVD; (d) $\delta\theta$ in EVD-WVU, for all runs and $\chi^2 \leq 9$.

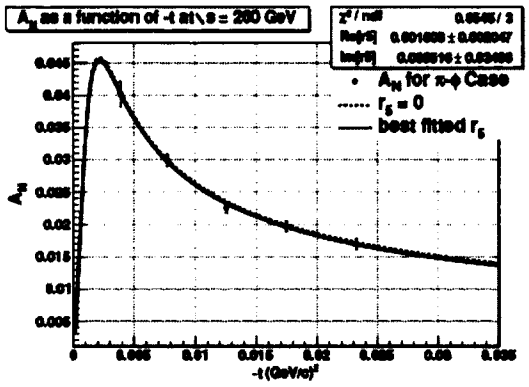

(a) A_N dependence on $-t$ (π - ϕ) case

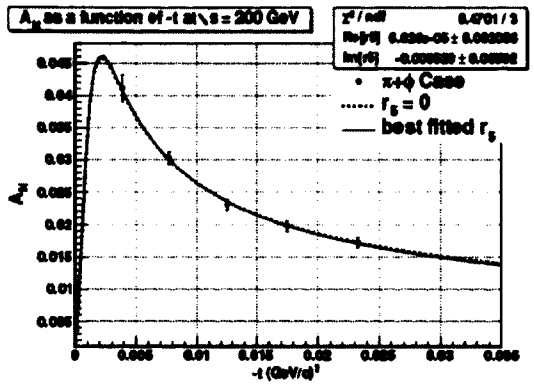

(b) A_N dependence on $-t$ (π + ϕ) case)

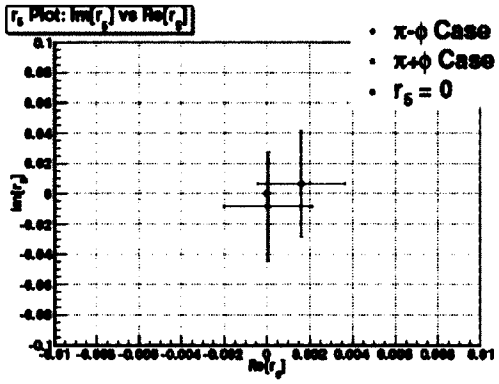

(c) r_5 plot: $Im(r_5)$ vs $Re(r_5)$ for Both Cases

FIG. 95. A_N dependence on $-t$ and r_5 plot for two cases: (π - ϕ) and (π + ϕ). Dotted curve in (a) and (b) is the theoretical calculation assuming no hadronic spin-flip amplitude ($r_5 = 0$), solid curve (blue in (a) and green in (b)) is the best fit to the data. In (c), the r_5 (Im[r_5] vs Re[r_5])value extracted from the fit is presented for each case, also including the statistical errors of the measurement (the vertical and horizontal bars).

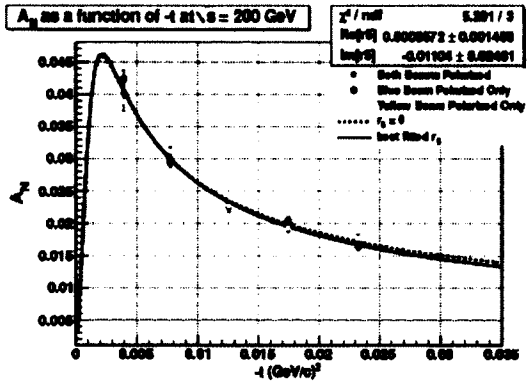

(a) A_N dependence on $-t$, only blue beam polarized case

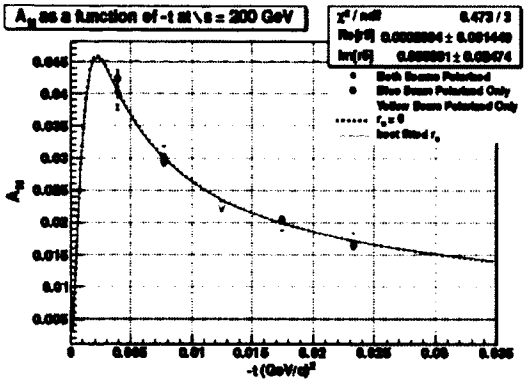

(b) A_N dependence on $-t$, only yellow beam polarized case

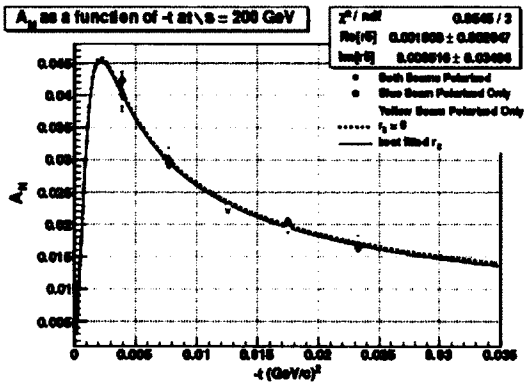

(c) A_N dependence on $-t$, one beam vs both beams polarized

FIG. 96. A_N dependence on $-t$ for one beam polarized case: (a) blue beam polarized only (blue data points and blue curve is the best fit to the data), (b) yellow beam polarized only (yellow data points and yellow curve is the best fit to the data) and (c) one beam (blue and yellow data points) vs both beams polarized (red data points and red curve is the best fit to the data) for (π - ϕ) case.

CHAPTER 8

SYSTEMATIC UNCERTAINTIES

In this chapter, I describe the systematic uncertainties of the results on the transverse single spin asymmetry A_N presented in Section 7.2.

8.1 SYSTEMATIC UNCERTAINTIES

The various contributions to the systematic uncertainties in this experiment can be listed in three groups:

- **Uncertainties affecting the determination of kinematic variables: momentum transfer squared t and azimuthal angle ϕ**

  - Transport matrix related uncertainties: the uncertainty in the transport matrix element L_{eff}

  - Beam and RP alignment/geometry related uncertainties:

    - Uncertainty in the beam transverse position at the IP, (x_0,y_0)

    - Beam angular divergence and unknown beam crossing angle

    - Beam position shift from the center at the RP location

    - Offset effect due to kicker magnets located before the RP location

    - RP survey errors

- **Uncertainties affecting the asymmetry value and A_N**

  - Backgrounds

  - Uncertainties in beam polarization measurement

- **Uncertainties affecting the measurement of the r_5 parameter**

  - All of the above uncertainties and uncertainties in the fitting parameters: the total cross section σ_{tot}, the ratio of the real to the imaginary parts of the scattering amplitude (the ρ parameter) and the slope parameter B

8.1.1 UNCERTAINTIES AFFECTING THE DETERMINATION OF t AND ϕ

The kinematic parameter t is calculated from the reconstructed scattering angles of elastic events, see Eq. (168). Therefore, uncertainties in determination of t are related to the uncertainties affecting the reconstruction of scattering angles: uncertainties in the transport matrix elements, beam and geometry related uncertainties. By examining Eqs. (171), (172) (showing the values of the transport matrix elements for West horizontal-RP as an example) and Eq. (173) given in section 6.1, we can conclude that the coefficients which magnify the mixing terms in Eq. (171) (y^d for θ_x^* and x^d for θ_y^*) are small when compared to the coefficient which magnifies the "non-mixing" terms x^d for θ_x^* and y^d for θ_y^*, see Eq. (173). Thus, the mixing terms are suppressed in Eq. (173), however they are included in the scattering angle calculation, as given in 173. In addition, the optimization of the matrix elements to achieve best parallel-to-point focusing (explained in 3.3), provides small values (see Eq. (172)) for the coefficients which magnify the unknown transverse beam position at the IP, specifically a_{11} and a_{33} magnifying x_0 and y_0. The values of x_0 and y_0 are considered to be 0 in this analysis, and could be as large as a couple mm. This, together with the uncertainties in matrix elements a_{11} and a_{33}, would introduce a negligible error in the calculation of the scattering angles θ_x^* and θ_y^*, see Eq. (173). After implementation of the appropriate values of transport matrix elements in Eq. (171), it becomes evident that the uncertainty in matrix element L_{eff} is of most concern in the determination of the scattering angle θ and kinematic variables t and ϕ.

Uncertainties in the transport matrix element L_{eff}

The transport matrix element L_{eff} (the effective length) given in Eq. (170), is the magnification of the scattering angle θ and the major term in the transport matrix. The uncertainty in the determination of the value of L_{eff} is due to the uncertainty in the magnetic field strength of the Q1-Q3 focusing magnets, which is a result of the calibration of the magnet current measurements. A correction to the magnet field strength was determined by analyzing the position and angle of the elastic events falling in the overlapping acceptance region of the horizontal and vertical RPs. An overall correction of 0.5% was applied to the magnetic field strength of the focusing

quadrupoles [148]. This results to an uncertainty in the value of L_{eff} of 1%. The next step is to determine how the uncertainty in L_{eff} propagates to the uncertainty in t.

Starting with simplified transport matrix equations that relate the x,y positions of particles at the detection point with the scattering angles θ_x, θ_y:

$$\begin{aligned} x &\approx L^x_{eff} \cdot \theta_x \rightarrow \theta_x \approx x/L^x_{eff}, \\ y &\approx L^y_{eff} \cdot \theta_y \rightarrow \theta_y \approx y/L^y_{eff}. \end{aligned} \tag{192}$$

This simplification of the transport matrix equations can be safely done for this exercise since the other matrix elements are small. First, we assume that the uncertainty in L_{eff} is $\sigma_{L_{eff}}$. The polar angle is:

$$\theta \approx \sqrt{\theta_x^2 + \theta_y^2} \approx \frac{\sqrt{x^2+y^2}}{L_{eff}}, \tag{193}$$

given L^x_{eff} and L^y_{eff} are approximately the same. Errors in (x, y) positions and L_{eff}: σ_x, σ_y and $\sigma_{L_{eff}}$, propagate to the error in scattering angle θ as follows:

$$\begin{aligned} \sigma^2_\theta &= \sigma^2_{\theta_{x,y}} + \sigma^2_{\theta_L}, \\ \sigma^2_{\theta_{x,y}} &= \left(\frac{\delta\theta}{\delta x} \cdot \sigma_x\right)^2 + \left(\frac{\delta\theta}{\delta y} \cdot \sigma_y\right)^2, \\ \sigma_{\theta_L} &= \left(\frac{\delta\theta}{\delta_{L_{eff}}} \cdot \sigma_{L_{eff}}\right)^2. \end{aligned} \tag{194}$$

From Eq. (193) we get:

$$\begin{aligned} \frac{\delta\theta}{\delta x} &= \frac{x}{L_{eff}\sqrt{x^2+y^2}}, \\ \frac{\delta\theta}{\delta x} &= \frac{x}{L_{eff}\sqrt{x^2+y^2}}, \\ \frac{\delta\theta}{\delta_{L_{eff}}} &= \frac{-\sqrt{x^2+y^2}}{L^2_{eff}}. \end{aligned} \tag{195}$$

Substituting Eq. (195) in Eq. (194) and after some derivation, we obtain:

$$\sigma^2_{\theta_{x,y}} = \frac{\sigma^2}{L^2_{eff}}, \tag{196}$$

$$\sigma^2_{\theta_{L_{eff}}} = \frac{(\theta \cdot \sigma_{L_{eff}})^2}{L^2_{eff}}. \tag{197}$$

Equation (197) is the propagated uncertainty in the scattering angle θ due to the uncertainty in the transverse positions x,y or the spatial uncertainty, and equation 197 is the uncertainty in θ due to the uncertainty in L_{eff}. To obtain the uncertainty in momentum transfer squared t due to the spatial uncertainty and L_{eff}, we now need to relate the expression given in Eq. (197) and Eq. (197) to t. Starting from $-t = p^2\theta^2$ and taking the first derivative with respect to θ we obtain: $\Delta(-t) = 2p^2\theta \cdot \Delta\theta$. To obtain the momentum t for an elastic event in our analysis, we use the average value of the measured scattering angle in the East and West of the IP such as: $\theta_{ave} = 1/2(\theta_{East} + \theta_{West})$. The error on the average scattering angle θ_{ave} is:

$$\Delta\theta = \frac{\sigma_\theta}{\sqrt{2}}, \tag{198}$$

assuming that the error on θ_{East} and θ_{West} are uncorrelated. The error in t due to the uncertainty in L_{eff} can be calculated as follows:

$$\frac{\Delta(-t)}{-t} = \frac{2p^2\theta \cdot \Delta\theta}{p^2\theta^2} = \frac{2\Delta\theta}{\theta}. \tag{199}$$

From Eq. (197) we get:

$$\frac{\sigma_{\theta_{L_{eff}}}}{\theta} = \frac{\sigma_{L_{eff}}}{L_{eff}}. \tag{200}$$

Using Eq. (200) we obtain for $\Delta\theta/\theta = \frac{\sigma_{\theta_{L_{eff}}}}{\sqrt{2}\theta} = \frac{\sigma_{L_{eff}}}{\sqrt{2}L_{eff}}$. Since the uncertainty in L_{eff} is 1%, $\sigma_{L_{eff}}/L_{eff} = 0.01$, therefore $\Delta(-t)/(-t) = \sqrt{2} \times 0.01 = 0.0141$ or 1.4%, (uncertainty in t due to the uncertainty in the value of L_{eff}).

Beam and RP geometry/alignment related uncertainties

The error in t due to the spatial uncertainty can be calculated as follows:

$$\begin{aligned}
\frac{\Delta(-t)}{-t} &= \frac{2p^2\theta\Delta\theta}{p^2\theta^2} = \frac{2p\Delta\theta}{p\theta}, \\
\frac{\Delta(-t)}{-t} &= \frac{2p\Delta\theta}{\sqrt{-t}} = \frac{2p\sigma_\theta}{\sqrt{2}\sqrt{-t}}, \\
\frac{\Delta(-t)}{-t} &= \frac{\sqrt{2}p\sigma_\theta}{\sqrt{-t}}.
\end{aligned} \tag{201}$$

where we used the expression for the error in average scattering angle given in Eq. (198). The expression given in Eq. (201) is the error in t due to the spatial uncertainty σ_x and σ_y. In other words this error represents the error in t-scale due to the uncertainty in geometry or alignment of the detectors used in this experiment.

The spatial uncertainty given in Eq. (197) gives $\sigma_\theta = \sigma/L_{eff}$. σ represents the uncertainty in the geometry/alignment.

The alignment of the detectors was established first by using the survey information as explained in Section 5.5. The survey alignment gives the positions of the first silicon strip in each detector plane with respect to the center of the beam-pipe of the accelerator. Corrections to the survey alignment were introduced using a study of elastic events which fall in the overlapping acceptance region of horizontal and vertical RPs. The study of elastic events in the overlapping region provides a relative alignment of the detectors, taking one RP as a reference point on each side of the IP.

However, we need to know the position of the detectors with respect to the beam center to a reasonable precision. The reason for this is that the reference point for the scattering angle is the beam center. The beam itself may not be centered with respect to the beam-pipe center, and thus there might be a shift in the beam center from the accelerator center at the detector (RP) position along z. The beam might also be shifted from the center because of the kicker magnets located in front of the Roman Pots in the RHIC accelerator, which were left "On" during the 2009 RHIC run. In addition to these uncertainties, other properties/parameters of the beam are not well understood. For example, the beam transverse position at the IP (x_0,y_0) is unknown; also it is not easy to separate the beam angular divergence from the beam crossing angle. Therefore, a final correction to the survey alignment was applied to take into account all the above mentioned geometrical unknowns and uncertainties, including also the survey errors. The correction was determined by simulating the transport of elastically scattered protons through the RHIC magnets. The effect of the magnet apertures on the trajectories of the elastically scattered protons was studied and compared to the data. The (x,y) distributions of the scattered protons and the acceptance boundaries of the distributions, between the simulation and the data were compared. This study led to a correction only on the East side of the IP, of (Δx, Δy) = (2.5 mm, 1.5 mm). The uncertainty of the correction is $\approx$ 400 μm. Using $\sigma_\theta = \sigma/L_{eff}$ in Eq. (201), we obtain $\frac{\Delta(-t)}{-t} = \frac{\sqrt{2}p\sigma/L_{eff}}{\sqrt{-t}} = \frac{\sqrt{2}\times 100.2\times 0.4\times 10^{-3}}{25\sqrt{-t}} \rightarrow$ $\frac{\Delta(-t)}{-t} = 0.002/\sqrt{-t}$, (uncertainty in t due to the spatial/alignment uncertainty).

8.1.2 UNCERTAINTIES AFFECTING THE ASYMMETRY VALUE AND A_N

Backgrounds

The backgrounds in this experiment may be due to beam-gas interactions, particles from inelastic collisions and beam halo since the detectors approach the beam very closely. The background events may dilute/affect the asymmetry value. The collinearity condition used in the data analysis (χ^2) removes a large part of the non-elastic background in the elastic event distribution. The number of events after the collinearity condition is 12% less than the number of "matched" events, see Table 21 in Section 6.5. The fiducial cuts which were applied to the data after the colinearity condition reject events with hits in silicon strips closest to the beam. These events are most probably due to the beam halo. The number of events after the fiducial cuts is $\approx 1.5\%$ in all t-bins, with a bigger loss the two lowest t-bins ($-t < 0.005$ GeV/c^2 and $0.005 \leq -t \leq 0.01$ GeV/c^2). If the background is beam polarization independent the value of A_N will be changed by 1%, thus the uncertainty in A_N due to background events is $\delta A_N/A_N = 0.01$. This is a negligible error when compared to the total error on A_N determination (stat. + syst.), which will be shown later. Uncertainties that may arise from any geometrical acceptance and tracking efficiencies cancel out when using the square-root formula in the calculation of the asymmetries. The possibility of having all possible bunch polarization combinations for the two beams ($\uparrow\uparrow$, $\uparrow\downarrow$, $\downarrow\uparrow$, $\downarrow\downarrow$) makes the uncertainties from geometrical acceptance and tracking efficiencies cancel out in the calculation of the asymmetries, independent of the method used to calculate the asymmetry.

Uncertainties in the beam polarization measurement

Beam polarization values for each of the four RHIC stores during the 2009 RHIC run and the luminosity weighed average and the corresponding uncertainties are given in Section 5.1. The total uncertainty (stat. + syst.) in $P_b + P_y$, including also the overall uncertainty for normalization in polarization measurement, is 5.4%, making this the major contribution to the uncertainty in A_N.

We can use the expression derived for the uncertainty in t due to the uncertainty in L_{eff}: $\Delta(-t) = 0.0141 \times (-t)$, to calculate the uncertainty in t for each t-bin, where $(-t)$ in the expression is the mean value in t in each t bin. We can follow

TABLE 26. A_N values in 5 $-t$-ranges and corresponding statistical uncertainties and systematic uncertainties in (t) due to the uncertainty in transport matrix element (L_{eff}) and the uncertainty in Alignment; systematic uncertainty in (A_N) due to the uncertainty in polarization measurement (δP), for (π - ϕ) and "both beams polarized" with $\uparrow\uparrow$ and $\downarrow\downarrow$ spin combinations of bunches per beam".

$-t$ range $(GeV/c)^2$	< 0.005	0.005 - 0.01	0.01 - 0.015	0.015 - 0.02	> 0.02
No. of Events	494710	2175468	2848620	2872958	2566903
$\langle -t \rangle$ $(GeV/c)^2$	0.0039	0.0077	0.0125	0.0175	0.0233
δt $(GeV/c)^2$ (stat.)	9.8E-07	6.6E-07	7.3E-07	8.6E-07	1.0E-07
δt (syst.)					
δt (δL_{eff})	5.5E-05	1.1E-04	1.8E-04	2.5E-04	3.3E-04
δt (δAlign.)	1.4E-04	2.0E-04	2.5E-04	3.0E-04	3.5E-04
Total δt (syst.)	1.5E-04	2.3E-04	3.1E-04	3.9E-04	4.8E-04
Total δt (stat.+syst.)	0.00015	0.00023	0.00031	0.00039	0.00048
(π - ϕ) Case					
A_N	0.0402	0.0300	0.0226	0.0197	0.0170
δA_N (stat.)	0.0019	0.0009	0.0008	0.0008	0.0008
syst. error δA_N					
$\delta A_N(P + \delta P)$	-0.0021	-0.0015	-0.0012	-0.0010	-0.0009
$\delta A_N(P - \delta P)$	0.0023	0.0017	0.0013	0.0011	0.0010
δA_N(due to δP)	0.0022	0.0016	0.0012	0.0011	0.0009

the same procedure to calculate the uncertainty in t due to the spatial uncertainty or the uncertainty in alignment, using the expression previously derived $\frac{\Delta(-t)}{-t} = 0.002/\sqrt{-t}$. Table 26 presents the systematic errors in t due to the uncertainty in L_{eff} (6^{th} row) and alignment (7^{th} row). The total systematic error calculated by adding in quadrature the two systematic errors in t and the total error after adding the statistical error in the same way, are also presented.

The A_N dependence on t was studied after including δt due to the uncertainty in alignment, see Fig. 97 and δt due to the uncertainty in L_{eff}, see Fig. 98. δt was changed in each case, $\pm$ δt and the data was fit with the function given in Section 7.2. In each case, the Re[r_5] and Im[r_5] parameters were extracted from the fit. The results on the r_5 parameter are shown in Table 27.

The uncertainty in polarization measurement affects the A_N values in each t-bin. If $P_b + P_y = P_{sum}$, $\delta P_{sum} = 0.054 \times P_{sum}$. A_N decreases by 1/1.054 if P_{sum} increases by 0.054 ($A_N(+\delta P_{sum}) = 1/1.054 \times A_N$), and increases by 1.057 if P_{sum} decreases by

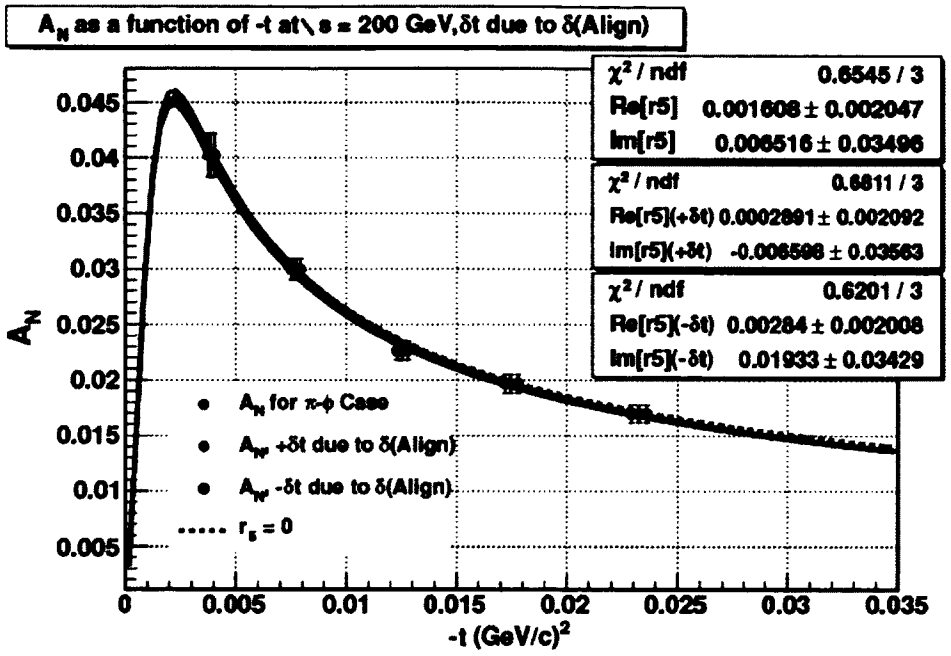

FIG. 97. A_N dependence on $-t$ for both beam polarized case, after including δt due to $\delta(Align)$.

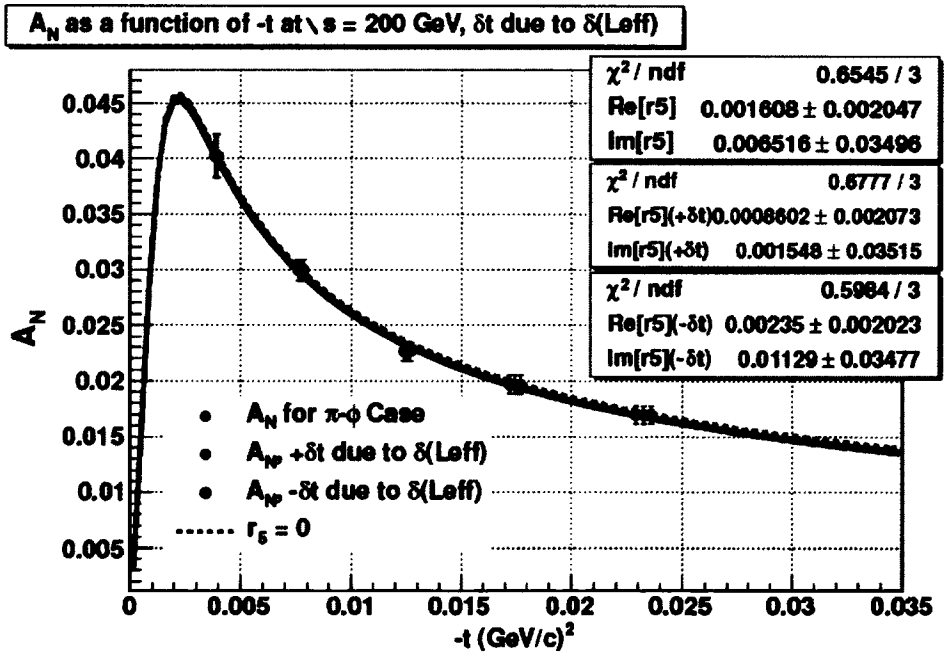

FIG. 98. A_N dependence on $-t$ for both beam polarized case, after including δt due to $\delta(L_{eff})$.

TABLE 27. Statistical and systematic errors in Re[r_5] and Im[r_5] due to systematic uncertainties in (L_{eff}), alignment, polarization measurement (δP) and uncertainties in the fitting parameters σ_{tot}, ρ and slope parameter B. Total systematic error in the r_5 parameter is calculated by adding in quadrature the listed systematic errors due to various factors. Total systematic and statistical error in the measurement of the Re[r_5] and Im[r_5] is also shown.

r_5 Parameter	Re[r_5]	Im[r_5]
	0.0016	0.0065
	δRe[r_5] (stat.)	δIm[r_5] (stat.)
	0.0021	0.0350
	δRe[r_5] (syst.)	δIm[r_5] (syst.)
$+\delta L_{eff}$	-0.0007	-0.0050
$-\delta L_{eff}$	0.0007	0.0048
due to δL_{eff}	0.0007	0.0049
$+\delta$Align.	-0.0013	-0.0131
$-\delta$Align.	0.0012	0.0128
due to δAlign.	0.0128	0.0130
$+\delta P$	0.0057	0.0457
$-\delta P$	-0.0065	-0.0507
due to δP	0.0061	0.0482
$+\delta\sigma_{tot}$	-0.0003	-0.0019
$-\delta\sigma_{tot}$	0.0003	0.0019
due to $\delta\sigma_{tot}$	0.0003	0.0019
$+\delta\rho$	2.2E-05	0.0004
$-\delta\rho$	-2.2E-05	-0.0004
due to $\delta\rho$	2.2E-05	0.0004
$+\delta B$	-1.1E-05	-0.0002
$-\delta B$	1.1E-05	0.0002
due to δB	1.1E-05	0.0002
Total Syst.	0.0063	0.0502
Total Stat.+Syst.	0.0066	0.0506

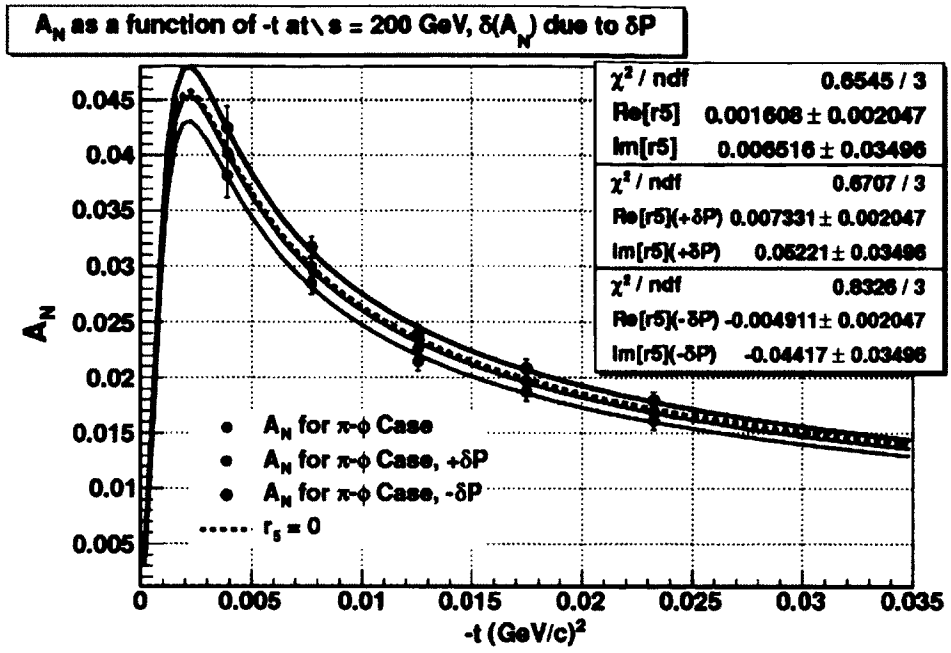

FIG. 99. A_N dependence on $-t$ for both beam polarized case, after including δA_N due to δP.

0.054 ($A_N(-\delta P_{sum}) = 1.057 \times A_N$).

Table 26 presents the A_N values for each t-bin, for $P_{sum}+\delta P_{sum}$ and $P_{sum}-\delta P_{sum}$.

Figure 99 shows A_N dependence on t for $P_{sum} + \delta P_{sum}$ and $P_{sum} - \delta P_{sum}$ cases, compared also to the original case without δP_{sum}. The r_5 parameter is extracted from the best fit in each case and presented in Table 27.

All the above studied uncertainties until here affect the r_5 value. In addition to these uncertainties, we also studied the uncertainties due to the fitting parameters σ_{tot}, ρ and B parameter: $\delta\sigma_{tot} = \pm\ 0.12$, $\delta\rho = \pm\ 0.0015$ and $\delta B = \pm\ 1.8$. The r_5 parameter attained in each case after changing the fitting parameters are also given in Table 27. Total systematic and total (syst. + stat.) errors are calculated after adding in quadrature the systematic errors in the r_5 parameter due to various factors.

CHAPTER 9

SUMMARY AND CONCLUSIONS

9.1 SUMMARY AND CONCLUSIONS

In this dissertation I presented a high precision measurement of the transverse single spin asymmetry A_N in polarized proton-proton elastic scattering at $\sqrt{s}$ = 200 GeV by the STAR collaboration at RHIC. The measured values of A_N and its t-dependence are consistent with the absence of a hadronic spin-flip amplitude at $\sqrt{s}$ = 200 GeV. The results have been recently published by the STAR collaboration in [69]. This result is in agreement with the measurements of A_N by the E704 experiment at 19.4 GeV and by RHIC polarimeters at 13.7 and 21.7 GeV. The contribution of the hadronic spin-flip is parametrized in terms of the ratio of hadronic single spin-flip amplitude to the hadronic non-flip amplitudes, the parameter $r_5 = \mathrm{Re}[r_5] + i\mathrm{Im}[r_5]$. Our result for the r_5-parameter (including only statistical and systematic errors is): $\mathrm{Re}[r_5] = 0.0016 \pm 0.0021$ (stat.) $\pm$ 0.0063 (syst.) and $\mathrm{Im}[r_5] = 0.0350$ (stat.) $\pm$ 0.0502 (syst.).

Various asymmetries (taking into account the various spin combinations of the two beams) were measured in five regions of the kinematic t-range of our experiment: $0.003 \leq |t| \leq 0.035$ $(\mathrm{GeV}/c)^2$ and for two cases (π - ϕ) and (π + ϕ). The two cases differ in the way the scattered proton counts (N) are measured in the left (L) and right (R) regions of the detectors in the azimuthal plane, namely for the first case: if $N_L = N(\phi)$ then $N_R = N(\pi - \phi)$; whereas for the second case: if $N_L = N(\phi)$ then $N_R = N(\pi + \phi)$. The second case is more appropriate to use if there is a tilt in the proton polarization direction from the vertical direction. For the first case, we apply a simple $\cos(\phi)$ fit function to the measured raw asymmetry, whereas for the second case an extra parameter is allowed in the $\cos(\phi + \delta\phi)$ fit-function, where $\delta\phi$ indicates the tilt from the vertical direction. Various asymmetries with all available spin combinations of the two beams (relative same orientation and opposite orientation), are calculated. Asymmetries were calculated also for the case when only one beam is polarized and for the (π - ϕ) case. The measured raw asymmetry is then

by the appropriate polarization value (sum or difference of P_b and P_y), in order to extract the single spin asymmetry A_N.

The results of measured asymmetries calculated in different ways were shown and compared. A_N values for the five t-bins, differ by $\sim$ 1.5% between (π - ϕ) and (π + ϕ) cases, with the biggest difference in the lowest t-bin, see Table 22. The $\delta\phi$ value measured in the (π + ϕ) case is about $\sim$ -7.4 $\pm$ 3.2 (stat.) degrees. The raw asymmetries measured for one beam polarized case (i.e. ϵ_B), versus the raw asymmetries for both beams polarized case (i.e. ϵ_1), both calculated for the (π - ϕ) case, show that $\epsilon^B/\epsilon_1 \approx 1/2$, as expected, see Table 23. Finally, the raw false asymmetry measured with relative opposite orientation of the polarization of the two beams, is very small and consistent with zero, as expected (see Table. 24), since this asymmetry is proportional to the difference of the P_b and P_y, which is about 0.016 $\pm$ 0.038.

The measured A_N values are fit to extract the Re[r_5] and Im[r_5] parameters. Two fits, one with the CNI curve (prediction without hadronic spin-flip amplitude) and the best fit to the data (using the same function, but including Re[r_5] and Im[r_5] as free parameters), are applied to the measured A_N values. The r_5 result for (π - ϕ) case is given in the first paragraph. For comparison purposes, the r_5 result for (π + ϕ) case is: Re[r_5] = 6.6*10^{-5} $\pm$ 0.0021 (stat.) and Im[r_5] = -0.0085 $\pm$ 0.0359 (stat.), see Table 25.

Systematic uncertainties related to the determination of t and A_N were studied. Various factors contributing to the uncertainties in the horizontal-t scales are: uncertainty in the largest transport matrix element L_{eff}, alignment uncertainties and uncertainty due to beam angular divergence. Results are shown in Table 26 for five t-bins. Factors affecting the determination of A_N are: backgrounds (negligible effect) and uncertainty in the beam polarization measurement (major contribution to the systematic error in A_N), see Table 26. The contributions of the above mentioned uncertainties to the systematic errors in Re[r_5] and Im[r_5] parameters are shown in Table 27.

The presented high-accuracy measurement of the single spin asymmetry A_N and the r_5 parameter in pp elastic scattering at $\sqrt{s} = 200$ GeV provides a strong constraint on the magnitude of the hadronic spin-flip amplitude at this energy, suggesting that the spin-dependent Pomeron amplitudes for elastic scattering are consistent with zero. This result may help to better understand the nature and, in particular, the

TABLE 28. Predicted Im[r_5] values from various models and measured by various experiments.

Models	Ref.	$\sqrt{s}$ (GeV)	Im[r_5]	δIm[r_5]
Anomalous Moment	[11]		0.13	
Quark-Diquark	[21]		-0.10	$\pm$ 0.05
Pion-Exchange	[19]		0.06	
Impact Picture	[20], [66]	200	-0.06	
Experiments	**Ref.**	$\sqrt{s}$	**Im[r_5]**	**δIm[r_5]**
FNAL E704	[73]	19.4	0.145	$\pm$ 0.311
PP2PP	[25]	200	-0.430	$\pm$ 0.560
H-jet	[22]	13.7	-0.015	$\pm$ 0.029
H-jet	[22]	6.8	-0.108	$\pm$ 0.038
H-jet	[23]	7.7	-0.016	
H-jet	[23]	21.7	-0.005	
STAR	[69]	200	0.007	$\pm$ 0.057

spin-dependence of the exchange mechanisms dominating at high energies.

It has been theoretically [17, 66] shown that the double spin-flip amplitudes are small. This was also measured by the PP2PP experiment [26]. Preliminary results on the double spin asymmetries A_{NN} and A_{SS} from this experiment are shown in Fig. 22 [68]. Small values of double spin amplitudes indicate that at very low $|t| \approx 0.002$ (GeV/c)^2, A_N can be evaluated as κ - 2Im[r_5] [149], emphasizing the values of Im[r_5]. Akchurin, Buttimore and Penzo compared values of Im[r_5] from various experiments [149]. Table 28, summaries results on Im[r_5] values from different experiments, including our experiment, compared also with calculations from the models which describe hadronic spin-flip. The theoretical models for the first three models are energy-independent. The errors associated with values of Im[r_5] measured in experiments are both statistical and systematic errors, combined.

The "Physics with Tagged Forward Protons at STAR" will continue its physics program in the upcoming RHIC runs, aiming to perform precise measurements on the spin-dependent observables, including longitudinal spin asymmetries at $\sqrt{s} = 500$ GeV, and precise measurement of spin-averaged observables (i.e. total and elastic cross sections) at 200 and 500 GeV cms energies, in polarized pp elastic scattering.

BIBLIOGRAPHY

[1] E. Leader, *Spin in Particle Physics*, Cambridge University Press (2001).

[2] L.N. Lipatov, Sov. Phys. - JETP **63**, 904 (1986).

[3] F.E. Low, Phys. Rev. D **12**, 163 (1975).

[4] S. Nussinov, Phys. Rev. Lett. **34**, 1286 (1975).

[5] V.S. Fadin, E.A. Kuraev and L.N. Lipatov, Phys. Lett. B **60**, 50 (1975).

[6] S. Bültmann *et al.*, *Spin Dependence in Proton-Proton Elastic Scattering at RHIC*, Experimental Proposal, (2003).

[7] L. Lukaszuk and B. Nicolescu, Lett. Al Nuovo Cimento **8**, 405 (1973).

[8] P. Gauron, B. Nicolescu and E. Leader, Phys. Rev. Lett. **54**, 2656 (1985).

[9] D. Joynson, E. Leader and B. Nicolescu, Il Nuovo Cimento B **30**, 345 (1975).

[10] P. Gauron, E. Leader and B. Nicolescu, Phys. Lett. B **397**, 126 (1997).

[11] M.G. Ryskin, Yad. Fiz. **46**, 611 (1987); Sov. J. Nucl. Phys. **46**, 337 (1987).

[12] A. Donnachie and P.V. Landshoff, Nucl. Phys. B **348**, 297 (1991).

[13] T. Chou and C.N. Yang, Phys. Lett. D **19**, 3268 (1979).

[14] J. Soffer, C. Bourrely and T.T. Wu, Nucl. Phys. B **247**, 15-28 (1984).

[15] S. Donnachie, G. Dosch and P. Landshoff, *Pomeron Physics and QCD*, Cambridge University Press (1998), ISBN: 9780521675703.

[16] N.H. Buttimore, B.Z. Kopeliovich, E. Leader, J. Soffer and T.L. Trueman, Phys. Rev. D **59**, 114010 (1999).

[17] T.L. Trueman, Phys. Rev. D **77**, 054005 (2008).

[18] G.G. Ohlsen and P.W. Keaton, Nucl. Instrum. & Methods **109**, 41 (1973).

[19] J. Pumplin and G.L. Kane, Phys. Rev. D **11**, 1183 (1975).

[20] J. Soffer, C. Bourrely and T.T Wu, Phys. Rev. D **19**, 3249 (1979).

[21] B.Z. Kopeliovich and B.G. Zakharov, Phys. Lett. B **226**, 156 (1989).

[22] I.G. Alekseev *et al.*, Phys. Rev. D **79**, 094014 (2009).

[23] A. Bazilevsky *et al.*, J. Phys: Conf. Ser. **295**, 012096 (2011).

[24] S. Bültmann *et al.*, Phys. Lett. B **579**, 245-250 (2004).

[25] S. Bültmann *et al.*, Phys. Lett. B **632**, 167-172 (2006).

[26] S. Bültmann *et al.*, Phys. Lett. B **647**, 98-103 (2007).

[27] V. Barone and E. Predazzi, *High-Energy Particle Diffraction*, Texts and Monographs in Physics, Springer-Verlag (2002), ISBN: 3540421076.

[28] T. Regge, Nuovo Cimento **14**, 951 (1959).

[29] C. Tang, PhD Thesis, Stony Brook University, 2001.

[30] HA. Bethe, Ann. Phys. **3**, 190-240 (1958).

[31] G.B. West and D.R. Yennie, Phys. Rev. **172**, 1413 (1968).

[32] N.H. Buttimore, E. Gotsman and E. Leader, Phys. Rev. D **18**, 694 (1978).

[33] R.N. Cahn, Z. Phys. C, **15**, 253-260 (1982).

[34] G. Mathiae, Nucl. Phys. B (Proc. Suppl.) **99**, 281-288 (2001).

[35] G. Antchev *et al.* (TOTEM Collaboration) EPL **96**, 21002 (2011).

[36] C. Augier *et al.* (UA4/2 Collaboration), Phys. Lett. B **315**, 503 (1993).

[37] W. Kienzle *et al.* (TOTEM Collaboration) CERN Letter of Intent, CERN/LHCC 97-49 (1997).

[38] N.N Khuri and T. Kinoshita, Phys. Rev. **137**, B720-B729 (1965).

[39] I.Ya. Pomeranchuk, Sov. Phys. - JETP **7**, 499 (1958).

[40] R.F. Peirels and L.L Foldy, Phys. Rev. Lett. **8**, 41 (1962).

[41] T. Chou and C.N. Yang, Phys. Lett. B **128**, 457 (1983).

[42] J. Soffer, C. Bourrely and T.T Wu, Phys. Lett. B **252**, 287 (1990).

[43] A. Donnachie and P.V. Landshoff, Phys. Lett. B **123**, 345 (1983).

[44] A. Sommerfeld, *Partial Differential Equations in Physics*, Academic Press (1949).

[45] G.F. Chew and S.C. Frautschi, Phys. Rev. Lett. **8**, 41 (1961).

[46] F. Carlson, Upsala thesis, (1914).

[47] S. Donnachie, G. Dosch, P. Landshoff and O. Nachtmann, *Pomeron Physics and QCD*, Cambridge University Press, **19**, (2002).

[48] P.D.B. Collins, *An Introduction to Regge Theory*, Cambridge University Press, (1977).

[49] T.T. Chou and C.N. Yang, Phys. Lett. B **244**, 113 (1990).

[50] H. Cheng and T.T. Wu, *Expanding Protons: Scattering at High Energies*, The MIT Press, (1987).

[51] A. Donnachie and P.V. Landshoff, Nucl. Phys. B **244**, 322 (1984).

[52] J. Soffer, C. Bourrely and T.T Wu, arXiv: 0707.2222v1 [hep-ph] (2007).

[53] H. Cheng and T.T. Wu, Phys. Rev. D **184**, 1868 (1969).

[54] J. Soffer, C. Bourrely and T.T Wu, Eur. Phys. J. C. **28**, 97 (2003).

[55] P.V Landshoff and J.C. Polkinghorne, Nucl. Phys. B **28**, 225 (1971).

[56] A. Donnachie and P.V. Landshoff, Nucl. Phys. B **231**, 189-204 (1984).

[57] N. Amos *et al.*, Nucl. Phys. B **262**, 715-726 (1985).

[58] P. Gauron, B. Nicolescu and E. Leader, Nucl. Phys. B **299**, 640 (1988).

[59] M.M. Block and R. N. Cahn, Phys. Lett. B **168**, 151 (1986).

[60] M. Froissart, Phys. Rev. **123**, 1053 (1961); A. Martin, Nuovo Cimento A **42**, 930 (1966).

[61] E. Leader and R.C. Slansky, Phys. Rev. **148**, 1491 (1966).

[62] E. Leader, Phys. Rev. **166**, 1599 (1968).

[63] R.F. Peierls and T.L. Trueman, Phys. Rev. **134** B1365 (1964).

[64] E. Leader and T.L. Trueman, Phys. Rev. D **61**, 077504 (2000).

[65] K.G. Boreskov, A.A. Grigiryan, A.B. Kaidalov and I.I. Levintov, Sov. J. Nucl. Phys. **27**, 432 (1978).

[66] C. Bourrely, H.A. Neal, G.A. Ogren, J. Soffer and T.T. Wu, Phys. Rev. D **26**, 1781 (1982).

[67] C. Bourrely, J. Soffer and D. Wray, Nucl. Phys. B **91**, 33 (1975).

[68] I.G. Alekseev for the STAR Collaboration, J. Phys. Conf. Ser. **295**, 012098 (2011).

[69] L. Adamczyk *et al.*, STAR Collaboration, Phys. Lett. B **719**, 62-69 (2013).

[70] T.L. Trueman, arXiv: hep-ph/0604153.

[71] N.H. Buttimore, AIP Conf. Proc. No. 95, High Energy Spin Physics, Brookhaven (1982) ed. G.M. Bunce, AIP, New York, 634 (1983).

[72] J. Schwinger, Phys. Rev. **73**, 407 (1948).

[73] N. Akchurin *et al.*, Phys. Lett. D **48**, 3026 (1993).

[74] B.Z. Kopeliovich and L.I. Lapidus, Yad. Fiz. **19**, 218 (1974) [Sov. J. Nucl. Phys. **19**, 114 (1974).

[75] N. Akchurin *et al.*, Phys. Lett. B **229**, 299 (1989).

[76] J.H. Snyder *et al.*, Phys. Rev. Lett. **41**, 781 (1978).

[77] M. Corcoran *et al.*, Phys. Rev. D **22**, 2624 (1980).

[78] G. Fidecaro *et al.*, Phys. Lett. B **76**, 369 (1978); G. Fidecaro *et al.*, *ibid.*, B **105**, 309 (1981).

[79] M. Borghini *et al.*, Phys. Lett. B **36**, 501 (1971).

[80] S.L. Kramer *et al.*, Phys. Rev. D **17**, 1709 (1978).

[81] D.G. Crabb *et al.*, Phys. Rev. Lett. **65**, 3241 (1990).

[82] A. Gaidot *et al.*, Phys. Lett. B **61**, 103 (1976).

[83] D.G. Crabb *et al.*, Nucl. Phys. B **121**, 231 (1977).

[84] H. Okada *et al.*, Phys. Lett. B **638**, 450 (2006).

[85] F.Z. Khiari *et al.*, Phys. Rev. D **39**, 45 (1989).

[86] J. Antille *et al.*, Nucl. Phys. B **185**, 1 (1981).

[87] G. Fidecaro *et al.*, Phys. Lett. B **105**, 309 (1981).

[88] G. Fidecaro *et al.*, Nucl. Phys. B **173**, 513 (1980).

[89] R.V. Kline *et al.*, Phys. Rev. D **22**, 553 (1980).

[90] G. Fidecaro *et al.*, Phys. Lett. B **76**, 369 (1978).

[91] G.W. Abshire *et al.*, Phys. Rev. Lett. **32**, 1261 (1974).

[92] F. Betz *et al.*, Phys. Rev. **148**, 1289 (1966).

[93] P. Grannis *et al.*, Phys. Rev. **148**, 1297 (1966).

[94] K. Hinotani *et al.*, Il Nuovo Cimento A **52**, 363 (1979).

[95] J. Tojo *et al.*, Phys. Rev. Lett. **89**, 052302 (2002).

[96] O. Jinnouchi *et al.*, Proceedings of the 16^{th} International Spin Physics Symposium *SPIN 2004*, eds. F. Bradamante *et al.*, World Scientific, (2005).

[97] B.Z. Kopeliovich and T.L. Trueman, Phys. Rev. D **64**, 034004 (2001).

[98] M. Harrison, S. Peggs and T. Roser, *The RHIC Accelerator*, Annu. Rev. Nucl. Part. Sci. **52**, 425-469, (2002).

[99] A.N Zelenski *et al.*, *Optically-pumped polarized H^- ion sources for RHIC and HERA colliders*, PAC Proc. 106 (1999).

[100] A.N Zelenski *et al.*, Rev. Sci. Instrum. **71**, 1237 (2000).

[101] A.N Zelenski *et al.*, AIP. Conf. Proc. **915**, 987 (2007).

[102] I. Alekseev *et al.*, Nucl. Instrum. & Methods in Phys. Res. A **499**, 392 (2003).

[103] L.H. Thomas, Philos. Mag. **3** (1927); V. Bargmann, L. Michel, V.L. Telegdi, Phys. Rev. Lett. **2**, 435 (1959).

[104] M. Froissart, R. Stora, Nucl. Instrum. & Methods **1**, 297 (1960).

[105] Ya.S. Derbenev *et al.*, Part. Accel. **8**, 115 (1978).

[106] J.L. Rosen *et al.*, AIP Conf. Proc. **26**, 287 (1975).

[107] W.R. Lozowski, J.D. Hudson, Nucl. Instrum. & Methods A **334**, 173 (1993).

[108] I. Nakawaga *et al.*, AIP Conf. Proc. **980**, 380 (2008).

[109] I. Nakawaga *et al.*, Eur. Phys. Jour. **162**, 259 (2008).

[110] O. Jinnouchi *et al.*, arXiv nucl-ex/0412053 (2004).

[111] A. Bazilevksy, EPAC08 Proc. TUPC039, 1140 (2008).

[112] A. Zelenski *et al.*, *Polarimetry at RHIC: RHIC Polarized Beam in Run 2011*, Brookhaven National Laboratory, (2011).

[113] H. Okada *et al.*, arXiv: 0712.1389 [nucl-ex] (2007).

[114] K.O. Eyser *et al.*, SPIN 2004 Proc. AIP Conf. Proc. **915**, 916 (2007).

[115] T. Russo *et al.*, Particle Accelerator Conference (PAC). IEEE, 2648 (2007).

[116] R. Battiston, *et al.*, Nucl. Instrum. & Methods A **238** 35 (1985).

[117] S. Bültmann *et al.*, Nucl. Instrum. & Methods A **535**, 415 (2004).

[118] C.J.S. Damerell, *Vertex Detectors: The State of the Art and Future Prospects*, Rutherford Appleton Laboratory, England (1995).

[119] N. Guler, Master's Thesis, University of Texas at Arlington (2001).

[120] W.R. Leo, *Techniques for nuclear and particle physics experiments: a how-to approach*, (Springer Verlag, 1994), p. 24-26.

[121] R. Yarema *et al.*, Fermi National Accelerator Laboratory, Fermilab-TM-1892, (1994), http://www-d0.fnal.gov/ lipton/svx2e/svxe.html.

[122] S. N. Ahmed *et al.*, Nucl. Instrum. & Methods A, **634**, 8-46 (2011).

[123] A. Drees, Brookhaven National Laboratory Collider Accelerator Department Report No. XXX, *Analysis of Vernier Scans during the PP2PP run9 (pp at 100 GeV/beam)*, 2011, (unpublished).

[124] J. de Favereau, X. Rouby, K. Piotrzkowski, Jour. of Instr. **2**, P09005 (2007).

[125] D. Plyku, (for the STAR Collaboration), AIP Conf. Proc. **1149**, 676-679 (2009).

[126] Collider Accelerator Department, Brookhaven National Laboratory, RHIC Configuration Manual, 2006, http://www.bnl.gov/cad/accelerator/docs/pdf/RHICConfManual.pdf.

[127] R. Brun and F. Rademakers, Nucl. Instrum. & Methods in Phys. Res. A **389**, 81-86 (1997).

[128] CERN, http://root.cern.ch.

[129] F.C Iselin, J.M. Jowett, J. Pancin, A. Adelman, *Methodical Accelerator Design*, CERN-SL-2000-026, http://mad.web.cern.ch/mad/.

[130] H. Grote and F. Schmidt, Proc. of the 2003 Part. Acc. Conf., 3497, 2003, http://madx.web.cern.ch/madx/.

[131] K. Wille and J. McFall, *The Physics of Particle Accelerators: An Introduction*, (Oxford Univ. Press, 2000).

[132] H. Wiedemann, *Particle Accelerator Physics I: Basic Principles and Linear Beam Dynamics*, (Springer-Verlag, 1999), p. 122.

[133] C. Montag *et al.*, *Proceedings of the 2010 International Particle Accelerator Conference on RHIC Performance as a 100 GeV Polarized Proton Collider in Run-9*, Kyoto, Japan, 2010, p. 1.

[134] S. Bültmann, http://www4.rcf.bnl.gov/~bueltman/Run09.htm.

[135] I. Alekseev *et al.*, http://www4.rcf.bnl.gov/~cnipol/pubdocs/Run09Offline.

[136] I. Alekseev *et al.*, Brookhaven National Laboratory (BNL) Collider Accelerator Department Report No. XXX, *Run-09 pC Polarimeter Analysis*, 20XX (unpublished).

[137] D. Plyku, *Acceptance for each RP position during Run09*, 2009, http://www.c-ad.bnl.gov/esfd/rmem_09/pp2pp_1.pdf.

[138] D. Plyku, Brookhaven National Laboratory STAR Collaboration Technical Note, *Technical Note on Survey Alignment of the Silicon Strip Detectors used in the Roman Pots at STAR during RHIC 2009 Run*, 2012 (unpublished), http://drupal.star.bnl.gov/STAR/subsys/pp2pp/anpaper-review/alignment-and-survey/note-survey-and-alignment-roman-pots.

[139] I. Alekseev, L. Koroleva, B. Morozov, D. Svirida (ITEP), Brookhaven National Laboratory STAR Collaboration Technical Note, *Roman pots alignment at run 2009*, 2011 (unpublished), http://drupal.star.bnl.gov/STAR/subsys/pp2pp/anpaper-review/alignment-and-survey/local-alignment.

[140] W. Guryn, Brookhaven National Laboratory STAR Collaboration Technical Note, *Correction to the Local Alignment*, 2012 (unpublished), http://drupal.star.bnl.gov/STAR/system/files/GlobalAlignment2012_0.pdf.

[141] STAR Collaboration μDST Documentation, http://www.star.bnl.gov/webdata/dox/html/index.html.

[142] K. Yip, Brookhaven National Laboratory STAR Collaboration Analysis Note, *Analysis Note for the Single Transverse-Spin Asymmetries (A_N) in elastic p+p collisions at $\sqrt{s}$ = 200 GeV*, 2012 (unpublished).

[143] T. Obrebski, Brookhaven National Laboratory STAR Collaboration Technical Note, *E_{min} cuts analysis*, 2010 (unpublished), http://drupal.star.bnl.gov/STAR/system/files/Technical_note_cuts_0.pdf.

[144] L. Whitehead, Brookhaven National Laboratory PP2PP Collaboration Analysis Note, *A Study of Channel Noise and Gain in the May 2003 Physics Run of PP2PP*, 2004 (unpublished).

[145] R. Gill and D. Lynn, Brookhaven National Laboratory PP2PP Collaboration Technical Note, *PP2PP Pedestal, Noise, dE/dx and Gain Summary*, (unpublished).

[146] W. Guryn and I. Alekseev, STAR Collaboration Note, *Trigger Definitions for pp2pp Run09 at STAR*, (2009).

[147] D. Plyku (for the STAR Collaboration), J. Phys. Conf. Ser. **295**, 012129 (2011).

[148] P. Pile, private communication, (2012)

[149] N. Akchurin, N.H. Buttimore and A. Penzo, *Spin effects in high energy proton scattering*, Jour. Phys. Conf. Ser. **295**, 012101 (2011).

[150] T. Armstrong *et al.* (E760 Collaboration), Phys. Lett. B **385**, 479 (1996).

[151] C. Augier *et al.* (UA4/2 Collaboration), Phys. Lett. B **316**, 448-454 (1993).

[152] N. Amos *et al.*, Phys. Lett. B **247**, 127 (1990).

[153] D. Bernard *et al.*, Phys. Lett. B **198**, 583 (1987).

[154] A. Breakstone *et al.*, Phys. Rev. Lett. (1985).

[155] M. Bozzo *et al.* (UA4 Collaboration), Phys. Lett. (1985).

[156] F. Abe *et al.* (UA1 Collaboration), Phys. Rev. D **50**, 5518 (1994).

[157] G. Arnison *et al.* (UA1 Collaboration), Phys. Lett. (1983).

[158] R. Battiston *et al.*, Phys. Lett. (1983).

[159] N. Amos *et al.*, Phys. Lett. B **128**, 343 (1983).

[160] D. Kaplan *et al.*, Phys. Rev. D (1982).

[161] M. Ambrosio *et al.*, Phys. Lett. (1982).

[162] R. Battiston *et al.*, Phys. Lett. (1982).

[163] E. Nagy *et al.*, Nucl. Phys. B **150**, 221-267 (1979).

[164] U. Amaldi *et al.*, Nucl. Phys. B **145**, 367-401 (1978).

APPENDIX A

OPTICAL THEOREM AND PSEUDORAPIDITY

The optical theorem introduces the relationship between the behavior of the imaginary part of the forward scattering amplitude or the scattering amplitude at $t = 0$, the scattering angle and the total cross section.

$$\mathrm{Im} f_{el}(t = 0) = \frac{p}{4\pi}\sigma_{tot}, \tag{202}$$

where f_{el} is the scattering amplitude of elastic scattering, p is the magnitude of the center of mass three-momentum of the incident particle, and σ_{tot} is the total cross section.

The optical theorem states that the imaginary part of the forward amplitude, which is proportional to the total cross section, grows with energy, while no such constraint exists over the real part [27].

The pseudorapidity η is a commonly used spatial coordinate in experimental particle physics. The pseudorapidity η describes the angle of a particle relative to the beam axis. It is defined as:

$$\eta = -\ln\left[\tan\left(\frac{\theta}{2}\right)\right] \tag{203}$$

where θ is the angle between the particle momentum p and the beam axis. As the scattering angle θ increases from 0 (the forward direction), the pseudorapidity decreases from ∞ (see Fig. (100)).

For a massless particle of energy E and momentum along the z-axis p_{L}, the pseudorapidity is numerically close to the rapidity y, given as:

$$y = \frac{1}{2}\ln\left(\frac{E + p_{\mathrm{L}}}{E - p_{\mathrm{L}}}\right) \tag{204}$$

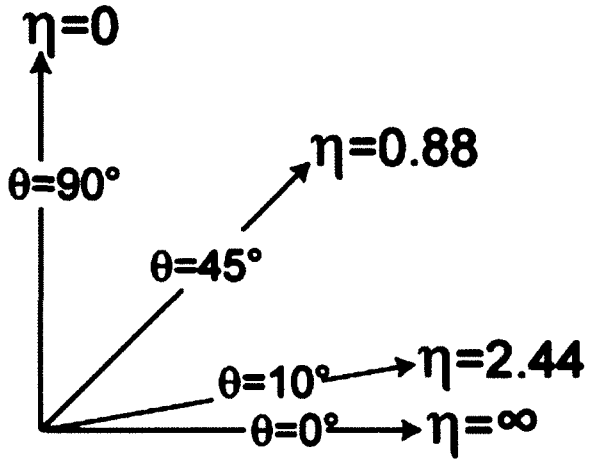

FIG. 100. As the scattering angle θ increases from 0, the pseudorapidity decreases from ∞.

APPENDIX B

OVERVIEW OF PP AND $P\bar{P}$ WORLD EXPERIMENTS

TABLE 29. Overview of pp and $p\bar{p}$ elastic scattering experiments in the world

Collider Accelerator Facility	Type of Experiment	cms Energy $\sqrt{s}$ (GeV)	$\|t\|$ Range (GeV^2)	Year	Ref.
RHIC	pp	200	0.010 - 0.019	2003	[24]
FNAL	$p\bar{p}$	3.1 - 3.8	0.001 - 0.02	1996	[150]
CERN SPS	$p\bar{p}$	541	0.0075 - 0.12	1993	[151]
FNAL	$p\bar{p}$	1800	0.034 - 0.65	1990	[152]
CERN SPS	$p\bar{p}$	546	0.00225 - 0.03475	1987	[153]
CERN ISR	pp and $p\bar{p}$	53	0.5 - 4.0	1985	[154]
CERN SPS	$p\bar{p}$	546	0.45 - 1.55	1985	[155]
CERN ISR	$p\bar{p}$	30.6, 52.8, 62.3	0.00037 - 0.055	1985	[57]
	pp	23.5			[57]
FNAL	$p\bar{p}$	546 and 1800	0.025 - 0.29	1984	[156]
CERN ISR	pp and $p\bar{p}$	540	0.04 - 0.45	1983	[157]
CERN SPS	$p\bar{p}$	540	0.21 - 0.5	1983	[158]
CERN ISR	pp and $p\bar{p}$	30.7	0.0007 - 0.02	1983	[159]
		62.5	0.008 - 0.06	1983	[159]
FNAL	pp and $p\bar{p}$	100	0.5 - 2.5	1982	[160]
		200	0.9 - 4.0		[160]
CERN ISR	pp and $p\bar{p}$	52.8	0.01 - 1.0	1982	[161]
CERN SPS	$p\bar{p}$	540	0.05 - 0.19	1982	[162]
CERN ISR	pp	23 - 63	0.8 - 10	1979	[163]
CERN ISR	pp σ_{tot}	23 - 63		1978	[164]

APPENDIX C

DERIVATION OF VARIABLES IN POLARIZED *PP* ELASTIC SCATTERING

Note on Spin Formalism for PP2PP

(by I.G. Alekseev, V.P. Kanavets, L.I. Koroleva, B.V. Morozov, D.N. Svirida)

Below we will give several relations suitable for the determination of spin parameters in the PP2PP experiment.

General Formulae

The spin-dependent differential cross-section for two vertically polarized beams is given by:

$$\sigma = \sigma_0[1 + A_N(\vec{P}_b + \vec{P}_y)\cdot\vec{n} + A_{NN}\cdot(\vec{P}_b\cdot\vec{n})(\vec{P}_y\cdot\vec{n})], \tag{205}$$

where $\vec{n} = (\vec{k}_b \times \vec{k}_s)/|\vec{k}_b \times \vec{k}_s|$ is the normal to scattering plane, $\vec{k}_b$ and $\vec{k}_s$ are the momenta of the beam and the scattering proton, $\vec{P}_b$ and $\vec{P}_y$ are polarization vectors of two colliding beams at RHIC, named blue and yellow.

The counting rate for $\uparrow\uparrow$ spin combination is given by:

$$N_{++} = N_0[1 + A_N(\vec{P}_b^{\,(+)} + \vec{P}_y^{\,(+)})\cdot\vec{n} + A_{NN}\cdot(\vec{P}_b^{\,(+)}\cdot\vec{n})(\vec{P}_y^{\,(+)}\cdot\vec{n})], \tag{206}$$

and the counting rates formulae for the other spin combinations are equivalent. If $|\vec{P}_b^{\,(+)}| = |\vec{P}_b^{\,(-)}| = \vec{P}_b$ and $|\vec{P}_y^{\,(+)}| = |\vec{P}_y^{\,(-)}| = \vec{P}_y$, the counting rates can be written:

$$\begin{aligned}
N_{++} &= N_0[1 + A_N(\vec{P}_b + \vec{P}_y)\cdot\cos\phi + A_{NN}\cdot\vec{P}_b\vec{P}_y\cdot\cos^2\phi)], \\
N_{--} &= N_0[1 - A_N(\vec{P}_b + \vec{P}_y)\cdot\cos\phi + A_{NN}\cdot\vec{P}_b\vec{P}_y\cdot\cos^2\phi], \\
N_{+-} &= N_0[1 + A_N(\vec{P}_b - \vec{P}_y)\cdot\cos\phi - A_{NN}\cdot\vec{P}_b\vec{P}_y\cdot\cos^2\phi], \\
N_{-+} &= N_0[1 - A_N(\vec{P}_b - \vec{P}_y)\cdot\cos\phi - A_{NN}\cdot\vec{P}_b\vec{P}_y\cdot\cos^2\phi],
\end{aligned} \tag{207}$$

where ϕ-angle is the angle between the normal to the scattering plane and the vertical direction (up).

Spin parameters can be expressed from Eq. (207):

$$A_N \vec{P}_b \cdot \cos\phi = (N_{++} - N_{--} + N_{+-} - N_{-+})/N, \quad (208)$$

$$A_N \vec{P}_y \cdot \cos\phi = (N_{++} - N_{--} - N_{+-} + N_{-+})/N, \quad (209)$$

$$A_{NN} \vec{P}_b \vec{P}_y \cdot \cos^2\phi = (N_{++} + N_{--} - N_{+-} - N_{-+})/N, \quad (210)$$

where $N = N_{++} + N_{--} + N_{+-} + N_{-+}$. N_{ij} are the normalized counting rates. They take into account the luminosity for each spin combination.

It is easy to obtain from Eq. (207) the formulae containing only N_{++}, N_{--}, N_{+-} and N_{-+} combinations.

$$\frac{A_N(\vec{P}_b + \vec{P}_y) \cdot \cos\phi}{1 + A_{NN} \vec{P}_b \vec{P}_y \cdot \cos^2\phi} = (N_{++} - N_{--})/(N_{++} + N_{--}), \quad (211)$$

$$\frac{A_N(\vec{P}_b - \vec{P}_y) \cdot \cos\phi}{1 - A_{NN} \vec{P}_b \vec{P}_y \cdot \cos^2\phi} = (N_{+-} - N_{-+})/(N_{+-} + N_{-+}). \quad (212)$$

In our conditions the value of $A_{NN} \vec{P}_b \vec{P}_y \cos\phi$ is much less than 1. It means that we are able to get A_N, only from experimental data on N_{++} and N_{--} with relative systematic error of $\pm 0.6\%$, if we neglect this factor.

Usually one refers to the right hand part of Eq. (211) and (212) as the "raw asymmetry". It is clear from this formulae that the relative error of A_N is equal to the relative error of "raw asymmetry". In our case the statistics for determination of the "raw asymmetry" in Eq. (211) and (212) is approximately the same, but the value of the "raw asymmetry" in Eq. (212) is $(\vec{P}_b - \vec{P}_y)/(\vec{P}_b + \vec{P}_y)$ times less than the one in Eq. (211). So we can obtain A_N from Eq. (212) with the error $(\vec{P}_b + \vec{P}_y)/(\vec{P}_b - \vec{P}_y)$ times larger than from Eq. (211). **In other words, in case of nearly equal blue and yellow beams polarization practically only N_{++} and N_{--} combinations carry information on A_N parameter. The counting rates N_{+-} and N_{-+} carry information about the difference of polarizations of blue and yellow beams. They may be used as indications of systematic errors of the result only if we are sure that the polarization of the two beams are equal to each other with good precision.**

It is interesting to compare the precision of A_N in the case of one beam polarized and the other unpolarized, in the very small beam polarization limit (i.e. yellow beam) and in the case of our spin pattern variant at equal statistics. In our case

we only use half of the total statistics, but the "raw asymmetry" is two times larger. Thus we have a gain of $\sqrt{2}$ times in statistical precision of A_N measurement. Of course if the spin pattern consisted of only $\uparrow\uparrow$ and $\downarrow\downarrow$ combinations, it would be possible to get even better precision in A_N with an additional gain of $\sqrt{2}$.

Square Root Formula

The main advantage of using Eq. (211) and (212) is the possibility to use the so called "square root" formulae [18] to extract the physical asymmetry for unnormalized counting rates. This formula is based on theoretical knowledge of the counting rates azimuthal angle dependence. We can write the numbers of eight measured combinations in the form:

$$
\begin{aligned}
L_{++} &= \eta_L I_{++}[1 + A_N(\vec{P}_b + \vec{P}_y)\cdot\cos\phi + A_{NN}\vec{P}_b\vec{P}_y\cdot\cos^2\phi], && (213)\\
L_{--} &= \eta_L I_{--}[1 - A_N(\vec{P}_b + \vec{P}_y)\cdot\cos\phi + A_{NN}\vec{P}_b\vec{P}_y\cdot\cos^2\phi], && (214)\\
L_{+-} &= \eta_L I_{+-}[1 + A_N(\vec{P}_b - \vec{P}_y)\cdot\cos\phi - A_{NN}\vec{P}_b\vec{P}_y\cdot\cos^2\phi], && (215)\\
L_{-+} &= \eta_L I_{-+}[1 - A_N(\vec{P}_b - \vec{P}_y)\cdot\cos\phi - A_{NN}\vec{P}_b\vec{P}_y\cdot\cos^2\phi], && (216)\\
R_{++} &= \eta_R I_{++}[1 - A_N(\vec{P}_b + \vec{P}_y)\cdot\cos\phi + A_{NN}\vec{P}_b\vec{P}_y\cdot\cos^2\phi], && (217)\\
R_{--} &= \eta_R I_{--}[1 + A_N(\vec{P}_b + \vec{P}_y)\cdot\cos\phi + A_{NN}\vec{P}_b\vec{P}_y\cdot\cos^2\phi], && (218)\\
R_{+-} &= \eta_R I_{+-}[1 - A_N(\vec{P}_b - \vec{P}_y)\cdot\cos\phi - A_{NN}\vec{P}_b\vec{P}_y\cdot\cos^2\phi], && (219)\\
R_{-+} &= \eta_R I_{-+}[1 + A_N(\vec{P}_b - \vec{P}_y)\cdot\cos\phi - A_{NN}\vec{P}_b\vec{P}_y\cdot\cos^2\phi], && (220)
\end{aligned}
$$

where L $\rightarrow$ R corresponds to $\cos\phi \rightarrow -\cos\phi$, η_L and η_R represent the efficiency (and/or acceptance) of the left and right detectors, I_{ij}-luminosities of the corresponding spin combination.

It follows from Eqs. (213, 214, 217 and 218):

$$
\begin{aligned}
\sqrt{L_{++}R_{--}} &= \sqrt{\eta_L\eta_R I_{++}I_{--}}[1 + A_{NN}\vec{P}_b\vec{P}_y\cos^2\phi + A_N(\vec{P}_b + \vec{P}_y)\cos\phi],\\
\sqrt{L_{--}R_{++}} &= \sqrt{\eta_L\eta_R I_{++}I_{--}}[1 + A_{NN}\vec{P}_b\vec{P}_y\cos^2\phi - A_N(\vec{P}_b + \vec{P}_y)\cos\phi],\\
\frac{\sqrt{L_{++}R_{--}} - \sqrt{L_{--}R_{++}}}{\sqrt{L_{++}R_{--}} + \sqrt{L_{--}R_{++}}} &= \frac{A_N(\vec{P}_b + \vec{P}_y)\cdot\cos\phi}{1 + A_{NN}.\vec{P}_b\vec{P}_y\cdot\cos^2\phi} = \epsilon_1. \qquad (221)
\end{aligned}
$$

From other products of L_{ij} and R_{ij} we get the following formulae:

$$\eta_L/\eta_R = \frac{\sqrt{L_{++}L_{--}}}{\sqrt{R_{++}R_{--}}}, \tag{222}$$

$$I_{++}/I_{--} = \frac{\sqrt{L_{++}R_{++}}}{\sqrt{L_{--}R_{--}}}. \tag{223}$$

Comparison of the Eqs. 221 and 211 shows that ϵ_1 is a raw asymmetry in the case of using N_{++} and N_{--} counting rates for A_N determination.

Using Eqs. (215, 216, 219 and 220) we get analogous formulae:

$$\frac{\sqrt{L_{+-}R_{-+}} - \sqrt{L_{-+}R_{+-}}}{\sqrt{L_{+-}R_{-+}} + \sqrt{L_{-+}R_{+-}}} = \frac{A_N(\vec{P}_b - \vec{P}_y)\cdot\cos\phi}{1 - A_{NN}\vec{P}_b\vec{P}_y\cdot\cos^2\phi} = \epsilon_2, \tag{224}$$

$$\eta_L/\eta_R = \frac{\sqrt{L_{+-}L_{-+}}}{\sqrt{R_{+-}R_{-+}}}, \tag{225}$$

$$I_{+-}/I_{-+} = \frac{\sqrt{L_{+-}R_{+-}}}{\sqrt{L_{-+}R_{-+}}}, \tag{226}$$

ϵ_2 is a raw asymmetry in the case of using N_{+-} and N_{-+} counting rates for A_N determination.

APPENDIX D

SETUP INFRASTRUCTURE AND RUNNING CONDITIONS DURING RUN09

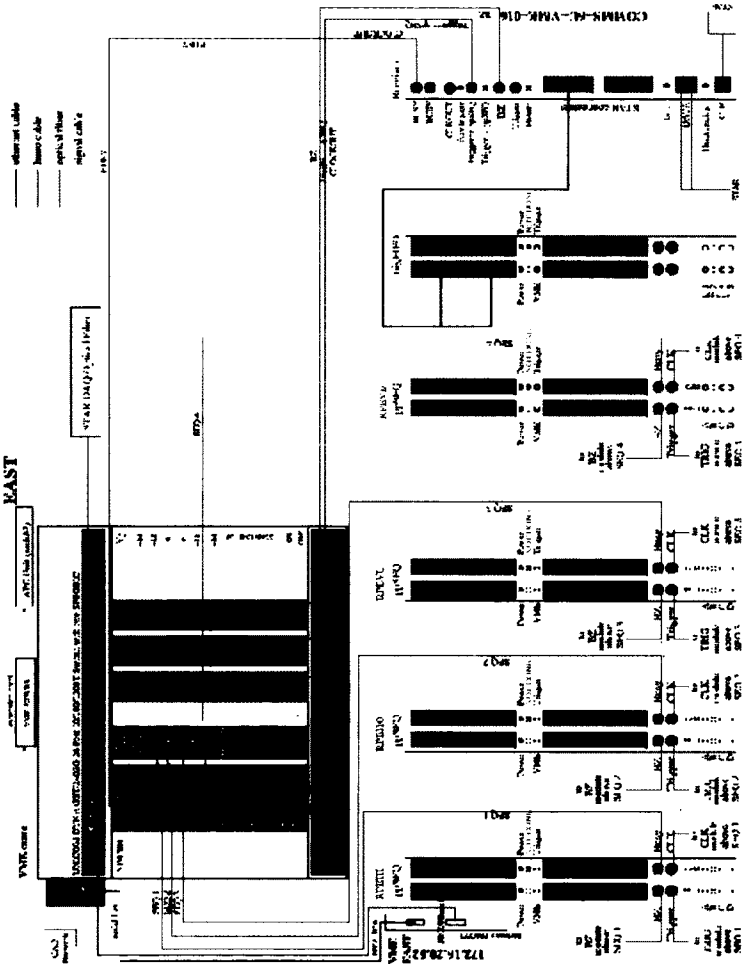

FIG. 101. Setup and infrastructure for the RPs and detector packages in the East of STAR.

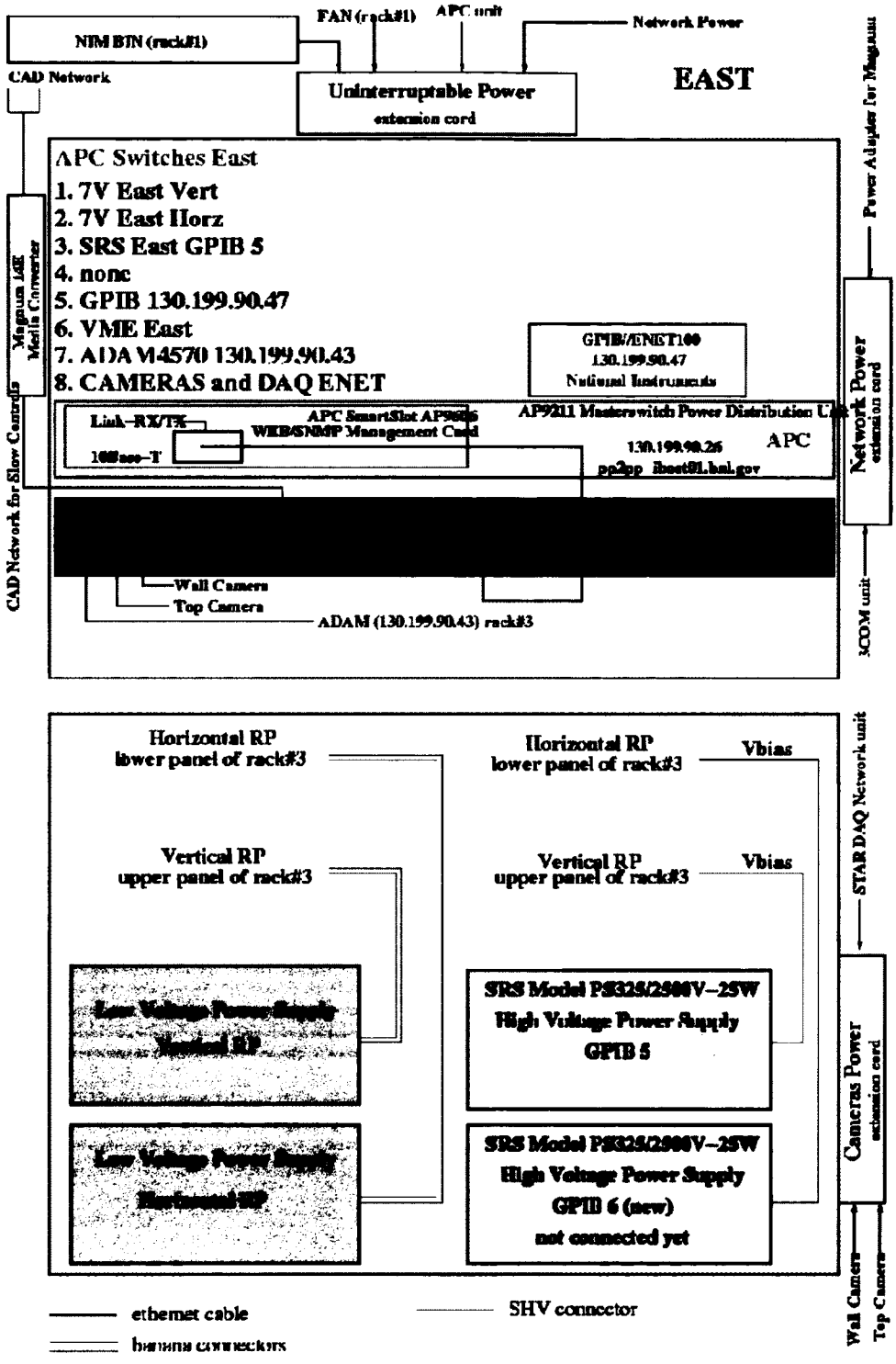

FIG. 102. Setup and infrastructure for the low/high voltage supplies in the East.

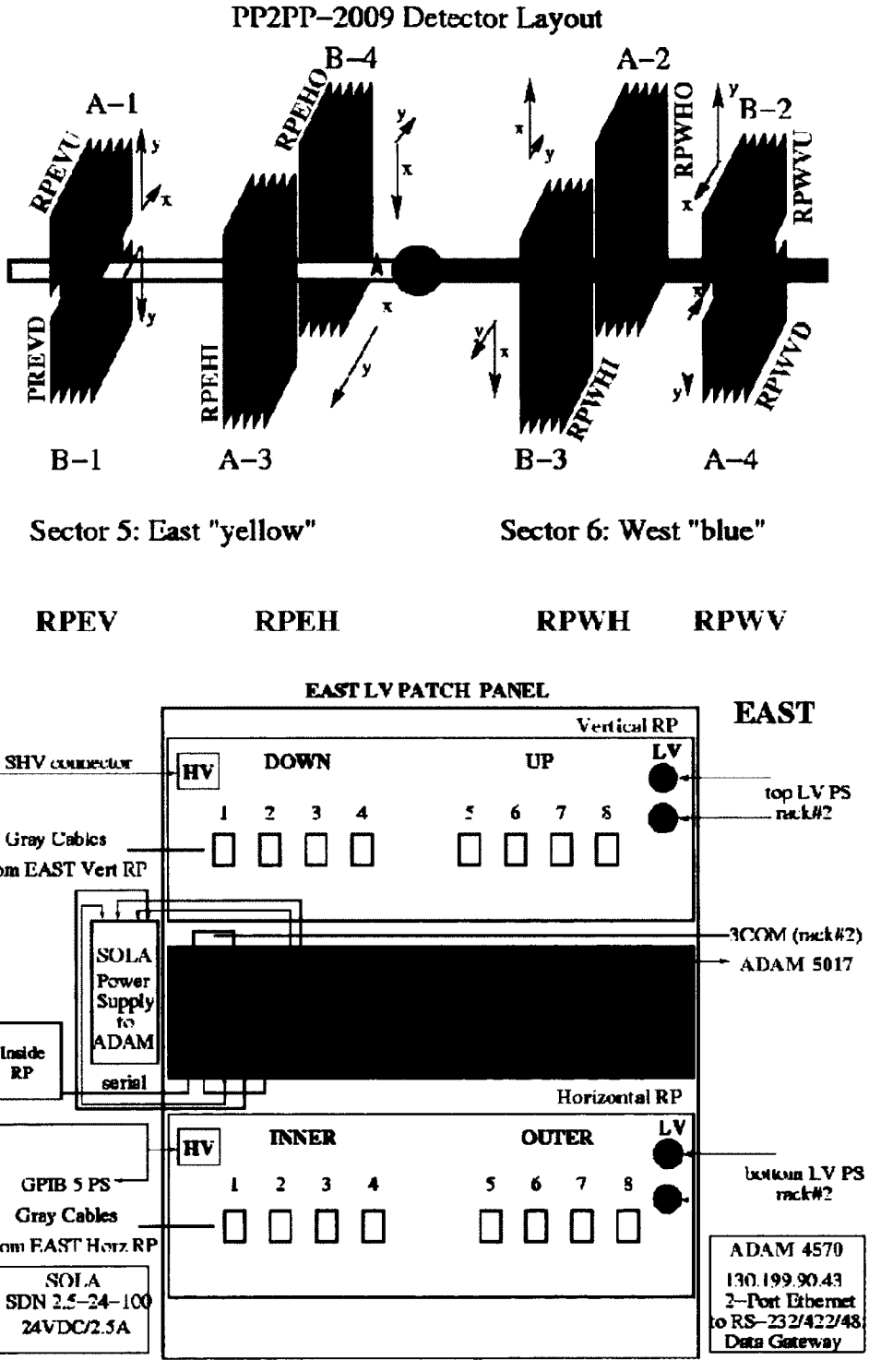

FIG. 103. Top figure shows the RP setup for Run09 (both East and West). Bottom figure shows the setup and infrastructure of the low voltage patch panels and sequence of the detector packages connected to low voltage supplies.

Run #	Date	Start	Stop	Dura	# Events	# Elastic	Elas Frac	Comment	Store	Pos
10181085	30-Jun	22:53	23:21	0:28	999833	548950	0.55		1	1
10181086	30-Jun	23:23	0:16	0:53	1999935	972055	0.49		1	1
10182001	1-Jul	0:17	0:32	0:15	559257	270138	0.48		1	1
10182002	1-Jul	0:34	1:29	0:55	1999945	970560	0.49		1	1
10182003	1-Jul	1:31	1:33	0:02	10001		0.00	pedestal	1	1
10182004	1-Jul	1:34	2:32	0:58	1999950	964171	0.48		1	1
10182005	1-Jul	2:33	3:32	0:59	1999839	962600	0.48		1	1
10182006	1-Jul	3:34	4:36	1:02	1999942	950144	0.48		1	1
10182011	1-Jul	5:58	6:00	0:02	10001		0.00	pedestal	1	1
10182015	1-Jul	7:13	8:15	1:02	1999916	1016735	0.51		1	2
10182016	1-Jul	8:20	9:31	1:11	1999957	980482	0.49		1	2
10182021	1-Jul	10:12	10:36	0:24	675560	333461	0.49		1	2
10182025	1-Jul	10:57	12:02	1:05	1593827	741882	0.47		1	2
10183005	2-Jul	0:16	0:17	0:01	10001		0.00	pedestal	2	3
10183013	2-Jul	1:44	2:03	0:19	778275	312823	0.40	no STAR	2	3
10183014	2-Jul	2:04	2:17	0:13	484155	204489	0.42	no STAR	2	3
10183015	2-Jul	2:20	3:12	0:52	1999933	799304	0.40		2	3
10183016	2-Jul	3:13	4:08	0:55	1999935	795409	0.40		2	3
10183017	2-Jul	4:10	5:09	0:59	1999969	793377	0.40		2	3
10183018	2-Jul	5:23	6:19	0:56	1999933	842789	0.42		2	4
10183019	2-Jul	6:22	6:24	0:02	10001		0.00	pedestal	2	4
10183020	2-Jul	6:27	7:27	1:00	1999960	838079	0.42		2	4
10183021	2-Jul	7:29	8:32	1:03	1999942	833429	0.42		2	4
10183025	2-Jul	8:50	8:51	0:01	10001		0.00	pedestal	2	5
10183027	2-Jul	9:10	9:46	0:36	1394100	638263	0.46		2	5
10183028	2-Jul	9:53	11:24	1:31	3428889	1578849	0.46		2	5
10183034	2-Jul	12:59	13:33	0:34	998537	448586	0.45		2	6
10183035	2-Jul	13:36	14:16	0:40	1096472	479953	0.44		2	7
10183036	2-Jul	14:17	14:18	0:01	267		0.00	CP trig test	2	7
10183037	2-Jul	14:20	15:34	1:14	1999962	879881	0.44		2	7
10183038	2-Jul	15:35	15:42	0:07	160125	70097	0.44	beam abort	2	7
10183061	2-Jul	21:05	21:07	0:02	10001		0.00	X-shift 15	3	8
10183062	2-Jul	21:07	21:07	0:00	154		0.00	X-shift 17	3	8
10183065	2-Jul	21:16	21:17	0:01	10001		0.00	X-shift 11	3	8
10183066	2-Jul	21:18	21:20	0:02	10001		0.00	X-shift 13	3	8
10184002	3-Jul	1:08	1:10	0:02	10001		0.00	pedestal	4	9
10184016	3-Jul	4:09	4:52	0:43	1855459	805218	0.43		4	10
10184017	3-Jul	4:53	5:43	0:50	1999853	866765	0.43		4	10
10184018	3-Jul	5:45	6:36	0:51	1999925	804721	0.40		4	11
10184019	3-Jul	6:37	7:28	0:51	1999957	798679	0.40		4	11
10184020	3-Jul	7:30	8:24	0:54	1999951	796463	0.40		4	11
10184021	3-Jul	8:25	8:30	0:05	181881	72200	0.40		4	11
10184030	3-Jul	10:55	11:54	0:59	1999956	883236	0.44		4	12

Run #	Date	Start	Stop	uration	# Events	# Elastic	Elas Frac	Comment	Store	Pos
10184031	3-Jul	11:54	12:53	0:59	1999935	885745	0.44		4	12
10184032	3-Jul	12:54	13:53	0:59	1999939	887591	0.44		4	12
10184033	3-Jul	13:54	14:53	0:59	1999969	899709	0.45		4	12
10184034	3-Jul	14:53	14:55	0:02	288	1	0.00	beam abort	4	12
10184038	3-Jul	15:25	15:27	0:02	10001		0.00	pedestal	5	13
10184044	3-Jul	18:35	18:37	0:02	10001		0.00	pedestal	5	13
10185001	4-Jul	0:29	0:30	0:01	27297	10982	0.40	TPC limit	6	14
10185002	4-Jul	0:32	0:32	0:00	8866	3991	0.45	rate limit	6	14
10185003	4-Jul	0:34	0:40	0:06	253838	116882	0.46	TPC limit	6	14
10185004	4-Jul	0:42	1:28	0:46	1999884	978901	0.49		6	14
10185005	4-Jul	1:29	2:16	0:47	1999912	971976	0.49		6	14
10185006	4-Jul	2:17	3:10	0:53	1999923	958470	0.48		6	14
10185007	4-Jul	3:16	3:46	0:30	1125		0.00	Vernier scan	6	15
10185008	4-Jul	3:47	3:52	0:05	320		0.00	VPD min bias	6	15
10185013	4-Jul	4:32	4:35	0:03	10001		0.00	pedestal	6	15
10185015	4-Jul	5:00	5:02	0:02	10001		0.00	pedestal	6	16
10185016	4-Jul	5:17	5:25	0:08	59102	31092	0.53	no-0 supp	6	16
10185018	4-Jul	5:28	6:14	0:46	1999921	1068287	0.53		6	16
10185019	4-Jul	6:19	7:04	0:45	1999908	1064505	0.53		6	17
10185020	4-Jul	7:04	7:48	0:44	1999758	1086820	0.54		6	17
10185023	4-Jul	7:58	8:32	0:34	1469066	799732	0.54	beam abort	6	17

FIG. 104. Running conditions during Run09, I. Run information: run number; starting and stopping date and time for each run; run duration; number of events taken in each run; number and fraction of elastic events for each run; run type/comment; store number and RP positions for each run.

Run #	Date	Start	Pos	B Left	B Right	B Top	B Bot	Y Left	Y Right	Y Top	Y Bot
10181085	30-Jun	22:53	1	10.3	10.3	15.4	15.2	10.4	10.6	10.3	10.5
10181086	30-Jun	23:23	1	10.3	10.3	15.4	15.2	10.4	10.6	10.3	10.5
10182001	1-Jul	0:17	1	10.3	10.3	15.4	15.2	10.4	10.6	10.3	10.5
10182002	1-Jul	0:34	1	10.3	10.3	15.4	15.2	10.4	10.6	10.3	10.5
10182003	1-Jul	1:31	1	10.3	10.3	15.4	15.2	10.4	10.6	10.3	10.5
10182004	1-Jul	1:34	1	10.3	10.3	15.4	15.2	10.4	10.6	10.3	10.5
10182005	1-Jul	2:33	1	10.3	10.3	15.4	15.2	10.4	10.6	10.3	10.5
10182006	1-Jul	3:34	1	10.3	10.3	15.4	15.2	10.4	10.6	10.3	10.5
10182011	1-Jul	5:58	1	10.3	10.3	15.4	15.2	10.4	10.6	10.3	10.5
10182015	1-Jul	7:13	2	8.9	10.3	10.2	10.2	10.2	10.3	5.0	10.3
10182016	1-Jul	8:20	2	8.9	10.3	10.2	10.2	10.2	10.3	5.0	10.3
10182021	1-Jul	10:12	2	8.9	10.3	10.2	10.2	10.2	10.3	5.0	10.3
10182025	1-Jul	10:57	2	8.9	10.3	10.2	10.2	10.2	10.3	5.0	10.3
10183005	2-Jul	0:16	3	10.2	10.3	10.2	10.2	16.9	17.2	15.9	16.6
10183013	2-Jul	1:44	3	10.2	10.3	10.2	10.2	16.9	17.2	15.9	16.6
10183014	2-Jul	2:04	3	10.2	10.3	10.2	10.2	16.9	17.2	15.9	16.6
10183015	2-Jul	2:20	3	10.2	10.3	10.2	10.2	16.9	17.2	15.9	16.6
10183016	2-Jul	3:13	3	10.2	10.3	10.2	10.2	16.9	17.2	15.9	16.6
10183017	2-Jul	4:10	3	10.2	10.3	10.2	10.2	16.9	17.2	15.9	16.6
10183018	2-Jul	5:23	4	10.2	10.3	10.2	10.2	14.5	14.7	10.9	12.8
10183019	2-Jul	6:22	4	10.2	10.3	10.2	10.2	14.5	14.7	10.9	12.8
10183020	2-Jul	6:27	4	10.2	10.3	10.2	10.2	14.5	14.7	10.9	12.8
10183021	2-Jul	7:29	4	10.2	10.3	10.2	10.2	14.5	14.7	10.9	12.8
10183025	2-Jul	8:50	5	6.4	9.0	8.9	8.9	7.6	12.8	7.8	9.6
10183027	2-Jul	9:10	5	6.4	9.0	8.9	8.9	7.6	12.8	7.8	9.6
10183028	2-Jul	9:53	5	6.4	9.0	8.9	8.9	7.6	12.8	7.8	9.6
10183034	2-Jul	12:59	6	8.9	8.4	10.2	10.2	7.0	7.8	7.1	7.1
10183035	2-Jul	13:36	7	8.9	8.4	10.2	10.2	8.0	8.8	8.1	8.1
10183036	2-Jul	14:17	7	8.9	8.4	10.2	10.2	8.0	8.8	8.1	8.1
10183037	2-Jul	14:20	7	8.9	8.4	10.2	10.2	8.0	8.8	8.1	8.1
10183038	2-Jul	15:35	7	8.9	8.4	10.2	10.2	8.0	8.8	8.1	8.1
10183061	2-Jul	21:05	8	20.0	20.0	20.0	20.0	20.0	20.0	20.0	20.0
10183062	2-Jul	21:07	8	20.0	20.0	20.0	20.0	20.0	20.0	20.0	20.0
10183065	2-Jul	21:16	8	20.0	20.0	20.0	20.0	20.0	20.0	20.0	20.0
10183066	2-Jul	21:18	8	20.0	20.0	20.0	20.0	20.0	20.0	20.0	20.0
10184002	3-Jul	1:08	9	25.0	25.0	25.0	25.0	25.0	25.0	25.0	25.0
10184016	3-Jul	4:09	10	10.3	10.3	14.1	11.4	19.5	16.0	16.5	19.1
10184017	3-Jul	4:53	10	10.3	10.3	14.1	11.4	19.5	16.0	16.5	19.1
10184018	3-Jul	5:45	11	10.3	10.3	15.3	12.6	19.5	16.0	16.5	19.1
10184019	3-Jul	6:37	11	10.3	10.3	15.3	12.6	19.5	16.0	16.5	19.1
10184020	3-Jul	7:30	11	10.3	10.3	15.3	12.6	19.5	16.0	16.5	19.1
10184021	3-Jul	8:25	11	10.3	10.3	15.3	12.6	19.5	16.0	16.5	19.1
10184030	3-Jul	10:55	12	9.1	9.1	9.6	8.9	8.3	8.3	8.4	8.4
10184031	3-Jul	11:54	12	9.1	9.1	9.6	8.9	8.3	8.3	8.4	8.4
10184032	3-Jul	12:54	12	9.1	9.1	9.6	8.9	8.3	8.3	8.4	8.4
10184033	3-Jul	13:54	12	9.1	9.1	9.6	8.9	8.3	8.3	8.4	8.4
10184034	3-Jul	14:53	12	9.1	9.1	9.6	8.9	8.3	8.3	8.4	8.4

Run #	Date	Start	Pos	B Left	B Right	B Top	B Bot	Y Left	Y Right	Y Top	Y Bot
10184038	3-Jul	15:25	13	25.0	25.0	25.0	25.0	25.0	25.0	25.0	25.0
10184044	3-Jul	18:35	13	25.0	25.0	25.0	25.0	25.0	25.0	25.0	25.0
10185001	4-Jul	0:29	14	9.0	9.8	19.3	16.6	20.1	17.9	17.3	19.1
10185002	4-Jul	0:32	14	9.0	9.8	19.3	16.6	20.1	17.9	17.3	19.1
10185003	4-Jul	0:34	14	9.0	9.8	19.3	16.6	20.1	17.9	17.3	19.1
10185004	4-Jul	0:42	14	9.0	9.8	19.3	16.6	20.1	17.9	17.3	19.1
10185005	4-Jul	1:29	14	9.0	9.8	19.3	16.6	20.1	17.9	17.3	19.1
10185006	4-Jul	2:17	14	9.0	9.8	19.3	16.6	20.1	17.9	17.3	19.1
10185007	4-Jul	3:16	15	70.0	70.0	70.0	70.0	70.0	70.0	70.0	70.0
10185008	4-Jul	3:47	15	70.0	70.0	70.0	70.0	70.0	70.0	70.0	70.0
10185013	4-Jul	4:32	15	70.0	70.0	70.0	70.0	70.0	70.0	70.0	70.0
10185015	4-Jul	5:00	16	6.5	8.4	10.2	7.0	13.2	10.9	10.3	12.8
10185016	4-Jul	5:17	16	6.5	8.4	10.2	7.0	13.2	10.9	10.3	12.8
10185018	4-Jul	5:28	16	6.5	8.4	10.2	7.0	13.2	10.9	10.3	12.8
10185019	4-Jul	6:19	17	7.1	8.4	10.8	7.6	13.2	10.9	10.3	12.8
10185020	4-Jul	7:04	17	7.1	8.4	10.8	7.6	13.2	10.9	10.3	12.8
10185023	4-Jul	7:58	17	7.1	8.4	10.8	7.6	13.2	10.9	10.3	12.8

FIG. 105. Running conditions during Run09, II. RP positions for each run and other run information: run number; starting and stopping date and time for each run; RP position; distance of approach of each RP to the center of the RHIC accelerator beam-line in (mm). RP notation is as follows: B Left (RPWHO); B Right (RPWHI); B Top (RPWVU); B Bot (RPWVD); Y Left (RPEHI); Y Right (RPEHO); Y Top (RPEVU); Y Bot (RPEVD).

APPENDIX E

FIRST SI STRIP POSITIONS FOR ALL RP POSITIONS (PHYSICS RUNS) DURING RUN09

TABLE 30. Calculated 1st silicon strip/channel positions x_0 (y_0) for RPEHI

	RPEHI			
RP Position	Plane A (mm)	Plane B (mm)	Plane C (mm)	Plane D (mm)
1	-12.171	-39.287	-12.190	-39.323
2	-11.921	-39.287	-11.940	-39.323
3	-18.879	-39.287	-18.898	-39.323
4	-16.342	-39.287	-16.361	-39.323
5	-14.455	-39.287	-14.474	-39.323
6	-9.389	-39.287	-9.408	-39.323
7	-10.390	-39.287	-10.409	-39.323
10	-17.619	-39.287	-17.638	-39.323
11	-17.619	-39.287	-17.638	-39.323
12	-10.049	-39.287	-10.068	-39.323
14	-19.533	-39.287	-19.552	-39.323
16	-12.561	-39.287	-12.580	-39.323
17	-12.561	-39.287	-12.580	-39.323

TABLE 31. Calculated 1^{st} silicon strip/channel positions x_0 (y_0) for RPEHO

RPEHO				
RP Position	Plane A (mm)	Plane B (mm)	Plane C (mm)	Plane D (mm)
1	13.650	39.635	13.650	39.635
2	13.381	39.635	13.381	39.635
3	20.339	39.635	20.339	39.635
4	17.801	39.635	17.801	39.635
5	10.824	39.635	10.824	39.635
6	10.178	39.635	10.178	39.635
7	11.184	39.635	11.184	39.635
10	22.883	39.635	22.883	39.635
11	22.883	39.635	22.883	39.635
12	11.496	39.635	11.496	39.635
14	23.536	39.635	23.536	39.635
16	16.474	39.635	16.474	39.635
17	16.474	39.635	16.474	39.635

TABLE 32. Calculated 1^{st} silicon strip/channel positions x_0 (y_0) for RPEVU

RPEVU				
RP Position	Plane A (mm)	Plane B (mm)	Plane C (mm)	Plane D (mm)
1	13.045	-39.017	13.070	-38.989
2	7.719	-39.017	7.744	-38.989
3	18.737	-39.017	18.762	-38.989
4	13.684	-39.017	13.709	-38.989
5	10.503	-39.017	10.528	-38.989
6	9.820	-39.017	9.845	-38.989
7	10.837	-39.017	10.862	-38.989
10	19.331	-39.017	19.356	-38.989
11	19.331	-39.017	19.356	-38.989
12	11.139	-39.017	11.164	-38.989
14	20.146	-39.017	20.171	-38.989
16	13.057	-39.017	13.082	-38.989
17	13.057	-39.017	13.082	-38.989

TABLE 33. Calculated 1^{st} silicon strip/channel positions x_0 (y_0) for RPEVD

RPEVD				
RP Position	Plane A (mm)	Plane B (mm)	Plane C (mm)	Plane D (mm)
1	-12.601	40.745	-12.605	40.742
2	-12.334	40.745	-12.338	40.742
3	-18.676	40.745	-18.680	40.742
4	-14.874	40.745	-14.878	40.742
5	-11.717	40.745	-11.721	40.742
6	-9.149	40.745	-9.153	40.742
7	-10.157	40.745	-10.161	40.742
10	-21.177	40.745	-21.181	40.742
11	-21.177	40.745	-21.181	40.742
12	-10.461	40.745	-10.465	40.742
14	-21.221	40.745	-21.225	40.742
16	-14.868	40.745	-14.872	40.742
17	-14.868	40.745	-14.872	40.742

TABLE 34. Calculated 1^{st} silicon strip/channel positions x_0 (y_0) for RPWHI

RPWHI				
RP Position	Plane A (mm)	Plane B (mm)	Plane C (mm)	Plane D (mm)
1	-12.106	39.188	-12.108	39.250
2	-12.070	39.188	-12.072	39.250
3	-12.103	39.188	-12.105	39.250
4	-12.103	39.188	-12.105	39.250
5	-10.833	39.188	-10.835	39.250
6	-10.196	39.188	-10.198	39.250
7	-10.196	39.188	-10.198	39.250
10	-12.120	39.188	-12.122	39.250
11	-12.120	39.188	-12.122	39.250
12	-10.856	39.188	-10.858	39.250
14	-11.619	39.188	-11.621	39.250
16	-10.172	39.188	-10.174	39.250
17	-10.172	39.188	-10.174	39.250

TABLE 35. Calculated 1^{st} silicon strip/channel positions x_0 (y_0) for RPWHO

RPWHO				
RP Position	Plane A (mm)	Plane B (mm)	Plane C (mm)	Plane D (mm)
1	13.249	-38.621	13.232	-38.651
2	11.856	-38.621	11.839	-38.651
3	13.194	-38.621	13.177	-38.651
4	13.194	-38.621	13.177	-38.651
5	9.351	-38.621	9.334	-38.651
6	11.857	-38.621	11.840	-38.651
7	11.857	-38.621	11.840	-38.651
10	13.259	-38.621	13.242	-38.651
11	13.259	-38.621	13.242	-38.651
12	12.018	-38.621	12.001	-38.651
14	12.013	-38.621	11.996	-38.651
16	9.474	-38.621	9.457	-38.651
17	10.103	-38.621	10.086	-38.651

TABLE 36. Calculated 1^{st} silicon strip/channel positions x_0 (y_0) for RPWVD

RPWVD				
RP Position	Plane A (mm)	Plane B (mm)	Plane C (mm)	Plane D (mm)
1	-17.470	-40.530	-17.489	-40.470
2	-12.396	-40.530	-12.415	-40.470
3	-12.403	-40.530	-12.422	-40.470
4	-12.403	-40.530	-12.422	-40.470
5	-11.138	-40.530	-11.157	-40.470
6	-12.396	-40.530	-12.415	-40.470
7	-12.396	-40.530	-12.415	-40.470
10	-13.623	-40.530	-13.642	-40.470
11	-14.889	-40.530	-14.908	-40.470
12	-11.135	-40.530	-11.154	-40.470
14	-18.849	-40.530	-18.868	-40.470
16	-9.233	-40.530	-9.252	-40.470
17	-9.828	-40.530	-9.847	-40.470

TABLE 37. Calculated 1^{st} silicon strip/channel positions x_0 (y_0) for RPWVU

RPWVU				
RP Position	Plane A (mm)	Plane B (mm)	Plane C (mm)	Plane D (mm)
1	18.947	40.064	18.949	40.030
2	13.818	40.064	13.820	40.030
3	13.815	40.064	13.817	40.030
4	13.815	40.064	13.817	40.030
5	12.553	40.064	12.555	40.030
6	13.779	40.064	13.801	40.030
7	13.779	40.064	13.801	40.030
10	17.629	40.064	17.631	40.030
11	18.904	40.064	18.906	40.030
12	13.201	40.064	13.203	40.030
14	22.745	40.064	22.747	40.030
16	13.804	40.064	13.806	40.030
17	14.435	40.064	14.437	40.030

APPENDIX F

CALCULATION OF ENERGY LOSS OF A PROTON IN A SI DETECTOR PLANE

When a proton with momentum 100 GeV/c hits the silicon detector it deposits when passing through the material with a thickness of 400 μm for each silicon detector plane. The detectors measure the dE/dx of the proton going through the silicon plane. The dE/dx of the proton hit can be calculated by the so called *Bethe – Bloch* formula, basic expression used for energy loss calculations of charged particles passing through matter [120].

$$\frac{dE}{dx} = 2\pi N_a r_e^2 m_e c^2 \rho \frac{Z}{A}\frac{z^2}{\beta^2}\left[ln\left(\frac{2m_e\gamma^2 v^2 W_{max}}{I^2}\right) - 2\beta^2 - \delta - 2\frac{C}{Z}\right], \qquad (227)$$

where $2\pi N_a r_e^2 m_e c^2 = 0.1535$ MeVcm$^2/g$ and the following constants are used.

$$\frac{dE}{dx} = \left(0.1535\frac{MeVcm^2}{g}\right)\rho\frac{Z}{A}\frac{1}{\beta^2}\left[ln\left(\frac{2m_e\gamma^2 v^2 W_{max}}{I^2}\right) - 2\beta^2 - \delta - 2\frac{C}{Z}\right]. \qquad (228)$$

Considering also the conditions of our experiment and the parameters of our detector, we have the following:

- r_e: classical electron radius = 2.817×10^{-13} cm
- m_e: electron mass = 0.511 MeV/c^2
- N_a: Avogadro's number = 6.022×10^{23} mol^{-1}
- I: mean excitation potential
  I = 173 eV for Si [120]
- Z: atomic number of absorbing material
  Z = 14 for Si
- A: atomic weight of absorbing material
  A = 28.0855 amu for Si

- ρ: density of absorbing material
  $\rho = 2.33\ g/cm^3$

- z: charge of the incident particle in the units of e
  $z = +1e$

- $\beta = v/c$ of the incident particle
  $\beta = 1$

- $\gamma = 1/\sqrt{1-\beta^2}$
  $\beta\gamma = 106.8$ for 100 GeV/c protons

- δ: density correction, $\delta = 4.6052 \cdot X + C + a(X_1 - X)^m$ [120]
  $\delta = 4.9871$ where $X = log_{10}(\beta\gamma) = 2.028571$; $X_1 = 2.87$, $m = 3.25$, $a = 0.1492$ for Si

- C: shell correction
  C = -4.44 for Si

- W_{max}: maximum energy transfer in a single collision, $W_{max} = 2m_e c^2(\beta\gamma)^2$ where $\beta\gamma = 106.8$
  $W_{max} = 11.657177$ GeV

- $2\frac{C}{Z}$ = -0.6342857

Replacing the above in Eq. (228), we get:

$-\frac{dE}{dx} = 5.295$ MeV/cm

Energy loss of a 100 GeV/c proton passing through 400 μm Si is $\Delta E = 0.212$ MeV.

VITA

Donika Plyku
Department of Physics
Old Dominion University
Norfolk, VA 23529

Education

- Ph.D., Department of Physics, Old Dominion University, Norfolk, VA, May 2013
- M.S., Department of Physics, Old Dominion University, Norfolk, VA, Dec. 2007
- Integrated B.S. and M.S. in Physics Education, Middle East Technical University, Ankara, Turkey, Jan. 2005

Academic Fellowships and Awards

- (Spring - Summer 2008) Virginia Modeling, Analysis and Simulation Center Graduate Fellowship
- (2007) College of Sciences and Old Dominion University's Outstanding Graduate Teaching Assistant

Conference Presentations

- (2012) Fall Meeting of the DNP 2012, APS, Newport Beach, CA
- (2010) 19^{th} International Spin Physics Symposium, Jülich, Germany
- (2008) 18^{th} International Spin Physics Symposium, Charlottesville, VA

Publications

- L. Adamczyk *et al.*, STAR Collaboration, *Single Spin Asymmetry A_N in Polarized Proton-Proton Elastic Scattering at $\sqrt{s}$ = 200 GeV*, Phys. Lett. B **D12**, 01054R1 (2013)
- D. Plyku (for the STAR Collaboration), *Performance of Silicon Detectors in Polarized Proton-Proton Elastic Scattering at RHIC*, J. Phys. Conf. Ser. **295** 012129 (2011)
- D. Plyku, (for the STAR Collaboration), *Polarized Proton-Proton Elastic Scattering at RHIC*, AIP Conf. Proc. **1149**, 676-679 (2009)

Typeset using LaTeX.